UNIFORM HIGH-ASPECT-RATIO 3D MICRO-AND NANOMANUFACTURING ON SILICON BY (ELECTRO)-METAL-ASSISTED CHEMICAL ETCHING: FUNDAMENTALS AND APPLICATIONS

A Dissertation
Presented to
The Academic Faculty

by

Liyi Li

In Partial Fulfillment
of the Requirements for the Degree
Doctor of Philosophy in the
School of Materials Science and Engineering

Georgia Institute of Technology
August, 2016

UNIFORM HIGH-ASPECT-RATIO 3D MICRO-AND NANOMANUFACTURING ON SILICON BY (ELECTRO)-METAL-ASSISTED CHEMICAL ETCHING: FUNDAMENTALS AND APPLICATIONS

Approved by:

Dr. Ching-Ping Wong, Advisor
School of Materials Science and Engineering
Georgia Institute of Technology

Dr. Rosario A. Gerhardt
School of Materials Science and Engineering
Georgia Institute of Technology

Dr. Zhong Lin Wang
School of Materials Science and Engineering
Georgia Institute of Technology

Dr. Farrokh Ayazi
School of Electrical and Computer Engineering
Georgia Institute of Technology

Dr. Preet Singh
School of Materials Science and Engineering
Georgia Institute of Technology

Date Approved: June 06, 2016

To my parents for their endless love

ACKNOWLEDGEMENTS

I wish to thank Prof. C.P. Wong, my advisor, for the generous support and continuous guidance to my study as a PhD student. His dedication to research and insight have fundamentally inspired me. I truly appreciate my committee members, Prof. Zhong Lin Wang, Prof. Preet Singh, Prof. Rosario A. Gerhardt, Prof. Farrokh Ayazi for their helpful suggestions and efforts in my research.

I am grateful to Prof. Jian Pei (Peking University, China) and Dr. Jia Luo (Peking University, China) for their inspiring education during my study as an undergraduate student, which has led my way towards continual research.

I highly appreciate my colleagues in Dr. C.P. Wong's group, including Dr. Kyoung-Sik Moon, Dr. Yagang Yao, Dr. Owen Hildreth, Dr. Wei Lin, Dr. Yan Liu, Dr. Ziyin Lin, Dr. Zhuo Li, Dr. Zhenkun Wu, Ms. Chia-Chi Tuan, Mr. Bo Song, Dr. Gang Lian, Mr. Cheng Zhang, Mr. Jinho Hah, Mr. Colin Holmes, Ms. Xueying Zhao, Dr. Guoyun Zhou, Dr. Guoping Zhang, Dr. Pin Hao and Dr. Xin Fang for their cooperation and help. I also appreciate the help from my collaborator, including Prof. Zhiqin Lin (School of Materials Science and Engineering, Georgia Tech), Dr. Bo Li (School of Materials Science and Engineering, Georgia Tech), Mr. Erwan Le Roy (Thin Film Electronics ASA) and Mr. Benoit Hamelin (School of Electrical and Computer Engineering, Georgia Tech).

My acknowledgement is extended to the staff in Institute of Electronics and Nanotechnology at Georgia Tech for their great technical training and consultancy: Mr. Gary Spinner, Mr. Charlie Suh, Mr. Devin Brown, Dr. Hang Chen, Mr. John Pham, Mr. Tran-Vinh Nguyen, Dr. Walter Henderson and Mr. Eric Woods.

I would like to thank the sponsors of my research: National Science Foundation, Advanced Research Projects Agency-Energy-U.S. Department of Energy and Solid State Equipment Company.

Finally, this dissertation is dedicated to my parents for their love and support.

TABLE OF CONTENTS

Page

ACKNOWLEDGEMENTS iv

LIST OF TABLES x

LIST OF FIGURES xi

LIST OF SYMBOLS AND ABBREVIATIONS xxv

SUMMARY xxvii

CHAPTER

1 Introduction 1

1.1 Manufacturing of High-Aspect Ratio Micro- and Nanostructures on Silicon 1

1.2 Current HAR structures fabrication technology on Si and limitations 2

1.2.1 Dry etching 3

1.2.2 Wet etching-KOH Etching 6

1.2.3 Wet Etching-Acidic Electrochemical Etching 8

1.3 Metal-assisted chemical etching: state of the art and challenges 14

2 MaCE by Separate Metal Particles as Catalyst 19

2.1 Introduction 19

2.2 Methods 19

2.3 Results and Discussion 20

2.2.1 Ag NPs Deposition 20

2.2.2 MaCE for HAR pores 21

2.2.3 MaCE by patterned Au NPs with regular shapes 23

2.2.4 Cu filling of the etched pores 24

2.4 Conclusion 26

3 Uniform HAR Vertical MaCE BY Nanoporous Catalyst 28

3.1 Introduction 28

3.2 Methods 29

3.3 Results and Discussion 30

3.4 Conclusion 49

4 Electric-Bias Attenuated MaCE 50

4.1 Introduction 50

4.2 Methods 50

4.3 Results and Discussion 54

4.4 Conclusion 79

5 Charge Transport in Uniform MaCE 80

5.1 Introduction 80

5.2 Methods-Experimental 81

5.3 Methods-Experimental 82

5.4 Results and Discussion 87

5.5 Conclusion 117

6 HAR Sub-micron Trench Etching on SOI Using MaCE for MEMS Resonators 119

6.1 Introduction 119

6.2 Methods 120

6.3 Results and Discussion 123

6.4 Conclusion 128

7 Combining MaCE and FESA 130

7.1 Introduction 130

7.2 Methods 134

7.3 Results and Discussion 135

7.4 Conclusion 148

8 Wafer-Level MaCE 150

8.1 Introduction 150

8.2 Methods 151

8.3 Results and Discussion 153

8.4 Conclusion 178

9 Conclusions and Suggested Future Works 179

9.1 Conclusions 179

9.2 Suggested Future Works 180

APPENDIX A: Molecular Engineering of Aromatic Amine Spacers for High-Performance Graphene-Based Supercapacitors 182

APPENDIX B: Author's Publications 233

REFERENCES 239

VITA 254

LIST OF TABLES

Page

Table 1 Parameters for *D* calculation 50

Table 2 Step height values in the center part used in **Figure 35** (a) 65

Table 3 Step height values in the corner part used in **Figure 35** (a)..... 65

Table 4 Dimensions of subunits C-F shown in Figure 45 before and after EMaCE..... 86

Table 5 IDs, dopant type and doping level of the Si substrates used in this 96

Table 6 Geometric data of patterns before MaCE and trenches after MaCE on U-Si ... 104

Table 7 Geometric data of patterns before MaCE and trenches after MaCE on P-Si.... 105

Table 8 Geometric data of patterns before MaCE and trenches after MaCE on N-Si ... 106

Table A. 1 Equivalent series resistance (R_s) and charge-transfer resistance (R_{ct}) extracted from Nyquist plot shown in **Figure A. 13** (b). 215

Table A. 2 Weight of reactants and products in modification of GO 220

Table A. 3 Atomic ratio of carbon (C), nitrogen (N) and oxygen (O) of the samples derived from X-ray photoelectron spectra (XPS) data. 223

Table A. 4 Ratio of chemical species from high-resolution N 1s and O 1s peak 229

Table A. 5 Position of peaks in XRD patterns and corresponding interlayer spacing[1]. 242

LIST OF FIGURES

Page

Figure 1 Applications of HAR structures on Si. (a) Through silicon vias. Reprinted with permission from [2]. Copyright 2009, IEEE; (b) MEMS. Reprinted with permission from [8]. Copyright 2001, IEEE; (c) Si nanowires. Reprinted with permission from [9]. Copyright 2013, John Wiley and Sons; (d) microfluidic channels. Reprinted with permission from [10]. Copyright 2013, IOP Publishing. 2

Figure 2 Schematic structure of a DRIE tool. Reprinted with permission from [14]. Copyright 2007, IOP Publishing. 5

Figure 3 A schematic DRIE processing flow for deep etching on Si. Reprinted with permission from [14]. Copyright 2007, IOP Publishing. 5

Figure 4 (a) An array of deep holes etched into Si by DRIE; (b) magnified image of the top of the holes in (a). Reprinted with permission from [13]. Copyright 2011, IEEE. 6

Figure 5 (a) A unit cell of Si crystal with miller index of orientation; (b) a Si atom with four covalent bonds with adjacent Si atoms. 8

Figure 6 Mechanisms of KOH etching reactions on (a) (100)–Si Surface and (b) (111)-Si surface. (c) Cross-sectional SEM image of a V-groove on (100)-Si substrates by KOH etching. 9

Figure 7 (a) A schematic setup of ECE and (b) a schematic charge transport process at the Si-electrolyte interface. Reprinted with permission from [17]. Copyright 1990, The Electrochemical Society. 11

Figure 8 (a) Current density (*J*)-voltage (*V*) curve of (100)-, (110)- and (111)- oriented Si in 5% wt HF solution. Reprinted with permission from [20]. Copyright 1993, The Electrochemical Society. (b) A schematic etching profile in PSF region. (c) A schematic etching profile in EPR region. 12

Figure 9 Mechanisms of ECE on (a) (100)-, (b) (111)-oriented Si in PSF region and (c) in EPR region. 13

Figure 10 The results of ECE on Si with branching on the sidewall of the etched pores. Reprinted with permission from [22]. Copyright 1999, The Electrochemical Society. ... 14

Figure 11 Limitations of current methods for HAR structures fabrication on Si. 15

Figure 12 Microscopic processes during MaCE. 1. Decomposition of H_2O_2 (Equation 4); 2. Transport of h^+; 3. Transport of HF; 4. Dissolution of Si (Equation 5); 5. Transport of SiF_6^{2-}; 6. Diffusion of excessive h^+. 16

Figure 13 SEM images of Au-coated Si after etching in HF-H_2O_2 for 30 s. The top surface is tilted 30 ° from normal to reveal both top surface and the cross section. (a) Au-coated area on p^+ Si, (b) off the Au-coated area on p^+ Si, and (c) off the Au-coated area on p^- Si. Reprinted with permission from [24]. Copyright 2000, AIP Publishing. 17

Figure 14 SEM images (at 45^o) of p-Si (100) samples after HF-H_2O_2 etching with different ρ values. Reprinted with permission from [25]. Copyright 2008, Elsevier. 18

Figure 15 (Color online) Schematic illustration of the experimental procedures for fabricating large-area arrays of ordered SiNWs: (a) deposition of monolayer silica colloidal crystal template on Si surface; (b) fabrication of 2D non-close-packed silica colloidal crystals on Si surface; (c) deposition of silver layer on Si surface through the non-close-packed colloidal crystal template; (d) formation of regular silver nanohole arrays by removing silica colloids by brief ultrasonication in water; and (e) formation of SiNWs by catalytic etching. The corresponding SEM micrographs on the right show the monolayer silica colloidal crystal template (a), the 2D nonclose-packed silica colloidal crystal template (b), the silver film with periodic nanohole arrays (d), and ordered SiNW arrays produced using catalytic silver film with periodic nanoholes (e). Reprinted with permission from [29]. Copyright 2007, AIP Publishing. 19

Figure 16 (a) Spiral movement of a star-shaped Au catalyst in MaCE. Reprinted with permission from [39]. Copyright 2012, American Chemical Society; (b) out-of-plane

rotation of a horseshoe-shaped Au catalysts in MaCE. Reprinted with permission from [42]. Copyright 2011, John Wiley and Sons. 20

Figure 17 Schematic processing flow of MaCE by separate metal particles: **(**a) bare Si preparation; (b) Ag NPs deposition; (c) MaCE; (d) Cu filling. 21

Figure 18 (a) Top view of the Si surface after deposition of Ag NPs. (b) Top view and (c) cross sectional SEM image of Si surface after MaCE; (d) magnified image in middle of (c). 25

Figure 19 SEM images of (e) lithography-patterned Au NPs on Si; (f) Si after MaCE by Au NPs, the magnified images of the top part and the bottom part are shown in (g) and (h), respectively. 26

Figure 20 Cross sectional SEM images of (a) Cu filled Si via; (b) magnified image of a straight via tip; (c) magnified image of a helical via tip. 28

Figure 21 Schematics of (a) metal catalysts on Si; (b) ideal etching profile by the metal; (c) real etching profile by the metal. (d) and (e) show SEM images of Si after MaCE using Au stripes as catalysts reported by two independent groups. Reprinted with permission from [51] and [52], respectively. Copyright 2012, Royal Society of Chemistry and Copyright 2013, American Chemical Society, respectively. 30

Figure 22 Cross-sectional SEM image of a SiO-10 nm Au catalyst on Si substrate viewed at 5^{o} tilting angle. Black arrows indicate nanopores in SiO-10 nm Au for through-catalyst mass transport. 35

Figure 23 (a) Schematic mechanism of a through-catalyst MT process. (b) Bird's eye view SEM images of SiO-10 nm catalyst. The inset shows the contact angle image of a water droplet on the Si-O surface. (c) Cross-sectional SEM image of the trench etched by SiO-10 nm catalyst shown in (b) for 1 min in $\rho(0.37)^{1.8}$ etchant. (d) Overall and (e) detailed AFM height sensor image (up) and cross-sectional diagram (bottom) of SiO-10 nm catalyst.* 36

Figure 24 (a) Schematic mechanism of an edge-only mass transport process. Bird's eye view SEM images of (b) SiO-20 nm and (c) SiH-10nm catalyst. Cross-sectional SEM images of the trenches etched in $\rho(0.37)^{1.8}$ etchant for 1 min by (d) SiO-20 nm and (c) SiH-10nm catalysts. The insets of (d) and (e) show the trenches etched for 10 min with other conditions the same as those in (d) and (e), respectively. 38

Figure 25 (a) Top view SEM image of a 2 μm-wide SiO-10 nm catalyst. (b) Top view SEM image of the trench etched by SiO-10 nm catalyst in $\rho(0.37)^{1.8}$ etchant for 40 min. Cross-sectional SEM images of the trench etched by SiO-10 nm catalyst in $\rho(0.37)^{1.8}$ etchant for (c) 10 min (d) 20 min, (e) 30 min and (f) 40 min. The inset in (f) shows the magnified image in the red circle in (f). (g) Schematic definition of geometric parameters of the etched trench shown in (c)-(f). The lateral dimensions are defined as the width of hole diffusion region (w_d), trench opening (w_o), trench top (w_t), and trench bottom (w_d). The vertical dimensions are defined as the depth of maximum penetration (d_{max}), opening region (d_o), linear region (d_l), bottom region (d_b), the angle between sidewall and Si top surface (θ). The tapering angle α is defined as the complementary angle of θ, i.e. $\alpha=90^o-\theta$. (h) Plot of d_{max} and θ of the trenches in (c)-(f) against the etching duration. 42

Figure 26 (a) A 2 μm-wide SiO-10 nm Au catalyst patterned by photolithography; (b) a single trench etched by the catalyst shown in (a) in $\rho(0.37)^{1.8}$ etchant for 10 min. 42

Figure 27 (a) Top view and (b) cross-sectional SEM images of a trench etched by a 2 μm-wide SiO-10nm Ag catalyst in $\rho(0.37)^{1.8}$ for 10 min. Inset of (a) shows an enlarged view of the bottom surface of the trench. 43

Figure 28 (a) Top view SEM of a 2 μm-wide SiO-5 nm catalyst. (b) Cross-sectional SEM images of a trench etched by the Au stripe in (a) in $\rho(0.37)^{1.8}$ for 10 min..... 44

Figure 29 Cross-sectional SEM images of the trenches etched in $\rho(0.37)^{1.8}$ for 10 min by SiO-10nm catalyst with (a)10-μm width and (b) 20-μm width. (c) and (d) show the enlarged view of the bottom and sidewall surface in the red circle in (b), respectively. (e) X-ray

energy dispersive spectrum (EDS) of the bottom red circle in (c). d_{max} and θ, are plotted against the catalyst width. 45

Figure 30 (a) A schematic fabrication process and direction of observation of the polymer replica of a trench. The green, blue and golden blocks refer to the Si substrate, the polymer replica and the Au stripe, respectively. SEM images of (b) the bottom of the trench filled with polymer replica; (c) the sidewall of the polymer replica from the view 45^o to horizontal plane; (d) top view of the polymer replica; (e) details of the red circle in (d). 47

Figure 31 Cross-sectional SEM images of the trench etched by a 2 μm-wide SiO-10nm catalyst in (a) $\rho(0.64)^{5.4}$ etchant for 1 min, (b) $\rho(0.64)^{5.4}$ etchant for 10 min on Si(111), (c) $\rho(0.37)^{1.8}$ etchant for 10 min on Si(111) and (d) $\rho(0.18)^{0.9}$ for 1 min. The insets of (a) and (d) shows the trench etched for 10 min under the same condition. (d) Modeling of the excessive h^+ concentration against the *x* axis after 1 minute's etching in a two dimensional coordinate system (CS). The golden and green blocks refer to the Au catalyst and the Si substrate. The solid line (—) and the dash line (----) correspond to the etching in $\rho(0.18)^{0.9}$ and $\rho(0.37)^{1.8}$ etchants, respectively. The inset corresponds to the h^+ distribution in $\rho(0.37)^{1.8}$ with smaller scale of *y*-axis. 51

Figure 32 Cross-sectional SEM images of trenches etched in $\rho(0.37)^{1.8}$ by (a) three paralleled 2 μm-wide SiO-10nm catalysts for 20 min and (b) three paralleled SiO-10 nm catalysts with widths of 2 μm, 5 μm and 10 μm for 10 min. 53

Figure 33 (a) A cross-sectional SEM image of trenches etched by 50 paralleled 2 μm-wide SiO-10nm Au catalysts with 2 μm spacing in $\rho(0.37)^{1.8}$ for 10 min at 75 ^{o}C. (b) shows an magnified view of one wall between two adjacent trenches. 53

Figure 34 (a) A schematics experimental setup of EMaCE. (b) A photograph and (c)-(d) schematics of the working electrode. 57

Figure 35 Top-view SEM images of 28 μm Au-Si(100) chips after MaCE for 1 min at 23 ^{o}C (a) and 100 ^{o}C (b). 59

Figure 36 (a) Schematic processing flow of MaCE by Au catalysts array. The blocks in green, purple and golden refer to the Si substrate (Si), the photoresist (PR) and the Au catalysts (Au), respectively. (b) A top-view SEM image of Au patterns on Si after lift-off of PR. The inset shows the morphology of Au catalysts under high magnification (scale bar=100 nm). (c) A schematic etching profile after MaCE and parameters used for describing the etching profile..... 61

Figure 37 SEM images of 28 μm Au-Si(100) chips after pre-etching by $\rho(0.22)^{0.9}$ droplet. (a) A cross-sectional image of one circular Au pattern and the Si below Au. (b) A top-view image of Au-Si boundary area. (c) and (d) Enlarged images of the red circle in (a). (e) Cross-sectional diagram of holes after pre-etching measured by profilometer. 62

Figure 38 Etching profiles of 28 μm Au-Si(100) in $\rho(0.37)^{1.8}$ for (a) 1 min, (b) 2 min, (c) 5 min and (d) 10 min at 23 ^{o}C as well as (e) 1 min, (f) 2 min, (g) 5 min and (h) 10 min at 100 ^{o}C. Top-view OCM images (top), optical cross sections (middle) and SEM cross sections (bottom) are shown in each set of figures. 64

Figure 39 (a) Evolution of *h* (solid lines) and etching rate (dashed lines) versus etching time (*t*). High-magnification cross-sectional (left) and top-view (right) SEM images of Au-Si boundary area after 1 min of etching at 23 ^{o}C (b) and 100 ^{o}C (c). (d)-(i) simulated 2D (top) and 1D (bottom) distribution of $c(h^{+})$ in arbitrary unit corresponding to experiments shown in **Figure 38** (a)-(f), respectively. The color bar indicates the relative value of $c(h^{+})$, where the red end represents higher $c(h^{+})$ and the blue end represents lower $c(h^{+})$. 68

Figure 40 Schematics of charge transport in (a) MaCE and (b) EMaCE. Cross-sectional SEM images of the chips (left) and polymer replica (right) after EMaCE at (c) -0.50 V, (d) -1.00 V, (e) -1.50 V and (f) -1.75 V for 10 min. (g) and (h) show the OCM image and cross-sectional diagram of the etched chip in (f)..... 72

Figure 41 (a) 28 μm Au-Si(100) and (b) 28 μm Au-polySi chips after EMaCE at -1.75 V for 10 min and cut for cross-sectional SEM imaging. 73

Figure 42 Evolution of h_{center} (black) and h_{corner} (red) measured from the polymer replica at bias shown in **Figure 40** (c)-(f)..... 73

Figure 43 (a) Current-bias (*I*-*V*) curve of 28 μm Au-Si(100) in $\rho(0.37)^{1.8}$ etchant(black line) and $\rho(1)^{1.8}$ etchant (red line) in a continuous EMaCE experiment. h and θ of the etching results shown in Figure 40 (c)-(f) are also plotted. (b) Evolution of applied bias and measured current versus etching time in a stepwise EMaCE experiment. Cross-sectional SEM of chips (c) and polymer replica (d)-(e) etched in condition of black line in (a). Cross-sectional SEM of chips (f) and polymer replica (g)-(h) etched in condition of (b)..... 77

Figure 44 (a), (b) Top-view and (c), (d) cross sectional SEM images of etching result corresponding to the red line in **Figure 43** (a). (b) and (d) shows the enlarged image in the red squares of (a) and (c). 78

Figure 45 Top-view (left) and cross-sectional (right) of the chips etched at -1.75 V for (a) 10 min in $\rho(0.37)^{1.8}$ (b) 25 min; (c) 60 min; (d) 90 min; (e) 120 min. (f) the sidewall of etched holes in (a) with high magnification. (g) the polymer replica of (d)..... 80

Figure 46 Top-view (a) and cross-sectional (b) SEM images of the 28 μm Au-Si(100) chips after etching in $\rho(0.65)^{5.2}$ at -1.75 V for 10 min..... 81

Figure 47 Top-view and cross sectional SEM images of (a) the chip and (b) replica etched at -1.75 V for 25 min. (c) Polymer replica of the chips etched at -1.75 V for 120 min. Contacts (indicated by white arrows) between photoresist and Si substrate after (d) EMaCE at -1.75 V for 120 min and (e) MaCE for 20 min. 82

Figure 48 (a) Top-view, (b) cross-sectional SEM images of a 29 μm Au-Si(111) chip after MaCE at -1.75 V and (c) corresponding replica. (d), (e) Top-view, (f) cross-sectional SEM images of a 29 μm Au-polySi chip after MaCE. (g), (h) Top-view, (i) cross-sectional SEM images of a 29 μm Au-polySi chip after MaCE at -1.75 V and (j), (k), (l) corresponding replica..... 84

Figure 49 (a)-(c) pattern of a complex feature after photolithography on Si(100) chip; (e), (f), (g), (h) show the chip after EMaCE at -2.00V for 10 min. (d) and (g) show the corresponding replica. 85

Figure 50 A circular h^+ Source in an Infinite Space 91

Figure 51 Schematic of the cross section of a line source moving at constant velocity *v* along z axis in infinite space. The line source is aligned in the *y* axis which is perpendicular towards the *x*-*z* plane. 0 is the point of origin of the immobile coordinate system *x*, *y*, *z*; 0_S is the point of origin of the coordinate system *x*, *y*, *z*' that moves with the source. 94

Figure 52 Processing flow in MaCE experiments: (a) photolithography for formation of line patterns blocks; (b) Au deposition; (c) MaCE; (d) lift-off of photoresist. The green, blue and golden colors represent the Si substrates, photoresist and Au catalysts, respectively. 97

Figure 53 Top-view SEM images of Si sample after photolithography and Au deposition: (a) a 2 μm×5@20 μm pattern. The brighter area are the Si that are in direct contact with Au, while the Si surface are covered by photoresist in other darker area (the same in the following images); (b) a 2 μm×1 pattern; (c) magnified image of the red circle in (b), showing the smooth edge of photoresist; (d) magnified image of the red circle in (c), showing the nanoporous morphology of Au catalysts; (e) a 5 μm×1 pattern; (f) a 10 μm×1 pattern. 98

Figure 54 (Top) top-view and (bottom) cross sectional atomic force microscope (AFM) image of the as-deposited Au catalysts on bare Si surface. The thickness of Au catalysts, 13.3±0.5 nm, is acquired by measuring the step height at the edge of Au. 99

Figure 55 Cross-sectional SEM images of the etching profile on U-Si. The name of blocks are labeled on top of each corresponding figure. All the scale bars have a length of 5 μm. 101

Figure 56 Cross-sectional SEM images of the etching profile on P-Si. The name of blocks are labeled on top of each corresponding figure. All the scale bars have a length of 5 μm. 102

Figure 57 Cross-sectional SEM images of the etching profile on N-Si. The name of blocks are labeled on top of each corresponding figure. All the scale bars have a length of 5 μm. 103

Figure 58 (a) Plot of the average etching depth (d) versus original width of the line patterns (w_0); (b) plot of the top width variation (Δw_t) versus w_0 of the single-line patterns; (c) plot of the top width variation (Δw_t) versus number of line patterns (n) with w_0 of 2 μm and spacing distance (s) of 20 μm; (d) plot of the top width variation (Δw_t) versus s with w_0 of 2 μm and n of 50; (e) plot of the top width variation (Δw_t) versus s with w_0 of 5 μm and n of 50; (f) plot of the top width variation (Δw_t) versus s with w_0 of 10 μm and n of 50. All the w_0 here refer to the designed value. The solid lines in (b)-(f) represent the Δw_t calculated from the diffusion model (labeled as P(M) and U(M) for P-Si and U-Si in the legend of each figure). 107

Figure 59 (Top) Cross-sectional SEM images of the etching profile in 10 μm×50@50 μm block on N(+)-Si with magnified image detailing the red circle; (Bottom) cross-sectional SEM images of the etching profile in 2 μm×50@50 μm block on P(+)-Si with magnified image detailing the red circle. 108

Figure 60 The evolution of etching depth in MaCE of 2 μm×1 pattern on N-Si. 112

Figure 61 Band diagram of an Au-Si Schottky junction. (a) Band diagram of Au and N-Si (left)/P-Si (right) without contact; (b) band diagram of Au and N-Si (left)/P-Si (right) with contact under no electric bias; (c) band diagram of Au and N-Si (left)/P-Si (right) with contact while Si is negatively biased towards Au. E_F, E_C, E_V, V_{bi} and V refer to the energy of Fermi level, conduction band bottom, valence band top, built-in potential and applied potential, respectively. The shadowed area shows the bands that are occupied by electrons. 117

Figure 62 (a) Schematic charge transport process during MaCE. CT1: charge transport from Au to the Si beneath; CT2: charge transport from Si on the sidewall to the etchant solution; (b) current density-voltage curve of bare Si substrates as the working electrode in 1.5 mol/L HF aqueous solution. 119

Figure 63 Calculated $c_{h+}(x,0,10\ min)$ in MaCE of 2 μm×1, 5 μm×1 and 10 μm×1 blocks using diffusion model. (a) and (b) show the overall curve and magnified curve of the near-Au edge part, respectively. In (b), the origin of x-axis is set at the boundary between the edge of Au and Si indicated by the vertical lines in (a). The horizontal line in both (a) and (b) is the line of $c_{h+}=c_{h+crit}=0.1645$. 125

Figure 64 Cross-sectional SEM images of the etching profile on P-Si with (111) crystalline orientation. The name of blocks are labeled on top of each corresponding figure. All the scale bars have a length of 5 μm. 126

Figure 65 SEM image of a MaCE-defined resonator. 129

Figure 66 Schematic process flow: (a) electron beam lithography or photolithography (b) Au evaporation (c) MaCE for 10 minutes in aqueous solution (d) Au and photoresist removal (e) HF releasing and drying. 130

Figure 67 Cross section of a submicron trench etched by MaCE in 10 minutes with aspect ratio of 16:1. 131

Figure 68 Top-view IR microscope image of (a) a partially released device and (b) a fully released device. 132

Figure 69 Sidewalls of trenches etched by (a) MaCE with absence of scalloping (b) DRIE. 133

Figure 70 (a) Schematic of MaCE-induced notching (b) Charge transport in Si during MaCE (c) Electrostatic forces enable good adhesion of Au on Si (d) Charging of BOX layer induce notching (e) Formation of porous Si at the trench top (b) Bottom of trench with Si residue and an additional trench by bouncing back of Au. 135

Figure 71 LDV measurements of a MaCE-defined resonator with HAR trenches (a) Magnitude (blue curve) and phase (red curve) of an EBL-patterned resonator (b) Sub-100 kHz frequency spectrum of a (c) PL-patterned resonator vibrating in its out-of-plane mode (inset). 137

Figure 72 Schematic illustration of the photolithography-plasma etching route and the FESA-MaCE route for HAR microstructures fabrication on Si: (a) coating of hard etching mask and photoresist; (b) photolithography; (c) geometry transfer on hard etching mask; (d) plasma etching of Si; (e) FESA; (f) deposition of metal catalyst; (g) MaCE. The blocks shown in blue, red, green, purple and golden refer to photoresist/polymer, hard etching mask, Si substrate, plate and metal catalyst, respectively..... 142

Figure 73 (a) Optical microscope image of the Si surface after FESA. The polymer assemblies patterned by FESA appear as the vertical black lines, while the green area in between the lines represents bare Si surface. (b)-(e) AFM image of the polymer lines after immersion in for 0 min, 10 min, 20 min and 60 min, respectively. The actual window size is 20×20 μm^2.The corresponding AFM cross sections are shown in (f), while the h_p and w_p measured from the AFM cross sections are shown in (g)..... 147

Figure 74 (a)-(f) AFM images of polymer lines patterned by FESA on Si after descum of 20 s, 60 s, 120 s, 180 s 210 s and 240 s, respectively. The corresponding cross sections are shown in (g), while the corresponding w_p and h_p descum time in (h). 149

Figure 75 Cross-sectional SEM images of Si sample after FESA and MaCE for 10 min in $\rho(0.34)^{1.6}$ etchant with descum time of (a) 1 min, (c) 2 min, (e) 3 min and (g) 3.5 min. (b), (d), (f) and (h) shows the sample in (a), (c), (e) and (g) with high magnification, respectively. Top-view SEM image of sample in (e) is shown in (i) and (j). The w_t, w_b and h of each sample are plotted against their corresponding descum time. Here the "Poly" refer to the polymer lines by FESA..... 150

Figure 76 Cross-sectional SEM images of Si sample after FESA with descum time of 3 min and MaCE for 10 min in etchant of (a) $\rho(0.34)^{1.6}$, (b) $\rho(0.43)^{2.3}$ and (c) $\rho(0.50)^{3.1}$. The w_t, w_b and h of each sample are plotted against their corresponding [HF]. 153

Figure 77 Cross-sectional SEM images of Si sample after FESA-MaCE in $\rho(0.34)^{1.6}$ with different descum time and MaCE time: (a) descum 2 min, MaCE 20 min; (b) descum 3 min, MaCE 20 min; (c) descum 3 min, MaCE 60 min. (d) shows the results of photolithography and MaCE for 60 min. (e) shows the schematic charge transport process during MaCE, where the blocks in green, blue and golden refer to Si, polymer lines and Au catalyst, respectively. (f) shows results of the same experiment in (b) with the addition of -1.5 V electric bias. Here "Poly" and "PR" refer to the polymer lines and photoresist used in FESA and photolithography, respectively..... 155

Figure 78 Optical image of water droplet on bare Si surface and Si surface after FESA-MaCE process with different descum time. Column A show the samples after washing in Piranha solution, while Column B show the samples after silane treatment. 157

Figure 79 Schematic processing flow for TSV fabrication by MaCE: (a) cleaning of bare Si; (b) photolithography; (c) metal deposition; (d) MaCE; (e) removal of photoresist and metal..... 164

Figure 80 (a) Optical microscope (OM) image of Si wafers after photolithography; (b) enlarge OM image of the red circle in (a); (c) SEM image of the red circle in (b), inset shows the enlarged SEM of the red circle in (c); (d) AFM image and cross section of the red circle in (c); (e) cross-sectional SEM image of the Si sample after photolithography and Au deposition by sputtering. Au can be observed on top of the photoresist (PR) and Si, as well as the sidewall of the PR; (f) cross-sectional SEM image of the Si sample after photolithography and Au deposition by evaporation. Au can be observed on top of the photoresist (PR) and Si. No Au can be observed on the sidewall of PR, which is blurred under SEM due to the charging effect. 165

Figure 81 (a) Top-view and (b) cross-sectional SEM images of a 1×5 cm2 Si slice after MaCE of 2 h. 167

Figure 82 Cross-sectional SEM images of 1×5 cm2 Si slices after MaCE of 2 h with an average Au thickness of (a) 11.0 nm and (b) 13.5 nm. 168

Figure 83 (a) A whole Si wafer after MaCE of 2 h. (b) shows the wafer in (a) after lift-off of photoresist. 169

Figure 84 Cross-sectional SEM images of Si wafers after MaCE of 2 h without stirring. The coordinates of the position and the depth (*d*) of TSV are labeled in each image. The coordinates are defined in **Figure 79** (a). The same in the following figures. 172

Figure 85 Schematics of stirring scheme during MaCE. (a) No stirring of etchant solution. (b) Corner-stir: the stir bar is put at the corner of the Si wafer and at the same height of Si. The stirrer spins horizontally; (c) Center-stir: the stir bar is put at the center of the Si wafer and below the Si. The stirrer spins horizontally. 172

Figure 86 Cross-sectional SEM images of Si wafers after MaCE of 2 h under "edge-stir" scheme. The coordinates of the position and the depth (*d*) of TSV are labeled in each image. 175

Figure 87 Cross-sectional SEM images of Si wafers after MaCE of 2 h under "center-stir" scheme. The coordinates of the position and the depth (d) of TSV are labeled in each image. 177

Figure 88 Cross-sectional SEM images of Si wafers after MaCE of 4 h under "center-stir" scheme. The coordinates of the position and the depth (d) of TSV are labeled in each image. 178

Figure 89 (a) SEM image of TSV by MaCE of 4 h at position (1,1). (b) Magnified cross-sectional SEM image of the middle of TSV shown in Fig. 10 at position (1,1). (c) SEM image of the red circle in (a). (d) Schematic processing flow for replica fabrication. (e) Cross section of the replica from TSV shown in (a). 179

Figure 90 Cross-sectional SEM images of the top Si wafer (wafer A) after MaCE of 4 h on two Si wafers under the "center-stir" scheme. The coordinates of the position and the depth (d) of TSV are labeled in each image. 182
Figure 91 Cross-sectional SEM images of the bottom Si wafer (wafer B) after MaCE of 4 h on two Si wafers under the "center-stir" scheme. The coordinates of the position and the depth (d) of TSV are labeled in each image. 184
Figure 92 (a) Vertical holes with designed width of 200 μm after MaCE of 1 hr. (b) Vertical holes with designed width of 6 μm after MaCE of 1 hr. Results in both figures are obtained from MaCE on 1 ×1 cm^2 Si substrates. 184
Figure 93 (a) Cross-sectional optical microscope image of a TSV in Fig. 9 which is filled by copper (Cu). A layer of SiO2 exists between Cu and Si substrate; (b) SEM of the red circle in (a) at high magnification; (c), (d) and (e) are the elemental signal maps of Cu, Si and oxygen (O), respectively, in the area of (b) by energy dispersive spectrometer..... 186
Figure 94 (a) Schematic layout of test vehicle for metal compatibility test in MaCE; (b) SEM image of a copper (Cu) pattern before covered by photoresist, a titanium (Ti) adhesion layer existed between Cu and Si substrate, the total thickness of the Ti/Cu pattern over the whole sample was measured to be 139 ±2 nm by AFM profile as shown in the embedded red curve; (c) SEM image of the test vehicle surface after immersion in HF-H_2O_2 solution for 30 min and removal of photoresist and polyimide covering, the vertical dash line indicate the boundary between PR and PM region; (d) enlarged SEM image of the Cu pattern in the PR region with corresponding AFM profile as shown in the red curve; (d) enlarged SEM image of the Cu pattern in the PM region with corresponding AFM profile as shown in the red curve. 188

LIST OF SYMBOLS AND ABBREVIATIONS

nm	nanometer, 1×10^{-9} meter
μm	micrometer, 1×10^{-6} meter
Si	silicon
DRIE	deep reactive ion etching
MaCE	metal-assisted chemical etching
TSV	through silicon vias
NP	nanoparticles
CT	charge transport
MT	mass transport
AR	aspect ratio
HAR	high-aspect-ratio
ECE	electrochemical etching
SEM	scanning electron microscope
AFM	atomic force microscope
h^+	electronic holes
EMaCE	electric bias-attenuated MaCE

CS	coordinate system
MEMS	microelectromechanical system
FESA	flow-enabled self assembly
TEM	transmission electron microscope
FTIR	Fourier transform infrared spectroscope
XRD	X-ray diffraction
CV	cyclic voltammetry

SUMMARY

This dissertation is focused on a novel wet etching method, named metal-assisted chemical etching (MaCE), for fabrication of uniform high-aspect-ratio (HAR) structures on silicon (Si) in micro- and nanometer scale. In MaCE, a layer of noble metal thin film is deposited on the surface of Si and serves as the catalyst. The metal-loaded Si is immersed in hydrofluoric acid (HF)-hydrogen peroxide (H_2O_2) solution. A redox reaction occurs at the metal-Si interface where the Si under the metal film is preferentially etched. The metal catalyst can continue etching into Si to form HAR structures. In this dissertation, the challenge of obtaining uniform HAR structures by MaCE is firstly addressed where random movements of the metal catalyst during MaCE are observed. Then suitable experimental conditions are presented, under which uniform HAR holes and trenches on Si are successfully fabricated. The uniform MaCE phenomena are explained by the microscopic transport processes of HF and electronic holes (h^+). Further, the influence of h^+ transport on the 3D etching profiles is discussed. By applying external electric bias, the 3D etching profiles is effectively controlled. Further, the transport of h^+ is also found to be influenced by the dopants type and the doping level of the Si substrates. Based the above findings, HAR trenches and holes with vertical sidewalls are successfully fabricated and devices built on these structures are demonstrated to work properly. The established method further shows compatibility with a novel low-cost lithography method, constituting an economic overall approach for HAR structures fabrication. Finally, uniformity of MaCE is achieved across multiple wafers that are etched simultaneously, paving the way for its application in high-volume manufacturing.

CHAPTER 1

INTRODUCTION

1.1 Manufacturing of High-Aspect Ratio Micro- and Nanostructures on Silicon

Silicon (Si) has been the dominant material in modern microelectronic industries for its role as the basis of integrated circuits (IC), the core of all computers around the world. Due to its fundamental impact on the evolution of modern society, the past few decades have been referred as "The Silicon Age". In IC, a huge number of devices with different functionalities, such as transistors, conductors, capacitors and resistors, are integrated on small Si chips. The promotion of the performance of an IC is majorly realized by increasing the number of devices integrated on the chips through miniaturization of the dimension scale of individual devices. Current state-of-the-art technologies are capable of manufacturing transistors with lateral dimension as small as 14 nm [1], which makes it possible to integrate billions of these devices on a chip. On the other hand, to fully utilize the volume of Si substrates, more components are built not only on the Si surface (2D components), but also inside the Si substrates (3D components). The use of 3D components has been considered a promising strategy to continue the performance promotion since the miniaturization of conventional 2D components is becoming more and more difficult. For example, vertically stacked ICs have been studied, where vertical electrical interconnects between each ICs, named through silicon vias (TSV), are used. The TSV penetrate through the Si substrates and enable the communication of electrical signals across each layer of the stacked ICs.[2]

Besides electronic and electrical devices, the idea of miniaturization has been extended to devices with mechanical and chemical functionality, such as micro-/nano-electromechanical system (MEMS/NEMS)[3], microfluidics [4], photonic devices[5], memory devices, energy harvesting and storage.[6, 7] Due to suitable mechanical

properties and chemical stability, Si also serve as the base material in these devices. From the view of geometry, these devices employ the structures, such as deep holes and deep trenches, with small lateral size (or width, *w*) and high depth (*d*) in the micrometer and nanometer scale. These structures are referred to as high-aspect ratio (HAR) structures in this dissertation.

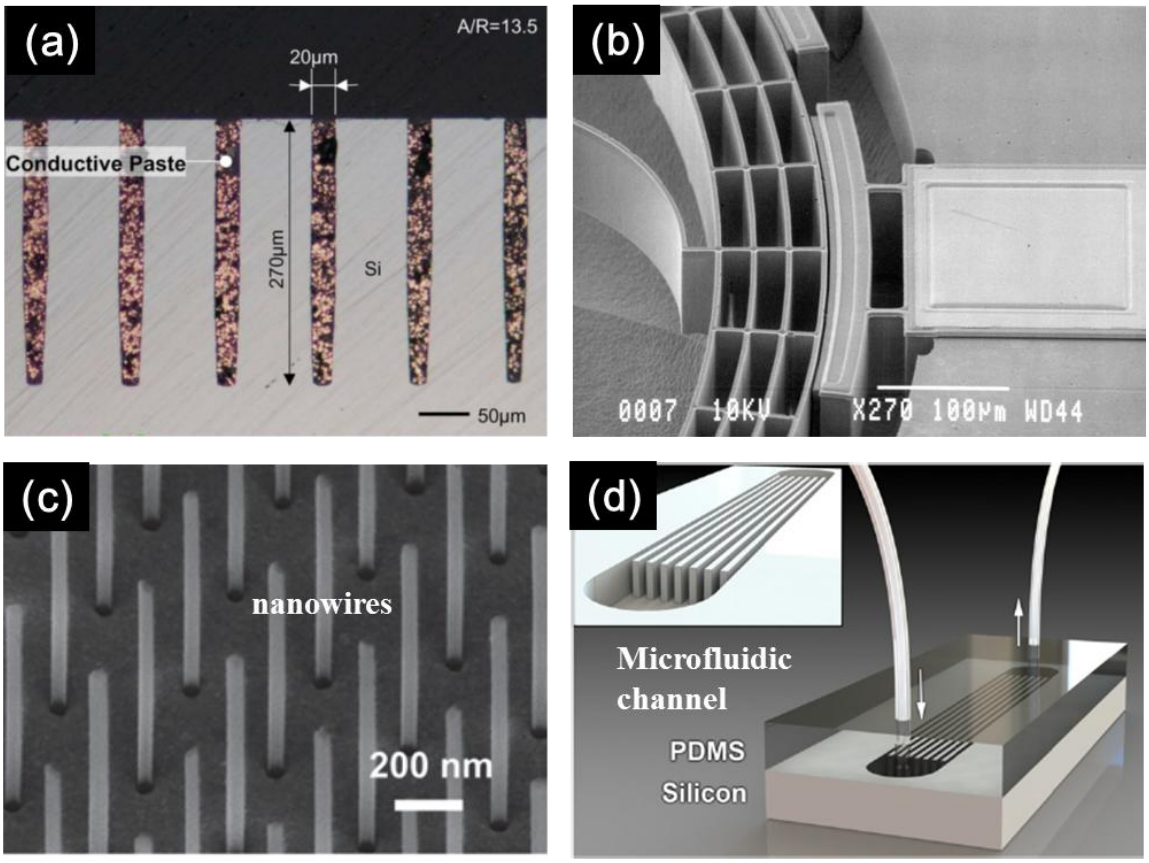

Figure 1 Applications of HAR structures on Si. (a) Through silicon vias. Reprinted with permission from [2]. Copyright 2009, IEEE; (b) MEMS. Reprinted with permission from [8]. Copyright 2001, IEEE; (c) Si nanowires. Reprinted with permission from [9]. Copyright 2013, John Wiley and Sons; (d) microfluidic channels. Reprinted with permission from [10]. Copyright 2013, IOP Publishing.

1.2 Current HAR structures fabrication technology on Si and limitations

Generally, the structures can be manufactured through either bottom-up or top-down strategies. In the bottom-up strategy, HAR structures are synthesized from Si atoms-containing precursors, such as silanes [11]. This strategy incurs high-temperature processing, which may be harmful to other electronic components in electronic systems. On the other hand, the top-down strategy is primarily adopted by the industry, where a certain volume of Si is removed from the substrates. The removal of Si is referred to as the etching of Si in this dissertation. A Si etching technology that is suitable for HAR structures fabrication should proceed towards a specific direction into the substrates while keeping the Si in other directions intact. In other words, a Si etching technology for HAR structures should be an anisotropic etching. A brief review of currently available HAR etching technologies together with their limitations will be presented in the following sections.

1.2.1 Dry etching

Depending on the status of chemicals used for etching Si, Si etching technologies can be categorized into dry etching and wet etching, where gaseous and liquid chemicals are involved, respectively. Because plasma is always involved in the dry etching, the dry etching is also called plasma etching in many cases. In current industry, HAR Si etching is primarily realized by deep reactive ion etching (DRIE) method, a type of dry etching methods specifically developed for HAR structures fabrication. In a typical DRIE process, Si substrates are coated with a patterned mask layer. The area to be etched is exposed to the etching gas while the other area is protected by the mask. The substrate with the mask is placed between two electrodes in a vacuum chamber (**Figure 2**) for deep etching. Two different steps, i.e. the etching step and the passivating step, alternate through the whole etching process (**Figure 3**). In the etching step, SF_6 plasma is generated inside the vacuum chamber and driven to bombard the exposed surface on the substrate by an electric bias. The bombardment of plasma causes etching of Si. After etching, the surface of etched

cavity is passivated by polymers generated by C_4F_8 plasma. Then the etching step takes place again. Since the electric bias that accelerates the SF_6 plasma is aligned vertical to the substrate, most etching occurs at the bottom of etched cavity while the passivation layer on sidewall remains relatively intact. As the etching step and the passivation step continue alternating, the etched cavity grows vertically into the substrate, which finally forms vertical HAR structures. The lateral geometry of etching profile can have high fidelity to the pattern in the mask layer, which can be arbitrarily defined by lithography technologies. The state-of-the-art DRIE technology has demonstrated capability of producing 35 nm-wide deep trenches with aspect ratio over 120:1.[12] However, expensive instruments and maintenance (~$200,000) are required for DRIE to produce HAR structures. In high-volume manufacturing, the cost even increases exponentially as the size of Si wafers increases. Thus, the economic viability of DRIE for industry is questionable. Also, since the etching proceeds in a pulsed fashion, the sidewalls possess intrinsic scalloping features with roughness of 50-200 nm (**Figure 4**). In order to achieve a low extent of scalloping for decent device performance, the etching rate has to be compromised.[13]

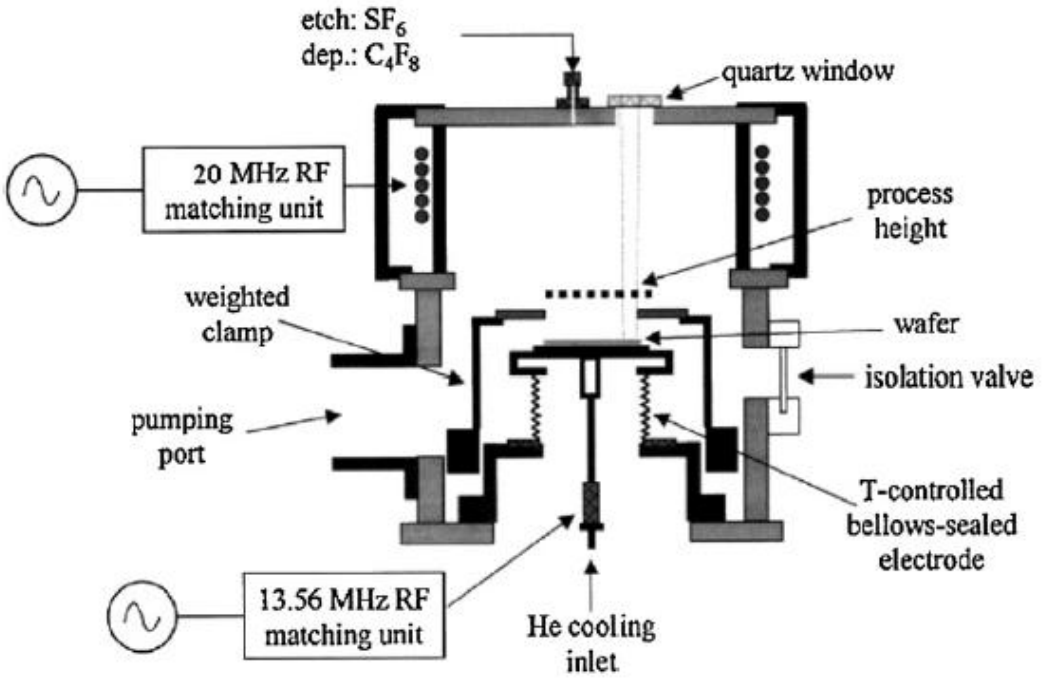

Figure 2 Schematic structure of a DRIE tool. Reprinted with permission from [14]. Copyright 2007, IOP Publishing.

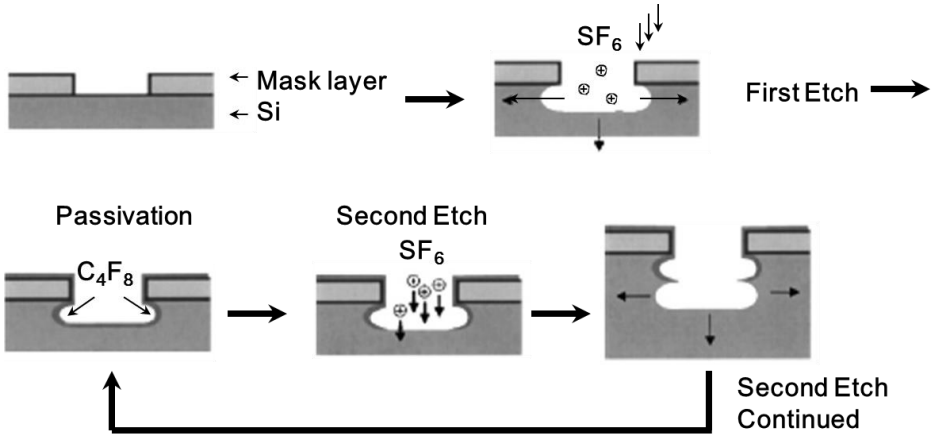

Figure 3 A schematic DRIE processing flow for deep etching on Si. Reprinted with permission from [14]. Copyright 2007, IOP Publishing.

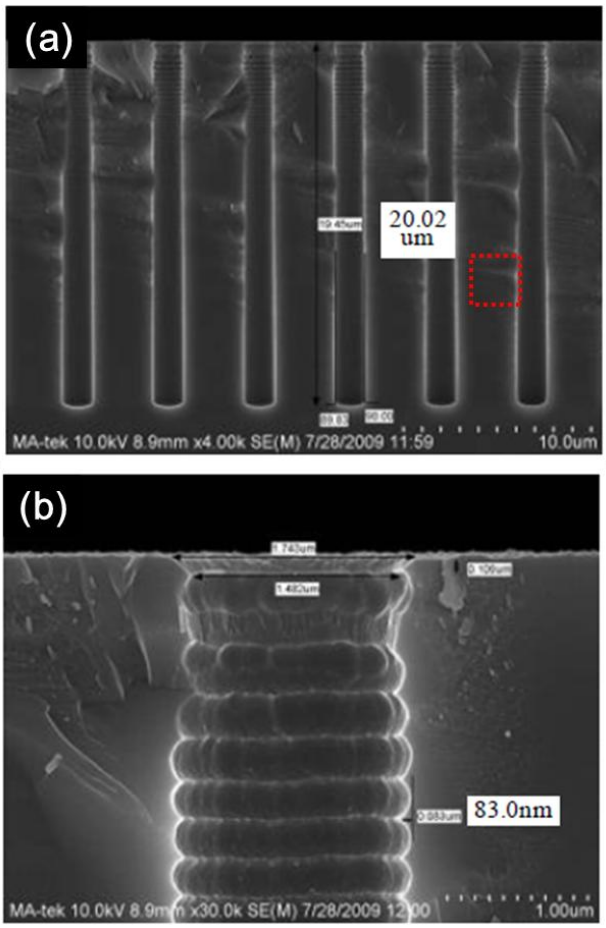

Figure 4 (a) An array of deep holes etched into Si by DRIE; (b) magnified image of the top of the holes in (a). Reprinted with permission from [13]. Copyright 2011, IEEE.

1.2.2 Wet etching-KOH Etching

A low cost etching method for HAR structures has always been desirable. It has long been known that certain HAR structures could be formed by simply dipping Si in basic etching solution. For example, Si can react with potassium hydroxide (KOH) solutions [15]:

$$Si+2KOH+2H_2O \longrightarrow 2K^+ +2H_2 +SiO_2(OH)_2^{2-} \quad (1)$$

In the KOH solution, the etching rate of Si differs in each of its crystalline planes. Si is a tetravalent element. Inside a piece of single crystalline Si substrates, Si atoms are

bonded with four neighboring ones through Si-Si bonds (**Figure 5** (a)). The four neighboring Si atoms form a tetrahedron (**Figure 5** (b)). However, Si atoms on the surface have to bond with heterogeneous atoms (mostly, oxygen (O) or hydrogen atoms (H) because they no longer have four neighboring Si atoms. These Si-O or Si-H bonds are named as the surface bonds. The crystalline orientation of the exposed surface determines how many surface bonds each surface Si atom has: for surface with <100> or <110> orientation, each Si atom has two surface bonds and two Si-Si back bonds; for surface with <111> orientation, however, each Si atom has one surface bond and three Si-Si back bonds (**Figure 5** (b)). During the KOH etching, the etching species, hydroxyl ion (OH^-), needs to break Si-Si back bonds before a surface Si atom leaves from the substrate. Etching on (111) plane thus becomes less favorable, because it requires breaking of three Si-Si back bonds per Si atom, which is more than those on <100> or <110> planes. In KOH etching experiments, V-trenches and vertical trenches are formed on (100)-Si (Si wafers with the top surface being (100) plane, the same in the following) and (110)-Si, respectively (**Figure 6**). Since the anisotropy of KOH etching originates from the chemical difference between crystalline planes, the surface of etching profile is smooth and roughness can be lower than 10 nm [16]. However, the type of HAR structures that can be made by KOH etching is highly limited to trenches with width larger than 1 μm.

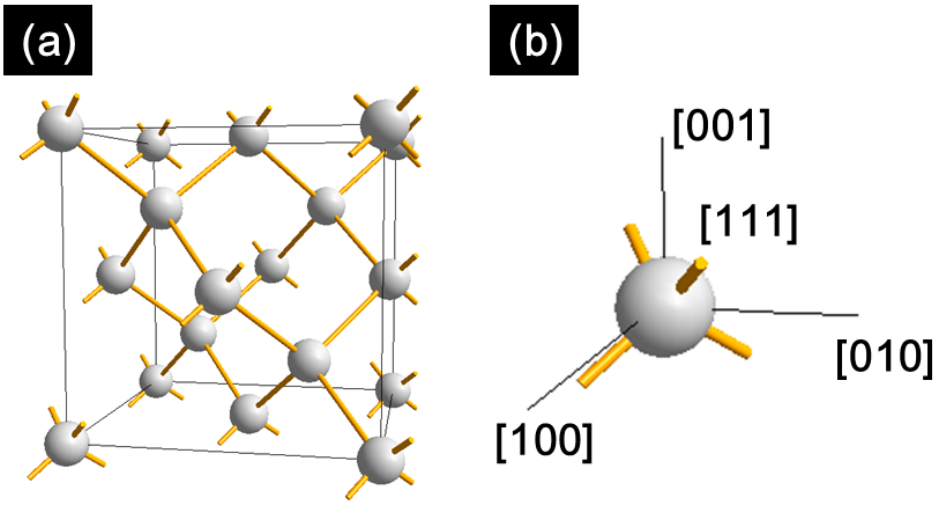

Figure 5 (a) A unit cell of Si crystal with miller index of orientation; (b) a Si atom with four covalent bonds with adjacent Si atoms.

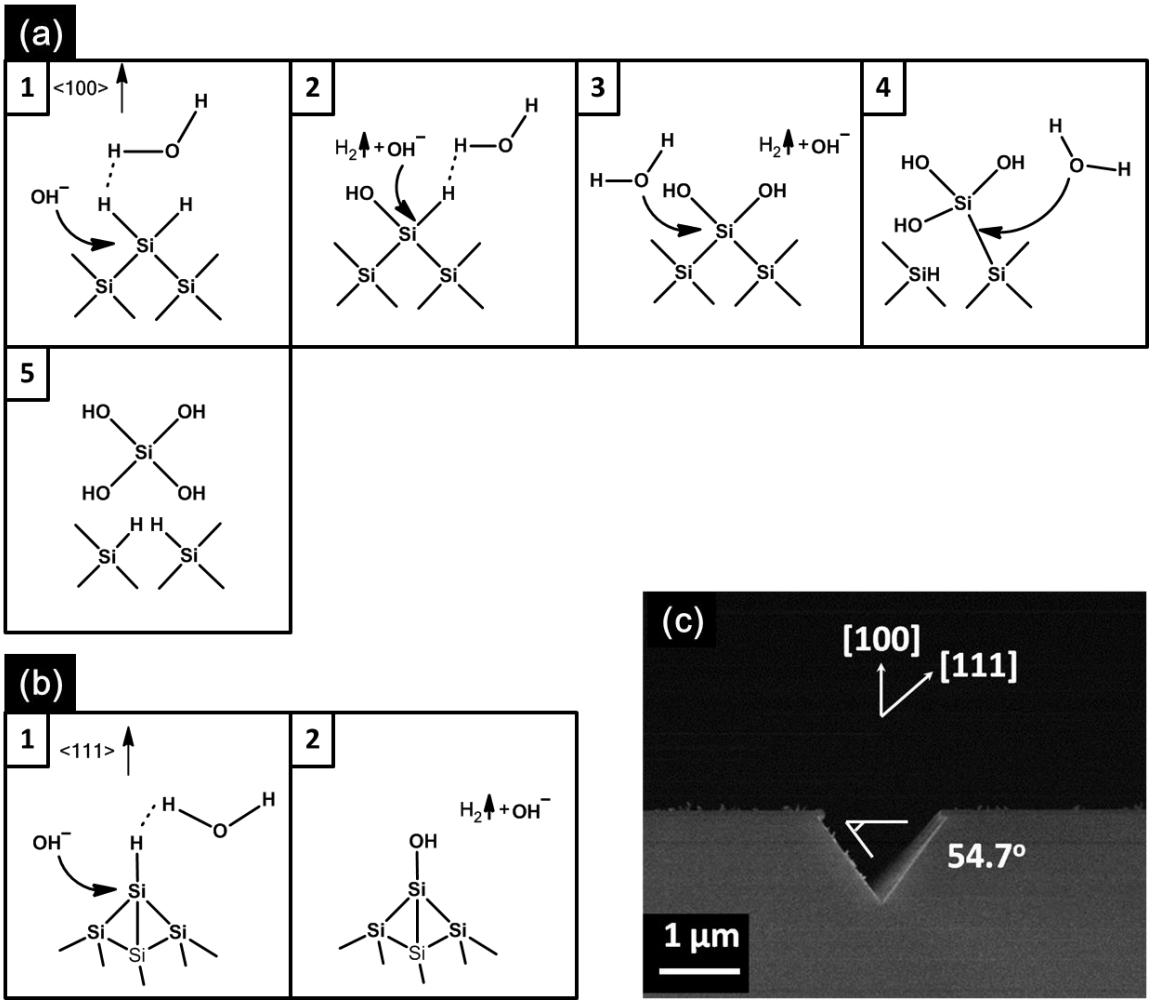

Figure 6 Mechanisms of KOH etching reactions on (a) (100)–Si Surface and (b) (111)-Si surface. (c) Cross-sectional SEM image of a V-groove on (100)-Si substrates by KOH etching.

1.2.3 Wet Etching-Acidic Electrochemical Etching

On the other hand, HAR pores with diameter between 0.3 μm to tens of microns have been fabricated by acidic electrochemical etching (ECE).[17-19] The method is based on the fact that Si can be dissolve by hydrofluoric acid (HF) solution with the existence of electronic holes (h^+):

$$Si+6HF+2h^{+} \longrightarrow 4H^{+}+H_2+SiF_6^{2-} \quad (2)$$

or $$Si+6HF+4h^{+} \longrightarrow 6H^{+}+SiF_6^{2-} \quad (3)$$

During etching, electron-h^+ pairs are generated in Si substrates under light illumination. The h^+ are driven to the front surface by an external electric bias and causes etching on the front surface of Si (**Figure 7** (a)). It has been proposed that h^+ will be concentrated at the tips of vertical pores (**Figure 7** (b)) [17], which facilitate the vertical growth of pores. It should be noticed that for vertical pores formation, the current density or the h^+ concentration ($c(h^+)$) needs to be smaller than a critical value, named as the critical current density (J_c), otherwise vertical pores will grow isotrapically into shallow dents. Since J_c is a function of c(HF), J_c can be written as $J(c(\text{HF}))$. The conditions where $c(h^+) < J(c(\text{HF}))$ and $c(h^+) > J(c(\text{HF}))$ are referred to as the porous Si formation region (PSF) and electropolishing region (EPR), respectively (**Figure 8**).[20] In PSF, the etching direction is found to follow <100> crystalline direction, which coincides with the vertical direction on (100)-Si. The crystalline-orientation dependent etching may be explained by the back bond theory similar to that in KOH etching. In EPR, since the amount of h^+ is abundant, the surface Si atoms are oxidized and Si-O-Si bonds are formed in Si-Si back bonds. Under this condition, the dissolution of Si by HF is actually the chemical dissolution of Si-O, which has an isotropic feature (**Figure 9** (a), (b), and (c)).[21] However, although vertical pores can be obtained on (100) substrate, branching of pores are observed in etching of both (100) substrates as well as non-(100) substrates (**Figure 10**).[19, 22] The branching behavior will generate a considerable amount of undesired defects which may be harmful in applications. Also, HAR structures other than pores are difficult to be fabricated by ECE.

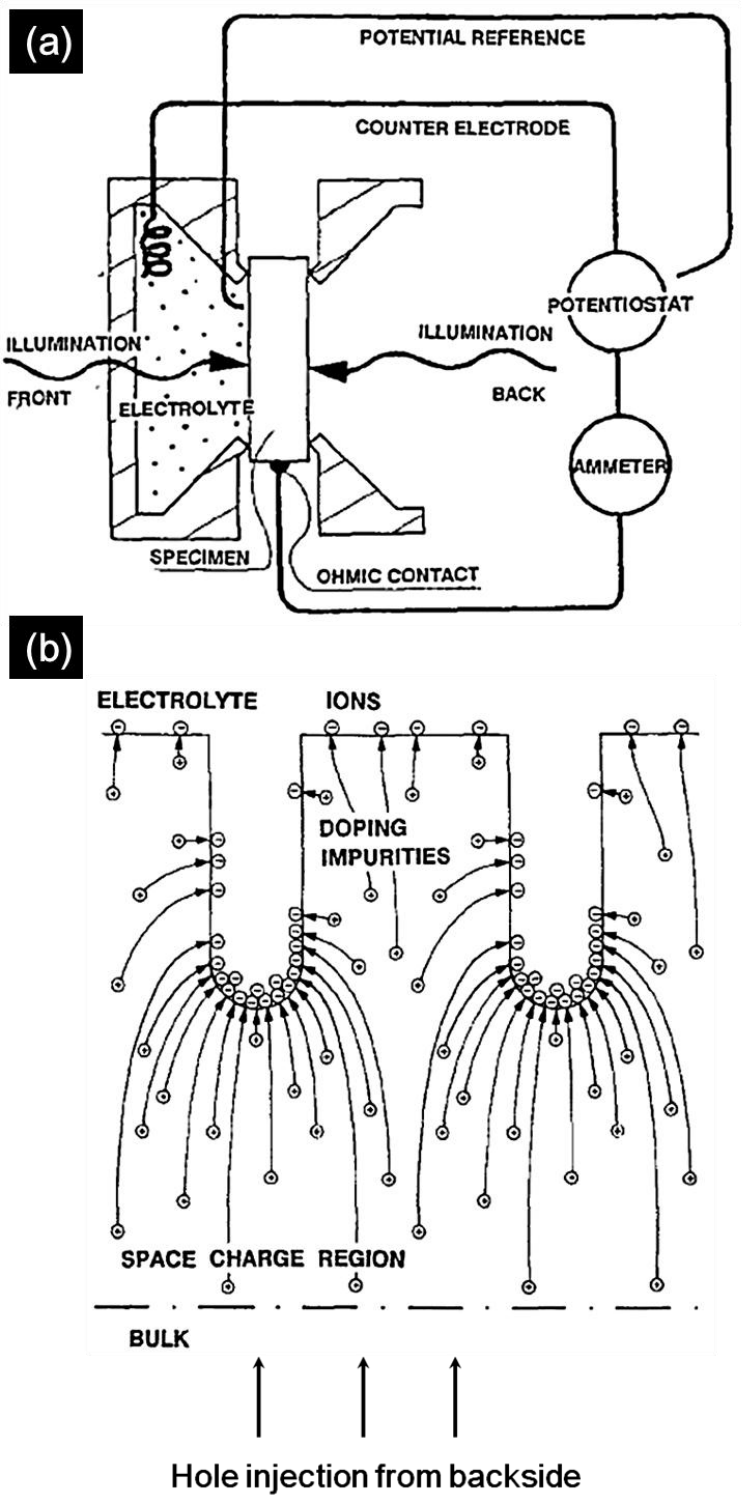

Figure 7 (a) A schematic setup of ECE and (b) a schematic charge transport process at the Si-electrolyte interface. Reprinted with permission from [17]. Copyright 1990, The Electrochemical Society.

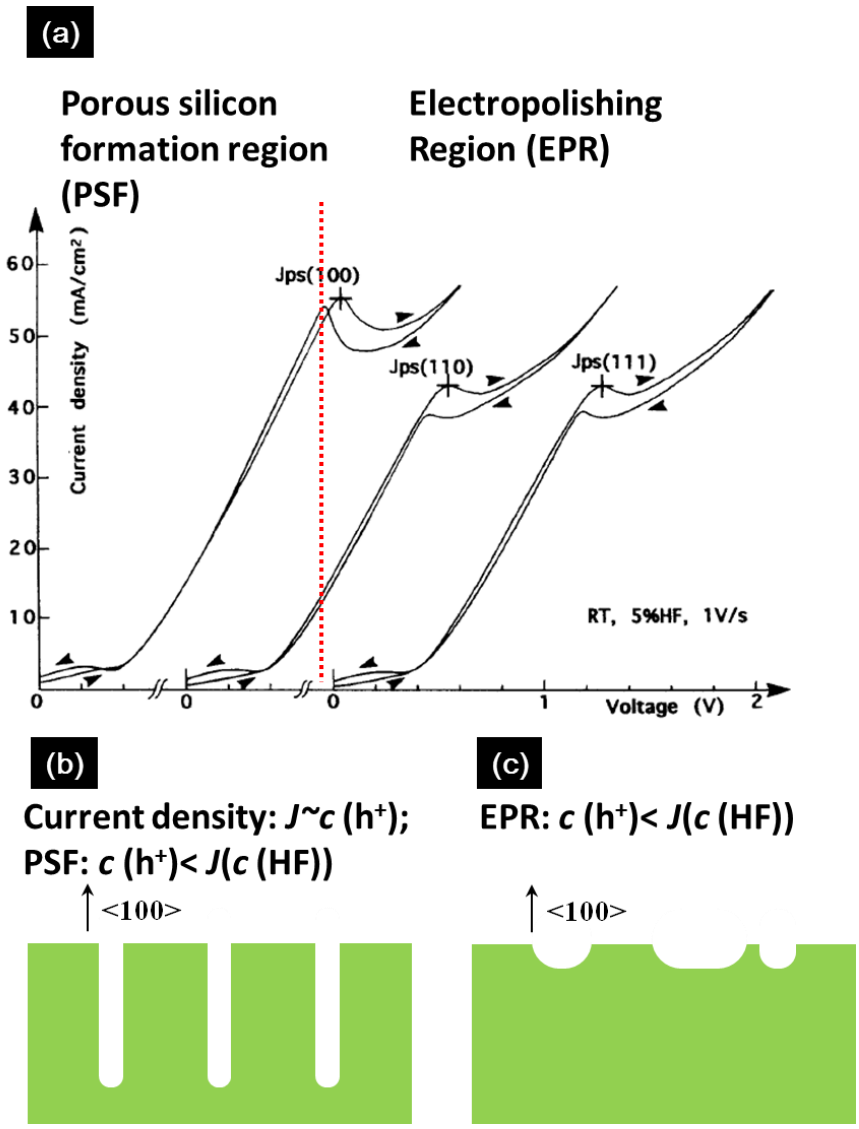

Figure 8 (a) Current density (*J*)-voltage (*V*) curve of (100)-, (110)- and (111)- oriented Si in 5% wt HF solution. Reprinted with permission from [20]. Copyright 1993, The Electrochemical Society. (b) A schematic etching profile in PSF region. (c) A schematic etching profile in EPR region.

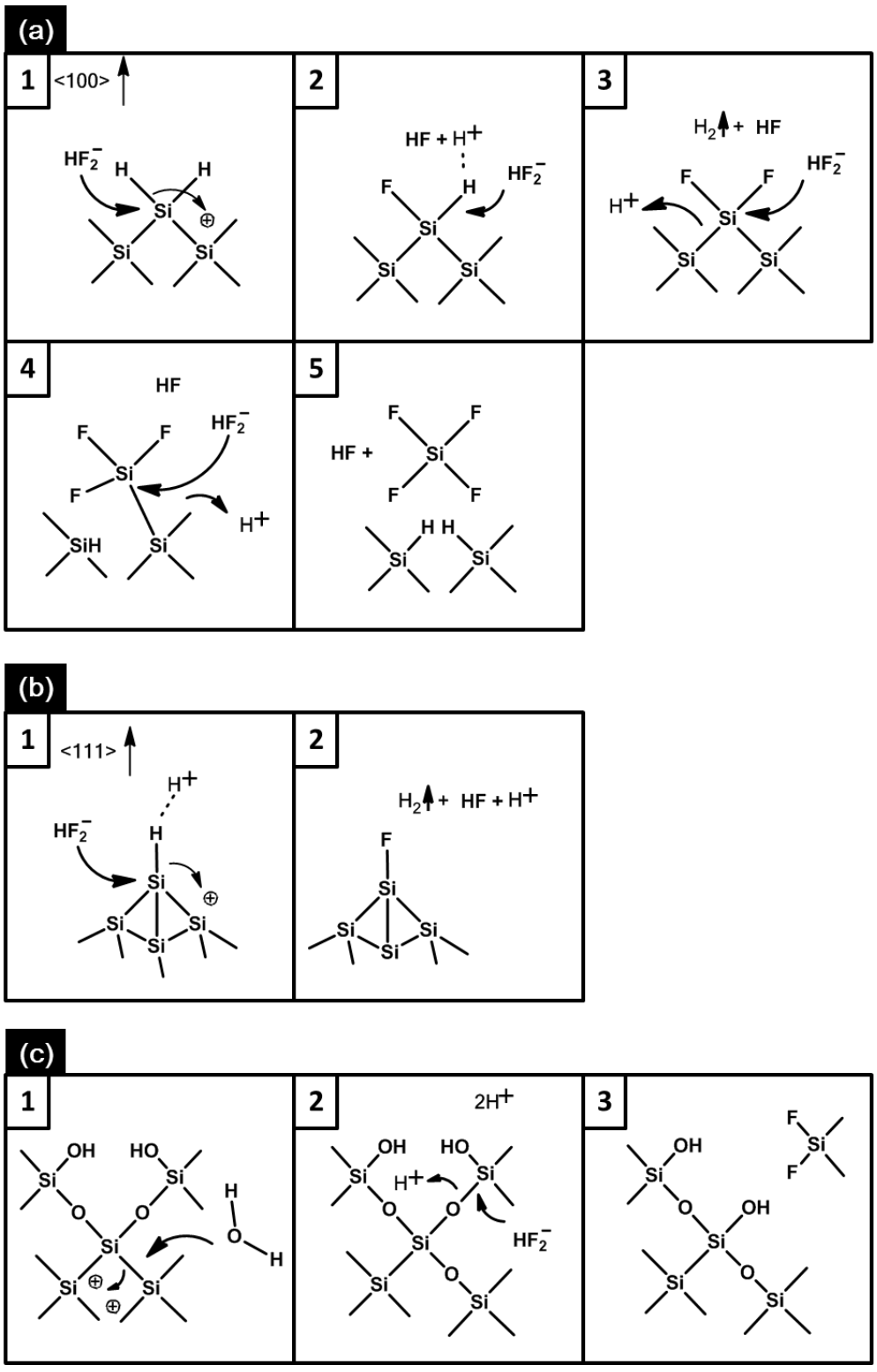

Figure 9 Mechanisms of ECE on (a) (100)-, (b) (111)-oriented Si in PSF region and (c) in EPR region.

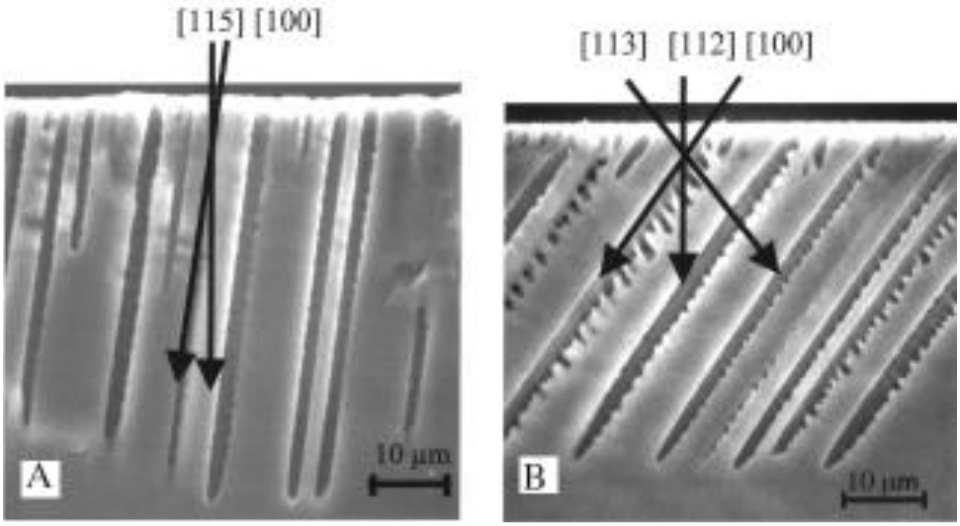

Figure 10 The results of ECE on Si with branching on the sidewall of the etched pores. Reprinted with permission from [22]. Copyright 1999, The Electrochemical Society.

In brief summary, for fabrication of HAR structures on Si, DRIE has been the most popular method due to its capability of etching structures with versatile lateral geometry. However, it suffers from poor economic viability in large scale production. As low cost alternatives, basic etching and ECE can etch trenches and pores with high aspect ratio, but the types of lateral geometry is highly limited. It is highly desirable that a novel etching technology is developed that combines the merits of low cost, arbitrary lateral geometry capability along with high etching rate and low surface roughness. Moreover, the etching direction of a novel etching method is expected to be tunable for fabricating HAR structures with 3D complexity.

Limitation/Method	DRIE	Basic Etching	ECE	MaCE
Lateral size	>100 nm	>1 µm	~300 nm-30 µm	No limit
Lateral geometry	No limit	Trenches	Pores with limited aligment	No limit
Direction	Vertical to substrate	Slowest at <111>	<100> prefered	Tunable in 3D space
Roughness	>50 nm scalloped	<10 nm	porous	<10 nm
Etching rate	~1-20 µm/min	~1 µm/min	~10 µm/min	>10 µm/min
Cost	Expensive	Cheap	Cheap	cheap

Figure 11 Limitations of current methods for HAR structures fabrication on Si.

1.3 Metal-assisted chemical etching: state of the art and challenges

In this dissertation, a novel etching method, named metal-assisted chemical etching (MaCE), is demonstrated to possess the desirable merits mentioned above. Inspired by the concept of ECE that Si can be etched by HF with the existence of h^+, MaCE etches Si using a layer of patterned metal as the cathode for local h^+ generation by chemical decomposition of H_2O_2. The etching occurs when the metal-loaded Si is immersed in a mixture solution of H_2O_2 and hydrofluoric acid (HF). H_2O_2 is catalytically reduced on catalyst surface. At the same time, electronic holes (h^+) are injected metal into the surrounding Si (Eq. 4), which is dissolved by the coexisted HF (Eq. 5):

$$H_2O_2 + 2H^+ \xrightarrow{\text{Noble Metal}} 2H_2O + 2h^+ \quad (4)$$

$$Si + 4h^+ + 6HF \rightarrow SiF_6^{2-} + 6H^+ \quad (5)$$

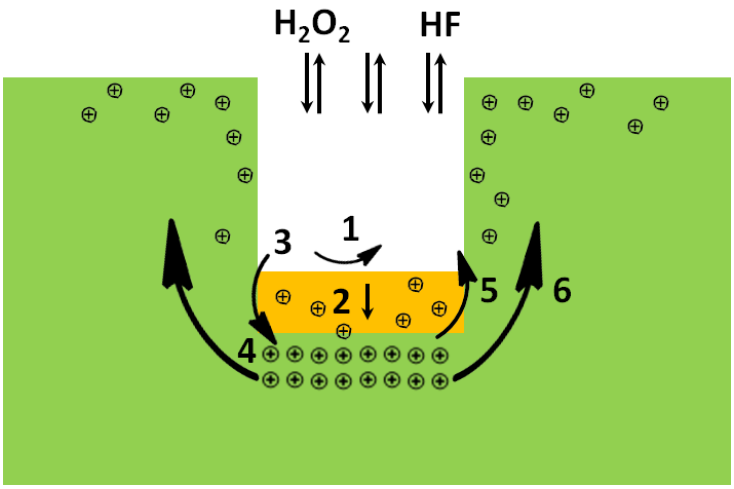

Figure 12 Microscopic processes during MaCE. 1. Decomposition of H_2O_2 (Equation 4); 2. Transport of h^+; 3. Transport of HF; 4. Dissolution of Si (Equation 5); 5. Transport of SiF_6^{2-}; 6. Diffusion of excessive h^+.

Subsequently, the catalyst moves into the etched space and assists further etching (**Figure 12**). Unlike ECE, since h^+ are locally generated from the metal catalyst in MaCE, only the volume of Si in proximity of catalyst is etched (it should be noted that bare Si without metal catalysts stays stable in H_2O_2-HF etchant with etching rate less than 20 nm per hour [23]). Another feature of MaCE is that the catalyst moves during etching, and the final etching profile reflects the trace of catalyst movement.

MaCE phenomenon was firstly reported in 2000 by Li et al. [24] In the report, separate Au, Pt and Au/Pd particles were deposited on Si substrates and the samples were etched in H_2O_2-HF solution. After etching, the surface of Si substrates became porous and the metal particles were found at the bottom of the pores (**Figure 13**). Heavily-doped P-type Si (p^+ Si) and lightly-doped P-type Si (p^- Si) were used in the experiments. The morphology of the etched Si varied with the doping level. MaCE using metal nanoparticles were further systematically studied by Chartier et al.[25] The authors used the term ρ to

denote the composition of the etching solution, where ρ=[HF]/([HF]+[H_2O_2]). In etching solutions with high ρ value, pores tended to form on Si in solutions with low ρ value, however, the whole top layer of Si was removed, similar to the electropolishing phenomena in the ECE of Si discussed in the section **1.2.3** (**Figure 14**). By conducting MaCE with separate metal particles, porous Si surface could be prepared with enhanced superhydrophobicity for potential applications in microelectronics. [26-28]

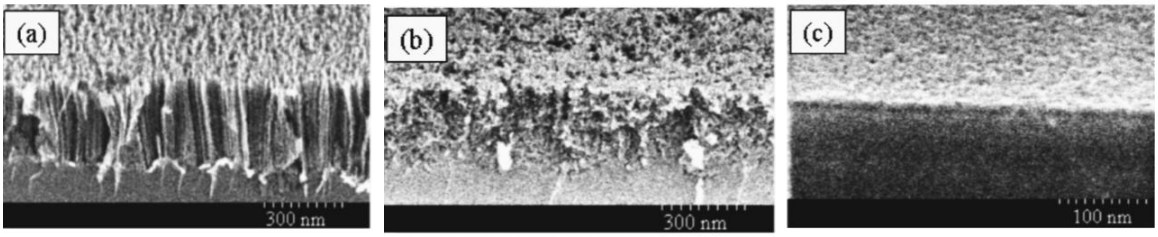

Figure 13 SEM images of Au-coated Si after etching in HF-H_2O_2 for 30 s. The top surface is tilted 30 ° from normal to reveal both top surface and the cross section. (a) Au-coated area on p^+ Si, (b) off the Au-coated area on p^+ Si, and (c) off the Au-coated area on p^- Si. Reprinted with permission from [24]. Copyright 2000, AIP Publishing.

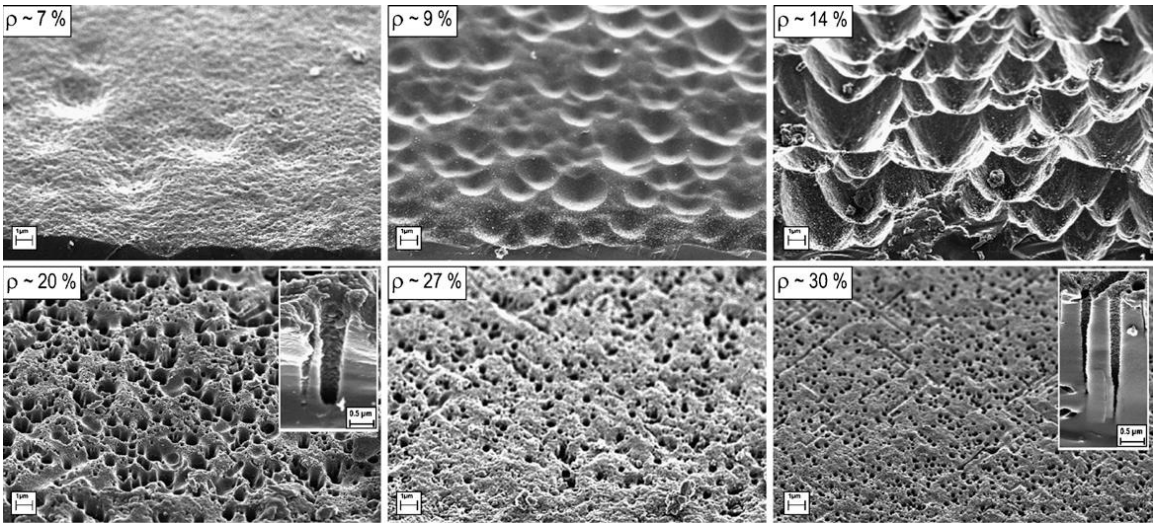

Figure 14 SEM images (at 45°) of p-Si (100) samples after HF-H_2O_2 etching with different ρ values. Reprinted with permission from [25]. Copyright 2008, Elsevier.

Besides the metal particles, metal meshes have also been used in MaCE to fabricate Si nanowires (NWs) or pillars. The metal mesh could be fabricated through deposition of metal on Si with a layer of silica particles as the mask. During MaCE, the metal mesh etched into Si; the Si without coverage of the metal remained hardly etched to form Si NWs (Figure 15).[29] The use of metal mesh in MaCE have achieved success in Si NWs fabrication with a broad range of diameters [30], doping levels [31, 32], crystal orientations [33, 34] and 3D geometries [35-37]. Due to the large lateral size and interconnected morphology, the metal mesh could etch stably into Si and form straight Si nanowires.

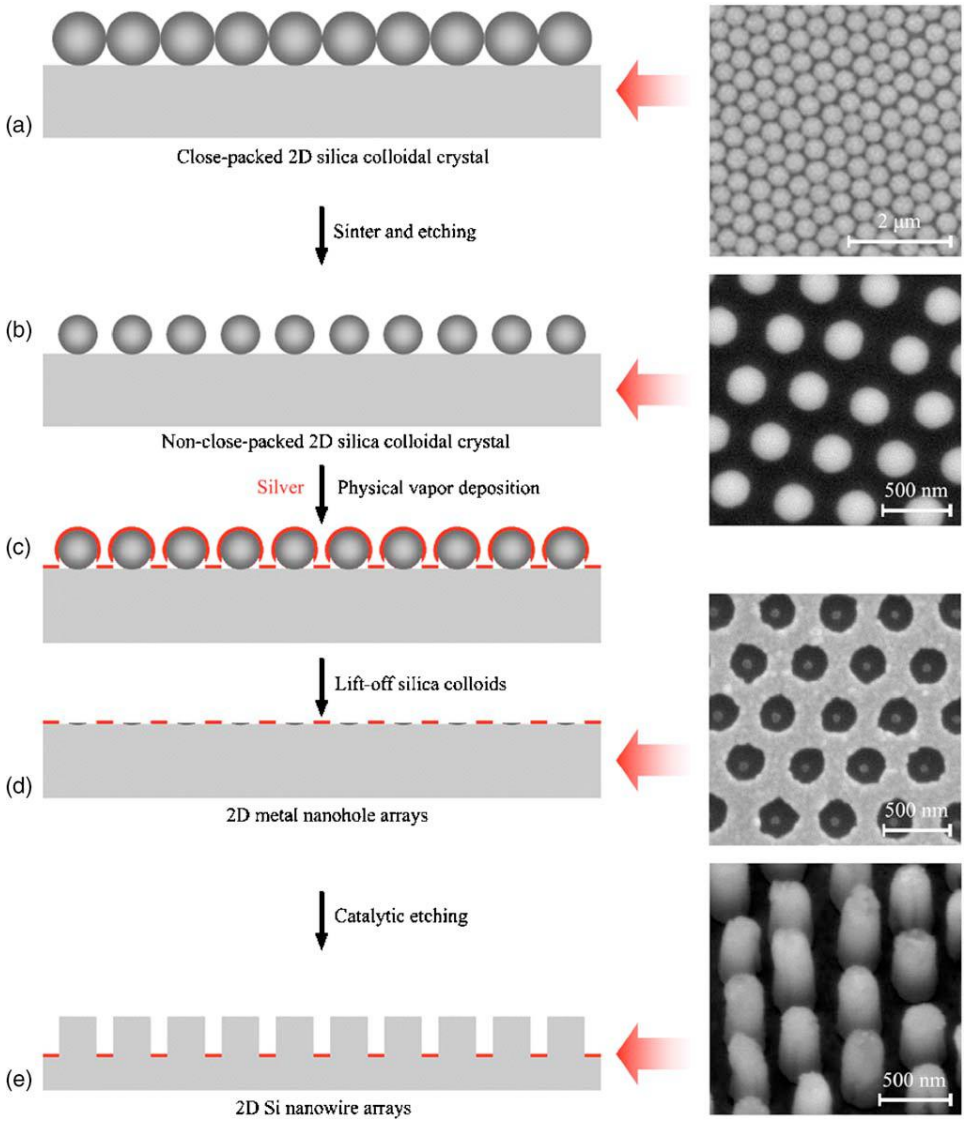

Figure 15 (Color online) Schematic illustration of the experimental procedures for fabricating large-area arrays of ordered SiNWs: (a) deposition of monolayer silica colloidal crystal template on Si surface; (b) fabrication of 2D non-close-packed silica colloidal crystals on Si surface; (c) deposition of silver layer on Si surface through the non-close-packed colloidal crystal template; (d) formation of regular silver nanohole arrays by removing silica colloids by brief ultrasonication in water; and (e) formation of SiNWs by catalytic etching. The corresponding SEM micrographs on the right show the monolayer silica colloidal crystal template (a), the 2D nonclose-packed silica colloidal crystal template (b), the silver film with periodic nanohole arrays (d), and ordered SiNW arrays produced using catalytic silver film with periodic nanoholes (e). Reprinted with permission from [29]. Copyright 2007, AIP Publishing.

By using lithographically defined catalyst, our group has previously demonstrated a series of controllable nonlinear etching behaviors in MaCE, such as spiraling of catalyst [38-40], folding of hinged catalyst [41], and out-of-plane rotation of pinned catalyst (**Figure 16**).[42-44] The forces that induced these nonlinear etching behaviors have been analyzed.[44] These movements produced a set of complicated shallow structures on Si, which cannot be fabricated by any other existing technology. However, these catalysts have much smaller lateral size and are separate from each other on the Si substrates, therefore bending and deformation have been observed during MaCE. It will be desirable that metal catalysts can move deeply into Si in a stable way to form uniform HAR structures for the applications mentioned above. The challenges of achieving this goal and the solutions for these challenges will be discussed throughout the following chapters. Based on a research of literatures, no successful solutions have been reported regarding these challenges.

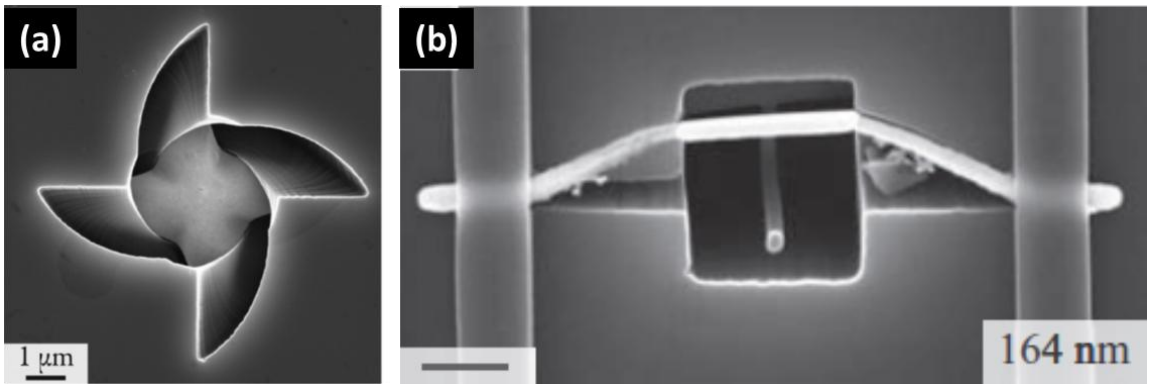

Figure 16 (a) Spiral movement of a star-shaped Au catalyst in MaCE. Reprinted with permission from [39]. Copyright 2012, American Chemical Society; (b) out-of-plane rotation of a horseshoe-shaped Au catalysts in MaCE. Reprinted with permission from [42]. Copyright 2011, John Wiley and Sons.

CHAPTER 2

MACE BY SEPARATE METAL PARTICLES AS CATALYSTS

2.1 Introduction

In this chapter, we start with silver (Ag) nanoparticles with diameter of 10-30 nm as catalyst to test if they can form HAR structures on Si through MaCE. The schematic process flow is shown **Figure 17**. This chapter have been partially published in [45] and reprinted here with permission. Copyright 2013, IEEE.

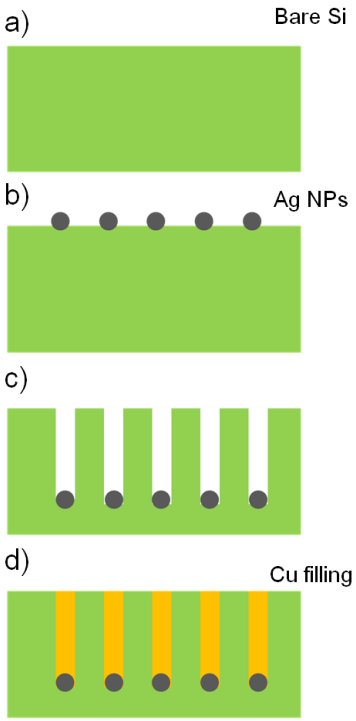

Figure 17 Schematic processing flow of MaCE by separate metal particles: **(**a) bare Si preparation; (b) Ag NPs deposition; (c) MaCE; (d) Cu filling.

2.2 Methods

All chemicals are directly used after purchase without extra processing unless mentioned. Single-side polished single crystalline (100) p-type boron-doped Si wafers with 100 mm diameter (Ultrasil, CA) with a resistivity of 1–10 Ω·cm were cleaved into 1 ×1 cm^2 pieces. The Si pieces were cleaned in Piranha solution (1:1 volume ratio H_2O_2:H_2SO_4) at 180 ^oC for 30 min, and then immersed in 1 wt% HF (aq) solution to remove the oxide layer. Deionzed water (DI water) was produced by a Thermo Scientific Barnstead Smart2Pure water purification system. Scanning electron microscope (SEM) images were taken from Ziess LEO 1550 thermally assisted field emission (TFE) SEM operating at 10 keV with a working distance between 2 and 7 mm with inserted Oxford EDS system. A VersaStat MC potentiostat by Princeton Applied Research was used for current-potential output and recording during Cu plating.

Ag nanoparticles (NPs) were deposited on clean Si surface by electroless metal deposition (EMD) method [25]. The Si samples were immersed in a solution containing $AgNO_3$ (Aldrich) and HF for a certain period. After rinsed by copious DI water and dried in N_2, the Si sample loaded with Ag NPs was immersed in a HF-H_2O_2 etching solution and quenched in DI water as the etching ended. The cross sectional SEM image were obtained by mechanically cleaving the etched sample.

The etched samples were subjected to a home-made working electrode for electroplating. A platinum wire was used as the counter electrode and Ag/AgCl in saturated KCl (aq) solution was used as the reference electrode. The plating solution contained $CuSO_4$, H_2SO_4 and other additives. After plating, the samples were rinsed and dried for SEM observation.

2.3 Results and Discussion

2.3.1 Ag NPs Deposition

Ag NPs were deposited on the Si surface through a substitution reaction:

$$4Ag^{+} + 6HF \rightarrow SiF_6^{2-} + Ag + 2H^{+} \quad (6)$$

The particle size of Ag NPs could be controlled by the concentration of $AgNO_3$. Under the condition used here, the size of Ag NPs was in a range of 10 to 50 nm **(Figure 18** (a)). The NPs were well separated and the surface density was estimated to be $10^3/um^2$ from the top view SEM images.

2.2.2 MaCE for HAR pores

The MaCE process was conducted by immersing the sample in the HF-H_2O_2 solution. After etching, the top surface of Si samples showed a porous morphology (**Figure 18** (b)). Based on the IUPAC recommendation [46], both mesopores and macropores were observed. The shape of the pores was random, which was different from the regular shape of pores by ECE. This suggests that the shape of the pores may be defined by the movement of metal catalyst, rather than the h^+ during etching or the crystalline direction of the Si substrates. From the top-view SEM images, some Ag NPs were observed remaining in the near-surface region. It is worth noting that the average diameter of these remaining Ag NPs was significantly larger than that of original Ag NPs. It has been proposed that the etching rate was inversely related to the size of metal catalyst. Thus some small particles might have etched into the Si sample, while the bigger catalysts were left near surface.

More relevant images that demonstrate the movement of those Ag NPs which etched into the bulk Si samples are the cross-sectional images (**Figure 18** (c) and (d)). Two layers could be distinguished simply by the contrast of the image. The higher contrast of the top layer under the electron microscope observation might be assigned to a higher h^+ injection rate, which makes the Si more oxidized. In the top layer of about 4 μm in depth, the number density of pores was higher. Both straight as well as winding pores could be found in images with higher magnification. It could be deduced that some Ag NPs moved

tortuously and finally stays in the near surface region, which was consistent with the observation in **Figure 18** (a).

In the bottom layer, vertically aligned pores with a maximum depth of 11 μm and a minimum diameter of 30 nm could be observed. The maximum AR reached 350. Ag NPs were found to reside in the bottom of most of pores, and the pore diameters exactly followed that of the residing Ag NPs. The result clearly demonstrates that MaCE is anisotropic, which is necessary for fabrication of HAR structures.

The anisotropy of MaCE is one of its most fascinating features. According to the mechanism of ECE, the <100> crystalline directions are the preferred etching direction in PSF region. In the result here, the vertical etching direction was preferred, which coincided with the <100> directions. The porous morphology of the etching results as well as the preferred directions along <100> direction implying that the transport of h^+ might be similar to that in the PSF region in ECE.

Although HAR structures could be observed from the results of MaCE, it is essential to find out why some of the Ag NPs moved randomly in the near-surface region. Intuitively, the shape variation between each particle may be a contributing factor. However, due to the resolution of SEM instrument, it is hard to compare the shape of the nano-sized particles. Another possibility is the aggregation of Ag NPs. It has been reported [47] that for micron-sized Au particles, the aggregation of multiple particles would etch more straightly than separate individual particles. Huang also reported highly ordered Si nanowires could be achieved by MaCE of high density Ag NPs [30, 33]. It is conceivable that in the nano-scale, since nearly all the particles do not have absolutely spherical shapes, the irregular shape may make the particles deviate from the favorable [100] direction due to the irregularity of the shape. In this sense, patterned metal NPs with regular shapes and spacing distance would be helpful to identify the origin of the random movement of the catalysts.

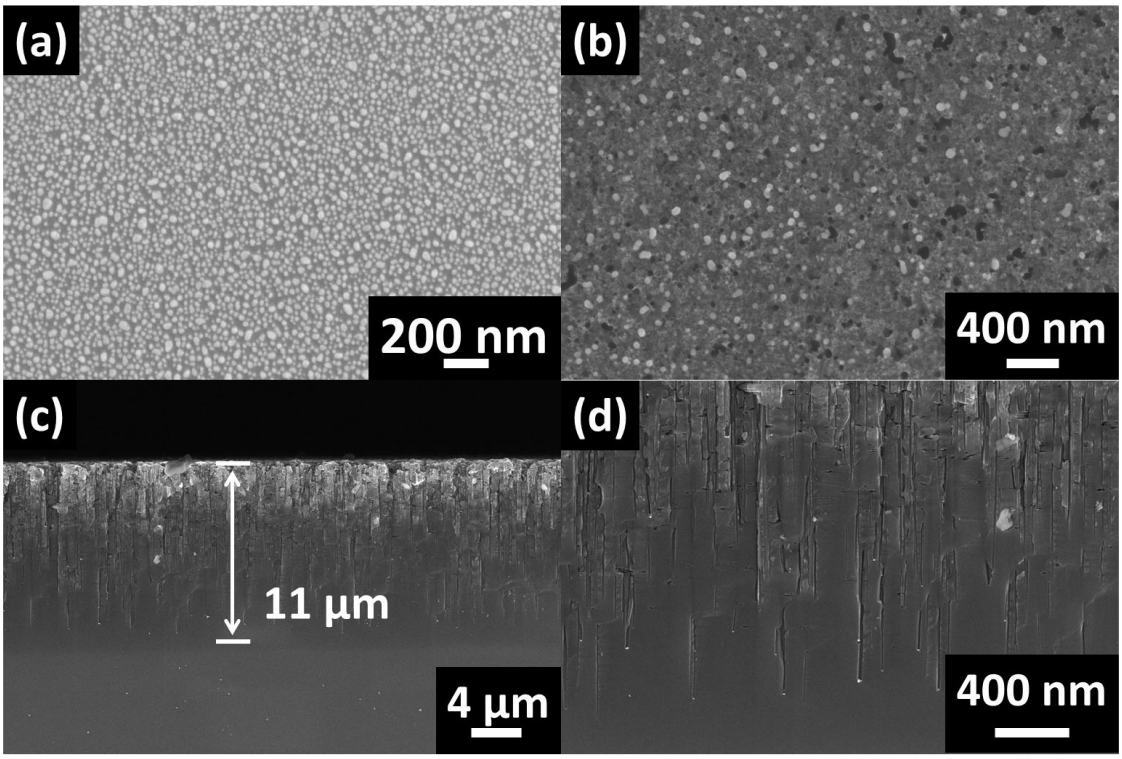

Figure 18 (a) Top view of the Si surface after deposition of Ag NPs. (b) Top view and (c) cross sectional SEM image of Si surface after MaCE; (d) magnified image in middle of (c).

2.2.3 MaCE by patterned Au NPs with regular shapes

Lithographically defined Au NPs array were used as the catalysts in MaCE. The diameter of the Au NPs was 120 nm with a spacing of 500 nm. (**Figure 19**). Some verticals holes with diameter of 200-400 nm and depth of 160 µm were also observed after MaCE for 15 min, corresponding to an aspect ratio of 400 to 800 and an etching rate of 10 µm/min. In comparison, in dry etching the rate ranges from 5-10 µm/min, with the highest aspect ratio being ~100:1. Also, since the etching proceeds continuously, the sidewall of holes by MaCE was smooth and free of scalloping, which was hard to be achieved by dry etching. However, pores with random shapes could be observed as well, which were similar to those

in results from MaCE by Ag NPs. The results imply that the irregularity of the shape of the catalysts might not be the major factor that caused the random etching.

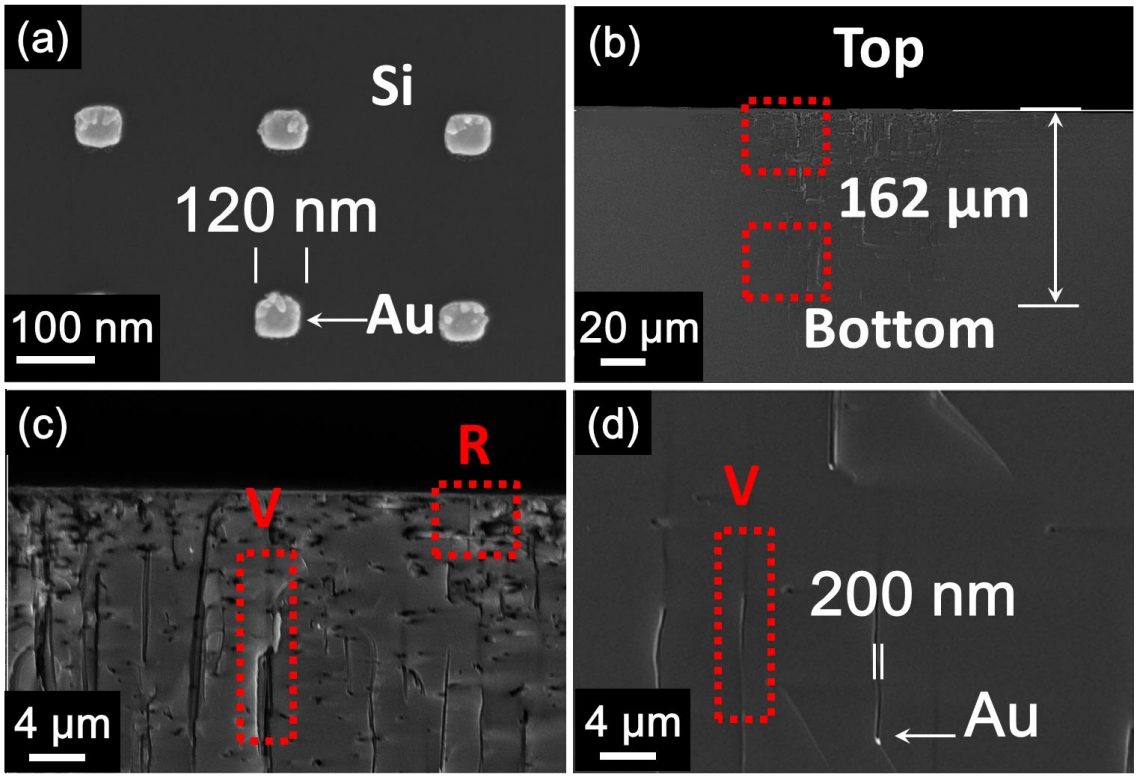

Figure 19 SEM images of (e) lithography-patterned Au NPs on Si; (f) Si after MaCE by Au NPs, the magnified images of the top part and the bottom part are shown in (g) and (h), respectively.

2.2.4 Cu filling of the etched pores

Another possible reason for the random etching is that due to the diameter of the pores was too small, the transport of the etching solution may be hindered which caused fluctuations in the local chemical environment at the catalyst-Si interface. To test the difficulty of solution transport within the narrow pores, Si samples with the etched pores

were electroplated with Cu in solution. It is noteworthy that compared to the blind holes etched by traditional DRIE method or wet etching, the bottom of the pores contains metal catalyst. These catalysts could not only accelerate the etching, but also serve as the seed layer for electroplating due to a lower overpotential of Cu reduction on metal surface compared to Si:

$$Cu^{2+} + 2e^{-} \xrightarrow{\text{metal}} Cu \quad (7)$$

From the electrochemistry data (not shown here), an anodic shift of 50-100 mV was observed for the reduction threshold potential of Cu on Ag NPs loaded Si compared to the bare Si.

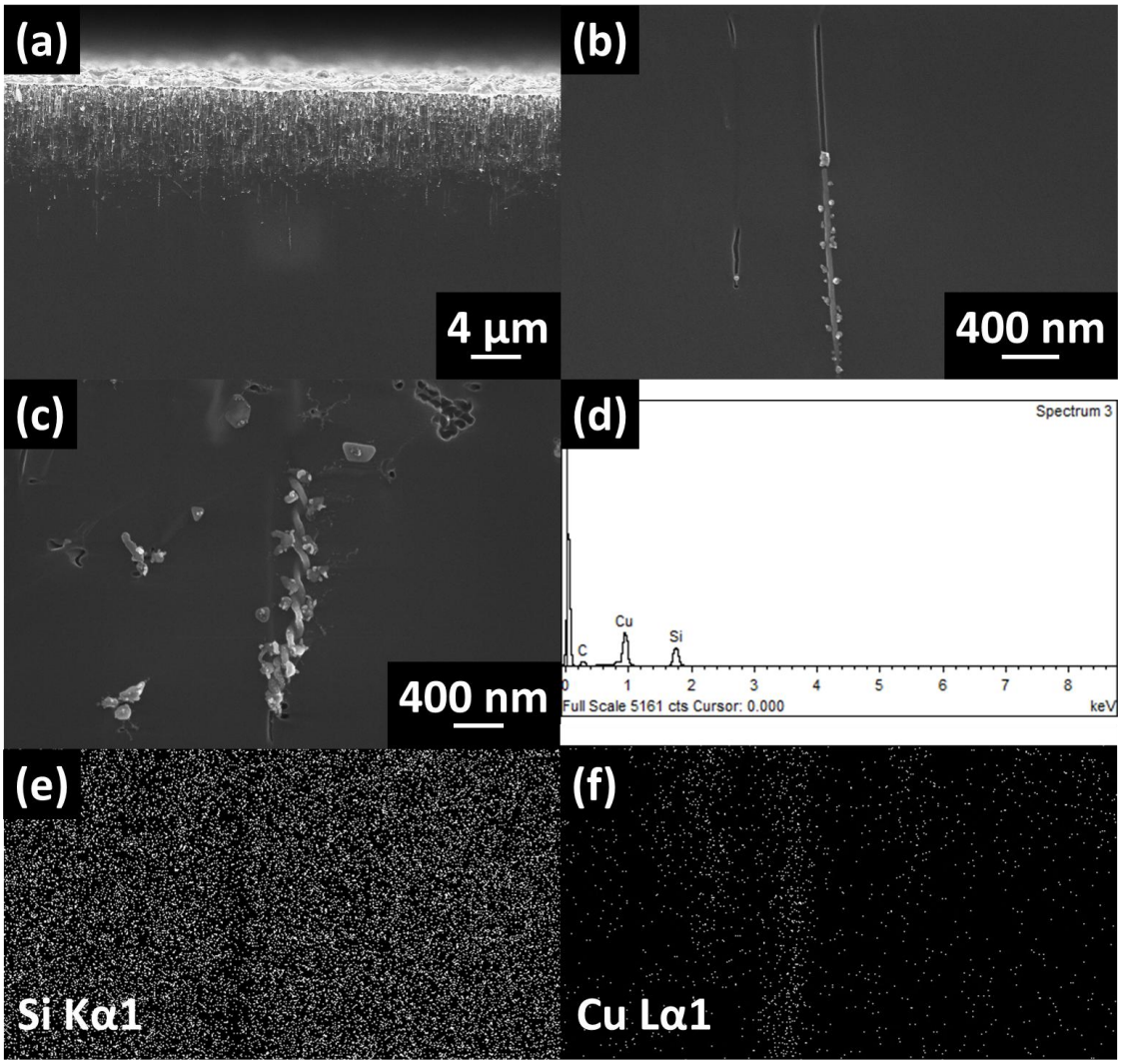

Figure 20 Cross sectional SEM images of (a) Cu filled Si via; (b) magnified image of a straight via tip; (c) magnified image of a helical via tip.

A complete Cu filling has been reported [48] for micro-sized pores by MaCE with Au microsphere at the bottom. Here a Cu filling in the sub-100 nm wide pore is firstly reported. **Figure 20** (a) and (b) showed that Cu could grow from the Ag NPs at the bottom of a 30nm-wide straight pore. What is more surprising is that a helical pore 11µm deep from top surface is also observed with Cu filling. The result indicates that the plating

solution was well able to reach the bottom of the pores with diameter as small as 30 nm and AR as high as over 100:1. And the transport of etching solution inside the HAR pores should be allowed.

2.4 Conclusion

The above findings demonstrate that the MaCE is a promising technology in nanomanufacturing of HAR structures with high aspect ratio, high etching speed and low surface roughness. However, ideally all the Au or Ag NPs should etch in the same way since they have the same geometry and are exposed to the same chemical environment (**Figure 21** (a) and (b)). In experiments, a considerable amount of Au and Ag NPs were found etching randomly, and the etching profiles under a given MaCE conditions is non-uniform. The non-uniform etching poses a fundamental challenge to the application of MaCE in HAR structures fabrication. In the manufacturing of real devices, the etching uniformity is highly demanded. Poor uniformity can induce severe degradation of device performance. For example, in 3D electronic packaging, roughness over 72 nm on the sidewall of through Si vias (TSVs) significantly raised up the leakage of signal communication [49]; in Si photonic crystals, the optical properties significantly degraded with a 2% size variation of each repeating unit [50]. Thus, it is imperative to understand *how* to achieve uniformity in MaCE before it is applicable in HAR structures fabrication. Based on our knowledge, the random etching phenomenon, as have been reported by several research groups (**Figure 21** (d) and (e)) [51, 52], is not fully understood and no feasible solution towards uniform MaCE (UMaCE) has been provided.

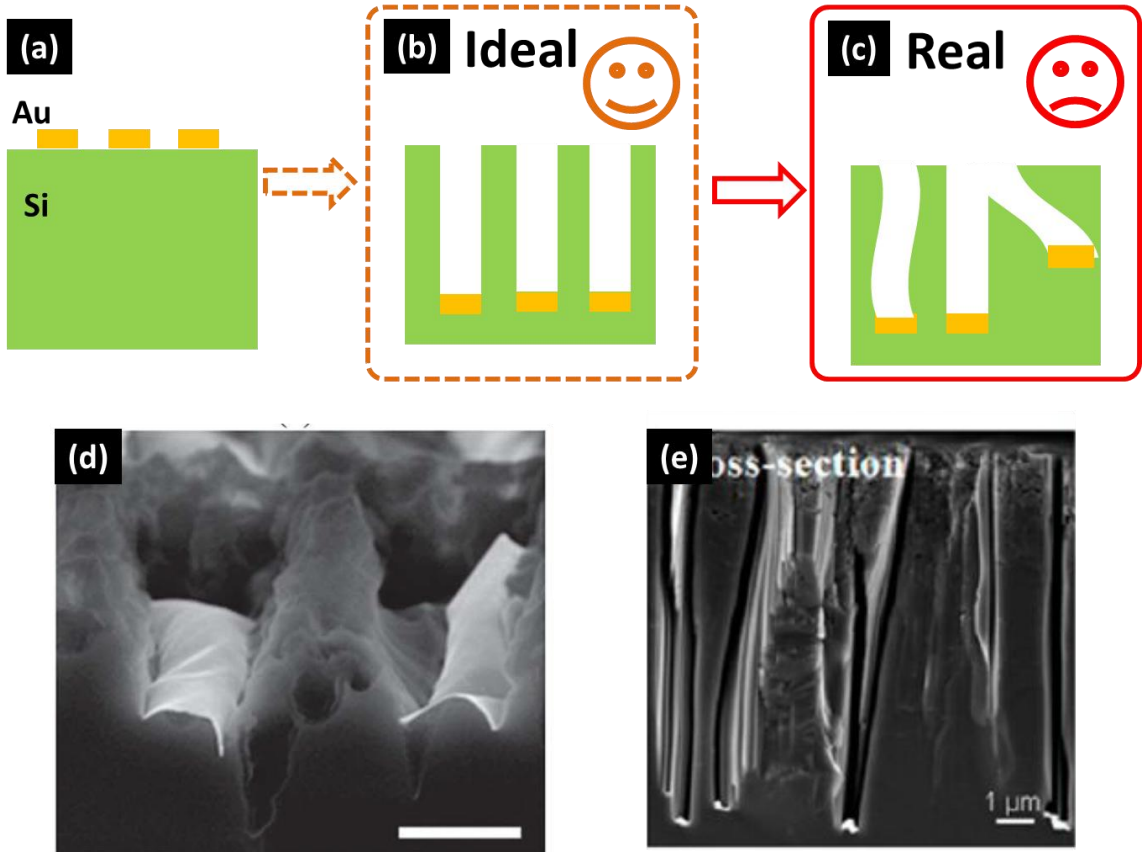

Figure 21 Schematics of (a) metal catalysts on Si; (b) ideal etching profile by the metal; (c) real etching profile by the metal. (d) and (e) show SEM images of Si after MaCE using Au stripes as catalysts reported by two independent groups. Reprinted with permission from [51] and [52], respectively. Copyright 2012, Royal Society of Chemistry and Copyright 2013, American Chemical Society, respectively.

CHAPTER 3

UNIFORM HAR VERTICAL MACE BY NANOPOROUS CATALYST

3.1 Introduction

In this chapter, the feasibility of using MaCE to fabricate uniform microstructures is demonstrated. The contents in this chapter have been partially published in [53] and reprinted here with permission. Copyright 2014, American Chemical Society.

From the view of mechanism, the process of MaCE can be divided into two parts: the mass transport process (MT) and charge transport process (CT). The MT includes the transport of reactants (HF and H_2O_2) and products (H_2O and H_2SiF_6), while the CT consists of the generation, transport and consumption of h^+. In experiment, MT can be controlled by the geometry and morphology of catalyst, while CT can be controlled by the concentration of HF and H_2O_2. The final etching profile is synergistically influenced by the MT and the CT. For the convenience of following discussion, here we adopt the term ρ=[HF]/([HF]+[H_2O_2]), where [HF] and [H_2O_2] are concentration of HF and H_2O_2 in mol/L. And we use the format of $\rho(x)^y$ to name a specific etchant of which $\rho=x$ and [HF]=y.

Regarding the non-uniform etching results reported in literature [51, 52], here we identify two major factors that caused the failure in prior literatures: (1) the catalysts adopted continuous-film morphology. During etching, the etching solution could hardly reach the region under the center of catalyst. Therefore, the etching rate of this region was slower than that near the catalyst edge.[54] The uneven etch rate finally induced the deformation of catalyst. (2) Etchant of high ρ value (0.80-0.95) was used, in which the number of generated h^+ was less that can be consumed up by the process described in Equation 5 [25]. This condition was found to cause the random movement of the catalyst.[51, 55]

Here, we solve these issues by two fundamental innovations: (1) Au stripes with nanoporous morphology are used as catalysts. The nanoporous morphology of Au stripes allows MT proceeding through the catalyst edge as well as the pores within the stripe (named through-catalyst MT, **Figure 23** (a)). The distance of MT is significantly shortened and evenly distributed, which guarantees a uniform high etching rate across the catalyst. We also demonstrate that the desired nanoporous Au catalyst can be facilely obtained by surface treatment of substrate and control of deposition thickness during electron beam evaporation, as described in the following session; (2) the ρ value of the etchant is lowered to 0.37. The low-ρ etchant induced an electropolishing-favoring type charge (EPF) transport. Under this condition, etching is favored only along the normal of substrate surface, which also facilitates the uniformity of vertical etching profile.

3.2 Methods

Boron-doped (100) and (111)-oriented Si wafers with (University Wafer, MA) with a resistivity of 1–10 Ω·cm were cleaned in Piranha solution at 120 ^{o}C for 10 min, and then dipped in 1% w/w aqueous HF solution to remove the oxide layer. The (100)-type Si substrates were used for most of the test unless specified. For electron beam lithography, a 350 nm-thick poly (methyl methacrylate) (PMMA A6, Microchem, MA) resist film was spun cast on Si wafer and exposed in a JEOL-9300FS EBL system with a base dose of 400 μC/cm^2. The exposed wafer was developed in the mixture of isopropanol and methyl isobutyl ketone with a volume ratio of 1:1 for 2 min. For photolithography, a 1.6 μm-thick layer of positive resist Microposit S1813 (Shipley) was spun cast on the wafer and exposed in a mask aligner (Karl Suss MA6) by 405 nm UV light. The exposed wafer was developed in Microposit MF 319 developer. All the wafers with patterned resist are treated with oxygen plasma (RF power: 22 W) in a RIE tool (Plasma Therm Inc.) to remove any polymer residue on exposed areas and render the Si surface as oxygen-terminated (Si-O); the Si-O surface can be altered as hydrogen terminated (Si-H) by immersing the Si-O

sample in a buffer oxide etch (6:1) solution for 1 min and rinsing with copious deionized water. Water contact angle measurements were performed with a Rame-Hart goniometer with a charge-coupled device camera equipped for image capture. Au catalysts were deposited by an electron beam evaporator at a rate of 0.5 Å/sec in a vacuum atmosphere of 3×10^{-6} Torr (CVC Product Inc.). In this chapter, the thickness refers to the nominal value measured by an in-situ monitor (Maxtek Sensor Crystal Gold 6MHz 74016-1139 P/N 103220, Inficon) unless specified.

To prepare the etchant, HF (48-52%wt in H_2O) and H_2O_2 (30%wt in H_2O, Anachemia Chemicals, LLC) were directly mixed without further processing. Deionzed water (DI water) was produced by a Thermo Scientific Barnstead Smart2Pure water purification system. The total volume of the etchant was fixed as 42 mL. The etching was conducted by gently immersed the sample in the etchant solution in a closed non-transparent polyethylene container for a certain amount of time at room temperature. No additional agitation was used. To fill the trench, an epoxy precursor (17g EPON Resin 862, Hexion Special Chemicals Inc.; 20 g Lindride 52D, Lindau Chemicals; one drop of imidazole catalyst, Shikoku) is cast on the etched sample and cured at 150 ^{o}C in an atmospheric oven for 1 hr. The polymer replica is isolated by completely removal of Si in the mixture of HNO_3 (70%wt), HF (49%wt) and H_2O with the volume ratio of 1:1:1 overnight. SEM were taken from Ziess LEO 1530 thermally assisted field emission (TFE) SEM operating at 10 keV with a working distance between 2 and 7 mm with inserted Oxford EDS system. Atomic force microscope data was collected by Veeco Dimension Edge AFM with Bruker TESP-SS Si tips (nominal tip radius: 2 nm). The Matlab7.0 software was used for modeling of hole concentration.

3.3 Results and Discussion

It has been reported that oxygen-terminated Si surface (Si-O) dewets Au.[56] At the early stage of physical vapor deposition of Au thin film on Si-O, separated islands of

Au atoms are formed by their self-agglomeration.[57] As the deposition proceeds, the islands grow and the gaps between them become narrower, before they finally coalesce into a continuous film. By control of the amount of deposited Au, i.e. its nominal thickness (referred as thickness in the following discussion unless specified), we can obtain a partially-coalesced Au film with few-nanometer-wide gaps between the Au islands. Based on this idea, (100)-oriented single crystal Si substrate (referred as Si in the following unless specified) was coated with a layer of polymer resist. A 2.00 ± 0.03 μm-wide stripe-shape exposed area was patterned by electron beam lithography (EBL) due to high patterning accuracy. EBL is used in the fabrication of all other patterns in this chapter unless specified. After treated with oxygen plasma, the exposed area on Si showed a water contact angle of 0^{o} (**Figure 23** (b) inset), an evidence of Si-O surface chemistry which was primarily composed of silanol group (Si-O-H).[21] Subsequently, Au of 10 nm thickness was deposited on Si-O (named as SiO-10 nm catalyst) by electron beam evaporation. Under SEM, the nanoporous morphology within SiO-10 nm catalyst can be clearly observed, with an average pore width of 5-10 nm (**Figure 22** and **Figure 23** (b)). The Au-loaded Si was immersed in $\rho(0.37)^{1.8}$ etchant for 1 minute. (In this chapter, the polymer resist was not lift-off before etching mainly because the process was found to partially remove the catalyst as well). After etching, the SiO-10 nm catalyst moved vertically into Si by 480 nm; the sidewall of the formed trench is smooth and the overall catalyst keeps flat (**Figure 23** (c)). The nanoporous morphology of SiO-10 nm catalyst was also characterized by atomic force microscope (AFM) using super-sharp tips. The AFM-measured thickness of SiO-10 nm catalyst is 10.0 ± 1.0 nm (**Figure 23** (d)), identical with the maximum peak-to-valley depth of 9.8 nm within the stripe (**Figure 23**(e)). This accordance implies that the pores penetrate through the whole layer of Au film, a necessary condition for through-catalyst MT to occur.

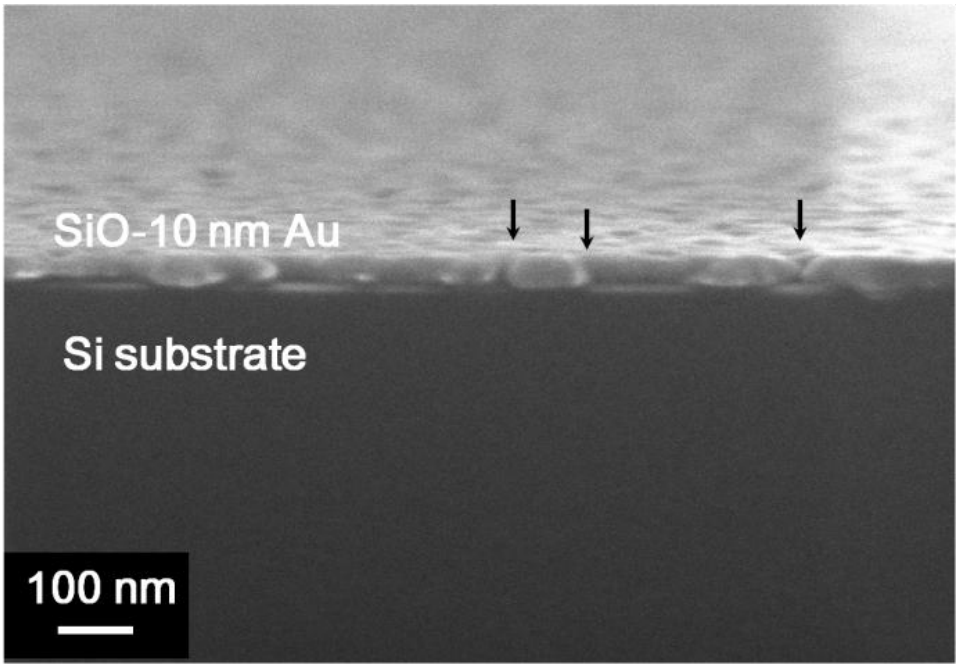

Figure 22 Cross-sectional SEM image of a SiO-10 nm Au catalyst on Si substrate viewed at 5° tilting angle. Black arrows indicate nanopores in SiO-10 nm Au for through-catalyst mass transport.

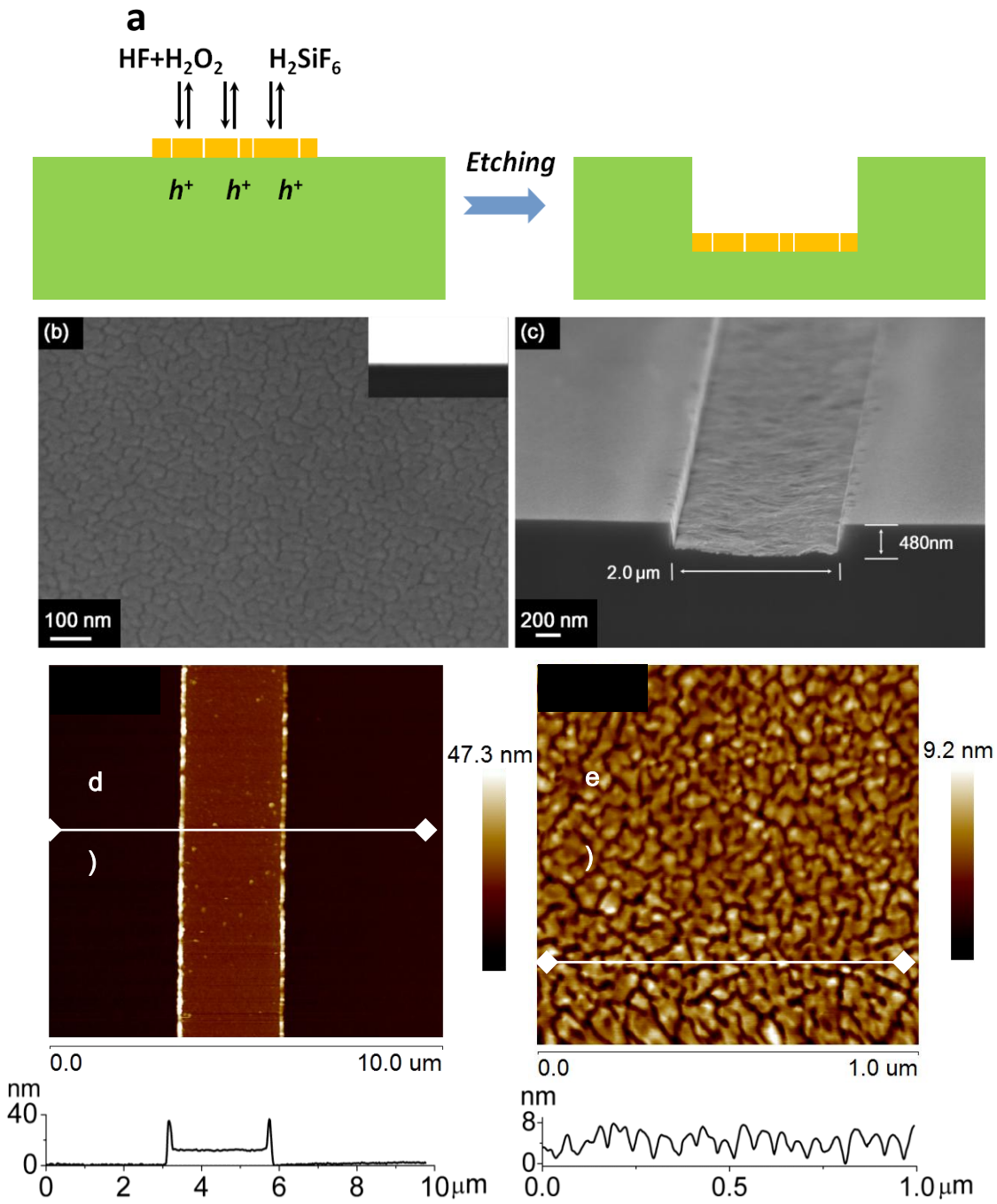

Figure 23 (a) Schematic mechanism of a through-catalyst MT process. (b) Bird's eye view SEM images of SiO-10 nm catalyst. The inset shows the contact angle image of a water droplet on the Si-O surface. (c) Cross-sectional SEM image of the trench etched by SiO-10 nm catalyst shown in (b) for 1 min in $\rho(0.37)^{1.8}$ etchant. (d) Overall and (e) detailed AFM height sensor image (up) and cross-sectional diagram (bottom) of SiO-10 nm catalyst.*

*Note: For AFM measurement, the Au stripes are patterned as an array using standard photolithography process described in the experimental session. The overall thickness is measured after lift-off of the photoresist. Since the adhesion between Au and Si-O surface is not strong enough to survive the lift-off process, the AFM image is collected from the remaining Au stripe. Here we assume the measured morphology and absolute thickness are the identical to the Au stripes patterned by EBL, because the same substrate and deposition condition are used.

In contrast, if the catalysts possess continuous morphology, they are supposed to easily deform after etching, since the mass transport is only enabled from the edge of catalyst (**Figure 24** (a)). To illustrate this point, we obtained continuous Au catalysts by increasing their thickness or treating the substrate surface to wet Au. **Figure 24** (b) shows a 20 nm-thick Au catalyst on Si-O surface (named as SiO-20nm catalyst); **Figure 24** (c) shows a 10 nm-thick Au catalyst (named as SiH-10 nm catalyst) on hydrogen-terminated Si surface (Si-H). The Si-H was obtained by treating Si with HF aqueous solution. The surface chemistry of the Si-H is illustrated by their water contact angle of 69^{o} (**Figure 24** (c) inset). [21] Since Si-H wets Au well, Au tends to spread over the surface and coalesce into continuous film rather than form islands as that on Si-O with the same thickness. Indeed, nanopores were hardly observed on the surfaces of SiO-20 nm and SiH-10 nm catalysts in **Figure 24** (b) and (c). After 1 minute's etching in the $\rho(0.37)^{1.8}$ etchant, the 20 nm-thick catalyst was seriously wrinkled. The volume of Si near the edge of the stripe was etched by 282 nm, while the volume under the central part of the catalyst kept intact (**Figure 24** (d)).[51] For SiH-10 nm catalysts, rough pits in Si were found near the edge, while the overall etching depth was significantly lower than that using SiO-10 nm catalyst (**Figure 24** (e)).

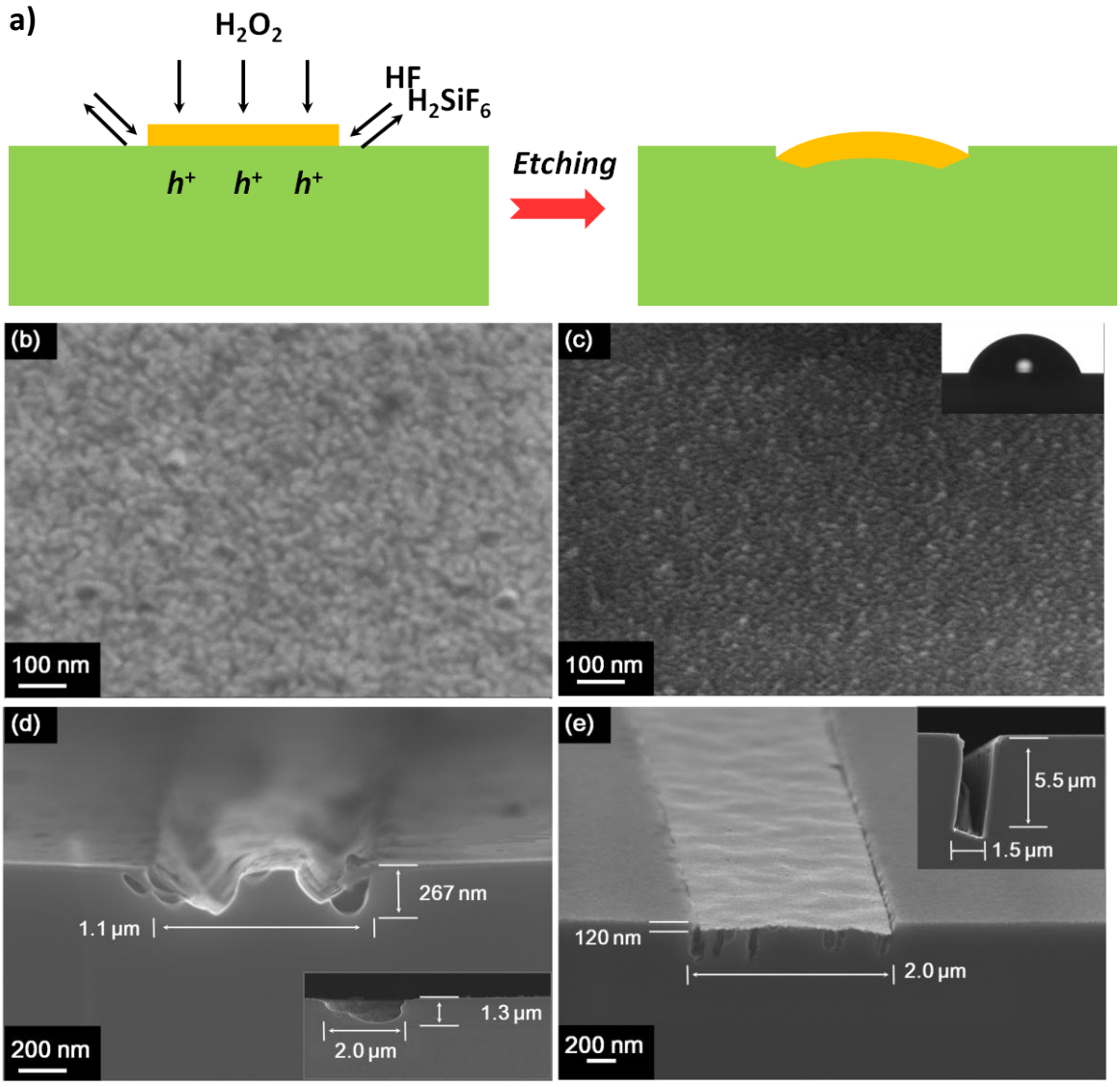

Figure 24 (a) Schematic mechanism of an edge-only mass transport process. Bird's eye view SEM images of (b) SiO-20 nm and (c) SiH-10nm catalyst. Cross-sectional SEM images of the trenches etched in $\rho(0.37)^{1.8}$ etchant for 1 min by (d) SiO-20 nm and (c) SiH-10nm catalysts. The insets of (d) and (e) show the trenches etched for 10 min with other conditions the same as those in (d) and (e), respectively.

The difference between the etching profiles of the nanoporous catalyst and the continuous catalyst became more significant when the etching duration was prolonged. After 10 minutes' immersion in $\rho(0.37)^{1.8}$ etchant, the trenches etched by both SiO-20nm and SiH-10nm were randomly tilted from the Si surface normal (insets of **Figure 24** (d) and (e)). In contrast, a uniform vertical trench was etched by SiO-10nm catalyst (**Figure 25** (c)). The vertical etching direction and the uniformity of geometry were well preserved even after etching 20 min, 30 min and 40 min as shown in **Figure 25** (d)-(f), respectively. From the top view, the width of the trench opening after 40 min's etching is 2.10 ± 0.50 μm (**Figure 25** (b)), slightly wider than that of the original catalyst (**Figure 25**(a)). The contours of the trenches' cross sections are schematically drawn in **Figure 25** (g) with the definition of geometric parameters. It should be noted that SiO-10 nm Au catalyst patterned by photolithography rendered similar results (**Figure 26**), except with an increased edge roughness due to the lower accuracy of photolithography. Along the normal of the substrate surface, the trench contour can be divided into three regions: a top region with roughened surface and enlarged tapering angle; a major linear region with vertical and smooth sidewall in the middle; a bottom region with bended surface. The maximum depth (d_{max}) and the sidewall angles (θ) of the trenches are plotted against the etching duration (**Figure 25** (h)). The d_{max} increased linearly against the etching duration: a constant etching rate is calculated to be 0.8 μm/min. This rate is significantly higher than the reported value using continuous catalyst [39, 51, 54] and mesh-shaped catalyst [34]. Also, unlike the trenches fabricated by DRIE [58], the sidewall of the trench etched by MaCE was intrinsically smooth without any scalloping, because no passivation step was involved during the whole etching process (**Figure 25** (f) inset). The value of θ kept within 89^o to 90^o across the 40 minutes' etching, indicating high verticality of the trenches. In addition, we also tried etching of a 2 μm-wide SiO-10nm Ag catalyst was immersed in $\rho(0.37)^{1.8}$ for 10 min. The lateral geometry of the etched trench was heavily enlarged, which is probably due to the dissolution of Ag in etchant and redeposition on sidewall of trenches (**Figure 27**). The

failure of Ag in producing vertical trench indicates that besides the controllability during etching, the chemical stability of metal catalyst cannot be ignored.

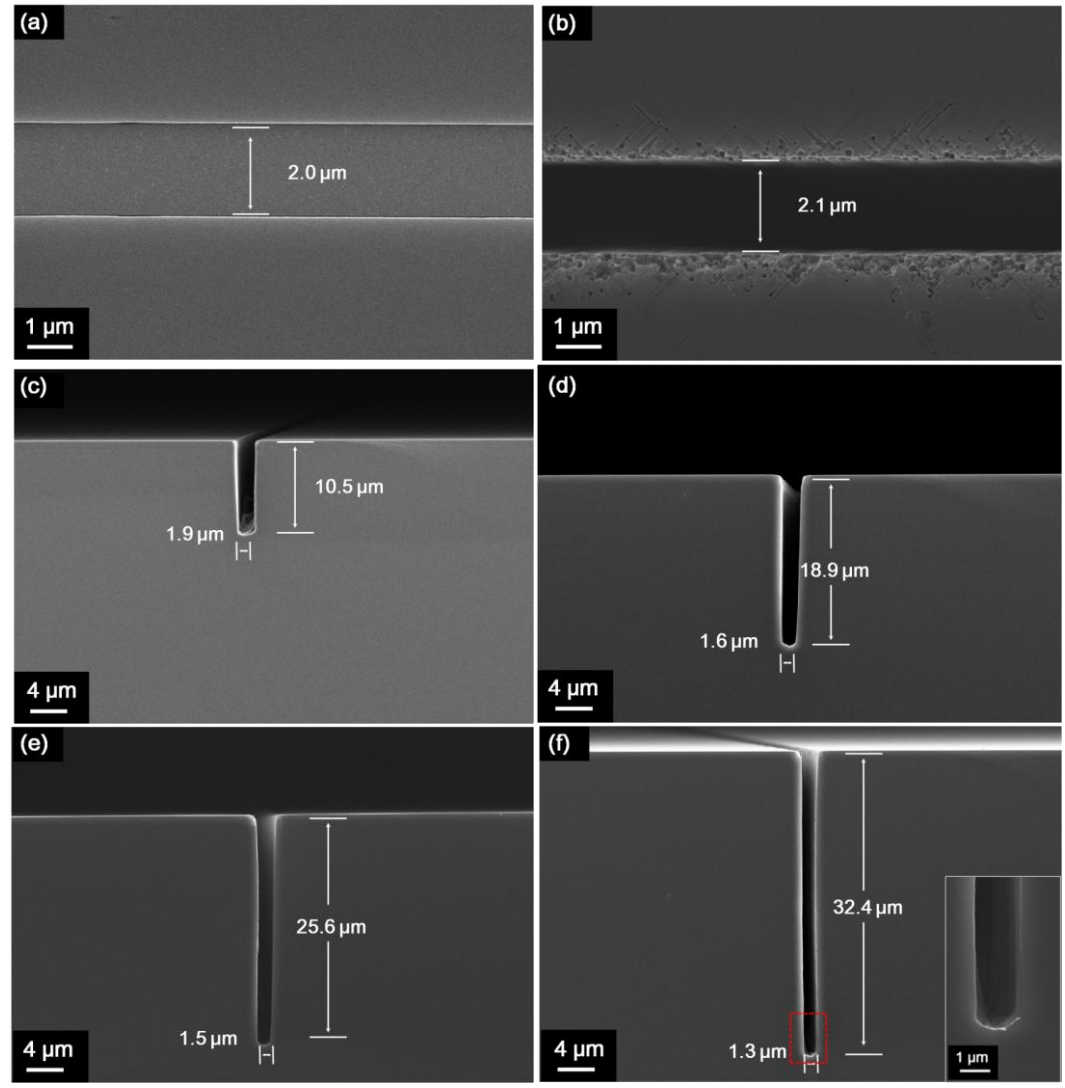
(a)
2.0 μm
1 μm
(b)
2.1 μm
1 μm
(c)
10.5 μm
1.9 μm
4 μm
(d)
18.9 μm
1.6 μm
4 μm
(e)
25.6 μm
1.5 μm
4 μm
(f)
32.4 μm
1.3 μm
4 μm
1 μm

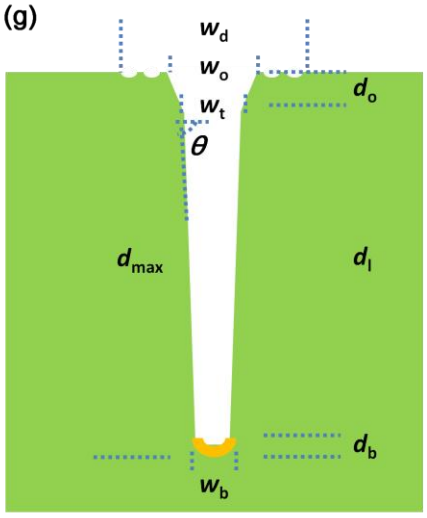
(g)
w_d
w_o
w_t
θ
d_o
d_{max}
d_l
d_b
w_b

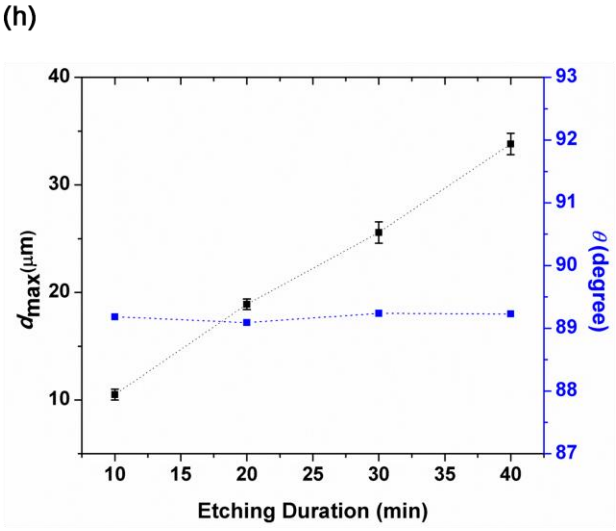
(h)
d_{max}(μm)
θ(degree)
Etching Duration (min)
10
15
20
25
30
35
40
87
88
89
90
91
92
93

Figure 25 (a) Top view SEM image of a 2 μm-wide SiO-10 nm catalyst. (b) Top view SEM image of the trench etched by SiO-10 nm catalyst in $\rho(0.37)^{1.8}$ etchant for 40 min. Cross-sectional SEM images of the trench etched by SiO-10 nm catalyst in $\rho(0.37)^{1.8}$ etchant for (c) 10 min (d) 20 min, (e) 30 min and (f) 40 min. The inset in (f) shows the magnified image in the red circle in (f). (g) Schematic definition of geometric parameters of the etched trench shown in (c)-(f). The lateral dimensions are defined as the width of hole diffusion region (w_d), trench opening (w_o), trench top (w_t), and trench bottom (w_d). The vertical dimensions are defined as the depth of maximum penetration (d_{max}), opening region (d_o), linear region (d_l), bottom region (d_b), the angle between sidewall and Si top surface (θ). The tapering angle α is defined as the complementary angle of θ, i.e. $\alpha=90^o-\theta$. (h) Plot of d_{max} and θ of the trenches in (c)-(f) against the etching duration.

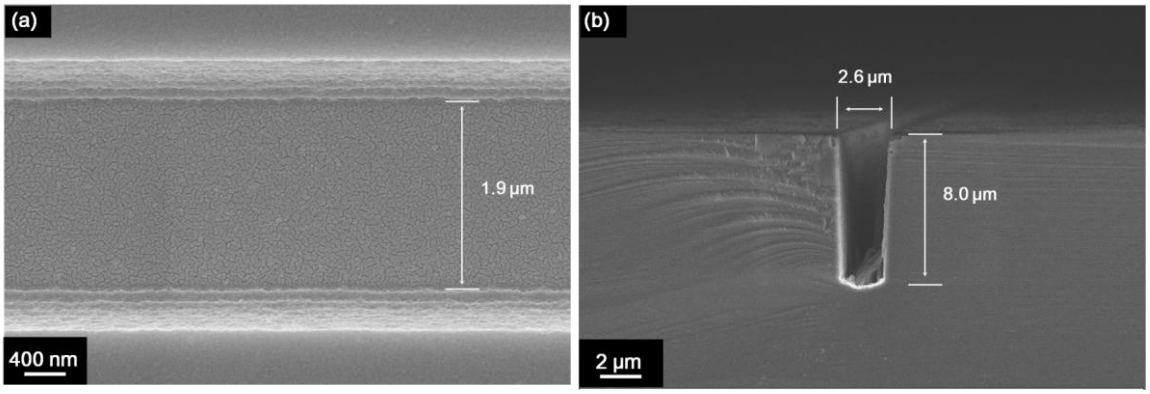

Figure 26 (a) A 2 μm-wide SiO-10 nm Au catalyst patterned by photolithography; (b) a single trench etched by the catalyst shown in (a) in $\rho(0.37)^{1.8}$ etchant for 10 min.

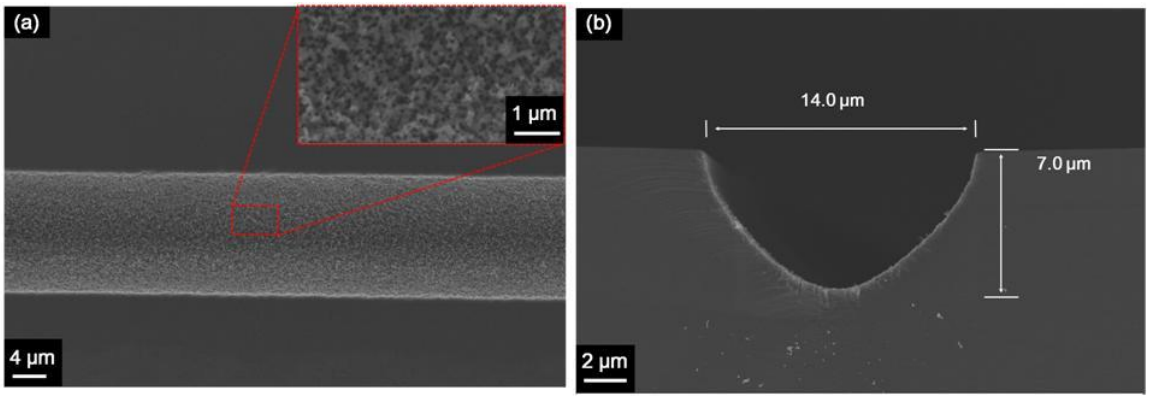

Figure 27 (a) Top view and (b) cross-sectional SEM images of a trench etched by a 2 μm-wide SiO-10nm Ag catalyst in $\rho(0.37)^{1.8}$ for 10 min. Inset of (a) shows an enlarged view of the bottom surface of the trench.

In literatures, some discontinuous metal catalyst, including separated nanoparticles [52, 59, 60] and continuous film with pores[34], have been used to obtain vertical etching profile. However, within the etched trenches, considerable Si remained not fully etched because large gaps existed between Au domains. In contrast, since the gaps in SiO-10 nm catalyst were so narrow, Si was completely removed as shown in **Figure 25** (c)-(f). In a control experiment, we studied the etching behavior of Au stripe with 5 nm thickness on Si-O (named as SiO-5 nm catalyst), where Au islands were found well separated by larger gaps compared to those in SiO-10nm catalysts (**Figure 28** (a)). After 10 min's immersion in $\rho(0.37)^{1.8}$ etchant , a considerable amount of Si remained not fully etched **Figure 28** (b). The resulting etching profile appeared as bundles of Si nanowires. The above results demonstrate the unique effect of the nanoporous morphology in producing uniform vertical deep trenches with high etching rate.

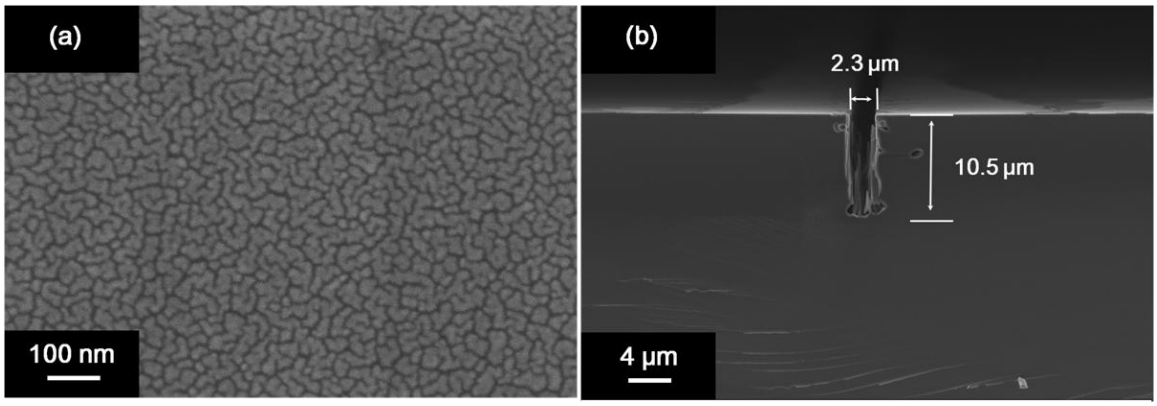

Figure 28 (a) Top view SEM of a 2 μm-wide SiO-5 nm catalyst. (b) Cross-sectional SEM images of a trench etched by the Au stripe in (a) in $\rho(0.37)^{1.8}$ for 10 min.

To further confirm that the through-catalyst MT was enabled by SiO-10nm catalysts, the etching behavior of wider Au stripes was investigated. It has been reported that if the mass transport was limited to the catalyst edge, the etching rate would decrease as the width of catalyst increases, due to the increasing difficulty of transport of HF to the Si beneath the center of Au stripes.[54] However, as shown in **Figure 29** (a) and (b), both the 10 μm and 20 μm-wide SiO-10 nm catalysts manage to penetrate a depth of ~10 μm vertically after 10 min's etching. The independence of etching rate on the width of catalyst supports the through-catalyst MT induced by SiO-10nm catalysts. Moreover, after etching, unlike the upward bending of the central region of SiO-20 nm catalyst (**Figure 24** (c)), we observed a slight downward bending at the middle of the 10 μm and 20 μm-wide SiO-10 nm catalysts (**Figure 29** (a) and (b)). The vertical bending distances (d_b) in the case of 10 μm and 20 μm-wide catalysts were identical, which were larger than that of 2 μm-wide catalyst case. The downward bending of catalyst's center was probably due to a higher local h^+ concentration compared to the edge. **Figure 29** (d) shows a direct observation of the sidewall of the trenches, which is smooth and uniform. After 10 min's etching, both SEM observation (**Figure 29** (c)) and energy dispersive spectrum (**Figure 29** (e)) confirm

that the Au catalysts locate on the bottom surface of the trench, illustrating that the etching is actually facilitated by the catalytic activity of Au catalyst.

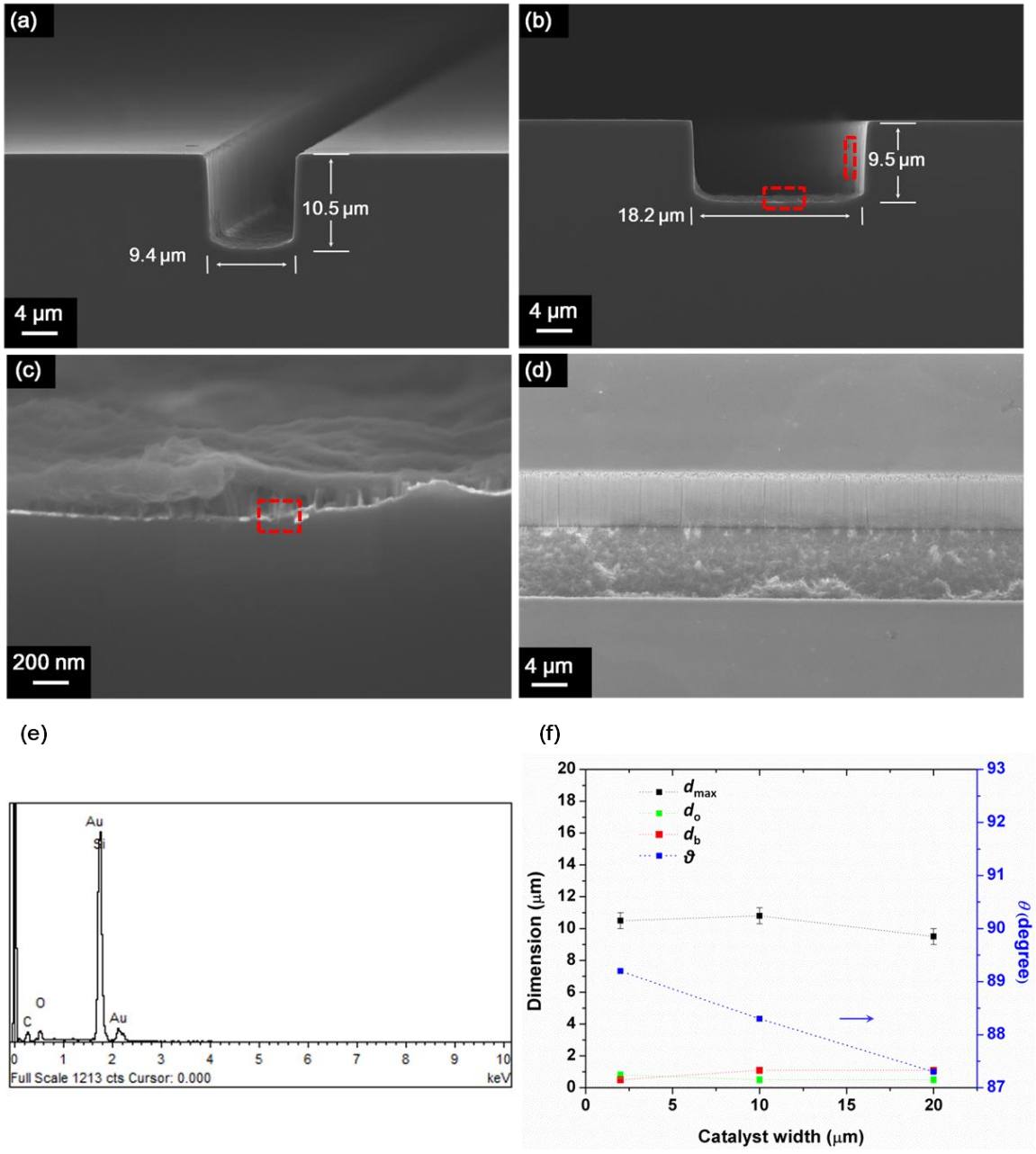

Figure 29 Cross-sectional SEM images of the trenches etched in $\rho(0.37)^{1.8}$ for 10 min by SiO-10nm catalyst with (a)10-μm width and (b) 20-μm width. (c) and (d) show the enlarged view of the bottom and sidewall surface in the red circle in (b), respectively. (e) X-ray energy dispersive spectrum (EDS) of the bottom red circle in (c). d_{max} and θ, are plotted against the catalyst width.

In order to prove that the trench etched by SiO-10nm catalyst in $\rho(0.37)^{1.8}$ etchant was uniform throughout 3D space, an epoxy resin replica of the trench shown in **Figure 25**(c) was fabricated (**Figure 30** (a)). A representative cross-sectional SEM image (**Figure 30** (b)) shows the complete filling of the trench by resin with negligible void on the epoxy-Si interface, which means the replica is able to provide reliable 3D geometric information of the deep trench. After curing the epoxy resin and removing the Si, the free-standing replica was viewed from top and side surface. The replica appears as a thin vertical sheet standing on a large flat plate. Across 55 μm along the sheet, the height is measured to be 11.0 ±0.5 μm (**Figure 30** (c)); the width is measured to be 1.8 ±0.3μm (**Figure 30** (d) and (e)). These geometric parameters are consistent with the d_{max} and w_b value measured from cross-sectional SEM images of the trenches. The highly uniform geometry of the replica in 3D space indicates that negligible deformation of catalyst occurred throughout the etching process.

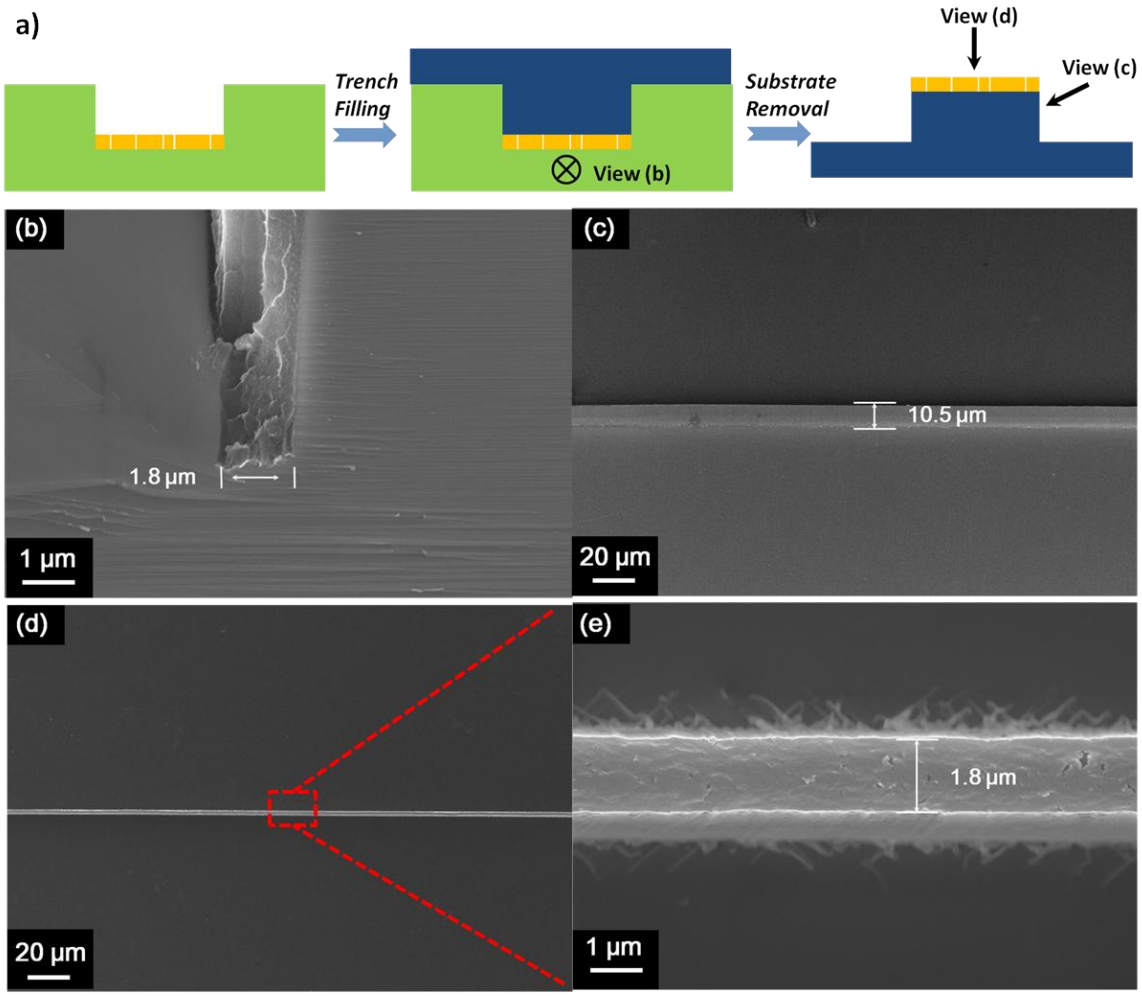

Figure 30 (a) A schematic fabrication process and direction of observation of the polymer replica of a trench. The green, blue and golden blocks refer to the Si substrate, the polymer replica and the Au stripe, respectively. SEM images of (b) the bottom of the trench filled with polymer replica; (c) the sidewall of the polymer replica from the view 45° to horizontal plane; (d) top view of the polymer replica; (e) details of the red circle in (d).

Besides the nanoporous morphology of the Au catalyst, another important factor that contributes to the uniform vertical etching profile is the low ρ value of 0.37. Previously, etchants with high ρ value (0.60-0.96) have been used in most MaCE-related literatures.

As control experiments, the etching behavior of SiO-10 nm catalyst in $\rho(0.64)^{5.4}$ etchant was studied. Both the vertical pores and tilted branches exist in the trench after immersion in $\rho(0.64)^{5.4}$ etchant for 1 minute (**Figure 31** (a) and 10 minutes (**Figure 31** (a) inset). Based on the results of repeated tests, we found the tilting angles of branches were randomly distributed. Here we provide a tentative explanation for the coexistence of randomly aligned branches. In high-ρ etchant where HF is relatively abundant, once holes are injected into Si, they will be consumed up right away by the Si dissolution reaction (Equation 5), thus the etching will favorably proceed along the direction where fewest Si-Si bonds are required to be broken,[61] i.e. the family of <100> crystalline directions . In the trench shown in **Figure 31** (a), the vertical pores were probably originated from the favorable [100] direction (i.e. the vertical direction on the (100)-oriented Si substrate), while the randomly aligned branches can be related to the tendency of etching along [010] or [001] direction. In contrast, in $\rho(0.37)^{1.8}$ etchant, since the concentration of H_2O_2 is high, holes generated from metal catalyst are too many to be consumed by Si dissolution reaction (Equation 5). Under this condition, a Si oxide layer on the Si surface tends to form following the distribution of h^+ concentration. The Si oxide layer is isotropically dissolved by HF (named electropolishing-type charge transport (EPF)):

$$\begin{aligned} &Si+4h^+ +H_2O \rightarrow SiO_x +H^+ \\ &SiO_x +HF \rightarrow SiF_6^{2-} + H^+ + H_2O \end{aligned} \tag{8}$$

Due to the thin film geometry of the catalyst, the region of highest h^+ concentration are located right beneath the film, and so are the Si oxide layer. In this sense, the etching only prefers to proceed along the surface normal.

To further elucidate the difference between etching profiles from $\rho(0.64)^{5.4}$ and $\rho(0.37)^{1.8}$ etchant, we studied the etching behavior of SiO-10 nm catalyst on (111)-oriented Si (Si (111)) substrate. As shown in **Figure 31** (b), after 10 minutes' etching in $\rho(0.64)^{5.4}$, a pore is observed at an angle of 54^o with the surface normal of Si (111), indicating its [100] orientation. Also, many randomly-aligned branches are observed. However, in

$\rho(0.37)^{1.8}$ etchant only one vertical uniform trench is observed after 10 minutes' etching on Si (111) (**Figure 31** (c)). These results are consistent with the experiments conducted on (100)-type Si substrate mentioned above. The results support the point that the favorable vertical etching direction $\rho(0.37)^{1.8}$ etchant follows the region of highest h^+ concentration rather than crystalline orientation of substrates, which is distinct from other wet etching technologies.

While high-ρ etchant deteriorates the uniformity of the vertical etching profile, the problem of excessive h^+ diffusion arises if the ρ value of the etchant is too low. In this chapter, the ρ value of $\rho(0.37)^{1.8}$ etchant is optimized so that most of the h^+ are consumed by the etching of Si beneath the catalyst. Only a small amount of excessive h^+ manages to diffuse away from the catalyst and induce extra etching of the top surface. From **Figure 25** (b), a 1 μm-wide roughened area adjacent the trench edge could be observed after 40 minutes' etching. The macroporous morphology of the roughened area can be related to macropore-formation CT in this region corresponding to a low concentration of diffused h^+.[19] In contrast, when $\rho(0.18)^{0.9}$ etchant was used, the etching rate dropped to 0.2 μm/min (**Figure 31** (d)). After 10 minutes' etching, the overall etching rate kept 0.3 μm/min (**Figure 31** (d) inset). Also, on the top surface, the region near the trench edge is removed by a depth of 1 μm. The region formed by extra lateral etching expanded a width of 5 μm with smoothly tapered surface. The smooth surface morphology indicates that in this region the excessive h^+ are so many that they prevail on the sidewall and the top surface, which induces an electropolishing type etching. Under the assumptions that the h^+ diffuse isotropically from a constant source [54] and the catalyst moves at a constant rate, we provide a quantitative description of excessive h^+ diffuse on in $\rho(0.37)^{1.8}$ and $\rho(0.18)^{0.9}$ etchant using a two-dimensional constant source diffusion model [51]:

$$\frac{C(x,t)}{C_0} = \operatorname{erfc}\left(\frac{x}{2\sqrt{Dt}}\right)\operatorname{erfc}\left(\frac{y}{2\sqrt{Dt}}\right) = \operatorname{erfc}\left(\frac{x}{2\sqrt{Dt}}\right)\operatorname{erfc}\left(\frac{vt}{2\sqrt{Dt}}\right) \quad (9)$$

where the t, C(x,t), C_0, D, v represent the etching duration, h^+ concentration at x position at time t, the constant h^+ concentration on the Au surface and the nominal diffusion coefficient, the vertical etching rate, respectively. x-axis is defined as the direction parallel to the Si surface and normal to catalyst; the origin point is set at the center of the catalyst before etching. The Au catalyst expands in the region of $-1<x<1$. D is experimentally calculated as 2.7×10^{-13} m^2 sec^{-1} from the data of etching profile in $\rho(0.18)^{0.9}$ etchant (**Figure 31** (d)), because significant extra etching region could be observed measured. The D value is experimentally defined as

$$\sqrt{Dt} = l_d = \sqrt{\left(d_{max} - d_b\right)^2 + \left(\left(w_o - w_b\right)/2\right)^2} \quad (10)$$

where the l_d represents the nominal diffusion length, and d_{max}, d_b, w_o and w_b are defined in **Figure 25** (g). The parameters are measured from **Figure 31**(d) and their values are listed in **Table 1**.

Table 1 Parameters for D calculation

Etchant	(d_{max}-d_b)/μm	((w_o-w_b)/2) /μm	l_d/μm	D/m^2 sec
$\rho(0.18)^{0.9}$	0.2	4	4	2.70×10^{-13}

The same D value was used in plotting the h^+ distribution of etching in $\rho(0.37)^{1.8}$ and $\rho(0.18)^{0.9}$ etchant, since the substrates and temperature were identical in both cases. **Figure 31** (e) shows the excessive h^+ concentration across the x axis after 1 minute's etching. It is clear that the regions of highest h^+ concentration are located right beneath catalyst ($-1<x<1$), supporting the point that in low-ρ etchant. In comparison, the amount of excessive h^+ in the $\rho(0.18)^{0.9}$ etchant is tens of magnitudes higher than that in the $\rho(0.37)^{1.8}$

etchant. The large amount of excessive holes explains the significant etching of sidewall and top surface in $\rho(0.18)^{0.9}$ etchant.

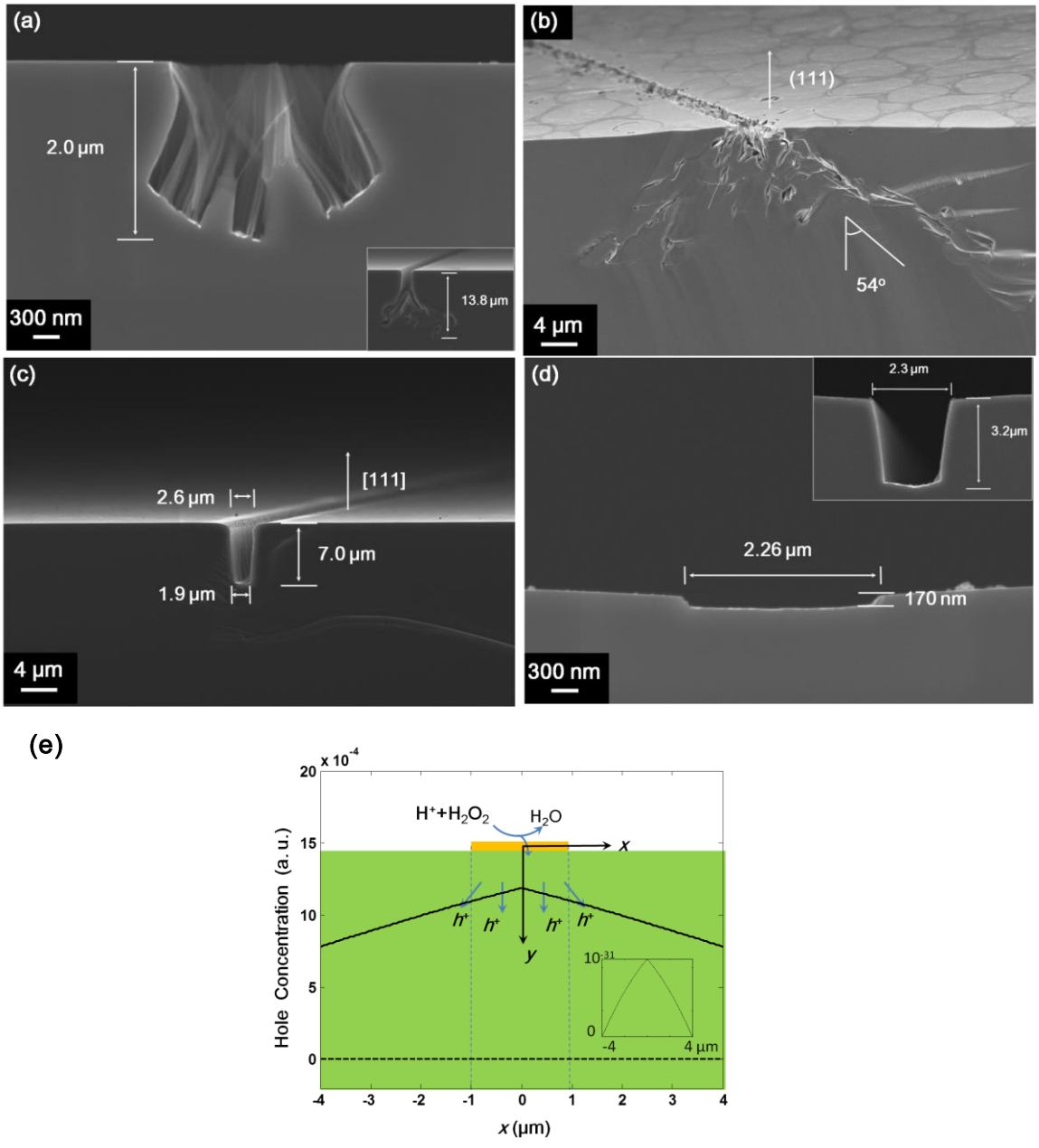

Figure 31 Cross-sectional SEM images of the trench etched by a 2 μm-wide SiO-10nm catalyst in (a) $\rho(0.64)^{5.4}$ etchant for 1 min, (b) $\rho(0.64)^{5.4}$ etchant for 10 min on Si(111), (c) $\rho(0.37)^{1.8}$ etchant for 10 min on Si(111) and (d) $\rho(0.18)^{0.9}$ for 1 min. The insets of (a) and (d) shows the trench etched

for 10 min under the same condition. (d) Modeling of the excessive h^+ concentration against the *x* axis after 1 minute's etching in a two dimensional coordinate system (CS). The golden and green blocks refer to the Au catalyst and the Si substrate. The solid line (—) and the dash line (----) correspond to the etching in $\rho(0.18)^{0.9}$ and $\rho(0.37)^{1.8}$ etchants, respectively. The inset corresponds to the h^+ distribution in $\rho(0.37)^{1.8}$ with smaller scale of *y*-axis.

To demonstrate broader range of applications, multiple trenches on the same substrate were etched using the reported method. **Figure 32** (a) shows that three identical trenches were successfully etched with high aspect ratio using two paralleled 2-μm wide SiO-10 nm catalyst in $\rho(0.37)^{1.8}$ etchant for 20 minutes. Their geometry highly resembles the single trench mentioned above (**Figure 25** (d)). Also, when varying the width of each SiO-10 nm catalyst to be 2 μm, 5 μm and 10 μm, three trenches were etched in $\rho(0.37)^{1.8}$ etchant with a lateral geometry variation accordingly (**Figure 32** (b)). This result proves that in MaCE the etching is catalytically induced by metal, and the etching profile can be individually tuned by the catalyst geometry on the same substrate. The capability of etching densely packed trenches with upright-standing sidewalls as narrow as 300 nm is also demonstrated in **Figure 33**.

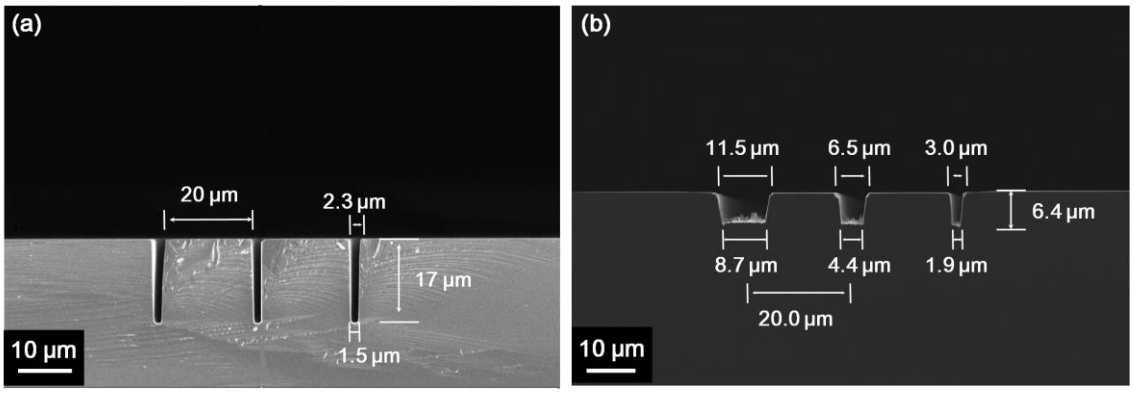

Figure 32 Cross-sectional SEM images of trenches etched in $\rho(0.37)^{1.8}$ by (a) three paralleled 2 μm-wide SiO-10nm catalysts for 20 min and (b) three paralleled SiO-10 nm catalysts with widths of 2 μm, 5 μm and 10 μm for 10 min.

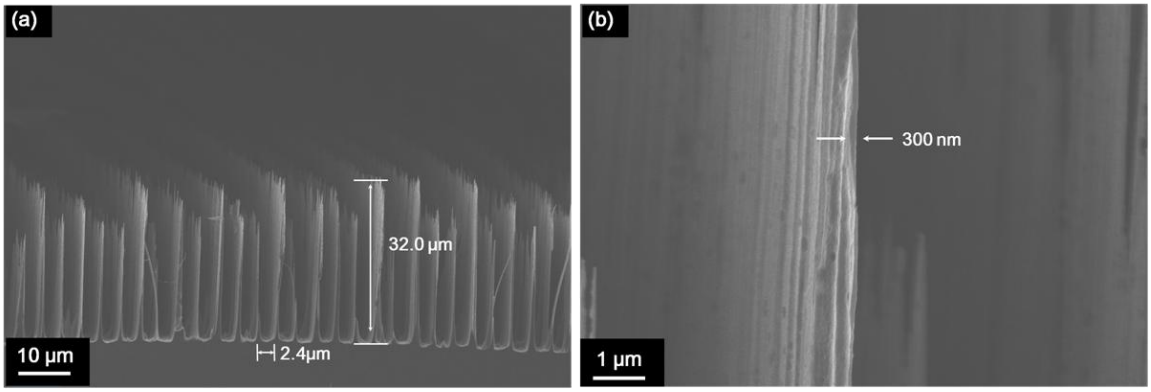

Figure 33 (a) A cross-sectional SEM image of trenches etched by 50 paralleled 2 μm-wide SiO-10nm Au catalysts with 2 μm spacing in $\rho(0.37)^{1.8}$ for 10 min at 75 ^{o}C. (b) shows an magnified view of one wall between two adjacent trenches.

3.4 Conclusion

In conclusion, micrometer-scale single deep trenches on Si as narrow as 2 μm with aspect ratio up to 16 were successfully etched by using nanoporous Au stripe as catalyst and low-ρ-value HF-H_2O_2 solution .The high geometric uniformity of the etched trench throughout the 3D space was revealed by its polymer replica. By comparative study, the

vertical uniform etching behavior is attributed to the synergetic effects of a through-catalyst film MT and an electropolishing favoring CT. The reported method not only solves the issues of random movement of the catalysts in traditional MaCE methods, but also overcomes the limitation on crystalline orientation of substrates and the lateral geometry flexibility of the etching profile generally existing in other types of wet etchings.

CHAPTER 4

ELECTRIC-BIAS ATTENUATED MACE

4.1 Introduction

It has been known that Si can be etched in hydrofluoric acid (HF) solution with the presence of electronic holes (Eq. 5). h^+ can be either generated by reduction of oxidative chemicals (for example, HNO_3) or injected from external electric power supply, as the cases in isotropic wet etching [62] or electrochemical etching, respectively [17, 63]. Since the etching of Si by pure HF is extremely slow [64], selective etching of Si in a HF-h^+ system can be realized by controlling the distribution of h^+ concentration inside the Si substrate. In the last chapter, we have identified the transport of HF and h^+ to be the two critical processes for uniform MaCE. Based on the understanding, we established the *uniform MaCE condition*, in which a HF-H_2O_2 solution with a low HF-to-H_2O_2 concentration ratio (ρ) was used as the etchant to enable an electropolishing-favored h^+ transport; a nanoporous gold (Au) thin film was used as the catalyst to enable a through-catalyst transport of HF. A single uniform 2 μm-wide trench was successfully fabricated under the uniform MaCE condition. In this chapter, we investigate the MaCE of multiples microstructures on P-type-doped Si with a broader range of shape and dimensions. We further investigate the influence of electric bias during the MaCE. The contents in this chapter have partially been published in [65] and reprinted here with permission. Copyright 2014, American Chemical Society.

4.2 Method

Substrate preparation: Boron-doped (100)–, (111)-oriented single crystalline Si wafers (1–10 Ω·cm) as well as polycrystalline Si wafers (boron-doped, 1–10 Ω·cm) with one-side polished were purchased from University Wafer (Boston, MA). In a Class-10 cleanroom, the wafers were cleaned in Piranha solution (1:3 volume ratio H_2O_2(30%wt):

H_2SO_4(96%wt)) at 120 ^oC for 10 min, and then dipped in 1% w/w aqueous HF solution to remove the oxide layer. The cleaned wafers were dried in N_2. For photolithography, a 1.6 μm-thick layer of negative photoresist NR9-1500PY (Futurrex, Inc., NJ) was spun cast on the front side (the polished side) of the cleaned wafer and exposed in a mask aligner (Karl Suss MA6) by 365-nm UV light with a dosage of 190 mJ/cm^2. The exposed wafer was developed by immersion in Resist Developer RD6 (Futurrex, Inc., NJ). All the wafers with patterned resist are treated with oxygen plasma (RF power: 22 W) in a RIE tool (Plasma Therm Inc.) to remove any polymer residue on exposed areas and make the Si surface terminated by oxygen (Si-O). Au catalysts were deposited on the front side by an electron beam evaporator at a rate of 0.5 Å/sec in a vacuum atmosphere of 3×10^{-6} Torr (CVC Product Inc.). Then 10 nm-thick titanium and 200 nm-thick copper was deposited on the back side of the wafers using the same method. In this chapter, the thickness refers to the nominal value measured by an in-situ monitor (Maxtek Sensor Crystal Gold 6MHz 74016-1139 P/N 103220, Inficon) unless specified.

Etching and characterization: The wafers were cut into 1×1 cm^2 chips and mounted on home-made carriers before etching. Briefly, the carriers were made by spreading a layer of copper foil (0.127 mm thick, Alfa Aesar) on 1.5×2.0 cm^2 a glass slide. A polymer-coated copper wire (0.50 mm conductor diameter, R24BLK-0100, OK Industries) was soldered on one corner of the copper foil. The edge of carrier was sealed by epoxy precursor and cured at 150 ^oC for 1 hr in an atmospheric oven. The epoxy precursor was prepared by mixing 17g EPON Resin 862, (Hexion Special Chemicals Inc.), 20 g Lindride 52D (Lindau Chemicals) and one drop of 2-ethyl-4-methyl-1H-Imidazole-1-propanenitrile (Aldrich) as catalyst. After the epoxy sealing, the chip was mounted on the copper foil, which had been wet by liquid gallium for good electric contact. The test vehicle was further sealed by polyimide tape to make only the front sides of chips exposed (**Figure 34**).

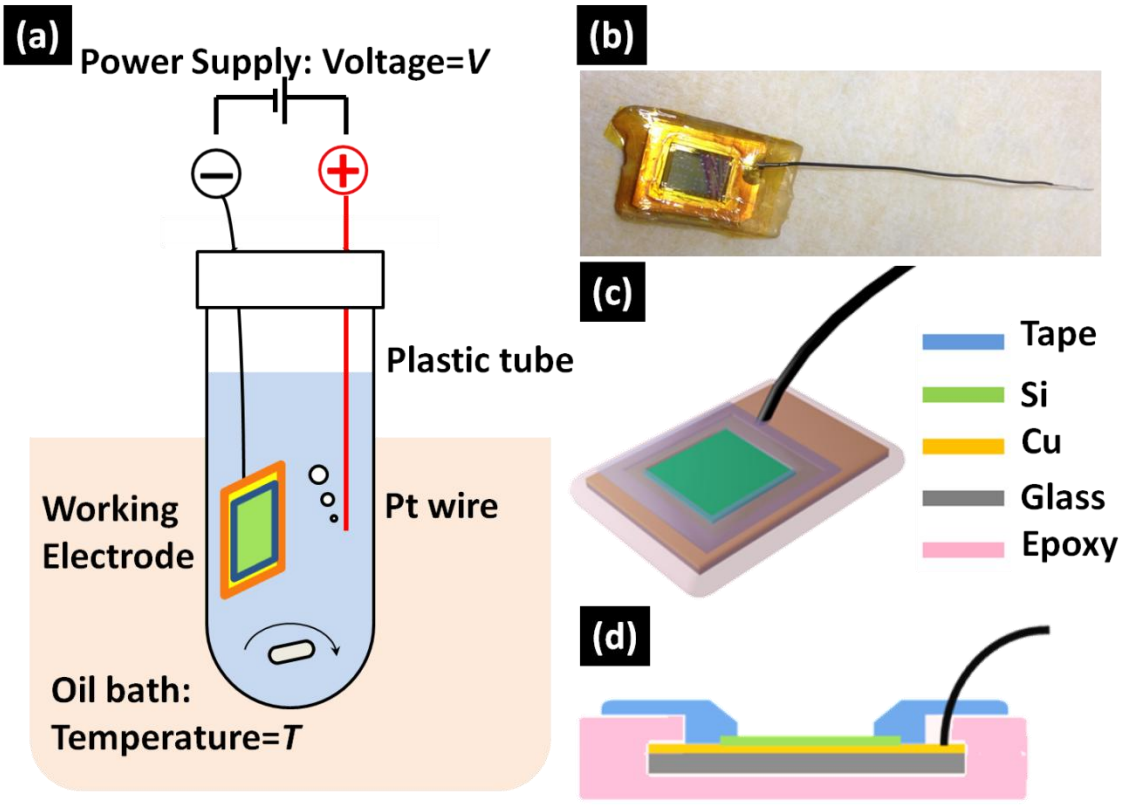

Figure 34 (a) A schematics experimental setup of EMaCE. (b) A photograph and (c)-(d) schematics of the working electrode.

To prepare the etchant, HF (48-52%wt in H_2O), H_2O_2 (30%wt in H2O, Anachemia Chemicals, LLC) and deionized water (DI water, resistivity ~18.2 MΩ) were directly mixed without further processing. DI water was produced by a Thermo Scientific Barnstead Smart2Pure water purification system. The total volume of the etchant was fixed to 32 mL. The etching was conducted by gently immersing the test vehicle in the etchant solution in a loosely-capped transparent polyethylene (PE) tube (VWR International, USA) for a certain amount of time. The PE tube with etchant was preheated in a silicone oil bath with controlled temperature on a hotplate (VWR International, USA) for 20 min before etching and kept immersed in the bath until etching was finished. After etching, the chips

were taken off from carriers and cleaned by Piranha solution described above. Note: HF-H_2O_2 mixture and Piranha solution is highly corrosive, thus the etching and cleaning was done in a well-ventilated fume hood with proper personal protection equipment. A constant bias was generated by a power supply (Farnell PSD 3510A). The variable voltage was produced and recorded by a potentiostat (Princeton Applied Research, VersaSTAT MC). The bias was applied 30 sec after the chip was immersed in the etchant to stabilize the Au catalysts. The polymer replica is fabricated by dipping the epoxy precursor on the front side of cleaned chips after etching and cured at 150 ^oC in a vacuum oven for 1hr. The replica is isolated by completely removal of Si in the mixture of HNO_3 (70 wt%), HF (49 wt%) with the volume ratio of 1:6 within 10 min at room temperature. The polymer replica was coated by Au (less than 20 nm thick) for SEM imaging in a DC-sputter (Denton DeskII). SEM images were taken from Zeiss LEO 1550 thermally assisted field emission (TFE) SEM or Hitachi SU8010 SEM operating at 10 keV with a working distance between 2 and 7 mm. Optical confocal microscope image and cross sections were obtained from Olympus LEXT OLS4000 laser confocal microscope. The depth of pre-etching step was measured by Tencor P15 Profilometer using stylus. The Matlab7.0 software was used for modeling of h^+ concentration.

Modeling of $c(h^+)$ distribution: In order to simulate the distribution of $c(h^+)$, we first define a orthogonal CS where the top surface of Si substrate with 9 Au patterns is set as *x-y* plane (Figure 3(d)-(i))). The shape of Au patterns is set to square rather than round shape to reduce the complexity of calculation. The length of one side of the squares is set to 30 μm and the spacing between the centers of two adjacent squares is set to 80 μm. *z* axis is defined as the normal of *x-y* plane.

For 1D simulation along *x* axis,

$$\frac{C(x,t)}{C_0} = \operatorname{erfc}\left(\frac{x}{2\sqrt{Dt}}\right)\operatorname{erfc}\left(\frac{z}{2\sqrt{Dt}}\right) = \operatorname{erfc}\left(\frac{x}{2\sqrt{Dt}}\right)\operatorname{erfc}\left(\frac{vt}{2\sqrt{Dt}}\right) \quad (11)$$

where the t, $C(x,t)$, C_0, D, v represent the etching duration, h^+ concentration at x position at time t, the constant h^+ concentration on Au and the nominal diffusion coefficient, the vertical etching rate, respectively.

For 2D simulation in x-y plane,

$$\frac{C(x,t)}{C_0} = \operatorname{erfc}\left(\frac{x}{2\sqrt{Dt}}\right)\operatorname{erfc}\left(\frac{y}{2\sqrt{Dt}}\right)\operatorname{erfc}\left(\frac{z}{2\sqrt{Dt}}\right) = \operatorname{erfc}\left(\frac{x}{2\sqrt{Dt}}\right)\operatorname{erfc}\left(\frac{y}{2\sqrt{Dt}}\right)\operatorname{erfc}\left(\frac{vt}{2\sqrt{Dt}}\right) \quad (12)$$

The nominal diffusion coefficient, D, is defined as:

$$\sqrt{Dt} = \sqrt{r^2 + h^2}$$

where r is the width of excessive etching region., r is measured to be 5.6 μm at 23 ^{o}C (**Figure 35** (a)) and 9.8 μm at 100 ^{o}C (**Figure 35** (b)). Corresponding D is then calculated to be 5.38×10^{-13} m^2 sec and 2.10×10^{-12} m^2 sec, respectively.

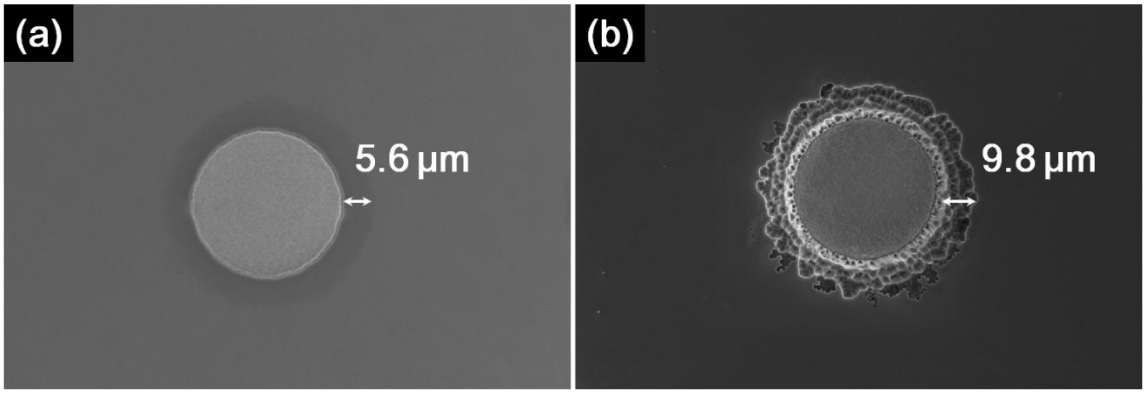

Figure 35 Top-view SEM images of 28 μm Au-Si(100) chips after MaCE for 1 min at 23 ^{o}C (a) and 100 ^{o}C (b).

4.3 Results and Discussion

An array of circular Au catalysts with diameters of 27.5 ±0.5 μm, spacing (distance between the centers of two adjacent patterns) of 80 μm and nominal thickness of 15 nm was successfully fabricated on (100)-oriented Boron-doped (resistivity: 1-10 ohm·cm) single crystalline Si wafers by photolithography and electron-beam evaporation (**Figure 36** (a), referred as the "28 μm Au-Si(100)" sample). Nanopores could be observed within the catalysts under SEM (**Figure 36** (b)).The sample was cut into 1 ×1 cm^2 chips (referred as the "chip" below) for MaCE tests. The number of Au patterns on one chip is estimated to be 10^4. One drop (ca. 0.2 mL) of $\rho(0.22)^{0.9}$ HF-H_2O_2 aqueous solution was slowly dropped on the whole surface of 28 μm Au-Si(100) chip and kept for 1 min before the chip was fully immersed in 32 mL $\rho(0.37)^{1.8}$ HF-H_2O_2 aqueous solution (used in all following experiments unless specified). The name of HF-H_2O_2 etchant is formatted as $\rho(x)^y$ to shows its composition, where x=[HF]/([H_2O_2]+[HF]) and y=[HF] ([HF] is the concentration of HF in mole per liter). The chip was etched with the photoresist on the top surface. Geometric parameters of the etching profile are defined in **Figure 36** (c), including top diameter (d_t), bottom diameter (d_b), sidewall angle (θ), maximum etching depth (h) and spacing (s). After pre-etching by the $\rho(0.22)^{0.9}$ droplet, Au catalysts moved uniformly into Si substrate (**Figure 37** (a), while Si surrounding Au was also etched by with a width of 232 nm (**Figure 37** (b)). Small etched pits were found right beneath the nanopores both near the Au-Si boundary (**Figure 37** (c)) and under the center of Au patterns (**Figure 37** (d)), indicating that HF was able to transport through the nanoporous Au catalysts. Also, we found the pre-etching step in the $\rho(0.22)^{0.9}$ etchant helped improve the reproducibility of experiments. The lower ρ value of pre-etching solution was found to facilitate a more stable etching at the initial stage. In a control experiment where the chip was directly immersed in bulk $\rho(0.37)^{1.8}$ etchant without the pre-etching, some Au patterns were lifted off from Si substrate before any etching occurred. The pre-etching process is conducted in

all the following experiments and the time of pre-etching is excluded from the etching time mentioned below.

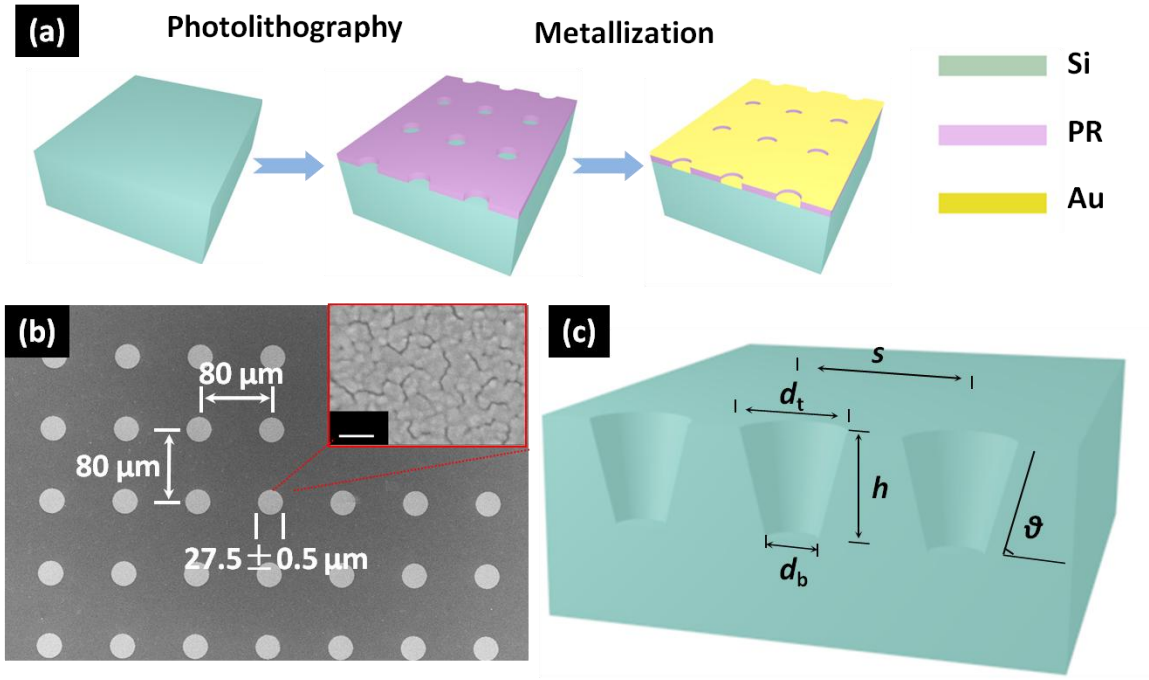

Figure 36 (a) Schematic processing flow of MaCE by Au catalysts array. The blocks in green, purple and golden refer to the Si substrate (Si), the photoresist (PR) and the Au catalysts (Au), respectively. (b) A top-view SEM image of Au patterns on Si after lift-off of PR. The inset shows the morphology of Au catalysts under high magnification (scale bar=100 nm). (c) A schematic etching profile after MaCE and parameters used for describing the etching profile.

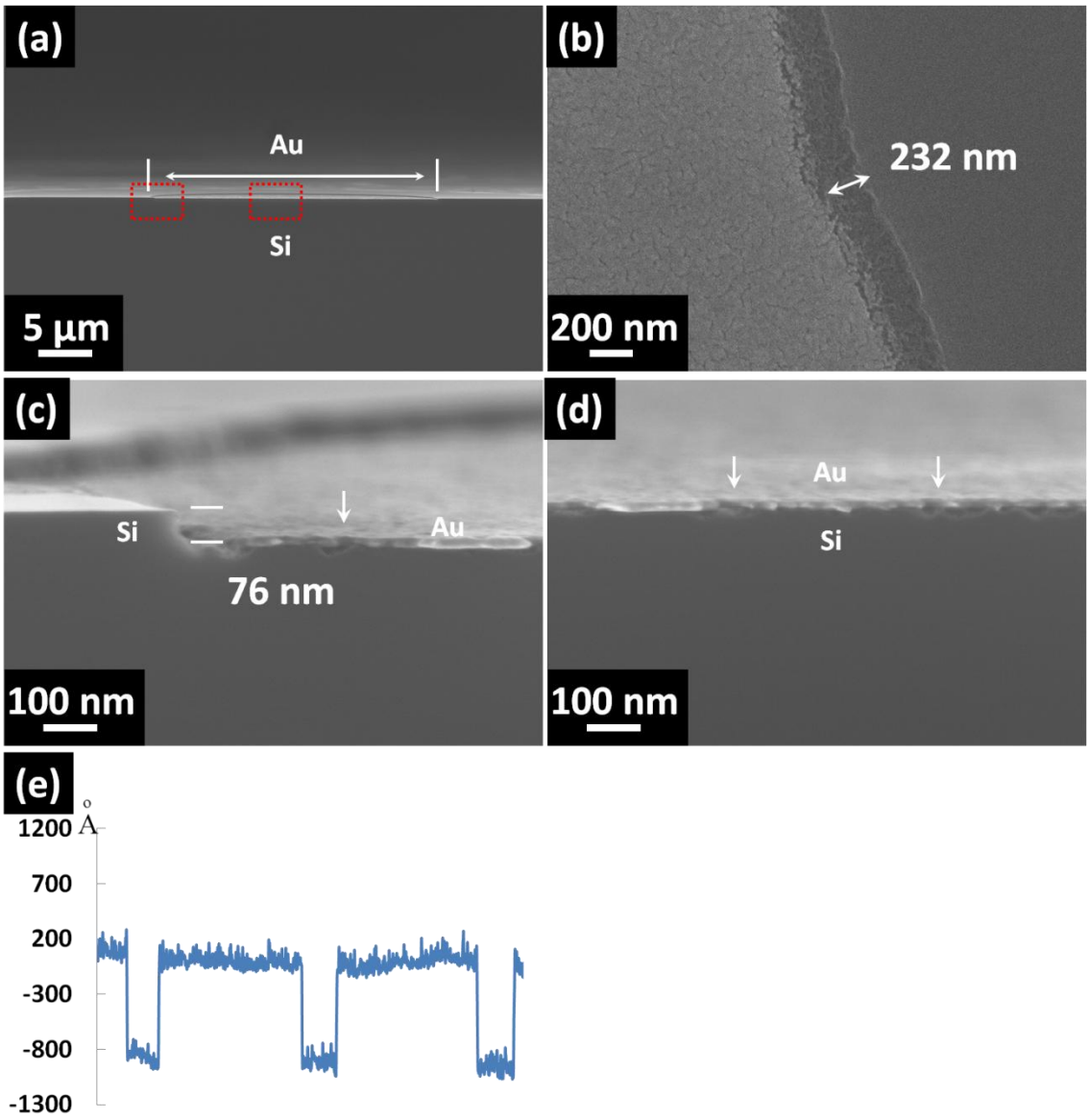

Figure 37 SEM images of 28 µm Au-Si(100) chips after pre-etching by $\rho(0.22)^{0.9}$ droplet. (a) A cross-sectional image of one circular Au pattern and the Si below Au. (b) A top-view image of Au-Si boundary area. (c) and (d) Enlarged images of the red circle in (a). (e) Cross-sectional diagram of holes after pre-etching measured by profilometer.

After immersion in the bulk $\rho(0.37)^{1.8}$ etchant, Au moved deeper into the Si chips. We studied the MaCE of 28 µm Au-Si(100) chips for 1min, 2 min, 5 min and 10 min at 23

°C and 100 °C. The etching profiles in each test are revealed by optical confocal microscopy (OCM) (top and middle images) and SEM (bottom images) in **Figure 38**. In the OCM images, Au and the Si between Au are shown in golden and blue. After etching, the catalysts moved vertically into the Si substrate and kept flat. *h* and etching rate of each test are summarized in **Figure 39** (a). The original data for plotting **Figure 39** (a) can be found in **Table 2** and **Table 3**. *h* was measured from OCM cross sections of 9 adjacent etched holes in both center part (averaged to give h_{center}) and corner part (averaged to give h_{corner}) of the 1×1 cm^2 chips. The etching rate is calculated by dividing *h* by corresponding etching time. After 10 min of MaCE, h_{center} reached 6.7 ± 0.1 μm at 23 °C and 43.7 ± 2.5 μm at 100 °C, while h_{corner} were 6.5 ± 0.2 μm at 23 °C, and 44.9 ± 2.7 μm at 100 °C. Across the 10 min, the etching rate ranges between 0.95-0.67 μm/min at 23 °C and 5.50-4.37μm/min at 100 °C. The uniformity and the speed of etching along the vertical direction at 100 °C is comparable to the commercial dry etching method.[13] The slight decrease of etching rate versus etching time may be due to the increasing difficulty of mass transport inside the etched holes.

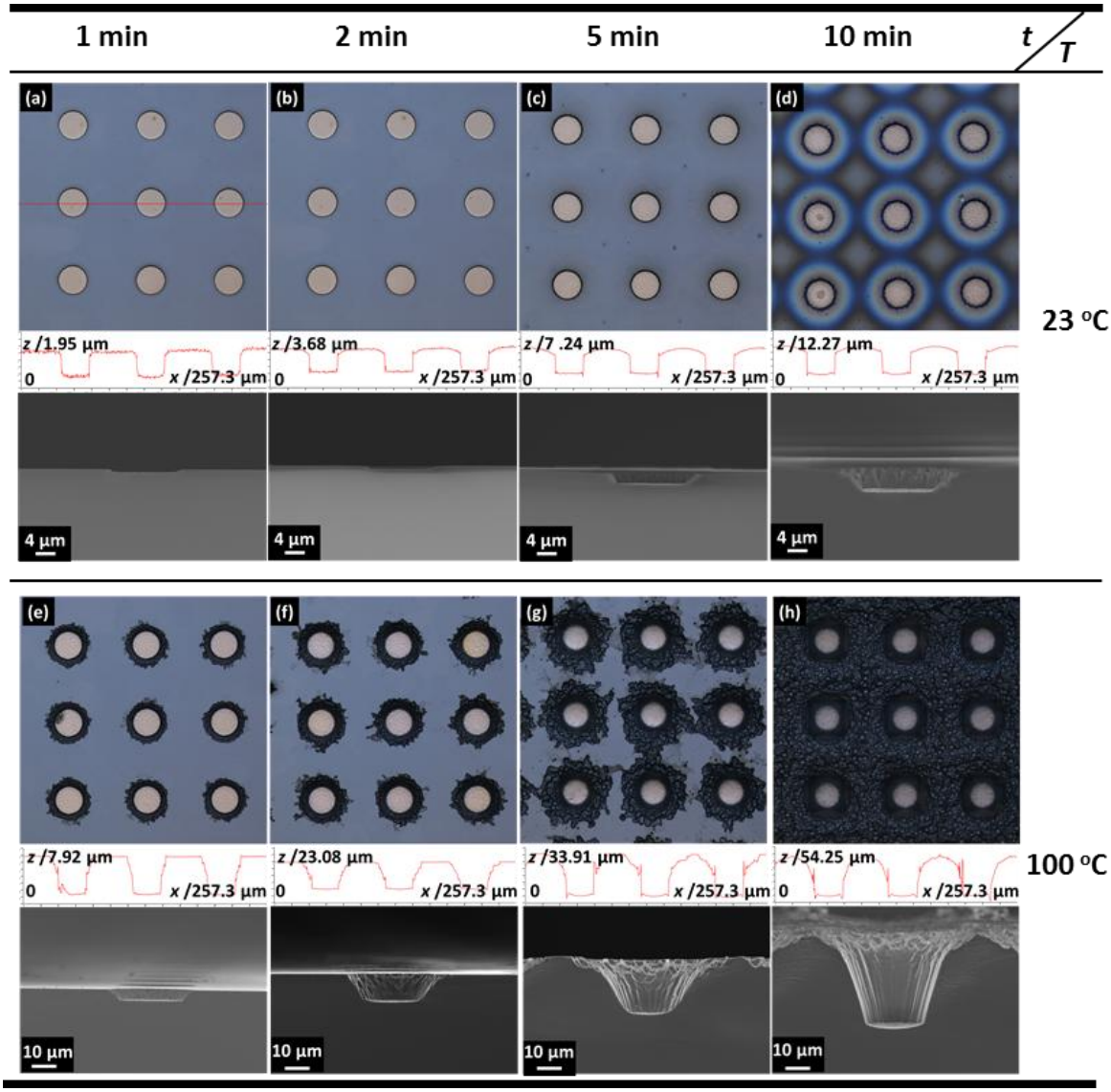

Figure 38 Etching profiles of 28 µm Au-Si(100) in $\rho(0.37)^{1.8}$ for (a) 1 min, (b) 2 min, (c) 5 min and (d) 10 min at 23 °C as well as (e) 1 min, (f) 2 min, (g) 5 min and (h) 10 min at 100 °C. Top-view OCM images (top), optical cross sections (middle) and SEM cross sections (bottom) are shown in each set of figures.

Table 2 Step height values in the center part used in **Figure 39** (a)

Temperature (°C)	23				100			
Etching Time (min)	1	2	5	10	1	2	5	10
Measured Step Height (μm)	0.94	1.56	3.41	6.74	5.53	11.67	26.27	41.68
	0.93	1.61	3.45	6.7	5.54	11.65	25.95	44.47
	1	1.46	3.33	6.54	5.5	11.45	26.32	44.34
	0.96	1.67	3.49	6.82	5.64	11.59	26.18	42.59
	0.98	1.68	3.52	6.76	5.39	11.43	26.46	43.41
	0.95	1.62	3.47	6.73	5.43	11.49	25.85	42.38
	0.9	1.68	3.54	6.58	5.47	11.48	26.28	44.16
	0.95	1.63	3.4	6.63	5.5	11.56	26.37	44.36
	0.97	1.66	3.58	6.76	5.5	11.51	25.63	46.22
Averaged Step height (μm)	0.95	1.62	3.46	6.7	5.5	11.54	26.14	43.73
Standard Deviation (μm)	0.03	0.07	0.08	0.09	0.07	0.09	0.28	1.38

Table 3 Step height values in the corner part used in **Figure 39** (a)

Temperature (°C)	23				100			
Etching Time (min)	1	2	5	10	1	2	5	10
Measured Step Height (μm)	0.74	1.46	3.36	6.26	5.96	11.79	24.52	43.75
	0.78	1.56	3.51	6.46	6.01	11.59	24.16	44.01
	0.84	1.5	3.53	6.47	5.96	11.4	24.21	44.6
	0.74	1.53	3.53	6.7	5.97	11.47	24.29	45.15
	0.76	1.58	3.45	6.48	5.97	11.53	24.33	44.45
	0.83	1.53	3.44	6.72	5.99	11.35	24.26	47.56
	0.7	1.64	3.52	6.5	5.92	11.77	24.17	43.44
	0.73	1.53	3.45	6.69	5.85	11.69	24.07	46.79
	0.78	1.63	3.48	6.65	5.92	11.85	24.19	43.97
Averaged Step height (μm)	0.77	1.55	3.47	6.55	5.95	11.6	24.24	44.86
Standard Deviation (μm)	0.05	0.06	0.06	0.15	0.05	0.18	0.13	1.42

In above MaCE experiments, besides the vertical etching, significant etching also occurred in non-vertical directions. After 10 min of MaCE, the top surface of Si between Au patterns turned colorful at 23 ^{o}C (**Figure 38** (d)) and became completely black at 100 ^{o}C (**Figure 38** (h)) as can be observed in OCM images. Under magnified SEM images, these regions show a porous surface morphology. Actually, formation of the porous regions started from the first 1 min of MaCE, when the Si near Au-Si boundary was found completely removed by 300 nm in width (completely removed region, CRR) at 23 ^{o}C, and a porous layer expanded with a width of 5.6 μm beyond the CRR (**Figure 39** (b)); at 100 ^{o}C, the surface of CRR was decorated with much larger pores and extended 9.8 μm out of Au-Si boundary (**Figure 39** (c)). The excessive etching on the sidewall can also be clearly observed in top-view SEM images **Figure 35**. Apparently, the porous region and CRR are detrimental to electronic components, thus it is imperative to suppress the excessive etching before MaCE can be applied to any components fabrication.

Given the fact that the etching of bare Si by H_2O_2-HF solution is negligible,[66] here we attribute the appearance of these regions to the electrochemical etching process (Eq. 5) induced by excessive h^+. In $\rho(0.37)^{1.8}$ etchant where $c(H_2O_2)$ is high, the amount of h^+ generated in Eq. 2 exceeds that can be consumed by the etching of Si underneath the Au catalysts (i.e. the vertical etching). The excessive h^+ tends to diffuse to the sidewall and top surface of Si, which induces the non-vertical excessive etching in these regions (**Figure 40** (a)). Since both the vertical etching and the excessive etching follow the same process in Eq. 5, they both become faster at elevated temperature.[67] To further illustrate the origin of excessive etching, we simulated the distribution of accumulated h^+ concentration ($c(h^+)$) by a 2D constant source model.[51, 53]. **Figure 39** (d)-(i) show the distribution of $c(h^+)$ plotted in 2D planes that contains 9 Au patterns (top images) and along 1D lines that intersect with 3 Au patterns (bottom images). Au patterns are set as the constant source of h^+. As visualized in both images, a significant amount of h^+ diffuses to the Si between Au ($c(h^+)_{Si}$) relative to that under the Au patterns ($c(h^+)_{Au}$) as the etching proceeds. At 23 ^{o}C,

$c(h^+)_{Si}$ reaches ca. 60% of $c(h^+)_{Au}$ after 10 min; at 100 °C, $c(h^+)_{Si}$ reaches ca. 45% of $c(h^+)_{Au}$ only after 2 min. The evolution of $c(h^+)_{Si}$ in both cases is consistent with the expansion of porous region and CCR, which supports our assumption that excessive h^+.

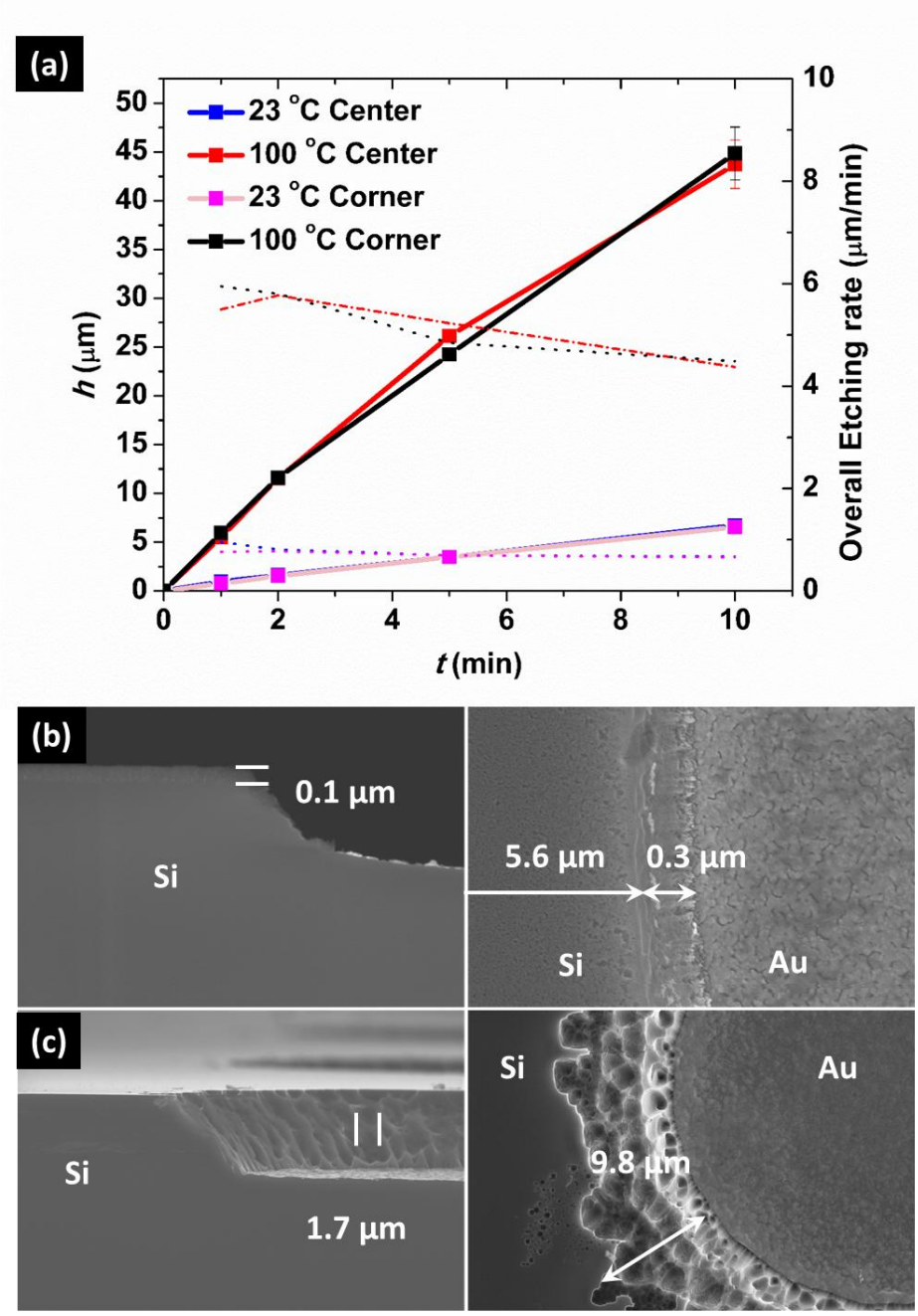

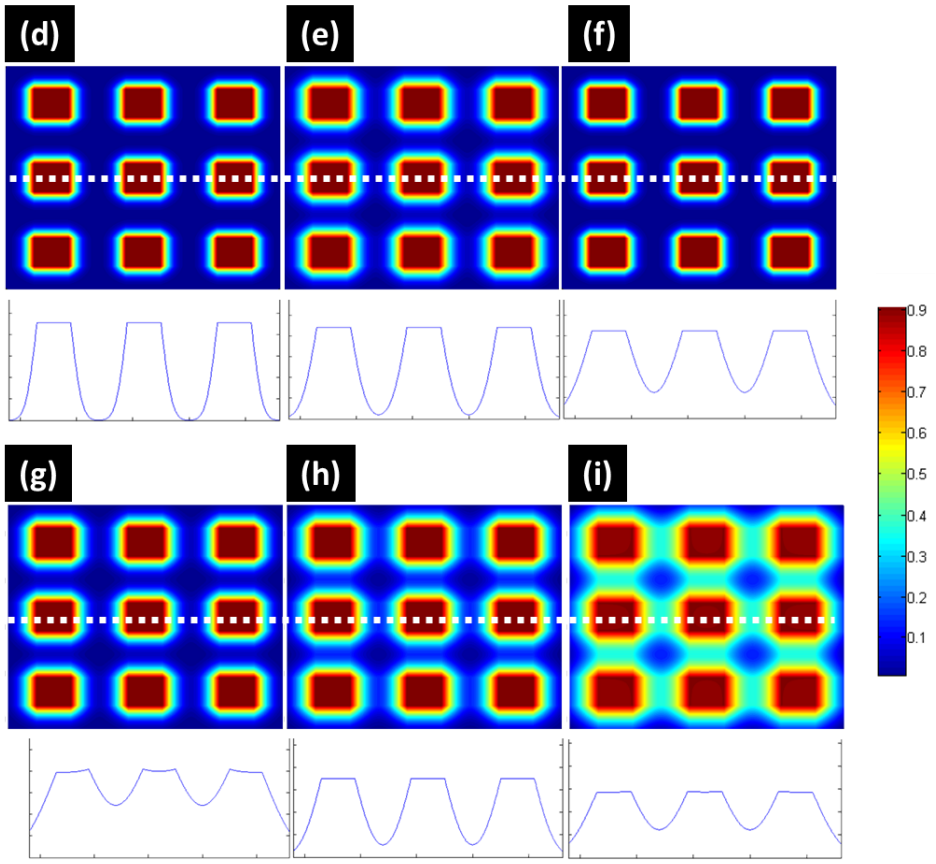

Figure 39 (a) Evolution of *h* (solid lines) and etching rate (dashed lines) versus etching time (*t*). High-magnification cross-sectional (left) and top-view (right) SEM images of Au-Si boundary area after 1 min of etching at 23 ^{o}C (b) and 100 ^{o}C (c). (d)-(i) simulated 2D (top) and 1D (bottom) distribution of $c(h^{+})$ in arbitrary unit corresponding to experiments shown in **Figure 38** (a)-(f), respectively. The color bar indicates the relative value of $c(h^{+})$, where the red end represents higher $c(h^{+})$ and the blue end represents lower $c(h^{+})$.

In this chapter, we demonstrate that the excessive etching can be controlled by using an external electric bias during MaCE process. We name the novel etching method as electric bias-attenuated MaCE (EMaCE). To maintain the high etching rate, all following experiments are done at 100 ^{o}C. Based on the above discussion, the excessive etching is supposed to originate from the excessive h^{+}. If a negative bias is applied from

the back side of the chips, excessive h^+ will be drawn away from sidewall and top surface to the back side of Si by electrostatic force, and the extent of excessive etching can be controlled by the strength of the bias (**Figure 40** (b)). The idea was realized by connecting the chip to the negative output terminal of a direct current electric power supply. To ensure good electrical contact between the chip and power supply, we mounted the chip on a gallium-wet copper foil which was wired to the power supply. The chip and copper foil was further packaged in a home-made carrier where all surfaces were covered by polymer except the front surface of the chip (**Figure 34**). The chip-copper-carrier assembly is referred as the working electrode. Meanwhile, a platinum (Pt) wire was connected to the positive terminal as the counter electrode. In EMaCE, both the two electrodes were immersed in the HF-H_2O_2 etchant, while a certain value of voltage (V) was set in the power supply so that the chip was negatively biased by V relative to the Pt wire (referred as "at –V"). The details of experimental setup and carrier fabrication are described in SI. The first 30 sec is included in the etching time mentioned below. d_t slight increased to 29 μm after the 30 sec of etching at no bias. After EMaCE, we used polymer replica to reveal the true 3D geometry of the etching profile. Due to imperfection of scriber-cutting, only the cross sections that intersect with the center of etched holes reveal their complete geometry (white arrow), while other cross sections only partially reveal the geometry of the etched holes (white arrow with red cross). So the polymer replica is necessary for revealing 3D geometry inside etched holes (**Figure 41**). The cross sections of the etched chips and corresponding polymer replica after EMaCE at -0.5V, -1.0 V, -1.5 V and -1.75 V for 10 min are shown in **Figure 40** (c)-(f), respectively. Both cross sections consistently show a decrease of θ and an increase of h as the bias becomes more negative (referred as "increase" of bias). The results support our proposed mechanism that diffusion of excessive h^+ can be influenced by negative bias; as the strength of bias increase, more h^+ that tend to diffuse towards top surface and sidewalls are driven towards the backside. In other words, the negative bias redistributes the $c(h^+)$ in 3D space, so that excessive etching is suppressed and the vertical

etching is enhanced. When the bias was increased to -1.75 V, the surface of Si between Au patterns keeps its original color and polished morphology (**Figure 40** (g)), and d_t remains 29 μm, indicating a complete suppression of excessive etching. **Figure 40** (h) shows the top-view OCM images and cross-sections of the chip etched at -1.75 V. h_{center} and h_{corner} are measured to be 59.8±0.5μm and 60.5±0.5μm, respectively. However, a much larger discrepancy was discovered between h_{center} and h_{corner} in EMaCE at -1.0V and -1.50 V (**Figure 42**). The smaller discrepancy of h_{center} and h_{corner} found at -1.75 V is probably due to a complete suppression of excessive h^+ diffusion across the whole chip. The fact that excessive etching can be experimentally suppressed by negative bias further supports the assumption that the excessive etching is caused by excessive h^+.

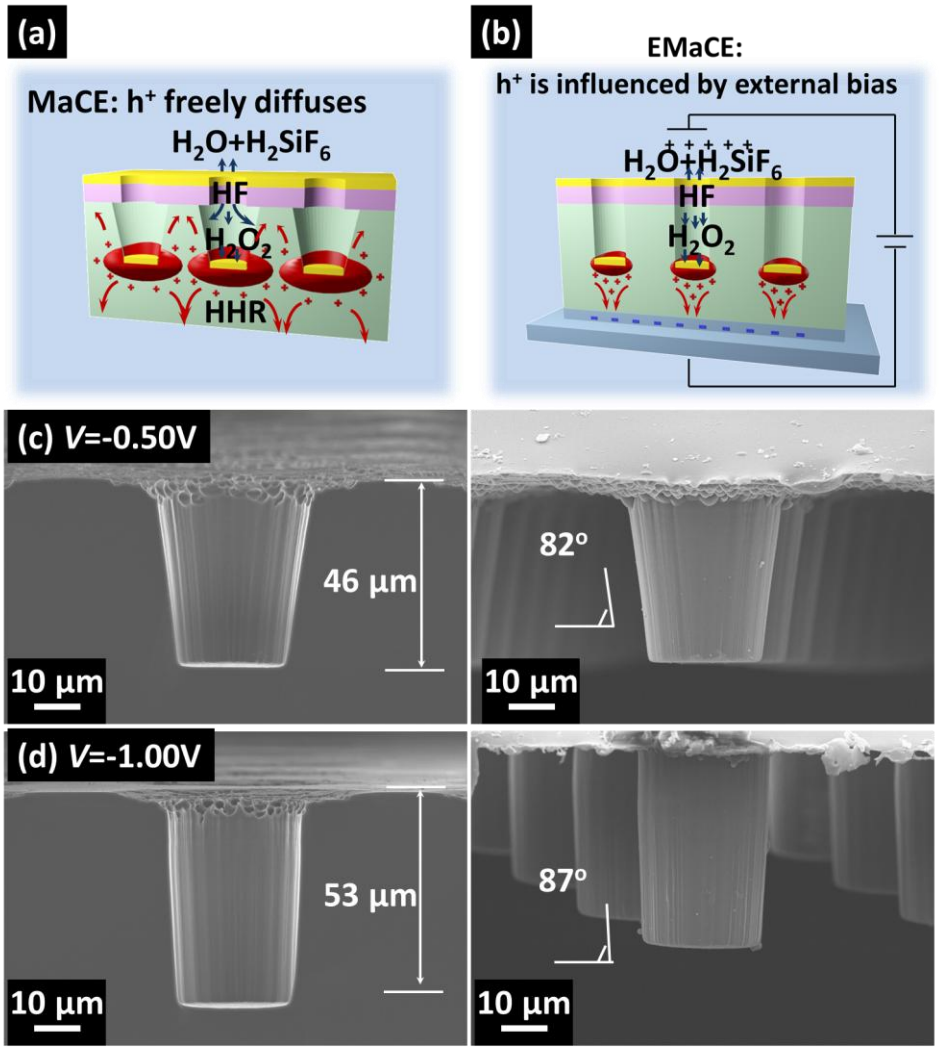
(a)
MaCE: h+ freely diffuses
H2O+H2SiF6
HF
H2O2
HHR
(b)
EMaCE:
h+ is influenced by external bias
H2O+H2SiF6
HF
H2O2
(c) V=-0.50V
46 µm
10 µm
82°
10 µm
(d) V=-1.00V
53 µm
10 µm
87°
10 µm

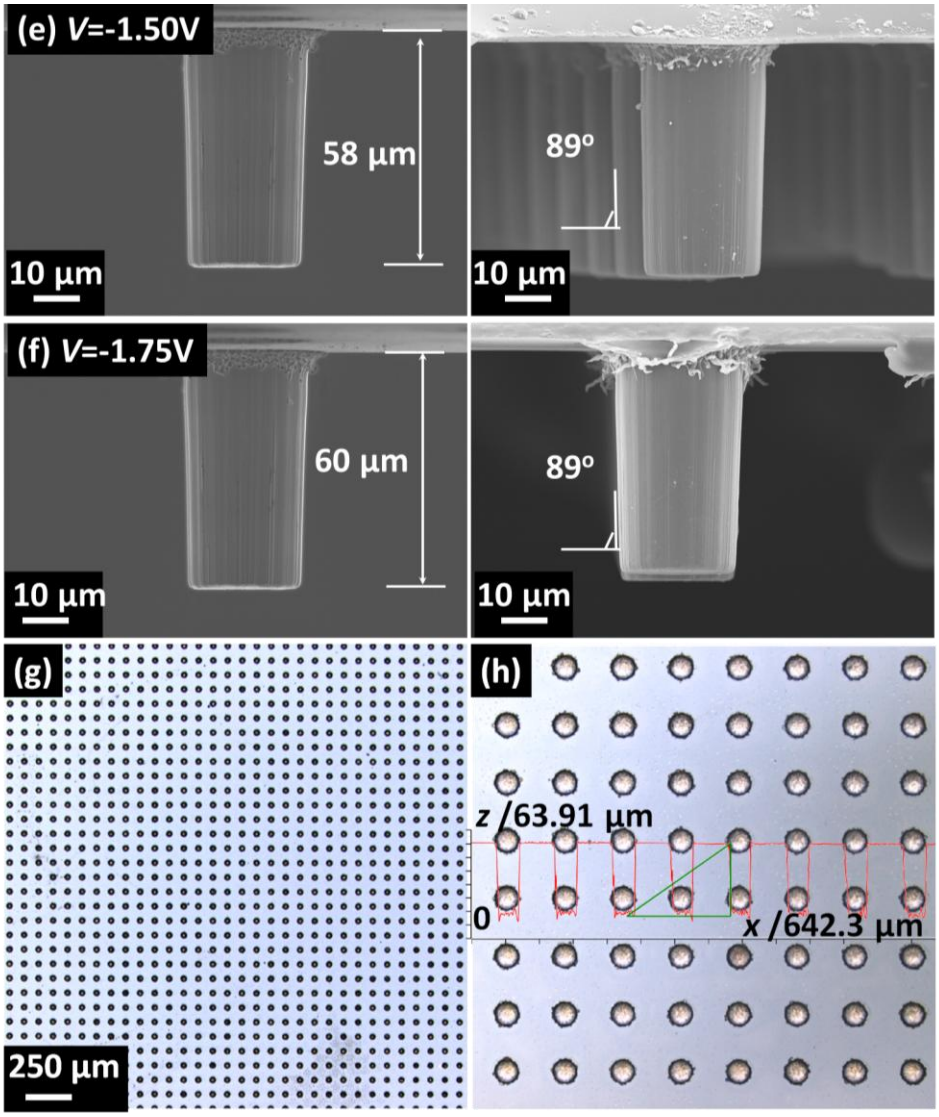

Figure 40 Schematics of charge transport in (a) MaCE and (b) EMaCE. Cross-sectional SEM images of the chips (left) and polymer replica (right) after EMaCE at (c) -0.50 V, (d) -1.00 V, (e) -1.50 V and (f) -1.75 V for 10 min. (g) and (h) show the OCM image and cross-sectional diagram of the etched chip in (f).

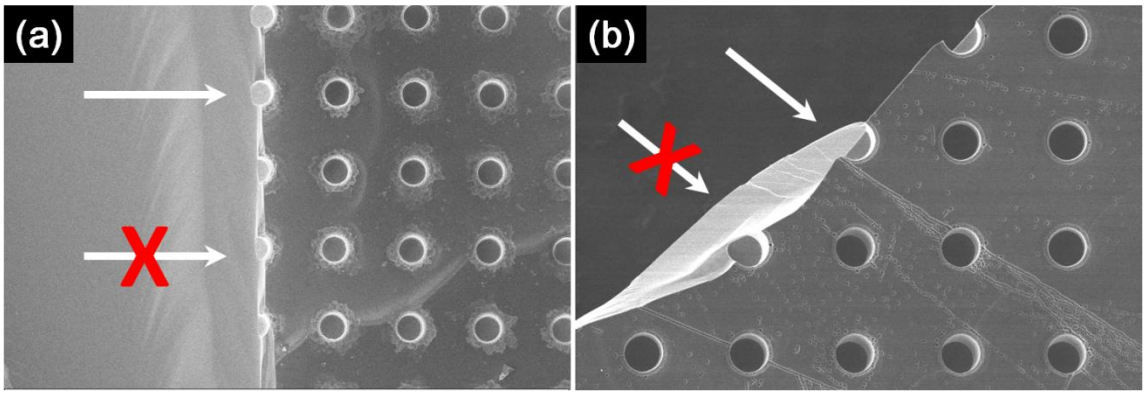

Figure 41 (a) 28 μm Au-Si(100) and (b) 28 μm Au-polySi chips after EMaCE at -1.75 V for 10 min and cut for cross-sectional SEM imaging.

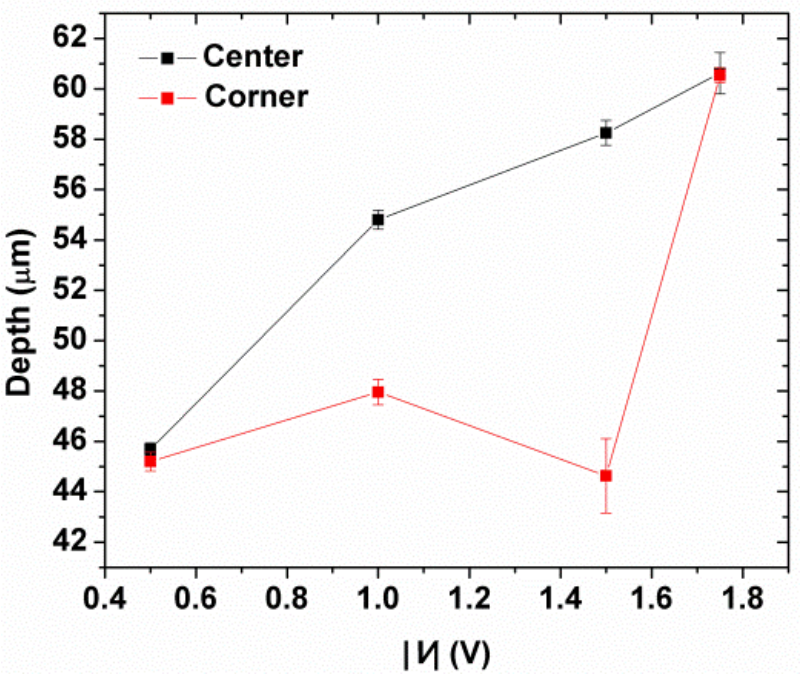

Figure 42 Evolution of h_{center} (black) and h_{corner} (red) measured from the polymer replica at bias shown in **Figure 40** (c)-(f).

To further illustrate the proposed mechanism of EMaCE, we replaced the constant bias by a variable bias which continuously increased from -0.10 V to -3.10 V at 5 mV/s

(referred as continuous EMaCE experiment). The current-bias (*I*-*V*) curve of the continuous EMaCE experiment is shown as the black line in **Figure 43**(a). The sign of current is defined as negative, meaning that h^+ is flowing away from the chip and electrons are injected into the chip. Since the Si substrate is p-type, the contact between the back side of Si and the copper foil can be treated as a forward-biased Schottky contact. The non-linear increase of current versus bias beyond the onset of ca. -0.6 V is characteristic for forward-biased Schottky contact. After the bias exceeds -1.5 V, the evolution of current became unstable, which may be due to the slowly depletion of excessive h^+. In contrast, when the same experiment was done in a $\rho(1)^{1.8}$ etchant (i.e. etchant without H_2O_2), the current stay negligibly low across the whole etching experiment (red line, **Figure 43** (a)). Actually, Au catalysts hardly etched into the substrate in $\rho(1)^{1.8}$, only some pores (<100 nm diameter) propagated along the family of <100> crystalline orientation around the Au (**Figure 44**). The control experiment indicates that catalyzed reduction of H_2O_2 is the source of the current in EMaCE (black line **Figure 40**(a)), and the charge carriers of the current mainly consist of excessive h^+. Thus, EMaCE is essentially different from ECE [68] where h^+ were injected from external power supply. We also plot the value of $\tan\theta$ from **Figure 40** (c)-(f) against the bias as blue dots in **Figure 43** (a), which shows a decreasing trend similar to that of current. Since $\tan\theta$ approximately equals to $2h/(d_t\text{-}d_b)$, $\tan\theta$ can roughly represent the ratio of the vertical etching rate to the excessive etching rate. The similarity between the trends of *I*-*V* and $\tan\theta$-*V* indicates that the extent of excessive etching suppression can be related to the amount of h^+ that are drawn to the back side. Further, we did an EMaCE experiment where the applied bias varied versus etching time in a stepwise manner (referred as stepwise EMaCE). The evolution of applied bias and measured current versus the etching time are shown in **Figure 43** (b). The whole etching can be divided into four stages. In each stage, the bias stayed at a constant value for 300 s. The transition time of the bias and current between two stages are both less than 1 sec. The current changed and stabilized itself after the bias was altered to a new value with delay time less than 1

sec. The slight increase of current in each stage may be caused by the geometric evolution of the etching profile. The etching result of continuous EMaCE and stepwise EMaCE are shown in **Figure 43** (c)-(e) and (f)-(h). In continuous EMaCE, the sidewall angle increased as the Au etched deeper; the sidewall angle become 90^{o} around 20 μm below the top surface. In stepwise EMaCE, the sidewall angle increased stepwise. In both cases, some discontinuity on the smooth sidewall can be observed (insets of **Figure 43** (d) and (f)). These sharp turns show the geometric response of etching profile to the attenuation of applied bias.[69, 70] Also, the etching profiles are uniform across the whole chips, as illustrated by the low-magnification SEM images of polymer replica (**Figure 43** (e) and (h)). The success of continuous EMaCE and stepwise EMaCE demonstrates that both the lateral and the vertical geometry of the etching profile can be controlled in a real-time manner by the facile attenuation of bias over etching time.

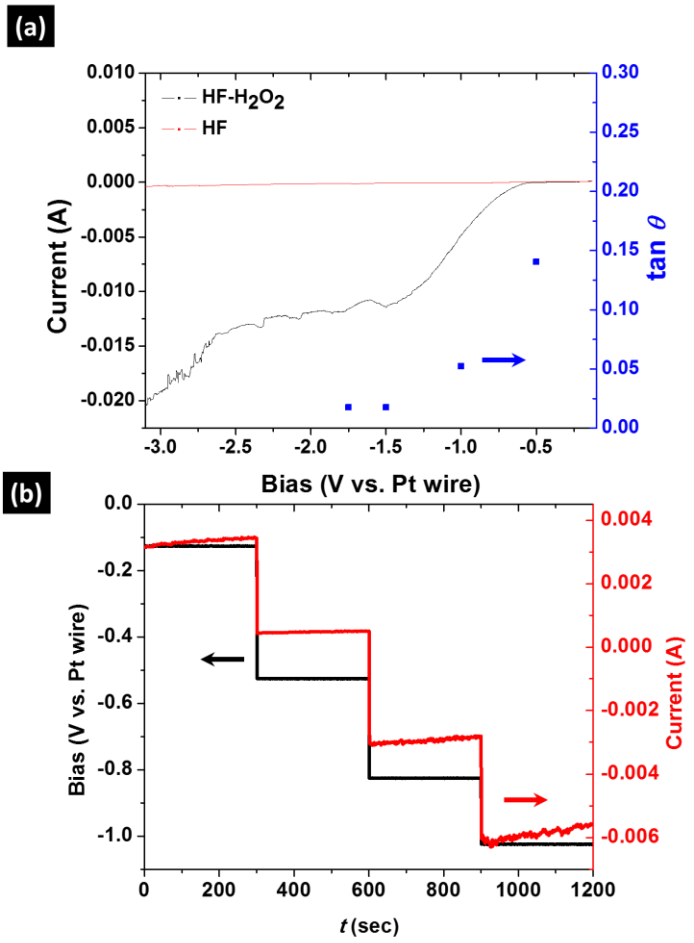
(a)
HF-H2O2
HF
Current (A)
tan θ
(b)
Bias (V vs. Pt wire)
Current (A)
t (sec)

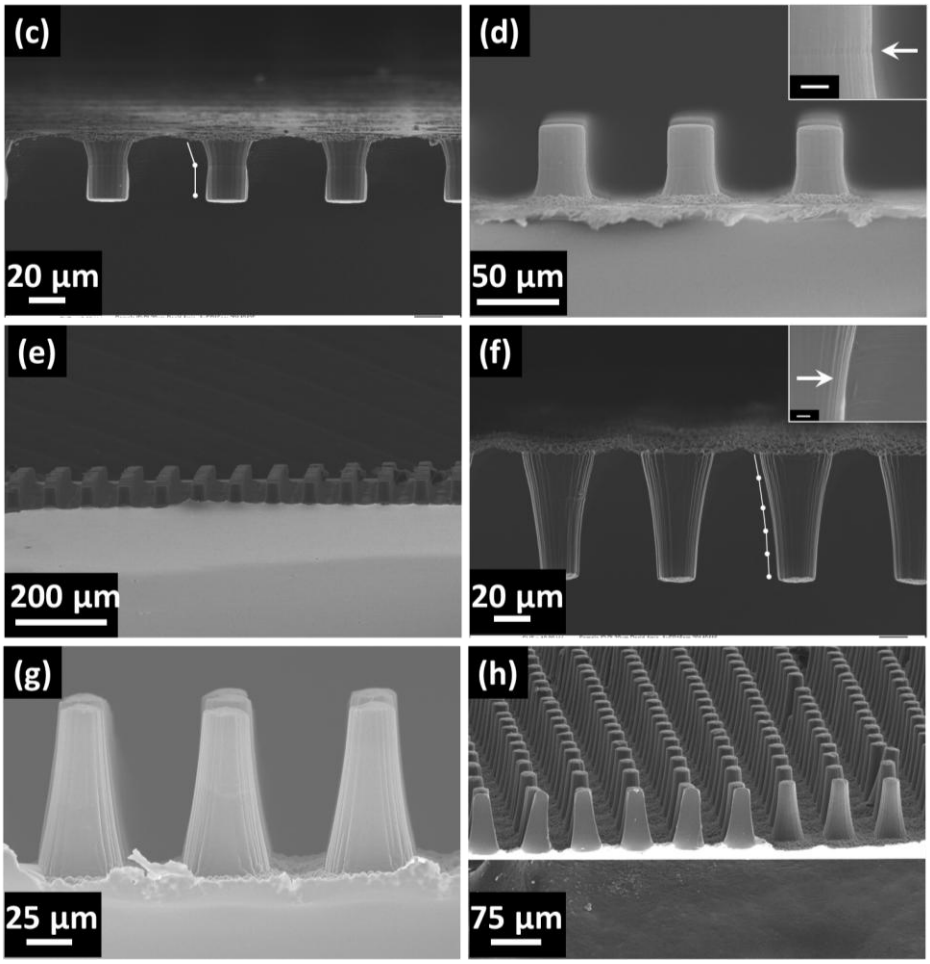

Figure 43 (a) Current-bias (*I*-*V*) curve of 28 µm Au-Si(100) in $\rho(0.37)^{1.8}$ etchant(black line) and $\rho(1)^{1.8}$ etchant (red line) in a continuous EMaCE experiment. h and θ of the etching results shown in Figure 40 (c)-(f) are also plotted. (b) Evolution of applied bias and measured current versus etching time in a stepwise EMaCE experiment. Cross-sectional SEM of chips (c) and polymer replica (d)-(e) etched in condition of black line in (a). Cross-sectional SEM of chips (f) and polymer replica (g)-(h) etched in condition of (b).

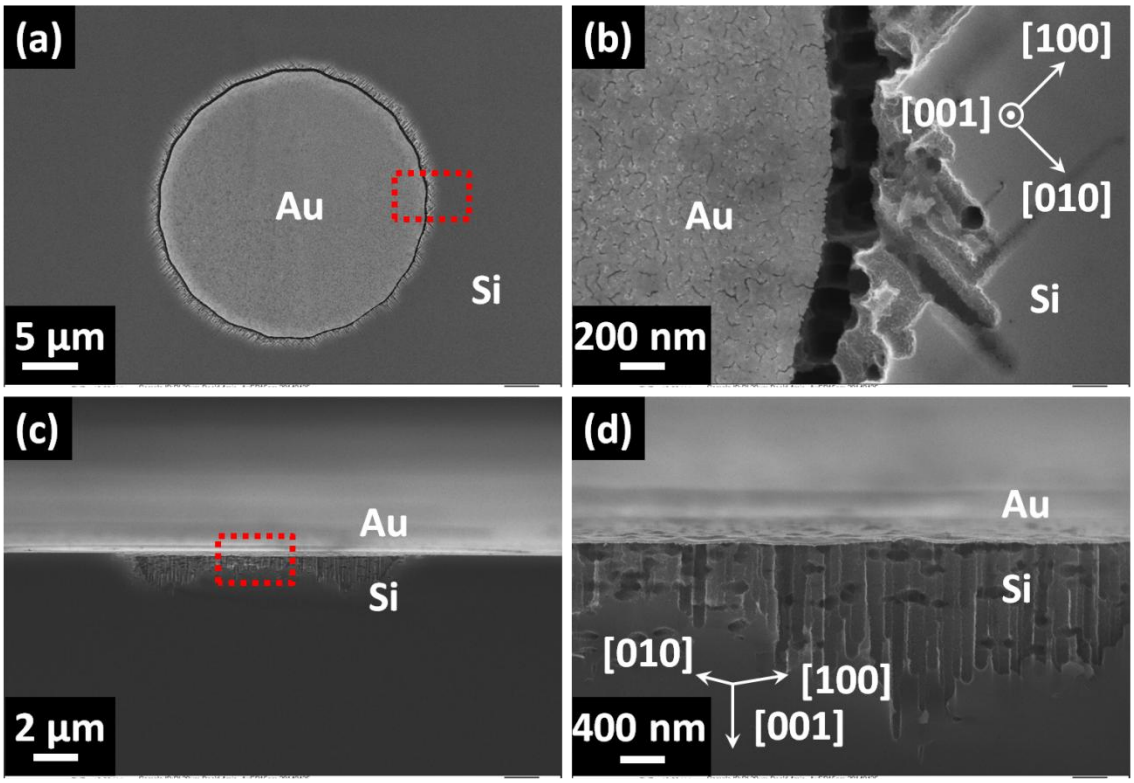

Figure 44 (a), (b) Top-view and (c), (d) cross sectional SEM images of etching result corresponding to the red line in **Figure 43** (a). (b) and (d) shows the enlarged image in the red squares of (a) and (c).

To investigate capability of high-speed etching by EMaCE, we did EMaCE in $\rho(0.55)^{3.6}$ etchant. After 10 min of etching, the catalysts penetrated 113 µm into the Si substrate with sidewall angle >89° (**Figure 45** (a)-(b)). When viewed under SEM with high magnification, the sidewall shows a roughness well below 50 nm (**Figure 45** (f)). The low sidewall roughness (<50 nm) at high etching speed (>10 µm/min) makes the etched holes as ideal candidates for high performance TSV. In contrast, in dry etching the sidewall roughness is usually compromised at etching rate higher than 5 µm/min.[13] It should be further increasing the ρ value of the etchant may cause the breaking of the catalysts. As

shown in **Figure 46**, after etching in $\rho(0.65)^{5.2}$ at -1.75 V for 10 min, Au catalysts broke into separated particles. Randomly-aligned pores were formed on both top surface and bottom of the etched holes (**Figure 46** (a) and (b)), because a porous Si-formation h^+ transport was enabled in the high-ρ etchant (**Chapter 3**). Further, we investigated the capability of EMaCE in etching structures with high aspect ratio. **Figure 45** (b)-(d) show the chips after EMaCE in $\rho(0.37)^{1.8}$ at -1.75 V for 25 min, 60 min, 90 min and 120 min. In each test, the etchant was agitated by a stir bar at 400 rpm after 10 min of EMaCE. d_t remained 29 μm in each test. h for each time were measured from cross sections of the etched chips, which are 94μm, 235 μm, 278 μm and 323 μm respectively. The low-magnification images of the chips after 25 min of etching show good uniformity across the whole chips (**Figure 47** (a) and (b)). After etching of 120 min, the vertical etching direction was still preferred. The Au catalysts stayed as integrity without breaking; the sidewall roughness kept as low as that in **Figure 45** (f).We also tried to use polymer replica to reveal the 3D geometry of these high-aspect-ratio structures. However, because of the limited mechanical property of epoxy replica, only straight polymer replica with the height of 218 μm was found. Some replica with height of 270 μm can also be found while tilting from the vertical direction (**Figure 47** (c)). It should be noted that after etching of 120 min at -1.75 V, the photoresist stayed in close contact with the top surface of Si substrate (**Figure 47** (d)). In contrast, the top surface was significant etched and a gap appeared after 20 min of MaCE at no bias (**Figure 47** (e)) and finally caused the delaminating of photoresist. The results shown in **Figure 45** (b)-(e) demonstrates the EMaCE is capable of producing microstructures deeper than 300 μm with aspect ratio over 10:1 while completely suppresses the excessive etching over the long time of etching.

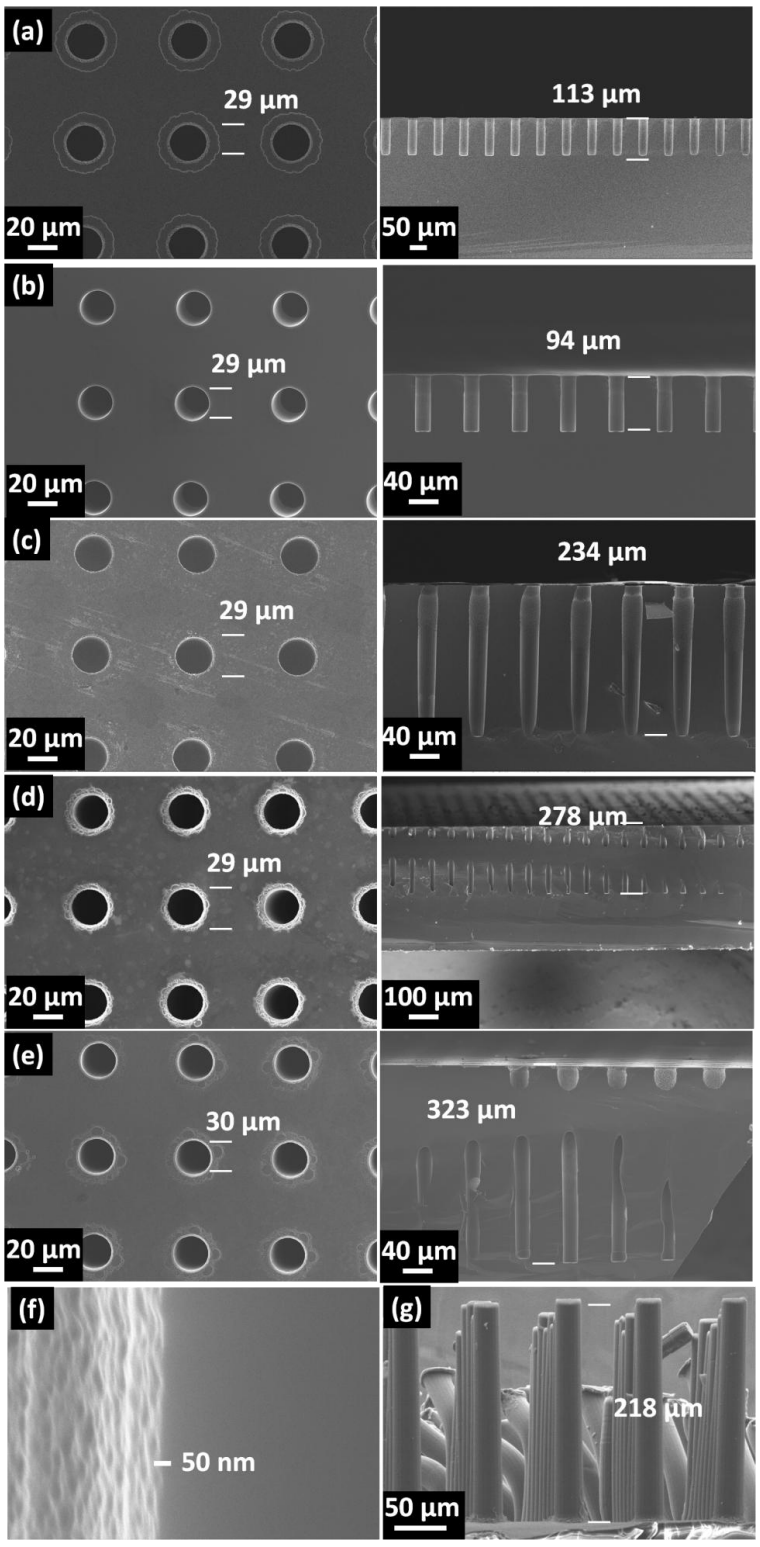

Figure 45 Top-view (left) and cross-sectional (right) of the chips etched at -1.75 V for (a) 10 min in $\rho(0.37)^{1.8}$ (b) 25 min; (c) 60 min; (d) 90 min; (e) 120 min. (f) the sidewall of etched holes in (a) with high magnification. (g) the polymer replica of (d).

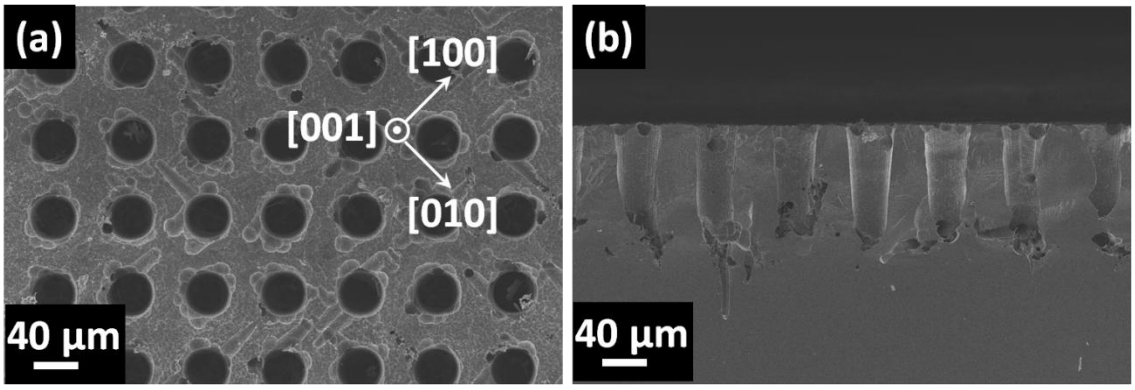

Figure 46 Top-view (a) and cross-sectional (b) SEM images of the 28 µm Au-Si(100) chips after etching in $\rho(0.65)^{5.2}$ at -1.75 V for 10 min.

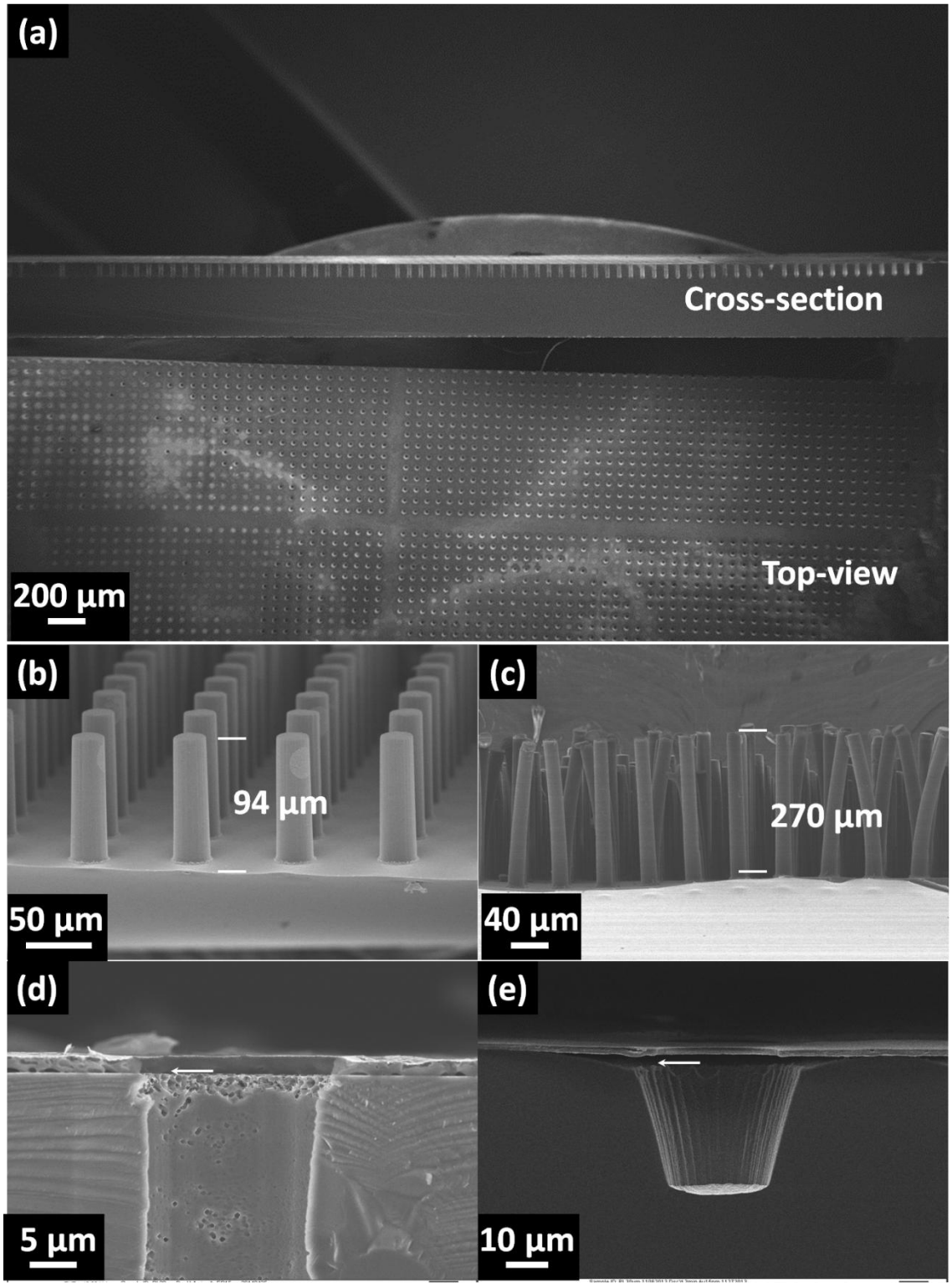

Figure 47 Top-view and cross sectional SEM images of (a) the chip and (b) replica etched at -1.75 V for 25 min. (c) Polymer replica of the chips etched at -1.75 V for 120 min. Contacts (indicated

by white arrows) between photoresist and Si substrate after (d) EMaCE at -1.75 V for 120 min and (e) MaCE for 20 min.

To extend the range of application, we applied the established EMaCE method to the etching of (111)-oriented Si substrate and polycrystalline Si (polySi) substrate. **Figure 48** (a)-(c) shows the top-view and cross-sectional SEM images of a 29 μm Au-Si(111) chip after EMaCE for 10 min at -1.75 V and the corresponding replica. Uniform vertical holes can be found across the whole chip. For polySi substrate, we first studied the etching behavior at no bias (**Figure 48** (d)-(f)). After etching of 10 min, Au catalysts moved vertically into the substrate. However, a considerable amount of grooves and pits were found on the Si between Au (**Figure 48**(d)). It has long been known that chemical etching of Si is preferable along the defects of Si substrates._ENREF_31[71]Thus the grooves were probably formed by the excessive etching of the boundary between two adjacent Si crystal grains. At higher magnification, some grooves were found to penetrate below the Au catalysts, indicating that the excessive etching of grain boundary even exceeded the MaCE process (indicated by the white arrow **Figure 48** (e)). Also, the sidewall of the etched holes tapered like those shown in **Figure 38**. In contrast, when a -1.75 V bias was applied, both the groove-formation and sidewall-tapering were suppressed (**Figure 48** (g)-(i)). Although some shallow grooves were still observable, the grooves only penetrated into the very top layer of Si substrates, as revealed from the etched chip (**Figure 48** (h)) and corresponding replica (**Figure 48** (j)). Also, etching in vertical direction was significantly enhanced by the bias (**Figure 48** (i)) compared to that at not bias (**Figure 48** (f)). The SEM of polymer replica in low magnification (**Figure 48** (k) and (l)) shows that the vertical etching was preferred across the chip and all the etched holes bear high geometric uniformity. The crystalline orientation-independent etching behavior is highly desirable for etching on broader range of substrates.

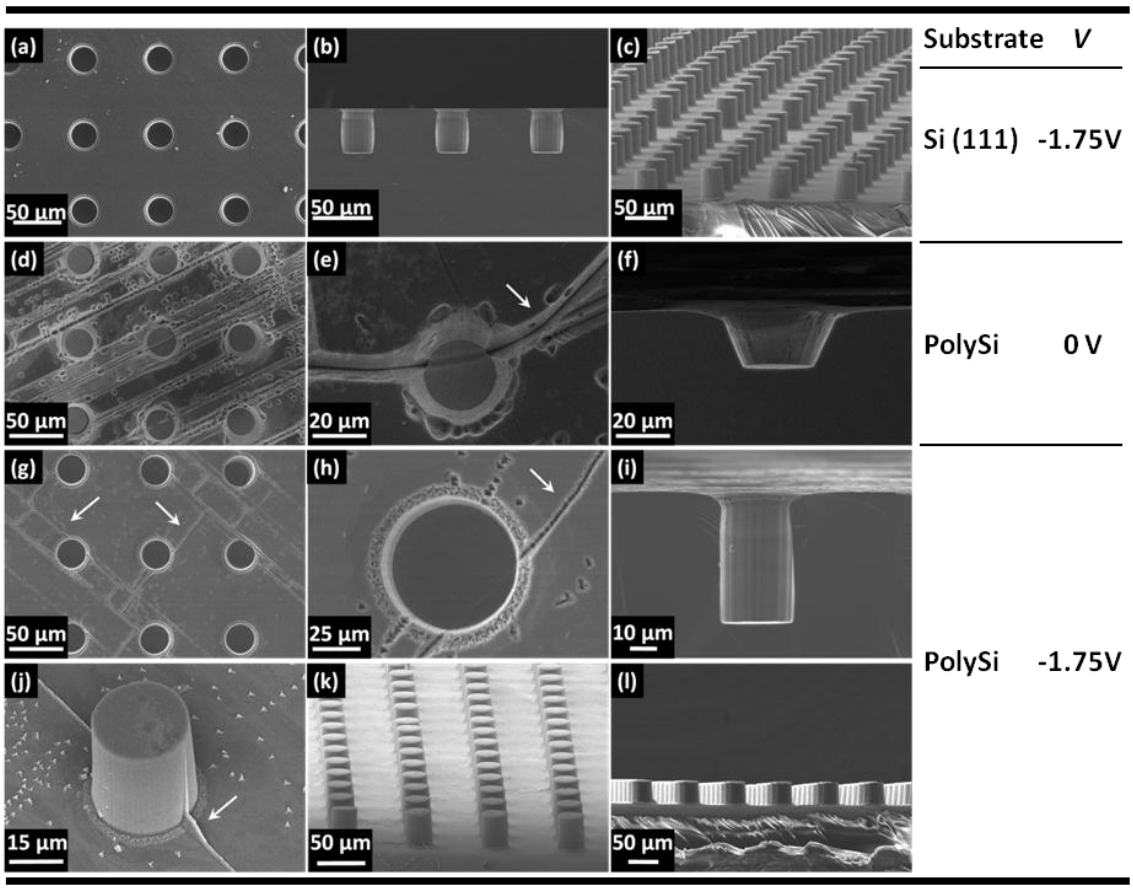

Figure 48 (a) Top-view, (b) cross-sectional SEM images of a 29 µm Au-Si(111) chip after MaCE at -1.75 V and (c) corresponding replica. (d), (e) Top-view, (f) cross-sectional SEM images of a 29 µm Au-polySi chip after MaCE. (g), (h) Top-view, (i) cross-sectional SEM images of a 29 µm Au-polySi chip after MaCE at -1.75 V and (j), (k), (l) corresponding replica.

Finally, we tested the etching of complex features by EMaCE. **Figure 49** (a)-(c) show the original pattern of a complex feature after photolithography. Five sets of subunits with critical dimension of (A) 500 µm, (B) 50 µm, (C) 11.7 µm, (D) 5.8 µm (E) 3.1 µm and (F) 0.8 µm can be observed in the images with increasing magnification. We increased the bias to -2.00 V because a larger amount of excessive h^+ was produced by the larger area of Au catalysts. After 10 min of EMaCE, Au catalysts on all units etched uniformly and

vertically into the Si substrate, as shown in the polymer replica (**Figure 49** (d) and (g)). d_t and d_b were measured from the etched chips (**Figure 49** (e) and (f)) and corresponding polymer replica (**Figure 49** (g)), respectively. The values are listed in **Table 4**. The variance between d_t and d_b of each subunit is less than 1 μm, both of which have a variance less than 1 μm to their origin dimensions (d_{orig}). Besides the accuracy of dimensions, EMaCE also possesses the fidelity in transferring the shape of original feature, as found in the sharp corners (**Figure 49** (h)) and interconnections between feature B and C (**Figure 49** (i)).

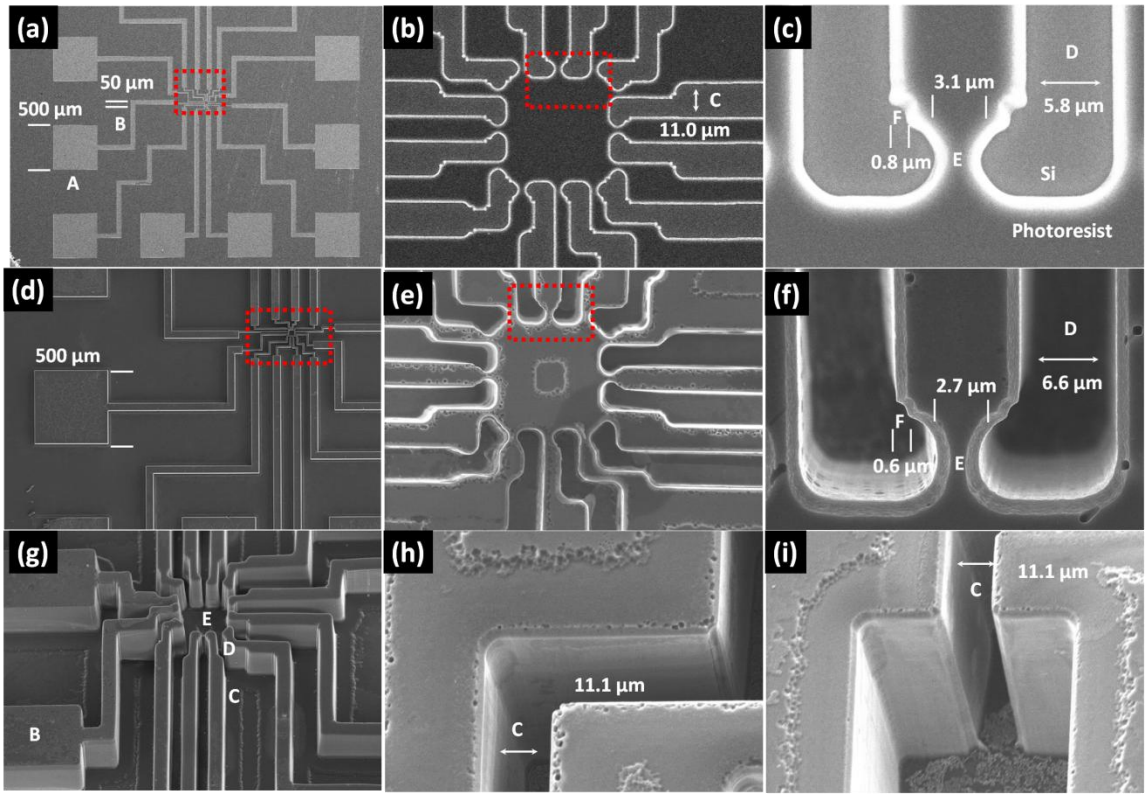

Figure 49 (a)-(c) pattern of a complex feature after photolithography on Si(100) chip; (e), (f), (g), (h) show the chip after EMaCE at -2.00V for 10 min. (d) and (g) show the corresponding replica.

Table 4 Dimensions of subunits C-F shown in Figure 49 before and after EMaCE

Feature ID	C	D	E	F
d_{orig}(μm)	11.0	5.8	3.1	0.8
d_t(μm)	11.1	6.6	2.7	0.6
d_b(μm)	10.2	5.0	2.7	0.8

4.4 Conclusion

In conclusion, a novel Si etching method, named electric bias-attenuated metal-assisted chemical etching (EMaCE), is established based on the *uniform MaCE condition*. A negative electric bias was applied from the back side of Si substrate during MaCE process to solve the issue of excessive etching found in traditional MaCE process. Over 10,000 vertical holes with diameter of 28 μm were successfully fabricated on a 1×1 cm^2 chips with high speed, high aspect ratio and low sidewall roughness. By programming the variation of bias versus etching time, the 3D geometry of the etching profile can be attenuated in real time. Etching of vertical holes was also realized by EMaCE on Si (111) and polySi substrate. Complex features with lateral dimensions of 0.8 μm-500 μm were also fabricated with high geometric accuracy. The established EMaCE is not only readily applicable for manufacturing TSVs in large scale with low cost, but also available for MEMS devices with complex lateral geometry. Also, EMaCE provides a viable solution for direct deep etching of polycrystalline Si, which has been challenging so far. Further, EMaCE with variable bias is promising to create novel micro- and nanostructures with arbitrarily-defined 3D complexity.

CHAPTER 5

CHARGE TRANSPORT IN UNIFORM MACE

5.1 Introduction

The geometry of HAR structures in the 3D space plays the key role in the performance of the devices where they are involved. Thus, controllability over the 3D geometry of the etching profile (referred to as "3D profile" in the following discussion) is essential for any HAR Si etching method. In DRIE, the 3D profile can be controlled by the chemistry of plasma.[72, 73] In MaCE for nanowires fabrication (referred to as nano-MaCE), it has been reported that the 3D profile could be influenced by the etchant composition [74], the doping type and doping level of Si substrates.[75]

The chemistry in microscale uniform MaCE is fundamentally different from nano-MaCE. In nano-MaCE, etchant with high ρ value (generally, over 0.60) is preferred for high shape-transfer fidelity.[37] However, if microscale uniform MaCE was conducted in such high-ρ etchant, deformation and disintegration of the catalysts were observed ([53]). In order to obtain decent etching uniformity, ρ has to be lowered to ensure the stable movement of catalyst in micro-MaCE. The use of low-ρ etchant can be regarded as a uniform MaCE (UMaCE) condition. In the low-ρ etchant solution, the sidewall of the 3D profile can be either vertical or tapered, as shown in **Chapter 3 and 4**. In the context of MaCE for microstructures fabrication (referred to as micro-MaCE), controllability of the 3D profile has not been well studied.

In this chapter, we propose that under the UMaCE condition, the 3D profile in micro-MaCE can be correlated to the charge transport process during etching. Considering the fact that MaCE is essentially a redox reaction where electron holes (h^+) are involved, the transport of h^+ may critically influence the 3D profiles of MaCE. To investigate the

correlation between the CT and the 3D profile, the effects of two sets of "intrinsic" parameters are investigated in this work: the intrinsic property of the Si substrates and the geometry of the catalyst. A series of experiments under the UMaCE condition are conducted on Si substrates with different dopant type and doping level; straight-line shapes Au catalysts with different number of patterns, width and spacing distance are used in each experiment. Interestingly, the 3D profiles in these experiments show sharp contrast as presented below. The contents in this chapter have been partially published in [76] and reprinted here with permission. Copyright 2015, The Electrochemical Society.

5.2 Methods-Experimental

All the Si substrates in this work were single crystalline with (100)-orientation from University Wafer, MA. The received Si was washed in Piranha solution at 120 ^{o}C for 10 min and rinsed by deionized (DI) water. After dried in N_2 gas, a layer of photoresist (Shipley S1813) was spin-cast onto the Si and exposed under 405 nm light in a Karl Suss Mask Aligner for photolithography. After developing in MF-319 developer (Shipley), the Si was cleaned by argon/oxygen plasma (Advanced Vacuum Vision RIE system). A layer of Au was then deposited by a Denton Explorer E-Beam Evaporator at a rate of 0.5 Å/sec in a vacuum chamber of 3×10^{-6} Torr. The nominal thickness of all the Au film used in the work is 10 nm. Atomic force microscope (AFM) image of the Au film was collected from a Veeco Dimension Edge AFM system with a Si tip (Bruker MPP 11100-10). The Au-loaded Si substrates were cut into pieces (1×2 cm^2 in lateral size) and directly immersed in HF-H_2O_2 etchant solution for MaCE of 10 min. Each piece contains one block of line-shaped patterns with same geometry. HF and H_2O_2 were provided by VWR International and directly used without further processing. All the MaCE experiments were conducted in the mixture solution of 1.5 mol/L HF and 3.1 mol/L H_2O_2 in DI water with a total

volume of 32 mL at room temperature with ambient light illumination. No significant effect of illumination was observed in the etching profile. After MaCE, the samples were rinsed by DI water and the photoresist was lift off by acetone. The etching results were observed under SEM (Hitachi SU8010). For the cross sectional SEM images, Si samples were mechanically cleaved by a scriber along the direction that was perpendicular to the line patterns. Au layer is not removed because it is too thin (only ~10 nm) to make any difference in the SEM images that describe the overall geometry of etching profile. In the real application where Au needs to be removed, Au can be facilely removed by immersion in potassium iodide (KI, 10.0 wt%)/iodine (I_2, 2.5 wt%) aqueous solution at room temperature within 10 sec. The current-voltage (*I-V*) curve of bare Si substrates in HF solution was acquired by connecting the Si to a potentiostat (Princeton Applied Research, VersaSTAT MC) as the working electrode; a platinum wire was used as the counter electrode. A home-made carrier was used to facilitate the electric connection between Si substrate and the potentiostat. The *I-V* curves are collected under the same ambient light as existed in all the MaCE experiments. The details of carrier fabrication and configuration have been reported in **Chapter 4**.

5.3 Methods-Modeling of h^+ distribution

The h^+ distribution was calculated by a Matlab software (version R2014b) based on an isotropic diffusion model as derived the following. h^+ concentration distribution functions in Cartesian CS and cylindrical CS are set as

$$c_{h+} = c_{h+}(x,y,z,t) = c_{h+}(r,\omega,z,t) \tag{13}$$

Consider 2D Isotropic Diffusion Equation in cylindrical CS (Fick's Second Law):

$$\begin{aligned} \frac{\partial c_{h+}}{\partial t} &= D \bullet \nabla^2 c_{h+} \\ &= D \bullet \left(\frac{\partial^2 c_{h+}}{\partial r^2} + \frac{2}{r} \frac{\partial c_{h+}}{\partial r} \right) \end{aligned} \tag{14}$$

where D is the diffusion constant.

If we consider h^+ are emitting from the boundary of a circular source with radius of r_s (**Figure 50**), and we set the first boundary condition-1 (BC-1) as: At t=0, an impulse of h^+ with the total amount of C_s is input from the void source:

$$-\frac{\partial c_{h+}}{\partial t}\bigg|_{r=r_s} = \frac{C_s}{4\pi r_s^2}\delta(t) = c_s \delta(t) \tag{15}$$

$\delta(t)$: Dirac Function. $\delta(t)$=0, when $t \neq 0$.

Also we set the second boundary condition (BC-2) as:

$$c_{h+}\big|_{r\to\infty} = 0 \tag{16}$$

Also the initial condition is

$$\theta\big|_{t=0} = 0 \tag{17}$$

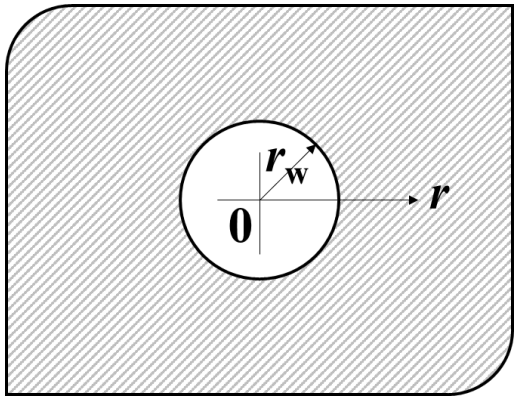

Figure 50 A circular h^+ Source in an Infinite Space

To solve Eq.15, we define the Laplace transform of a function *f*(t) as:

$$\mathscr{L}\left\{f(t)\right\} = \overline{f}(s) = \int_0^\infty e^{-st} f(t)\,dt \tag{18}$$

Let $f(t)$ be continuous and have a piecewise continuous derivative $\frac{\partial f}{\partial t}$ in every finite interval $0 \le t \le T$. Then

$$\mathscr{L}\left\{\frac{\partial f(t)}{\partial t}\right\} = sF(s) - f(0) \tag{19}$$

Once Eq.19 is applied to Equation 8, BC-1, BC-2, we have

$$\mathscr{L}\left\{c_{\mathrm{h}+}(t)\right\} = \overline{c_{\mathrm{h}+}}(s) \tag{20}$$

$$\frac{\partial^2 \overline{c_{\mathrm{h}+}}}{\partial r^2} + \frac{2}{r}\frac{\partial \overline{c_{\mathrm{h}+}}}{\partial r} - q^2 \overline{c_{\mathrm{h}+}} = 0 \tag{21}$$

$$-\left.\frac{\partial \overline{c_{\mathrm{h}+}}}{\partial t}\right|_{r=r_s} = c_s \tag{22}$$

$$\left.\overline{c_{\mathrm{h}+}}\right|_{r\to\infty} = 0 \tag{23}$$

Where $q^2 = s/D$ .The general solution of Equation 15 has the form

$$\overline{c_{\mathrm{h}+}} = A\frac{e^{qr}}{r} + B\frac{e^{-qr}}{r} \tag{24}$$

Once Eq. 23 is accounted for, one has *A*=0 and Eq. 24 is simplified to

$$\overline{c_{\mathrm{h}+}} = B\frac{e^{-qr}}{r} \tag{25}$$

When Eq. 22 is accounted, the solution becomes

$$\overline{c_{\mathrm{h}+}} = \frac{c_s r_w^2}{1+qr_w}\frac{e^{-q(r-r_w)}}{r} = \frac{C_s}{4\pi(1+qr_w)}\frac{e^{-q(r-r_w)}}{r} \tag{26}$$

If now consider that $r_w \to 0$ so that the circular source becomes a point source, then

$$\overline{c_{\mathrm{h}+}} = \frac{C_s}{4\pi}\frac{e^{-qr}}{r} \tag{27}$$

Given the fact that

$$\mathscr{L}^{-1}\left(\frac{e^{-qr}}{r}\right)=\frac{e^{-r^2/(4Dt)}}{2t\sqrt{\pi Dt}} \tag{28}$$

Then we have the transient h^+ distribution function from an impulse point source in an infinite space:

$$c_{h^+}(r,t)=\frac{C_s}{(4\pi Dt)^{3/2}}e^{-r^2/4Dt} \tag{29}$$

Similarly, for the transient h^+ distribution function from an impulse line source in an infinite space:

$$c_{h^+}(r,t)=\frac{C_{SL}}{4\pi Dt}e^{-r^2/4Dt} \tag{30}$$

Where $C_{SL}=C_S/L$, with L being the length of the line. Conceivably, the diameter of the line approaches 0.

Now we can consider the h^+ distribution in an infinite space with a moving line source which continuously emits h^+ with a rate of C_{SL}. The source can be treated as the sum of an infinite number of impulse sources that continuously emit h^+ at an infinitely small time intervals. Thus the h^+ concentration at an arbitrary point P in the space after time t_1 ($\theta_P(x, z, t_1)$) can be calculated by superimposing the concentration of h^+ that diffuse from the moving source in every time interval in the time domain of $[0, t_1]$ (**Figure 51**). By applying the h^+ concentration distribution function by impulse line source, the increase in h^+ concentration at P at an arbitrary time point τ can be expressed as:

$$\Delta c_{h^+P}(x,z,\tau)=\frac{C_{SL}\Delta\tau}{4\pi D(t_1-\tau)}\exp\left(-\frac{x^2+z'^2}{4D(t_1-\tau)}\right)$$
$$=\frac{C_{SL}\Delta\tau}{4\pi D(t_1-\tau)}\exp\left(-\frac{x^2+(z-v\tau)^2}{4D(t_1-\tau)}\right) \quad (31)$$

Then

$$c_{h^+P}(x,z,t_1)=\int_0^{t_1}\frac{C_{SL}}{4\pi D(t_1-\tau)}\exp\left(-\frac{x^2+(z-v\tau)^2}{4D(t_1-\tau)}\right)d\tau \quad (32)$$

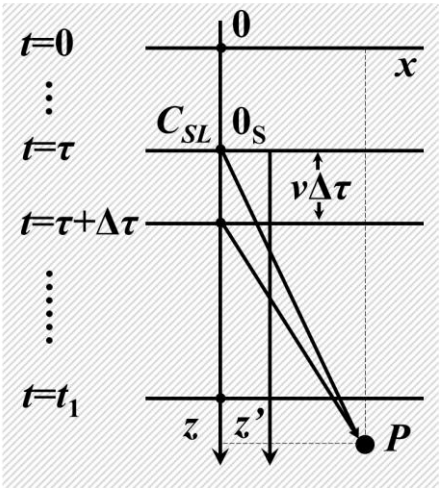

Figure 51 Schematic of the cross section of a line source moving at constant velocity *v* along z axis in infinite space. The line source is aligned in the *y* axis which is perpendicular towards the *x*-*z* plane. 0 is the point of origin of the immobile coordinate system *x*, *y*, *z*; 0_S is the point of origin of the coordinate system *x*, *y*, *z*' that moves with the source.

An Au line with width of w_0 that continuously emits h^+ into Si can be treated as an array of closely packed paralleled line source with infinitesimal diameter. In this sense, the h^+ distribution in MaCE by one Au line after time t_1 can be described as

$$c_{h^+}(x,z,t_1)=\int_{-w_0/2}^{w_0/2}dw\int_0^{t_1}\frac{C_{SL}}{4\pi D(t_1-\tau)}\exp\left(-\frac{(x-w)^2+(z-v\tau)^2}{4D(t_1-\tau)}\right)d\tau \quad (33)$$

In the case of MaCE by multiple Au lines, by assuming that c_{h^+} from the contribution of each Au line are additive, then we have

$$c_{h^+}(x,z,t_1)=\sum_{n=1}^{n}\int_{-w_0/2}^{w_0/2}dw\int_0^{t_1}\frac{C_{SL}}{4\pi D(t_1-\tau)}\exp\left(-\frac{(x-w-n\times s)^2+(z-v\tau)^2}{4D(t_1-\tau)}\right)d\tau \quad (34)$$

where n and s are the number and spacing of the Au lines.

Using the density of Si [77] as ρ=2.329 g/cm^3 the vertical etching rate r_z under an Au line with both width and length of 1 μm is:

$$r_z=\frac{\rho V}{M_{Si}t}=\frac{6\mu m\times 1\mu m\times 1\mu m\times 2.329 g/cm^3}{28.09 g/mol\times 600 s}=8.3\times 10^{-16} mol/s$$

where V is volume of Si that has been etched. Assuming etching of one Si atom consumes 4 h^+ (Eq. 2 in main text), then the current density of h^+ is

$$I=\frac{4\times r_z\times N_A\times e^-}{S}=\frac{4\times 8.3\times 10^{-16} mol/s\times 6.02\times 10^{23}/mol\times 1.6\times 10^{-19} C}{1\mu m\times 1\mu m}=32.0 mA/cm^2$$

Considering the fact that $|r_z|$ shows little dependence on the lateral geometry of the Au lines (**Figure 58** (a)), the current density value should be applicable in all MaCE experiments on P-Si.

5.4 Results and Discussion

As listed in **Table 5**, n-type and p-type doped Si with resistivity are labeled as N-Si and P-Si for the convenience of discussion. Undoped Si is named as U-Si, while the heavily dope n-type and p-type Si are named as (N+)-Si and (P+)-Si. To study the effect of Si type and catalyst geometry, all the other experimental conditions were strictly fixed as described in the Experimental section, including the catalyst thickness and morphology, etchant solution composition and volume, etching time, temperature and etc. The overall processing flow is illustrated in **Figure 52**. At the initial step, blocks of line patterns are

transferred onto Si by photolithography. Each block contains a certain number (n) of parallel line patterns ("lines" for short) with the same line width w_0 and line spacing distance s. Each block is named by its n, w_0 and s value in the format of $w_0 \times n@s$. Within the lines, bare Si surface is exposed; while the Si surface outside the lines is covered by photoresist. As reported in **Chapter 4**, the photoresist has been proven to block the etching of Si in MaCE of 2 hr. After deposition of Au, only the Au in the line pattern (referred to as "Au lines") is in direct contact with Si surface and able to induce MaCE. Thus the pattern number, width and spacing distance of the Au catalyst that are actually involved in MaCE equal to w_0, n and s, respectively. SEM images of some selected blocks of lines after Au deposition are shown in **Figure 53**. The lines show uniform geometry: the line edge roughness and variation of width along an individual line are well below 0.2 μm. Width variation of line patterns within one block is also below 0.2 μm. The real thickness of Au catalyst on all Si is measured to be 13.3±0.5 nm by AFM (**Figure 54**). Nanoporous morphology of the Au catalyst can be observed under high-magnification SEM (**Figure 53** (d)). These nanopores allow the access of HF to remove the oxidized Si beneath the Au catalyst, which also ensures the uniformity of MaCE (**Chapter 3**).

Table 5 IDs, dopant type and doping level of the Si substrates used in this chapter

Substrate ID	Dopant	Resistivity (Ω cm)	Doping Density (cm^{-3})[1]
U-Si	Undoped	>3000	$<10^{13}$
P-Si	Boron	1-10	10^{15}-10^{16}
N-Si	Phosphorus	1-10	10^{14}-10^{15}
P(+)-Si	Boron	0.001-0.005	10^{19}-10^{20}
N(+)-Si	Phosphorus	0.007-0.020	10^{18}-10^{19}

Note:

1. The doping density is estimated from the resistivity using the table in Ref. [21].

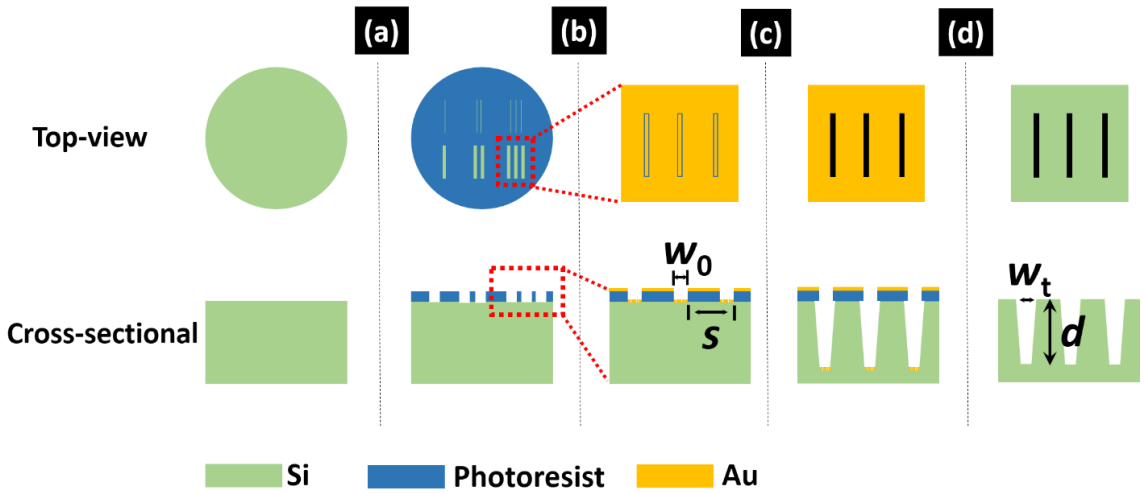

Figure 52 Processing flow in MaCE experiments: (a) photolithography for formation of line patterns blocks; (b) Au deposition; (c) MaCE; (d) lift-off of photoresist. The green, blue and golden colors represent the Si substrates, photoresist and Au catalysts, respectively.

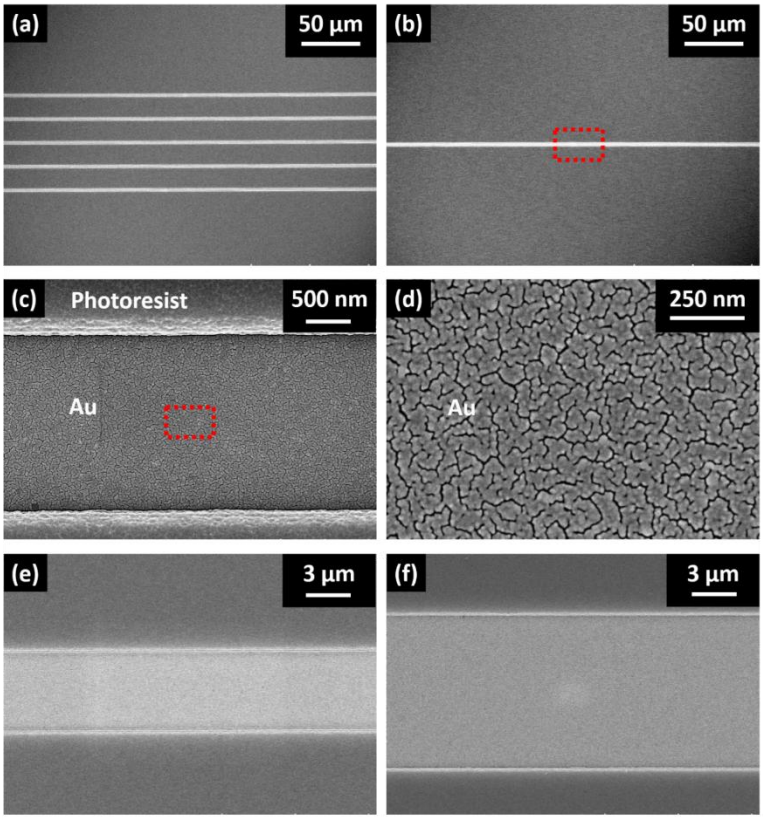

Figure 53 Top-view SEM images of Si sample after photolithography and Au deposition: (a) a 2 µm×5@20 µm pattern. The brighter area are the Si that are in direct contact with Au, while the Si surface are covered by photoresist in other darker area (the same in the following images); (b) a 2 µm×1 pattern; (c) magnified image of the red circle in (b), showing the smooth edge of photoresist; (d) magnified image of the red circle in (c), showing the nanoporous morphology of Au catalysts; (e) a 5 µm×1 pattern; (f) a 10 µm×1 pattern.

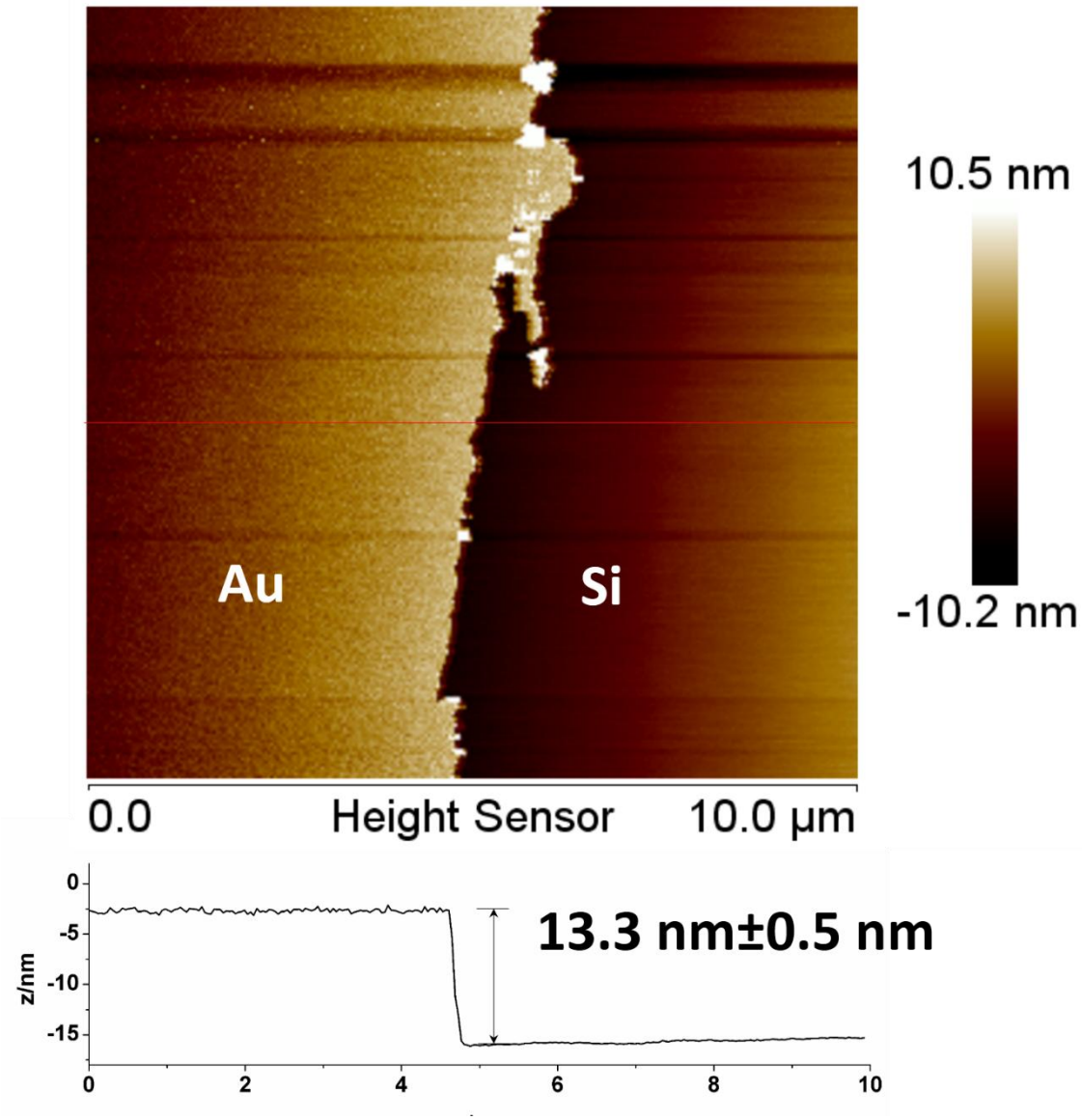

Figure 54 (Top) top-view and (bottom) cross sectional atomic force microscope (AFM) image of the as-deposited Au catalysts on bare Si surface. The thickness of Au catalysts, 13.3±0.5 nm, is acquired by measuring the step height at the edge of Au.

After MaCE, Au was found moving vertically into the Si and deep trenches were formed. Cross-sectional SEM images of the trenches on U-Si, P-Si and N-Si are shown in

Figure 55 to **Figure 57**, respectively. The depth (d) and the top width variation (Δw_t) of trenches are measured from the SEM images. As illustrated in **Figure 52**, d is defined as the vertical distance between the top edge and the bottom of a trench, while Δw_t is defined as the difference between the top width of the trench after MaCE and the original width of the line pattern before MaCE: $\Delta w_t = w_t - w_0$. The value of d and Δw_t are averaged from five independent measurements at different locations of a block are listed in **Table 6**-**Table 8** and plotted against w_0, n and s in **Figure 58**. Under the same condition, MaCE experiments were also conducted on N(+)-Si and P(+)-Si. However, unlike the uniform trenches shown in **Figure 55** to **Figure 57**, trenches on these heavily-doped Si are non-uniform. Also, porous region can be observed between the trenches (**Figure 59**). The difference among the SEM images (**Figure 55** to **Figure 57**) clearly indicates that the 3D profile of MaCE is dependent on both the property of the Si and the geometry of the patterns.

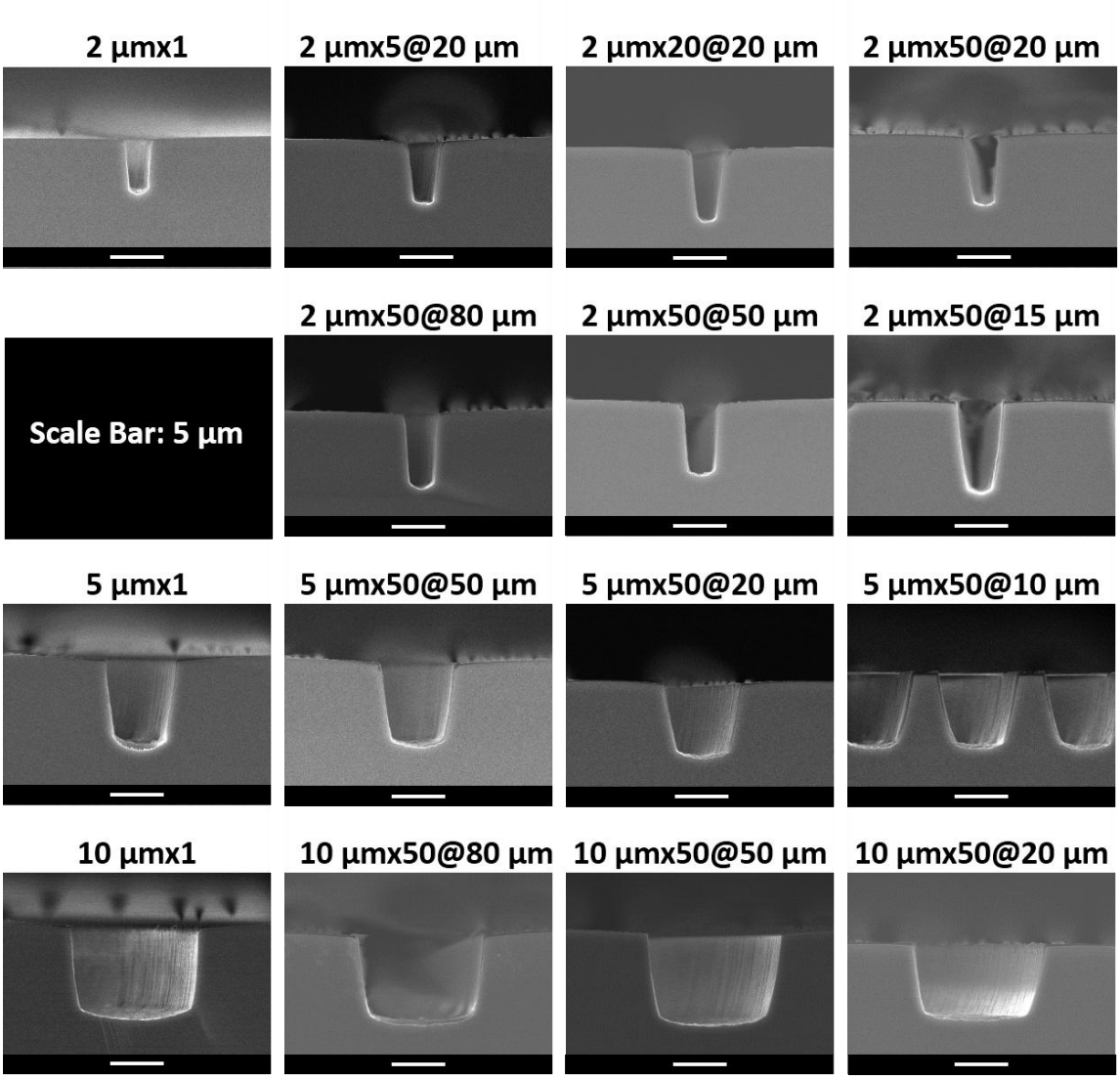

Figure 55 Cross-sectional SEM images of the etching profile on U-Si. The name of blocks are labeled on top of each corresponding figure. All the scale bars have a length of 5 µm.

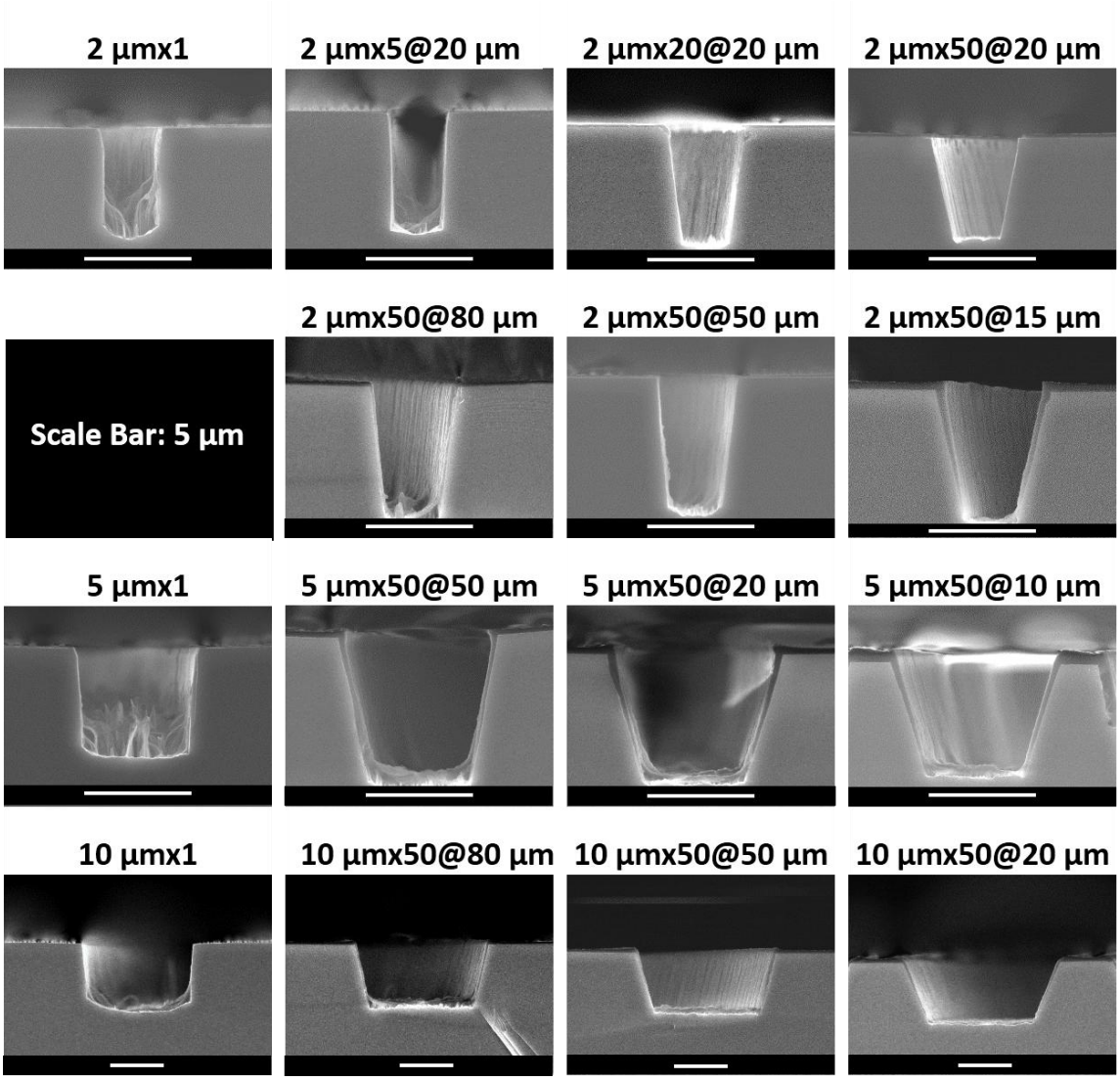

Figure 56 Cross-sectional SEM images of the etching profile on P-Si. The name of blocks are labeled on top of each corresponding figure. All the scale bars have a length of 5 µm.

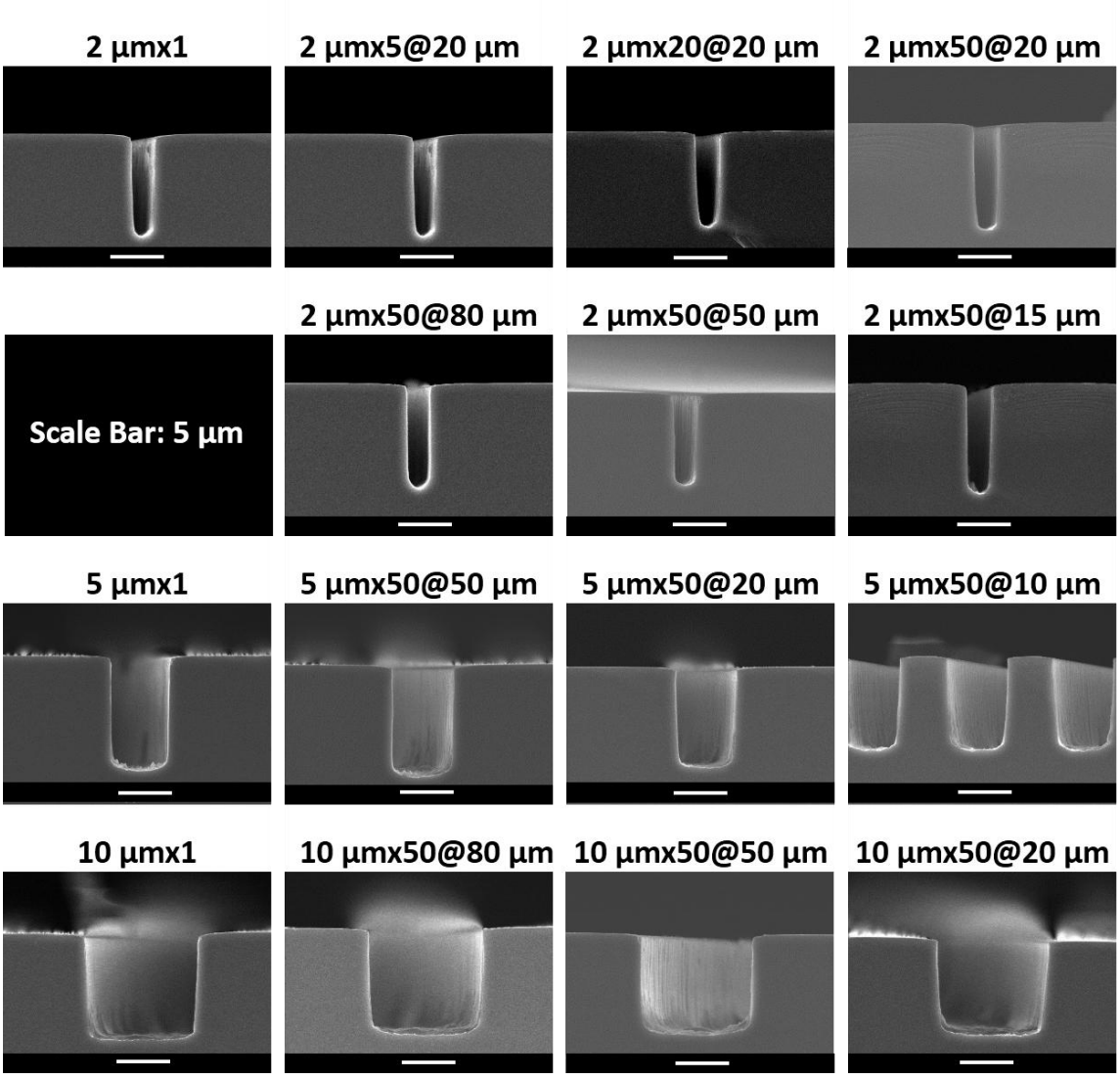

Figure 57 Cross-sectional SEM images of the etching profile on N-Si. The name of blocks are labeled on top of each corresponding figure. All the scale bars have a length of 5 µm.

Table 6 Geometric data of patterns before MaCE and trenches after MaCE on U-Si

Designed Value (μm)			Measured Value (μm)						
w_0	n	s	w_0	std(w_0)	w_t	std(w_t)	d	std(s)	Δw
2	1	0	2.36	0.23	3.1	0.2	6.79	0.2	0.74
2	5	20	2.3	0.01	3.43	0.1	5.64	0.46	1.13
2	20	20	2.19	0.04	3.49	0.25	6.48	0.73	1.3
2	50	20	2.21	0.05	3.58	0.11	6.55	0.23	1.37
2	50	15	2.61	0.03	4.39	0.12	8.68	0.29	1.78
2	50	50	2.67	0.03	3.86	0.27	6.84	1.04	1.19
2	50	80	2.66	0.02	3.59	0.18	6.42	1.61	0.93
5	1	0	5.78	0.02	7.02	0.2	8.45	0.2	1.24
5	50	10	5.56	0.11	7.89	0.3	7.53	0.46	2.33
5	50	20	5.55	0.12	7.48	0.21	7.45	0.28	1.93
5	50	50	5.6	0.15	7.18	0.15	7.73	0.42	1.58
10	1	0	10.45	0.06	12.5	0.2	8.73	0.2	2.05
10	50	20	10.59	0.02	12.76	0.22	7.91	0.69	2.17
10	50	50	10.43	0.17	12.71	0.21	7.91	0.77	2.28
10	50	80	10.52	0.07	12.69	0.27	8.76	0.49	2.17

Table 7 Geometric data of patterns before MaCE and trenches after MaCE on P-Si

Designed Value (μm)			Measured Value (μm)						
w_0	n	s	w_0	std(w_0)	w_t	std(w_t)	d	std(s)	Δw
2	1	0	2.98	0.01	3.16	0.2	5.24	0.2	0.18
2	5	20	2.66	0.01	3.11	0.05	5.34	0.22	0.45
2	20	20	2.58	0.01	3.77	0.15	5.65	0.13	1.19
2	50	20	2.58	0.01	4.22	0.29	5.47	0.28	1.64
2	50	15	2.86	0.01	4.89	0.16	7.11	0.21	2.03
2	50	50	2.87	0.05	3.91	0.07	5.71	0.95	1.04
2	50	80	2.9	0.06	3.61	0.26	5.93	0.72	0.71
5	1	0	5.33	0.02	5.97	0.2	5.22	0.2	0.64
5	50	10	5.3	0.09	8.13	0.45	6.13	0.14	2.83
5	50	20	5.26	0.14	8.02	0.15	6.74	0.5	2.76
5	50	50	5.06	0.17	6.92	0.31	7.2	0.31	1.86
10	1	0	10.21	0.01	11	0.2	6.43	0.2	0.79
10	50	20	10.3	0.11	15.24	0.4	6.18	0.58	4.94
10	50	50	10.21	0.11	13.73	0.49	6.41	0.21	3.52
10	50	80	10.28	0.06	12.73	0.31	6.65	0.16	2.45

Table 8 Geometric data of patterns before MaCE and trenches after MaCE on N-Si

Designed Value (μm)			Measured Value (μm)						
w_0	n	s	w_0	std(w_0)	w_t	std(w_t)	d	std(s)	Δw
2	1	0	2.73	0.02	3.33	0.2	9.64	0.2	0.6
2	5	20	1.98	0.02	2.48	0.12	8.95	0.23	0.5
2	20	20	2.04	0.14	2.7	0.18	9.91	0.5	0.66
2	50	20	2.05	0.17	2.73	0.12	9.52	0.53	0.68
2	50	15	2.01	0.11	2.48	0.13	9.67	0.57	0.47
2	50	50	1.86	0.09	2.52	0.21	8.72	0.96	0.66
2	50	80	2.01	0.13	2.56	0.08	9.39	0.77	0.55
5	1	0	5.33	0.02	5.93	0.2	5.22	0.2	0.6
5	50	10	5.15	0.16	5.93	0.2	8.97	0.1	0.78
5	50	20	5.13	0.1	5.98	0.14	9.42	0.12	0.85
5	50	50	5.13	0.09	6.06	0.13	10.7	0.59	0.93
10	1	0	10.21	0.01	11	0.2	6.43	0.2	0.79
10	50	20	10.19	0.03	11.05	0.3	9.05	0.17	0.86
10	50	50	10.22	0.18	11.08	0.15	9.67	0.13	0.86
10	50	80	10.19	0.03	11	0.12	9.76	0.42	0.81

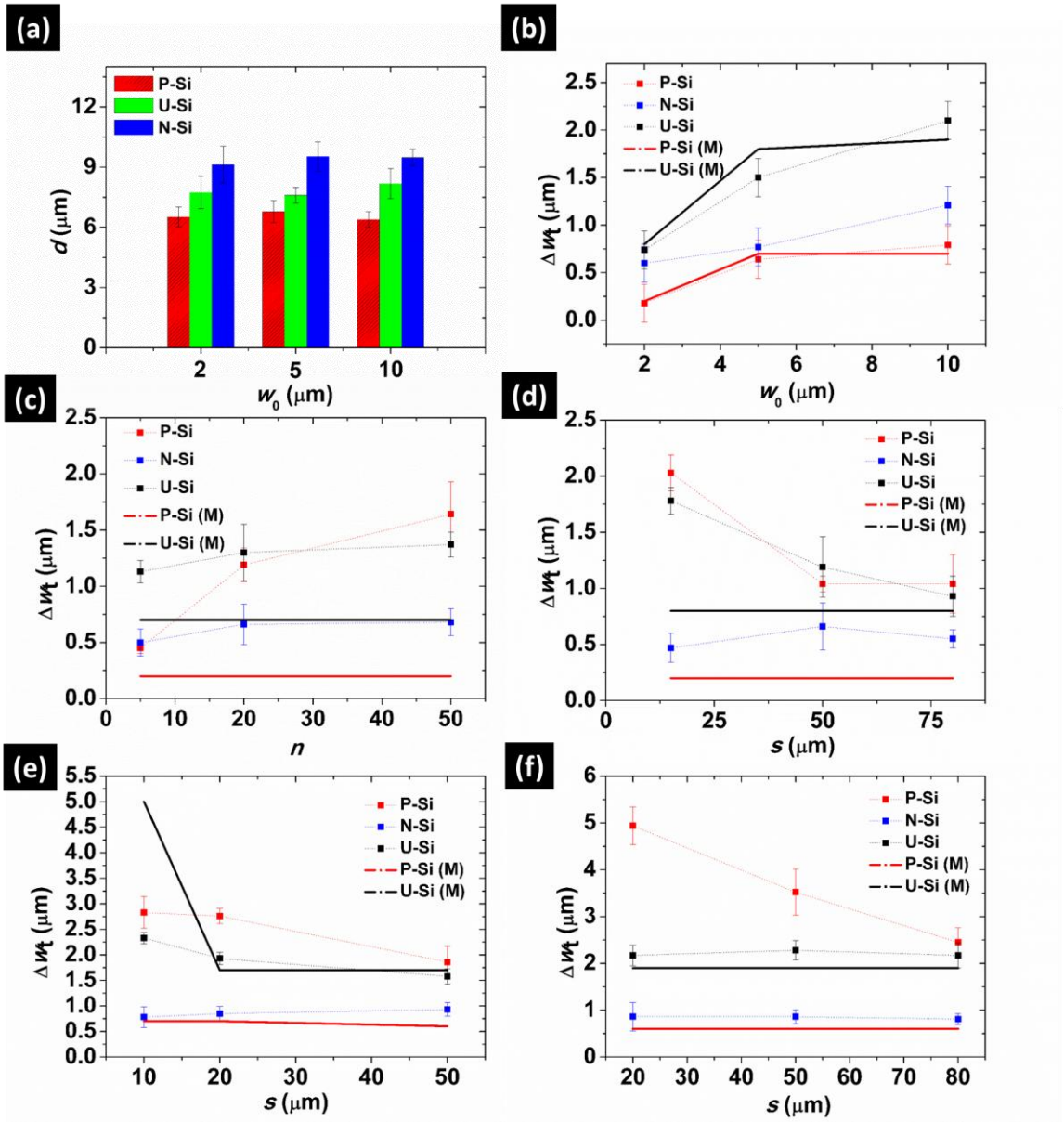

Figure 58 (a) Plot of the average etching depth (d) versus original width of the line patterns (w_0); (b) plot of the top width variation (Δw_t) versus w_0 of the single-line patterns; (c) plot of the top width variation (Δw_t) versus number of line patterns (n) with w_0 of 2 μm and spacing distance (s) of 20 μm; (d) plot of the top width variation (Δw_t) versus s with w_0 of 2 μm and n of 50; (e) plot of the top width variation (Δw_t) versus s with w_0 of 5 μm and n of 50; (f) plot of the top width variation (Δw_t) versus s with w_0 of 10 μm and n of 50. All the w_0 here refer to the designed value. The solid lines in (b)-(f) represent the Δw_t calculated from the diffusion model (labeled as P(M) and U(M) for P-Si and U-Si in the legend of each figure).

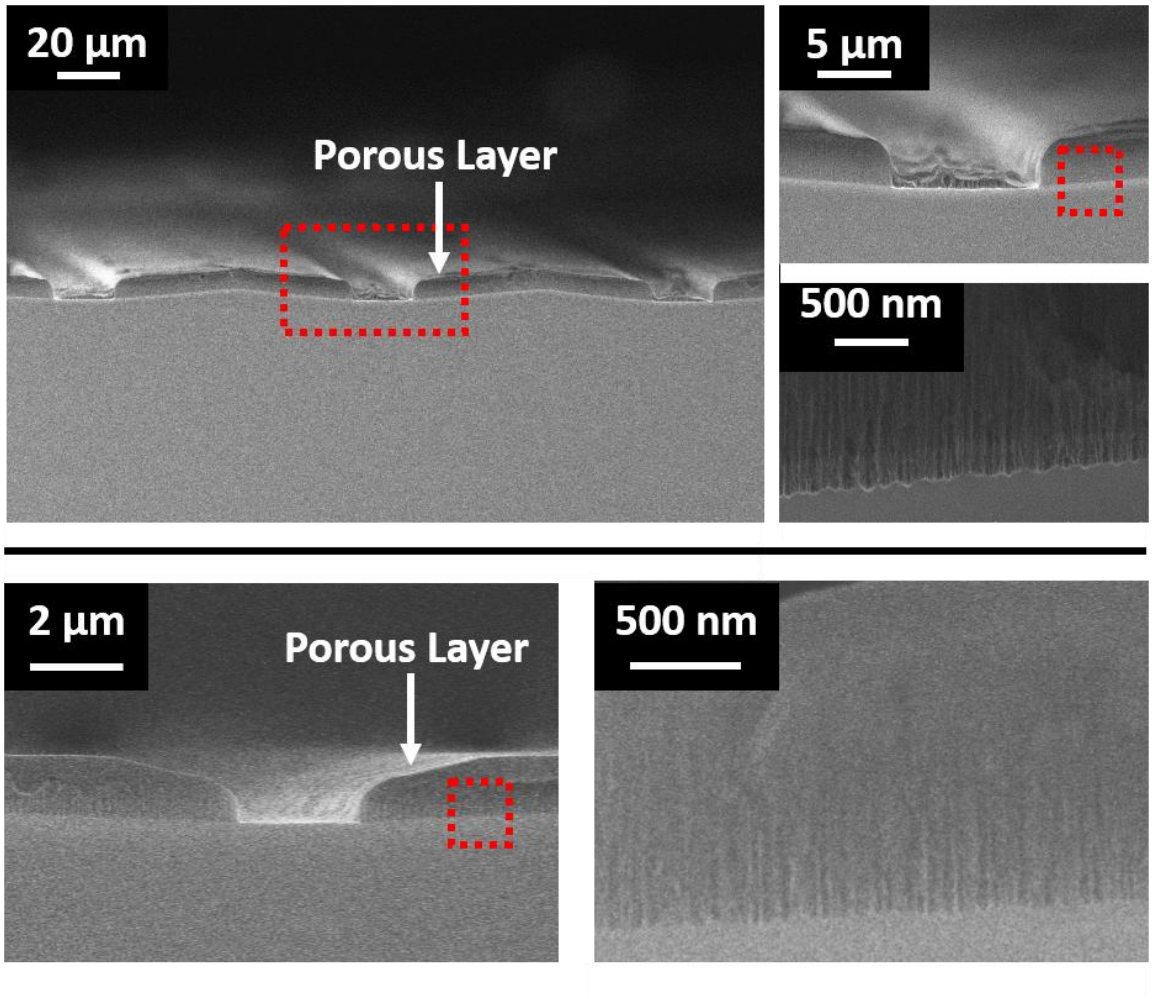

Figure 59 (Top) Cross-sectional SEM images of the etching profile in 10 µm×50@50 µm block on N(+)-Si with magnified image detailing the red circle; (Bottom) cross-sectional SEM images of the etching profile in 2 µm×50@50 µm block on P(+)-Si with magnified image detailing the red circle.

Several trends can be derived from **Figure 58**: (a) for d, it follows the order of d(P-Si)< d(U-Si)< d(N-Si), independent of w_0. Because d also shows little dependence on n and s, the d values are averaged from all the blocks that have the same w_0 (**Figure 58** (a)); (b) for Δw_t in the blocks which contain only one line (i.e. n=1), it follows the order of Δw_t(P-Si)< Δw_t (N-Si)< Δw_t (U-Si). Δw_t increases with w_0 on all the three substrates (**Figure 58** (b)); (c) for Δw_t in MaCE of the blocks which contain multiple lines (i.e. n>1) with w_0 of 2 µm and s of 20 µm, Δw_t sharply increases with n on P-Si, while showing little dependence on

n on N-Si (**Figure 58** (c)); (d) for Δw_t in MaCE of the blocks which contain 50 lines with w_0 of 2 μm, Δw_t sharply decreases with the increasing *s* on P-Si and U-Si (**Figure 58** (d); (e) as shown in **Figure 58** (e) and **Figure 58** (f)), if the w_0 increases to 5 μm and 10 μm while keeping *n*=50, the absolute value of Δw_t also increases accordingly on P-Si and U-Si, with keeping the same decreasing trend against *s*. However, with the same *s*, Δw_t(P-Si)> Δw_t(U-Si). For N-Si, Δw_t remains much lower than U-Si and P-Si through **Figure 58** (c) to (d), and showing little dependence on *n*, *s* and w_0.

To understand these trends, it is necessary to review the chemistry of MaCE. In MaCE, the chemical reactions can described by Equation 4 and 5. From these equations, HF and h^+ can be identified as the chemical species that directly induce the etching. Thus, the 3D profile is related to the distribution of HF and h^+ in the 3D space. In this regard, an orthogonal Cartesian CS is established where the origin is set at the geometric center of a line, and the *y* and *z* axis are set along the line and perpendicular to the Si surface, respectively (**Figure 62** (a)). The etching rate at position (*x*, *y*, *z*) and time *t* can be expressed as a vector $\vec{r}$:

$$\vec{r}(x,y,z,t) = C \cdot c_{\mathrm{HF}}(x,y,z,t)^a \cdot c_{\mathrm{h^+}}(x,y,z,t)^b \tag{35}$$

Where $c_{\mathrm{HF}}(x,y,z,t)$ and $c_{\mathrm{h^+}}(x,y,z,t)$ are the concentration of HF and h^+ at position (*x*, *y*, *z*) and time *t*, respectively; while *C*, *a* and *b* are constants to be determined. The vector $\overrightarrow{r_{h+}}$ is the unit vector that points to the direction of the h^+ movement. We further set the start time of MaCE as *t*=0. At *t*=0, $\left|\vec{r}(x,y,z,0)\right| = 0$. Since Δw_t is larger than 0 in all the etching results, the trenches width after etching is always larger than w_0. The increase in *w* during MaCE indicates that the Si both beneath the Au catalysts and on the sidewall are etched. We refer to these two etching processes as the vertical etching and sidewall

etching. Conceivably, d and Δw_t can be related to the reaction rate of vertical etching and sidewall etching, i.e. the components of $\vec{r}$ along the z- and x-axis:

$$\begin{aligned}\left|\vec{r}_z\left(x_b,y_b,z_b,t\right)\right| &= \frac{\Delta V_z}{\Delta t} = \frac{(w\cdot l)\cdot\Delta d}{\Delta t} \\ &= C\cdot c_{HF}\left(x_b,y_b,z_b,t\right)^a\cdot c_{h^+}\left(x_b,y_b,z_b,t\right)^b\end{aligned} \tag{36}$$

$$\begin{aligned}\left|\vec{r}_x\left(x_s,y_s,z_s,t\right)\right| &= \frac{\Delta V_x}{\Delta t} = \frac{\left(l\cdot d\right)\cdot\Delta w_t}{\Delta t} = \frac{\Delta w_t}{\Delta t} \\ &= C\cdot c_{HF}\left(x_s,y_s,z_s,t\right)^a\cdot c_{h^+}\left(x_s,y_s,z_s,t\right)^b\end{aligned} \tag{37}$$

Where w, l and d are the dimension along x, y and z axis, V is volume of Si being etched, while Δd, Δw and ΔV are the infinitesimal increase in d, w and V within the infinitesimal time period Δt. $\left(x_b,y_b,z_b\right)$ and $\left(x_s,y_s,z_s\right)$ refer to the arbitrary positions at the bottom of the etching profiles (i.e. the Au-Si interface) and on the sidewall, respectively. It has been demonstrated that under current UMaCE condition, $\left|\vec{r}_z\right|$ is constant within 10 min (**Chapter 3**). Then we can assume that the vertical etching is under a steady state: $c_{HF}\left(x,y,z,t\right)$ and $c_{h^+}\left(x,y,z,t\right)$ in Eq. 37 are constant over time. For HF, since the initial concentration of HF equals to that in bulk solution, then:

$$c_{HF}\left(x,y,z,t\right) = c_{HF}\left(x,y,z,0\right) = 1.5\ \text{mol/L} \tag{38}$$

Eq. 38 means that during the MaCE within 10 min, although the Au catalyst keeps moving into Si substrate, the etchant solution can quickly flow into the etched space above Au and a steady state is established within every infinitesimal time period, so that the local concentration of HF at the Au –Si interface maintains the constant value. It is conceivable that the $c_{HF}(x,y,z,t)$ in Eq. 37 also equals to $c_{HF}(x,y,z,0)$, since the sidewall and Au-Si are subjected to the same etchant solution.

To further confirm the steady state of MaCE within 10 min, a study on the evolution of etching depth (d) over etching time (t) in MaCE of 2 μm×1 pattern on N-Si is conducted.

The *d-t* curve is shown in **Figure 60**. The solution is kept at static state without agitation. Within the etching time of 10 min, the etching keeps constant. The result is consistent with our previous results of MaCE on circular patterns with diameter of 30 μm. At the point of *t*=15 min, the etching rate starts to drop. At the point of *t*=40 min, the etching rate significantly dropped. It should be noted that the consumption of the etchant solution is negligible over the MaCE of 40 min. To confirm this point, we immersed a 2 μm×1 sample in the etchant solution after MaCE of 40 min, the etching rate is identical to that in MaCE with freshly prepared etching solution. In contrast, in our previous etching experiment of 2 μm×1 pattern (**Chapter 3**), an etching depth of 32 μm is reached after MaCE of 40 min with stirring of the etching solution, much higher than the depth here in the static etching solution. These facts indicate that within 10 min, MaCE is reaction-controlled, while the process becomes diffusion-controlled as the etching proceeds. One of the probable factors that cause the transition is that as the etching proceeds, the aspect ratio of the etched trench is increasing and the difficulty of HF and H_2O_2 molecules diffusion to the etching front, i.e. the Au-Si, is also increasing. By agitation of the solution, the diffusion of HF and H_2O_2 can be promoted and a higher etching rate over long-time etching can be achieved. The reaction-controlled mechanism validates the assumption that HF concentration inside the etching profile keeps constant within 10 min (Eq. 38).

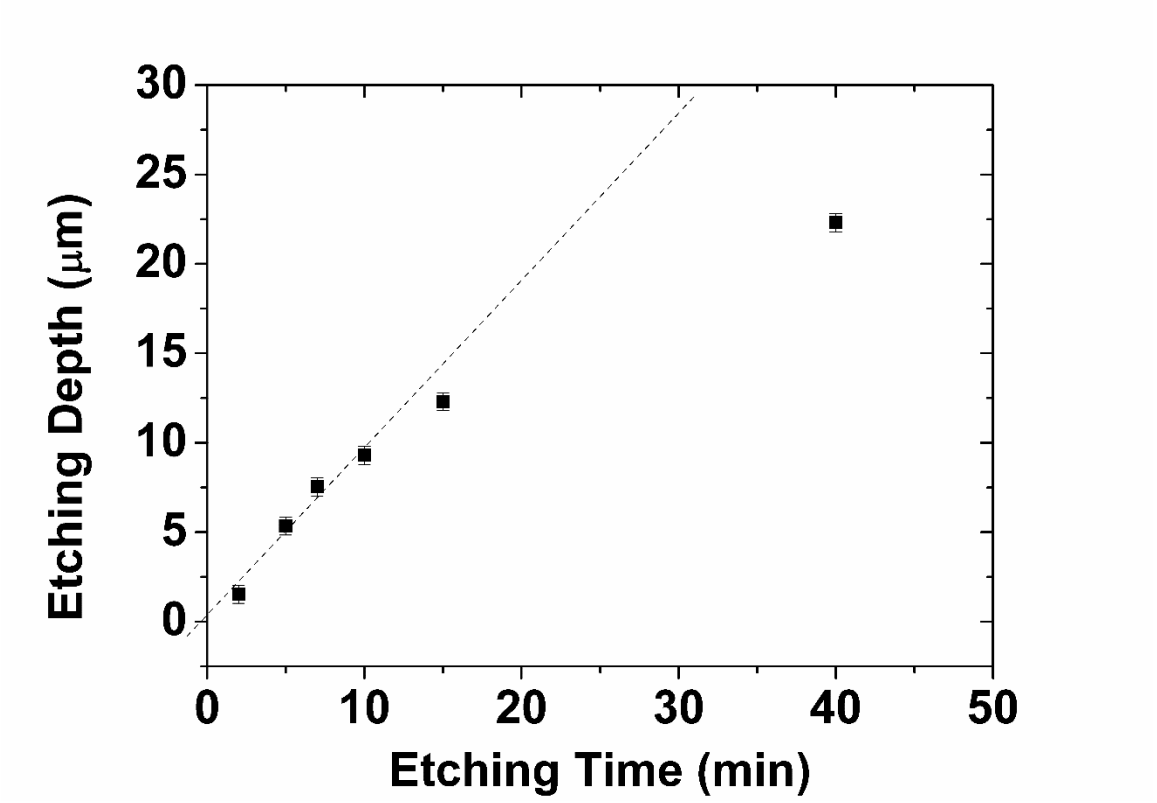

Figure 60 The evolution of etching depth in MaCE of 2 μm×1 pattern on N-Si.

If we assume that the etching is homogeneous along the *y*-axis, we can focus our study of etching rate on a 2D plane that is perpendicular to the *y*-axis (i.e. the *x*-*z* plane). Then Eq. 36 and 37 can be simplified to:

$$\begin{aligned}\left|\overline{r}_z\left(x_\mathrm{b},z_\mathrm{b},t\right)\right| &= \frac{w_0\cdot\Delta d}{\Delta t}=\frac{w_0\cdot d}{t}\\ &= C\cdot c_{\mathrm{HF}}\left(x_\mathrm{b},z_\mathrm{b},t\right)^a\cdot c_{h+}\left(x_\mathrm{b},z_\mathrm{b},t\right)^b\\ &= C_1\cdot c_{h+}\left(x_\mathrm{b},z_\mathrm{b},t\right)^b\end{aligned} \tag{39}$$

$$\begin{aligned}\left|\overline{r}_x\left(x_\mathrm{s},z_\mathrm{s},t\right)\right| &= \frac{d\cdot\Delta\left(\Delta w_\mathrm{t}\right)\Delta w_\mathrm{t}}{\Delta t}=\frac{d\cdot\Delta\left(w_\mathrm{t}-w_0\right)\Delta w_\mathrm{t}}{\Delta t}=\frac{d\cdot\Delta w_\mathrm{t}}{\Delta t}\\ &= C\cdot c_{\mathrm{HF}}\left(x_\mathrm{s},z_\mathrm{s},t\right)^a\cdot c_{h+}\left(x_\mathrm{s},z_\mathrm{s},t\right)^b\\ &= C_1\cdot c_{h+}\left(x_\mathrm{s},z_\mathrm{s},t\right)^b\end{aligned} \tag{40}$$

Where C_1 is a constant. Eq. 39 and 40 show that under the UMaCE condition where the vertical etching is in steady state, the 3D profile is only related to the $c_{h+}(x,z,t)$, which is determined by CT during MaCE.

It should be noted that in the HF-H_2O_2 etching solution, HF will undergo the following reaction:

$$HF \xrightleftharpoons{K_1} H^+ + F^-,\ K_1 = \frac{[H^+][F^-]}{[HF]} \tag{41}$$

$$HF + F^- \xrightleftharpoons{K_2} HF_2^-,\ K_2 = \frac{[HF_2^-]}{[HF][F^-]} \tag{42}$$

where K_1 and K_2 are the equilibrium constant of Eq. 41 and 42, respectively. [H^+], [F^-], [HF] and [HF_2^-] refer to the activity of the corresponding species. Thus the fluoride species that are actually involved in the dissolution of oxidized Si (Eq. 5) may contain HF, F^- and HF^{2-}. To qualitatively evaluate the effect of fluoride species concentration distribution, we did the MaCE on N-Si in etchant solution with H_2SO_4, $NH_3 \bullet H_2O$ and NH_4F as additives, respectively. We adopted the value of 1.3×10^{-3} and 0.104 for K_1 and K_2, respectively, at the ionic strength of 1 M.[78]. Here we neglect the change of these value over the ionic strength in the solution, and substitute all the activity terms with concentration in the expression of K_1 and K_2. Then the two values can be used to estimate the concentration of each fluoride species. It has been reported that in HF solution with concentration over 1 M, some polymer of HF ($(HF)_nF^-$, n=2-6) can be formed. Here the formation of HF is not taken into account to simplify the calculation of fluoride species concentration. Due to the low acidity of H_2O_2, the contribution of H^+ from H_2O_2 is also neglected. The calculated concentration of etching solution is listed in Table 9. In the etchant solution used in the aforementioned MaCE experiments without any additives, the majority fluoride species is HF. With addition of H_2SO_4, the c(HF) slightly increase, while c(HF_2^-) and c(F^-) sharply decrease. The etching depth slight decreases with the addition of

H_2SO_4. However, the etching depth has a significant increase with the addition of $NH_3•H_2O$ or NH_4F, where $c(H^+)$ decreases but $c(HF_2^-)$ and $c(F^-)$ increase. The results may be explained by the fact that HF_2^- dissolves the oxidized Si much faster than HF.[79] Considering the fact that H^+ is also involved in the reduction of H_2O_2 (Eq. 4), the relation between $c(H^+)$ and etching depth indicates that the dissolution of oxidized Si (Eq.5) may be the rate limiting step in MaCE. In order to simplify the following discussion, however, the term HF is used to represent all the fluoride species. This generalization of terminology will not impair the validity of the conclusion derived from the data in **Figure 58**, because all the etching experiments are conducted in the etchant solution with the same composition.

Table 9 Concentration of fluoride species and corresponding etching depth

Test#	Additive	Conc. (M)[1]	$c(H^+)$/M	c(HF)/M	$c(HF_2^-)$/ M	$c(F^-)$/M	Depth(μm) [2]	Std.Dev. [3]
1	None	0	0.048	1.506	0.006	0.041	8	0.13
2	H_2SO_4	0.064	0.09	1.531	0.004	0.022	7.39	0.45
3	H_2SO_4	0.319	0.326	1.552	0.001	0.006	7.15	0.23
4	H_2SO_4	0.638	0.641	1.556	0.001	0.003	7.5	0.19
5	NH_3 H_2O	0.232	0.008	1.292	0.028	0.211	10.01	0.29
6	NH_3 H_2O	0.463	0.003	1.048	0.046	0.421	11.92	0.49
7	NH_3 H_2O	1.39	1.40E-04	0.149	0.021	1.369	12.52	0.57
8	NH_4F	0.134	0.015	1.524	0.02	0.129	9.01	0.34
9	NH_4F	0.445	0.001	1.498	0.061	0.385	10.84	0.22
10	NH_4F	0.89	0.002	1.441	0.116	0.777	12.95	0.34

Note:

1. The concentration of additive molecules. For H_2SO_4 as the additive, the pK_{a2} for the second proton dissociation is 1.99, ~10 times higher than pK_a of HF, thus it is assumed that the H_2SO_4 molecules completely dissociate and provide two protons per molecules; for $NH_3•H_2O$ as the additive, the pK_b of $NH_3•H_2O$ is 4.75, it is assumed that all the $NH_3•H_2O$ molecules is bonded with protons in the solution; for NH4F as the additives, it is assumed that all NH4F dissociate into NH_4^+ and F^- ions. The pK_a and pK_b values mentioned above can be found in Ref. 37;
2. Depth of etching profile averaged from 5 independent tests on N-Si under the same condition as those used in Fig. 2-4;
3. Standard deviation of etching depth in μm.

CT in vertical etching and sidewall etching are illustrated in **Figure 62** (a) and labeled as CT1 and CT2, respectively. To study the $c_{h+}(x,z,t)$ in CT1 and CT2, the source of h^+ needs to be clarified first. Although it has been reported that the bare Si surface without the coverage of metal could also be etched in HF-H_2O_2, its etching rate is on the order of 0.1-1.0 nm/min[23], which is negligibly small compared to that of MaCE. Thus, h^+ in CT1 is primarily originated from the catalytic reduction of H_2O_2 on Au surface (Eq.1), It follows that in CT1 h^+ is transported from Au to Si, rather than from etchant solution to Si.

It has long been known that CT through a metal-semiconductor interface can be described by the Schottky junction model.[80] As shown in **Figure 61**, the h^+ transport process from Au to Si can be schematically illustrated using a band diagram of Au-Si Schottky junction. In Au, at thermal equilibrium the majority of electrons stay in the bands below Fermi level (E_F). In Si, the valence bands are filled with electrons while the conduction bands are empty. A band gap lies between the valence bands and the conduction bands. In undoped Si (U-Si), E_F lies in the middle of band gap. In N-Si which is doped with phosphorous (P), extra electrons from P fill in the bottom of conduction bands and the Fermi level is raised up versus the valence band top (E_V) and conduction band bottom (E_C). In P-Si which is doped with boron, extra h^+ fill in the top of conduction bands and the Fermi level (E_F) is lowered down versus the valence/conduction band edges (**Figure 61** (a)). When Au and Si are brought into contact, the E_F of Si aligns with that of Au. Charges will move across the Au-Si interface and a space charge region in Si is formed after equilibrium is reached. As a result, the E_C and E_V are bent downwards for N-Si, and upwards for P-Si. A built-in potential (V_{bi}) is established due to the band bending. Electrons transport from Au to Si is a thermionic process. For N-Si, the electron flux from Au to Si, can be expressed as

$$J_{\mathrm{Au}\rightarrow\mathrm{Si}} = C_1 \exp\left(-\frac{q\varphi_{\mathrm{bn}}}{kT}\right) \tag{43}$$

Where q, k, T, φ_{bn} are elementary charge, Schottky barrier height, Planck constant and temperature, respectively (**Figure 61** (b)). C_1 is a constant to be determined. Since the system is at thermal equilibrium, no net current exists across the Au-Si interface, thus

$$\left|J_{\mathrm{Si}\to\mathrm{Au}}\right| = \left|J_{\mathrm{Au}\to\mathrm{Si}}\right| = C_1 \exp\left(-\frac{q\varphi_{\mathrm{bn}}}{kT}\right) \tag{44}$$

When the N-Si is negatively biased towards Au with a bias of V, E_C and E_V on the Si side are raised up by a potential V, thus

$$J_{\mathrm{Au}\to\mathrm{Si}} = C_1 \exp\left(-\frac{q\varphi_{\mathrm{bn}}}{kT}\right) \tag{45}$$

$$J_{\mathrm{Si}\to\mathrm{Au}} = C_1 \exp\left(-\frac{q\left(\varphi_{\mathrm{bn}} - V\right)}{kT}\right) \tag{46}$$

Then the net electron flux is

$$J = J_{\mathrm{Si}\to\mathrm{Au}} - J_{\mathrm{Au}\to\mathrm{Si}} = C_1 \exp\left(-\frac{q\varphi_{\mathrm{bn}}}{kT}\right)\left(\exp\left(\frac{qV}{kT}\right) - 1\right) \tag{47}$$

Eq.47 indicates that a negative bias on N-Si increases the net electron flux from Si to Au, equivalent to an increase in h^+ flux from Au to Si.

Similarly, for P-Si, the net h^+ flux from Au to Si under the negative bias is

$$J = J_{\mathrm{Si}\to\mathrm{Au}} - J_{\mathrm{Au}\to\mathrm{Si}} = C_1 \exp\left(-\frac{q\varphi_{\mathrm{bn}}}{kT}\right)\left(1 - \exp\left(\frac{qV}{kT}\right)\right) \tag{48}$$

In contrast to the case of N-Si, as the bias strength increases, the h^+ flux from Au to Si is depressed in P-Si.

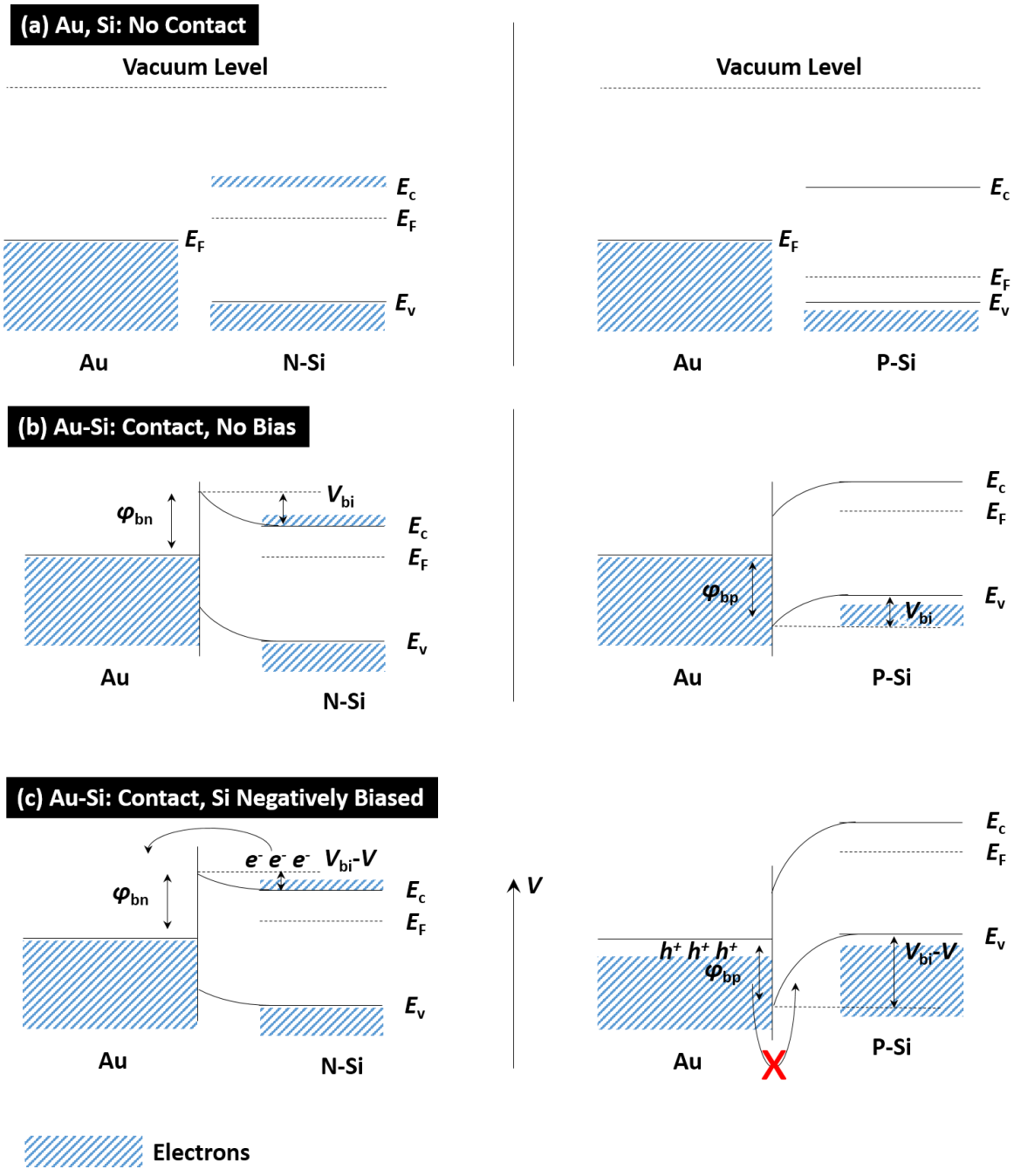

Figure 61 Band diagram of an Au-Si Schottky junction. (a) Band diagram of Au and N-Si (left)/P-Si (right) without contact; (b) band diagram of Au and N-Si (left)/P-Si (right) with contact under no electric bias; (c) band diagram of Au and N-Si (left)/P-Si (right) with contact while Si is negatively biased towards Au. E_F, E_C, E_V, V_{bi} and V refer to the energy of Fermi level, conduction

band bottom, valence band top, built-in potential and applied potential, respectively. The shadowed area shows the bands that are occupied by electrons.

In the context of vertical etching, metal and semiconductor correspond to Au and Si, respectively. Since h^+ are transported from Au to Si, Si can be regarded as negatively biased against Au (**Figure 62** (a)). The negative bias raises up the energy level of both the valence band and conduction band of the Si, regardless of its doping type. For N-Si, the negative bias favors the transport of h^+ from Au to Si (referred to as a "forward bias" for N-Si); for P-Si, however, the negative bias increases the difficulty in the h^+ transport (referred to as a "reverse bias" for P-Si). [80, 81] Then c_{h+} in Eq. 39 follows the order of: c_{h+}(P-Si)< c_{h+}(U-Si)< c_{h+}(N-Si). Accordingly, we have d(P-Si)< d(U-Si)< d(N-Si), which is consistent with the results in **Figure 58** (a).

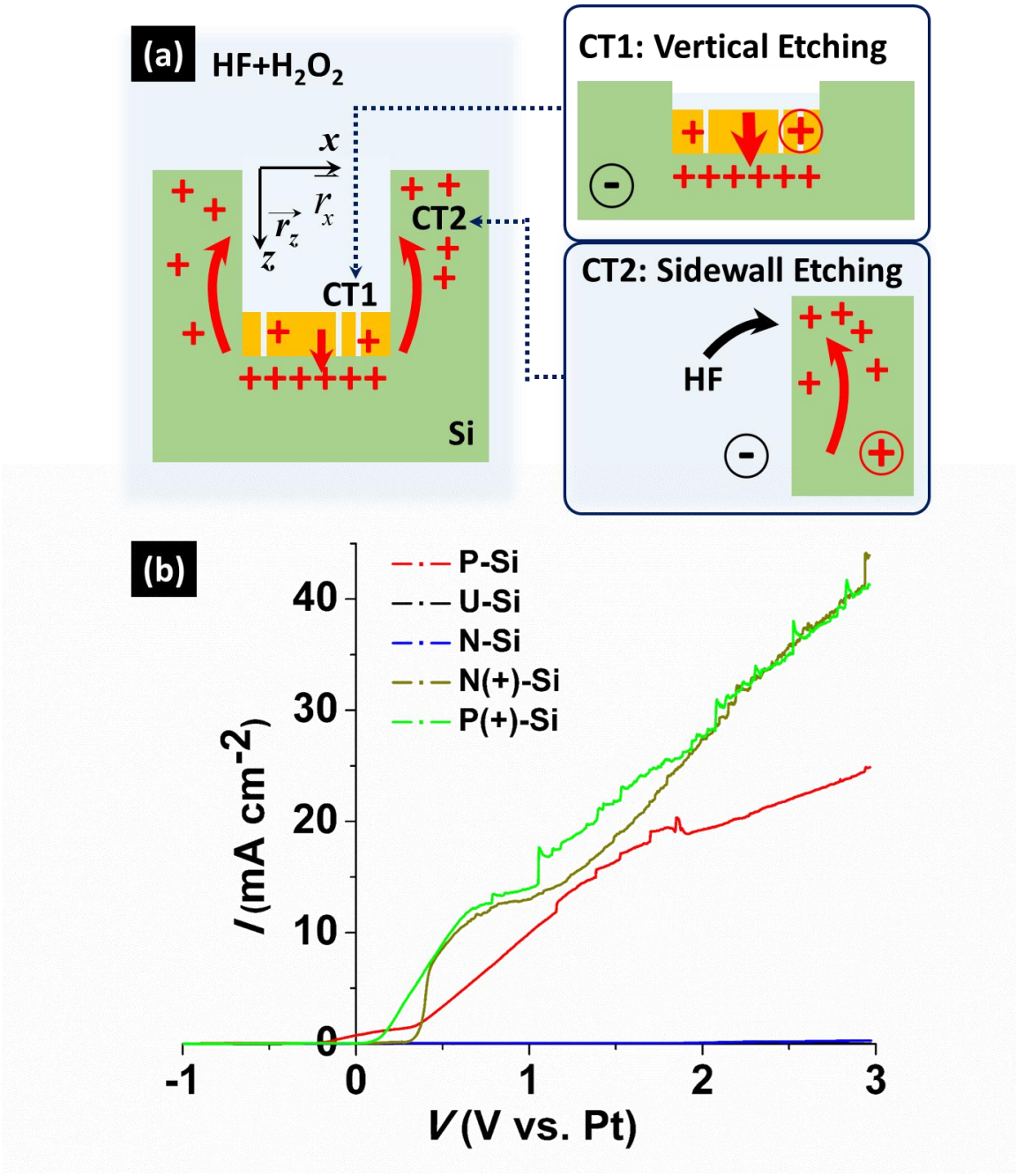

Figure 62 (a) Schematic charge transport process during MaCE. CT1: charge transport from Au to the Si beneath; CT2: charge transport from Si on the sidewall to the etchant solution; (b) current density-voltage curve of bare Si substrates as the working electrode in 1.5 mol/L HF aqueous solution.

Regarding CT2, etching on the sidewall have been attributed to the dissolution and redeposition process of metal catalyst in literature about nano-MaCE where silver (Ag) was used as the catalyst.[75, 82] It was assumed that Ag at the bottom of the etching profile could be partially dissolved by HF-H_2O_2 and redeposited on the sidewall. Once deposited by Ag, h^+ is transported from Ag to Si by a process similar to that in CT1. In the present work, if the sidewall etching is induced by the dissolution and redeposition of Au, CT2 should resemble CT1 and the variation of Δw_t should be the same as that of *d*. However, as can be clearly observed in **Figure 58** (b), Δw_t follows the order of Δw_t (P-Si) < Δw_t (N-Si) < Δw_t (U-Si); in **Figure 58** (c)-(f), Δw_t follows the order of Δw_t (N-Si) < Δw_t (U-Si) < Δw_t (P-Si). Both trends are in sharp contrast to that of *d*. Then the charge transport from Au to Si can be excluded in CT2. As mentioned before, under the UMaCE condition, low-ρ etchant is used and the h^+ generated from H_2O_2 on Au surface cannot be completed consumed by the vertical etching process. The excessive h^+ from Au have a chance to be transported to the sidewall and induce the sidewall etching. In this sense, contrary to the vertical etching, the sidewall etching is a pure electrochemical process as described in Eq. 5, where h^+ are transported from Si to the etchant solution. Under this condition, Si is positively biased against the etchant solution. The process resembles the well-known electrochemical etching of Si. The electrochemical etching could also be described by a Schottky junction model.[17, 21, 68] Here a positive bias is a forward bias for P-Si but a reverse bias for N-Si. Thus, in the sidewall etching the transport of h^+ is favored on P-Si but suppressed on N-Si. To further confirm this point, electrochemical etching experiments were conducted to mimic the sidewall etching process. Bare Si were connected to a potentiostat as the working electrode and immersed in a 1.5 mol/L HF solution. A linear-increasing voltage was applied to the bare Si and the corresponding current density value was recorded. As shown in **Figure 62** (b), for P-Si, when the voltage is scanned from -1.0 V (vs. Pt counter electrode) toward +4.0 V, current density increases sharply after the voltage passes -0.2 V. In contrast, for N-Si, no significant current density can be observed

within the scan range. Given the fact that the doping level of N-Si and P-Si are similar, the result supports the point that once a positive bias is applied, h^+ can be favorably transported from P-Si to HF solution, while h^+ transport from N-Si to HF solution is intrinsically suppressed. It is observed that the current density of U-Si is also low, which may be attributed to the low doping level of U-Si (**Table 5**). For P(+) and N(+)-Si, however, due to a high doping level, h^+ can easily tunnel through the Si-HF solution interface regardless of the dopant type, thus their current density increases faster than P-Si.[80] During MaCE of the heavily doped Si, the tunneling process not only induces sidewall etching, but also makes the Si between trenches highly porous on both substrates (**Figure 59**), which is consistent with results from previous results of electrochemical etching[83] and nano-MaCE [31, 32, 84] on heavily-doped Si.

Now that CT1 and CT2 have been discussed, we can further investigate the correlation between CT1 and CT2. As discussed above, h^+ in both CT1 and CT2 are originated from the reduction of H_2O_2 on Au surface. Under the steady state, c_{h+} in CT1 is constant over time, which means Au can be regarded as a source that constantly emits h^+ into Si while moving along the *z*-axis at constant velocity (*v*):

$$\begin{aligned} c_{h^+}(x,z,t) &= c_{h^+}(x,z,0) = \text{constant} \\ &= c_{h^+ECTH}(x,z,t) + c_{h^+EX}(x,z,t) \end{aligned} \tag{49}$$

where $c_{h+ETCH}(x,z,t)$ is the amount of h^+ that are consumed in the vertical etching, while $c_{h+EX}(x,z,t)$ is the amount of excessive h^+. Since the vertical etching rate is constant, then $c_{h+ETCH}(x,z,t)$ is constant, which makes $c_{h+EX}(x,z,t)$ also constant:

$$c_{h+EX}(x,z,t) = c_{h+EX} = \text{constant} \tag{50}$$

These excessive h^+ can be transported to the sidewall through diffusion or drift. Here the term "diffusion" refers to the movement of h+ driven by the gradient of c_{h+}, while "drift" refers to that driven by electric field. If we assume that the excessive h^+ is the only

source of h^+ in CT2 and transported to the sidewall only through diffusion, then we can establish a diffusion model to calculate c_{h+} in Eq. 8 by Fick's Second Law:

$$\frac{\partial c_{h+}(x,z,t)}{\partial t} = D\nabla^2 c_{h+}(x,z,t) \tag{51}$$

where D is the diffusion constant of h^+ in Si. Here D is set as constant over space and time. If we introduce a new variable $r=\sqrt{x^2+z^2}$, the boundary condition and initial condition can be written as:

$$\frac{\partial c_{h+}(r,t)}{\partial r}\Big|_{\sqrt{r}=vt} = c_{h+EX}(r,t)\delta(t) \tag{52}$$

$$c_{h+}(r,t)\big|_{r\to\infty} = 0 \tag{53}$$

$$c_{h+}(x,z,0) = 0 \tag{54}$$

Assuming the total c_{h+} is the sum of the contribution of each Au lines in a w_0×n@s block, we have[85]:

$$c_{h+}(x,z,t) = \sum_{n_i=1}^{n}\left(\int_{-w_0/2}^{w_0/2} dw \int_0^t \frac{c_{h+EX}}{4\pi D(t-\tau)} \exp\left(-\frac{(x-w-n_i\times s)^2+(z-v\tau)^2}{4D(t-\tau)}\right) d\tau\right) \tag{55}$$

It has been reported that in the electrochemical etching process, Si is completely removed when c_{h+} exceeds a certain critical value c_{h+crit}, while porous Si is formed when c_{h+} is below c_{h+crit}.[21] Then using the diffusion model, Δw_t can be calculated by Eq. 55 if we assume that Δw_t is only related to the c_{h+} on the Si top surface at z=0 (referred to as $c_{h+}(x,0,10\text{ min})$). The $c_{h+}(x,0,10\text{ min})$ equals to c_{h+crit} at the position of (Δw_t, 0). **Figure 63** (a) shows the calculated $c_{h+}(x,0,10\text{ min})$ in MaCE of 2 μm×1, 5 μm×5, 10 μm×1 blocks on U-Si along x-axis where the origin is set at the geometric center of Au lines. The c_{h+} is calculated by fitting Eq. 55 with Δw_t in **Figure 58** (b) and expressed in arbitrary unit (a.u.). The fitting gives nominal value of c_{h+crit}=0.164 and D=0.008 μm^2/s. The boundaries between the edge of Au and Si are indicated as the vertical dot lines at $x=\pm w_0/2$. For

example, the boundaries of 2 μm ×1 block locate at $x = \pm 1$ μm. As the w_0 increases, c_{h+} within the boundary increases and the curve extends farther out of the boundary, which is consistent with results in **Figure 58** (b). To calculate Δw_t, the c_{h+} curve outside the boundaries is detailed in **Figure 63** (b), where the x-axis is set to start at the boundary of Au in each curve of **Figure 63** (a) and extend out of the boundary. Then the curves in **Figure 63** (b) represent the c_{h+} in the sidewall, which is involved in CT2. Given c_{h+crit}=0.164, Δw_t of each curve in **Figure 58** can be identified by locating the intersection point of the curves with the c_{h+}=0.164 line (horizontal black dash line). We name these Δw_t value as the modeled value. The modeled Δw_t for P-Si and U-Si are plotted in **Figure 58** (b) as solid lines and labeled as P(M) and U(M), which shows good consistence with the experimentally measured value. The same c_{h+crit} and D value are used to obtain the modeled Δw_t in MaCE of other blocks, which are plotted in **Figure 58** (c) to (e). For U-Si, the modeled Δw_t are close to the measured value. For P-Si, c_{h+crit} and D are fit to be 0.340 and 0.003 μm^2/s from **Figure 58** (b). However, although the modeled Δw_t well match the measured value **Figure 58** (b), they are far below the measured value in **Figure 58** (c) to (e). The comparison between the modeled and measured Δw_t in **Figure 58** (b) to (e) indicates that for U-Si, h^+ transported from Au to the sidewall is likely to be a diffusion process mainly from the excessive h^+ around Au. For P-Si, in single line etching, h^+ is also transported from Au through diffusion; in multiple line etching, however, the actual h^+ concentration in the sidewall region is much higher than the amount that transported through diffusion. The sharp increase of Δw_t with n on P-Si has not been reported before. Considering the fact that a large amount of h^+ is transported from Au to Si, a strong electric field may be established around every Au lines. Based on the depth of etching as ~6 μm on P-Si, the amount of Si etched per unit area r_z in the etching of 10 min is:

$$r_z = \frac{\rho V}{M_{Si} t} = \frac{6\mu m \times 1\mu m \times 1\mu m \times 2.329 g/cm^3}{28.09 g/mol \times 600 s} = 8.3 \times 10^{-16} mol/s \quad (56)$$

Where ρ, V, M_{Si} are the density, etched volume and molecular weight of Si.[77] Assuming etching of each Si atom consumes 4 h^+, then the current density of h^+ is estimated to be:

$$I = \frac{4 \times r_z \times N_A \times e^-}{S} = \frac{4 \times 8.3 \times 10^{-16} mol/s \times 6.02 \times 10^{23}/mol \times 1.6 \times 10^{-19} C}{1\ \mu m^2} = 32.0 mA/cm^2 \quad (57)$$

According to **Figure 62** (b), the current correspond to a bias over 3 V. In MaCE of multiple Au lines, the increase of n may significantly increase the synergistic electric field from all Au lines, which resulted in an increased amount of intrinsic h^+ that are involved in CT2 and an accelerated movement of h^+ toward sidewall. Besides, in P-Si, a considerable amount of h^+ exist at the dopant atoms in Si as intrinsic h^+. These h^+ also have a chance to be transported to the sidewall under the electric field. Therefore, although in the single Au line etching, Δw_t (U-Si) is larger than Δw_t (P-Si) due to a higher amount of excessive h^+ in CT1 (**Figure 58** (b)), Δw_t (P-Si) quickly exceeds Δw_t (U-Si) as n increases (**Figure 58** (c)-(e)). However, further study is needed to figure out the spatial distribution of the electric field and its interaction with h^+ inside Si.

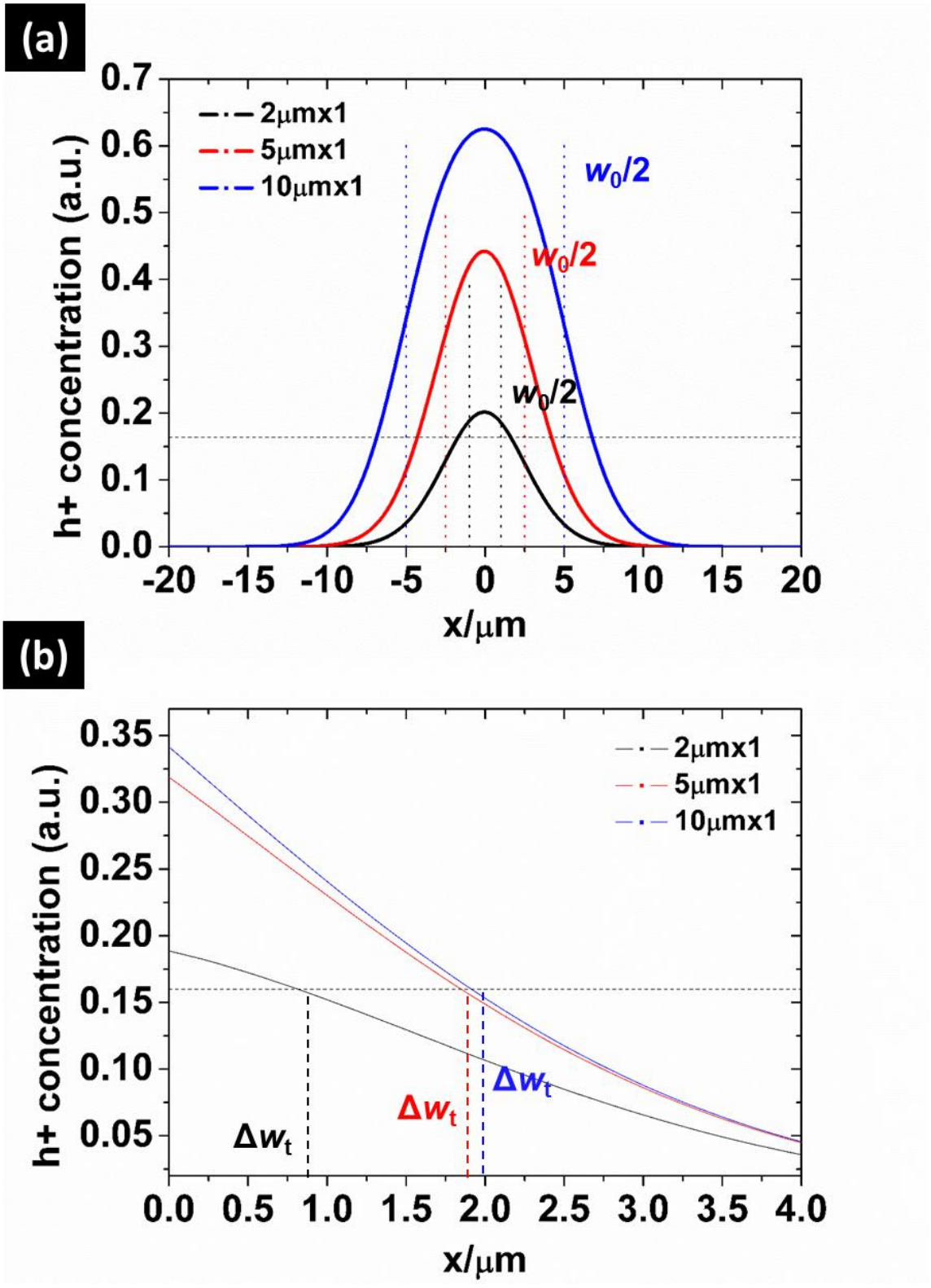

Figure 63 Calculated c_{h^+}(x,0,10 min) in MaCE of 2 μm×1, 5 μm×1 and 10 μm×1 blocks using diffusion model. (a) and (b) show the overall curve and magnified curve of the near-Au edge part,

respectively. In (b), the origin of x-axis is set at the boundary between the edge of Au and Si indicated by the vertical lines in (a). The horizontal line in both (a) and (b) is the line of $c_{h+}=c_{h+crit}=0.1645$.

In order to investigate the MaCE results on Si with other crystalline orientation, we conducted MaCE on the P-Si with (111)-orientation under the same condition as that on P-Si with (100)-orientation. As shown in **Figure 64**, after MaCE vertical trenches were formed on the (111)-Si substrates, in consistence with previous results.[21] Similar to the results from (100)-Si, here the Δw_t also shows an increase when n increases. The increase of Δw_t support the aforementioned mechanism that the charge transport during MaCE can be described by the Schottky models, where the doping of the Si plays the major role. The etching depth is much lower than that on (100)-Si. The slower etching rate on (111)-Si may be explained by the fact that the back bonds density is higher along the <111> orientation than that along <100> orientation.

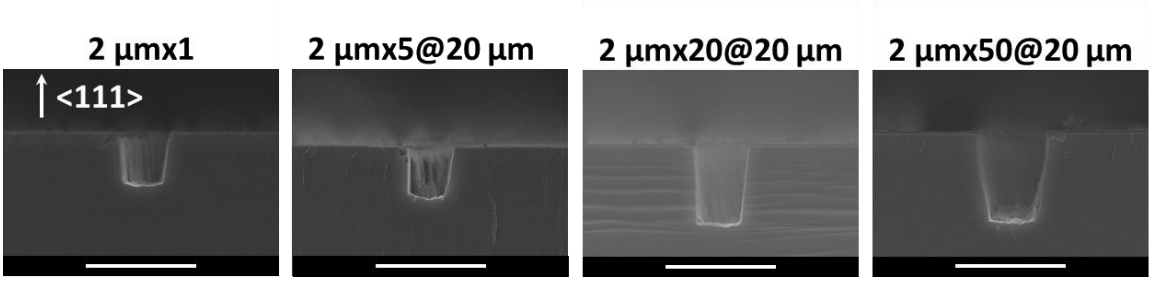

Figure 64 Cross-sectional SEM images of the etching profile on P-Si with (111) crystalline orientation. The name of blocks are labeled on top of each corresponding figure. All the scale bars have a length of 5 μm.

5.5 Conclusion

In conclusion, 3D profiles of MaCE using Au lines with different line width (w_0), number (n) and spacing distance (s) on P-Si, N-Si, USi, P(+)-Si and N(+)-Si have been presented. Uniform trenches were formed on P-Si, N-Si and U-Si, P(+)-Si and N(+)-Si. The depth d and lateral width variation Δw_t of the 3D profiles on P-Si, N-Si and U-Si are measured and correlated to the CT1 and CT2, respectively. The depth follows the order of d(P-Si)<d(U-Si)< d(N-Si) ,while the Δw_t of N-Si is lower than that of U-Si and P-Si. The variation of d and Δw_t over the dopant type of Si can be explained by Schottky junction model, which indicates that CT1 is favored on N-Si and CT2 is favored on P-Si. The variation of Δw_t over w_0, n and s can be further explained by the correlation between CT1 and CT2: in U-Si, h^+ in CT2 are mainly originated from excessive h^+ in CT1 through diffusion; in P-Si, the actual h^+ concentration in CT2 is much higher than that calculated from the diffusion model, which may be attributed to the drift of h^+.

The fundamental aspects revealed by this chapter will serve as a reference for future MaCE research. It is expected that by deeper study about the effect of electric bias, etchant composition and other parameters, a complete controllability of 3D profiles in MaCE can be achieved. The novel insight is also meaningful in general electrochemistry where charge transport process in micro- and nanoscale are concerned, such as microfluidics and MEMS. Practically, the results pave the way to the fabrication of high-density micro- and nanostructures by MaCE: vertical HAR structures can be readily formed on N-Si; the sidewall of the etched structures will be tapered on P-Si and U-Si as the pattern number and density increase, where the effect of lateral geometry of the structures should also be considered.

CHAPTER 6

HIGH-ASPECT-RATIO SUB-MICRON TRENCH ETCHING ON SOI USING MACE FOR MEMS RESONATOR

6.1 Introduction

Fabrication of three dimensional (3D) microstructures on Si substrate is a pivotal manufacturing process for various microelectromechanical systems (MEMS) including inertial sensors, critical angle transmission gratings, capacitive memory devices, and TSV. Presently, DRIE and derived technologies such as HARPSS^{TM} are prevalently used to selectively etch highly anisotropic trenches in bulk Si [3]. While DRIE-defined trenches suffer from roughness and scalloping owing to the pulsed nature of DRIE, the vast application of DRIE is hindered by instrumentation and maintenance cost as well as low through-put. On the other hand, Si can be etched in wet chemical bathes, such as basic solutions or acidic solutions with anodic electric bias. Although these traditional wet-etched trenches benefit from low roughness that is a key factor to reduce leakage current in TSVs and to achieve low surface thermoelastic damping in resonant sensors, the 3D profile of these wet-etch trenches is highly limited to a few types, including V-grooves and random pores. Moreover, these wet etching methods lack the capability of etching high aspect-ratio (HAR) submicron features with high controllability without following any specific crystalline orientation. In previous chapters, metal-assisted chemical etching (MaCE), a novel wet etch method has been demonstrated. Compared to the DRIE method, MaCE not only benefits from low cost and high through-put, but also excels in fabricating HAR structures with non-scalloping surfaces and versatile geometries. However, performance of MaCE on Si-on-insulator (SOI) substrates, which is one of the major substrates for MEMS devices, is unknown. In addition, uniform trench etching by MaCE at submicron scale remained challenging. This chapter addresses these two challenges and

paves the way to introduce MaCE in the fabrication of low-cost MEMS devices on SOI with HAR trenches defined by scallop-less, smooth sidewalls. Parts of the contents in this chapter have been published in [86] and reprinted here with permission. Copyright 2016, IEEE.

6.2 Methods

Fabrication of MaCE-defined microresonators (**Figure 65**) starts with photolithography (PL) or electron beam lithography (EBL) patterning of a photosensitive material (e.g. photoresist) spun on the device layer of an N-doped SOI substrate (**Figure 66**). Au is deposited and will act as a catalyst throughout MaCE, while the photoresist is left on Si as an etch mask in MaCE. Previous work has identified that through-catalyst (Au) mass-transport of oxidants is critical to achieve uniform etching and emphasized key parameters during Au deposition[87]. In particular, nanoporous morphology facilitates the diffusion of the etchant solution through the catalyst and ensures stable movement of the catalyst throughout MaCE.

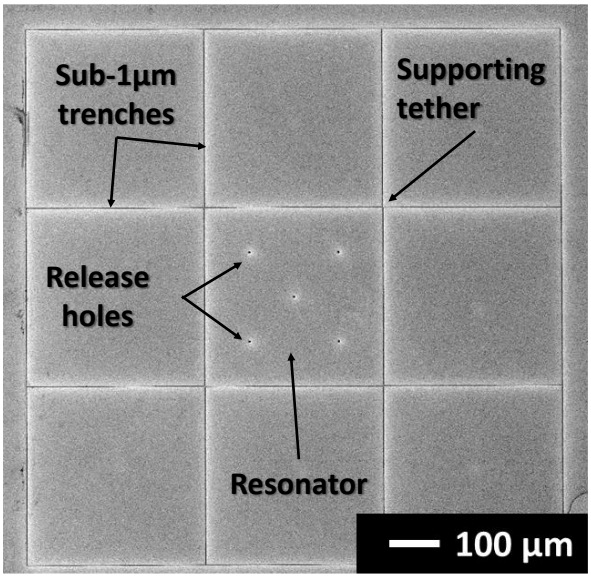

Figure 65 SEM image of a MaCE-defined resonator.

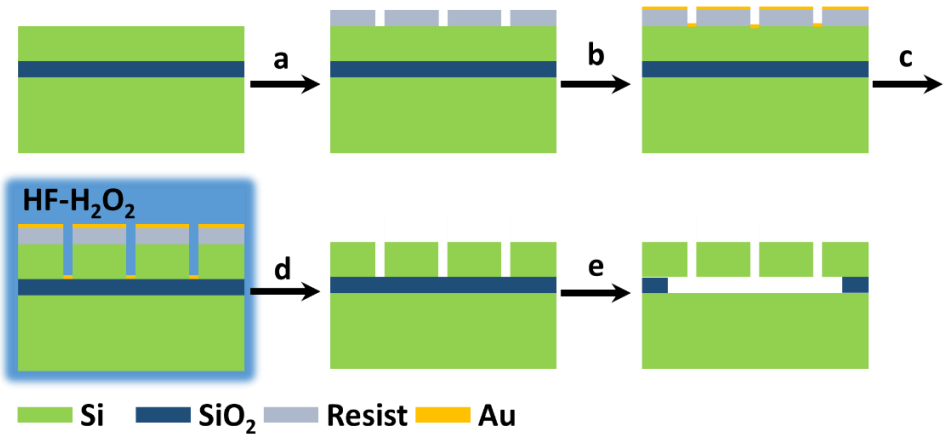

Figure 66 Schematic process flow: (a) electron beam lithography or photolithography (b) Au evaporation (c) MaCE for 10 minutes in aqueous solution (d) Au and photoresist removal (e) HF releasing and drying.

Nanoporous Au on Si is achieved by introducing an oxygen plasma clean of the exposed Si surface just prior depositing Au. Oxygen-terminated Si surface dewets the Au deposit and favors the formation of nanoporous Au. Evaporation of Au is preferred over sputtering to prevent deposition of Au on the sidewall of the photoresist layer which could induce sidewall roughness during MaCE. *Ex situ* monitoring of Au morphology via atomic force microscopy (AFM) measurements is required to control the exact thickness of the catalyst (Au) layer. Thickness deviation of the Au catalysts as small as 1 nm has significant impact on the uniformity of the etching results at wafer level, as will be shown in **Chapter 8**. Too thin Au layer breaks down during MaCE inducing non-uniform etching. Thick layers of Au coalesce and prevent diffusion of HF. In this case, as the oxidant solution can only diffuse through the sides of the Au catalyst, at the interface with bare Si, the Au layer wrinkles and induces randomly curved profile during MaCE.

After evaporation of nanoporous Au, cleaved SOI pieces (2×3 cm^2) are immersed in a simple etchant solution containing oxidants (hydrogen peroxide, H_2O_2) and hydrofluoric acid (HF). Etching in MaCE aqueous solution follows Equation 4 and 5 and is described in the next section.

After immersion in the wet etchant bath, the cleaved SOI pieces are thoroughly rinsed with deionized water; photoresist and Au are removed by acetone and potassium iodide (KI)/iodine (I_2) aqueous solution respectively. Optimum MaCE conditions lead to the formation of vertical HAR trenches. The buried oxide layer (BOX) acts as an etch stop during MaCE and limits the trench aspect ratio to 16:1 in this work (**Figure 67**). The cleaved SOI pieces are then covered by photoresist layer prior dicing; the photoresist mask covers the trenches and ensures that Si dust produced during dicing does not penetrate inside the trenches. The 1×1 cm^2 diced pieces of the cleaved SOI pieces are cleaned in a Piranha solution made of sulfuric acid (H_2SO_4) and hydrogen peroxide (H_2O_2) in 3:1 volume ratio for 1 hour at 120 ℃. The SOI dies are then released in HF for about 25min at the lateral etch rate of 1.5μm/min and stored in isopropanol (IPA) for several hours to dilute HF, and then dried in an Autosamdri 815B Super Critical Dryer in about 1 hour. Visual inspection of the released and dried SOI pieces under an infrared (IR) microscope ensures the complete release of the MaCE-defined MEMS resonators. The Si oxide beneath the Si device layer can be clearly viewed as darker part under IR microscope (**Figure 68**).

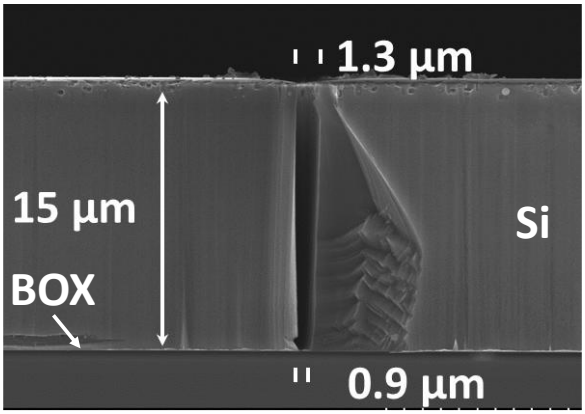

Figure 67 Cross section of a submicron trench etched by MaCE in 10 minutes with aspect ratio of 16:1.

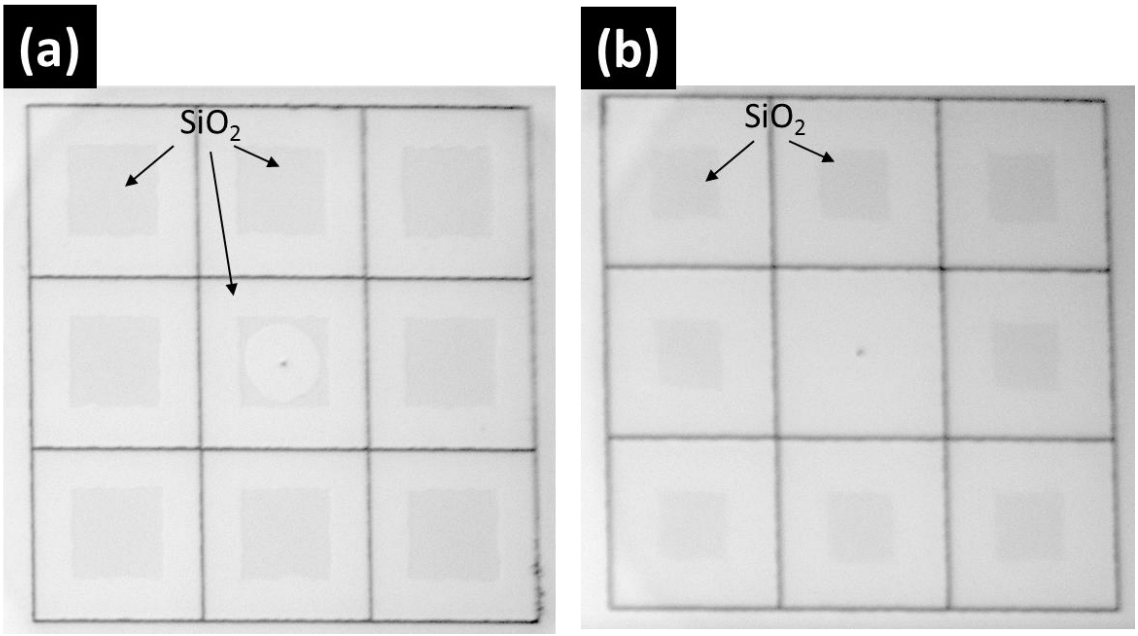

Figure 68 Top-view IR microscope image of (a) a partially released device and (b) a fully released device.

6.3 Results and Discussion

MaCE fabrication alleviates two main limitations of DRIE: cost and roughness at high etching rates. Cost incurred by DRIE includes deposition of a hard etching mask as well as high plasma-etching instrumentation and maintenance costs. DRIE also does not support multiple wafers being processed simultaneously. More importantly, owing to its pulse nature, DRIE produces undesired scalloping, especially at high etching rates which limits through-put and trench smoothness. While H_2 annealing and oxidation can reduce DRIE-induced roughness, these techniques require a high thermal budget as well as incur additional cost. On the other hand, MaCE does not suffer from these limitations. Owing to its 'wet' nature, MaCE can be scaled up, allows simultaneous processing of multiple wafers [88], does not incur significant instrumentation and maintenance cost while providing scallop-free HAR trenches at high etch rate (**Figure 69**).

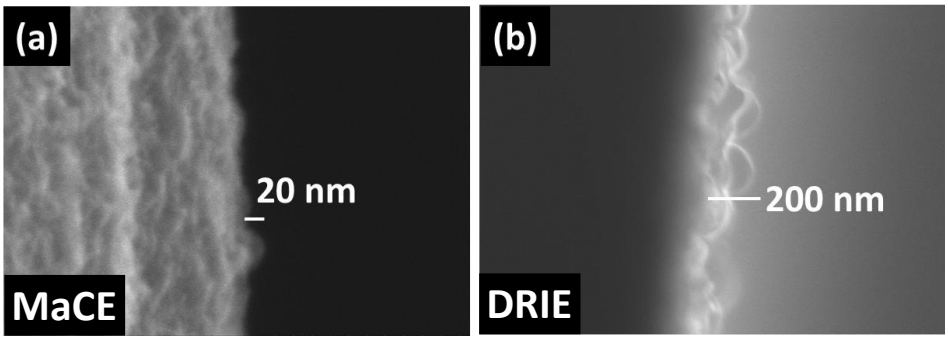

Figure 69 Sidewalls of trenches etched by (a) MaCE with absence of scalloping (b) DRIE.

Although MaCE suffers, like DRIE, from bullseye effect that relates to non-uniform spatial distribution of Si etchants, agitation of the etchant solution can significantly improve wafer-level MaCE uniformity. Since MaCE does not require passivation, unlike DRIE, MaCE does not suffer from micrograssing and polymerization. In particular, DRIE-defined trenches need to be thoroughly cleaned to remove the polymer that has been deposited on the sidewall of the trenches. However, and like DRIE, MaCE suffers from aspect-ratio-dependent etching (ARDE) and notching.

Notching, or footing, results, in DRIE, from accumulation of charges at the BOX layer. These charges deviate the course of charged species in the plasma which tend to etch Si horizontally at the bottom of the trench. Interestingly, MaCE suffers from a similar notching phenomenon when the trench is etched down to the BOX layer. However, the mechanism of notching in MaCE is fundamentally different. This chapter is first to report and explain this MaCE-induced notching phenomenon, as described in the next section.

MaCE-induced notching at the BOX layer (**Figure 70** (a)) can be explained at the light of charge transport (CT) that successfully models MaCE in bare Si [89]. While it is well known that CT in Si may induce lateral etching and formation of nanopores at the vicinity of MaCE-defined trenches, MaCE-induced notching originates, like in DRIE, from the accumulation of charges in the BOX layer.

As oxidants in the etchant solution diffuse through nanoporous Au, they generate h^+ according to (1). These h^+ are then transported to Si through the metal (Au)-

semiconductor (Si) interface (**Figure 70** (b)) and diffuse in bare Si if not consumed by dissolution of Si, according to (2) (**Figure 70** (b)). CT through this metal-semiconductor interface is described by the Schottky junction model. The depletion of charges in the semiconductor, at the vicinity of the metal-semiconductor interface, prevents ohmic contact. Since the positive charges h^+ are transported from Au to Si, Si appears negatively biased against Au (**Figure 70** (c)). The negative bias establishes attractive electrostatic forces between Au and Si. These forces contribute to the good adhesion of Au on Si throughout MaCE while Si appears negatively bias against Au.

When Si in the device layer of the SOI beneath the trench is fully etched, then the positive charges h^+ generated in the Au are transported to the BOX layer (**Figure 70** (d)). However, the interface metal-oxide can not be described as a Schottky model and charges accumulate in the BOX layer. The accumulation of charges in the BOX layer progressively diminishes the magnitude of the electrostatic forces, until full cancellation. Disapparition of these forces lead to poor adhesion of Au on the BOX layer. Meanwhile, the interfacial attraction force between Au and SiO_2 is weaker than between Au and Si [90]. Laterally, Au may be in contact with bare Si creating a new Schottky contact and establishing attractive electrostatic forces. Interestingly, formation of porous Si (pSi) at the vicinity of the trench may not be induced by the redeposition of Au, but by the diffusion of excessive positive h^+ charges in Si (**Figure 70** (e)). Both poor adhesion of Au on the BOX layer and horizontal attractive forces induce Au to bounce off from the BOX layer and penetrate Si to form a second trench in a random direction (**Figure 70** (f)).

Hence, it appears that while the BOX layer acts as an etch stop layer, secondary trenches are etched if MaCE is not timed properly. Several end-point detection mechanisms have been developed for DRIE including optical emission spectroscopy and laser interferometry to reduce over-etching. Similar techniques need to be developped for MaCE. In particular, thin Si traces may remain, near the BOX, in well-timed MaCE-defined trenches (**Figure 70** (f)). These thin traces may cause electrical shorts between two

otherwise electrically isolated structures. Ultrasonic agitation is used to remove these thin traces prior fully releasing these resonators in HF aqueous solution.

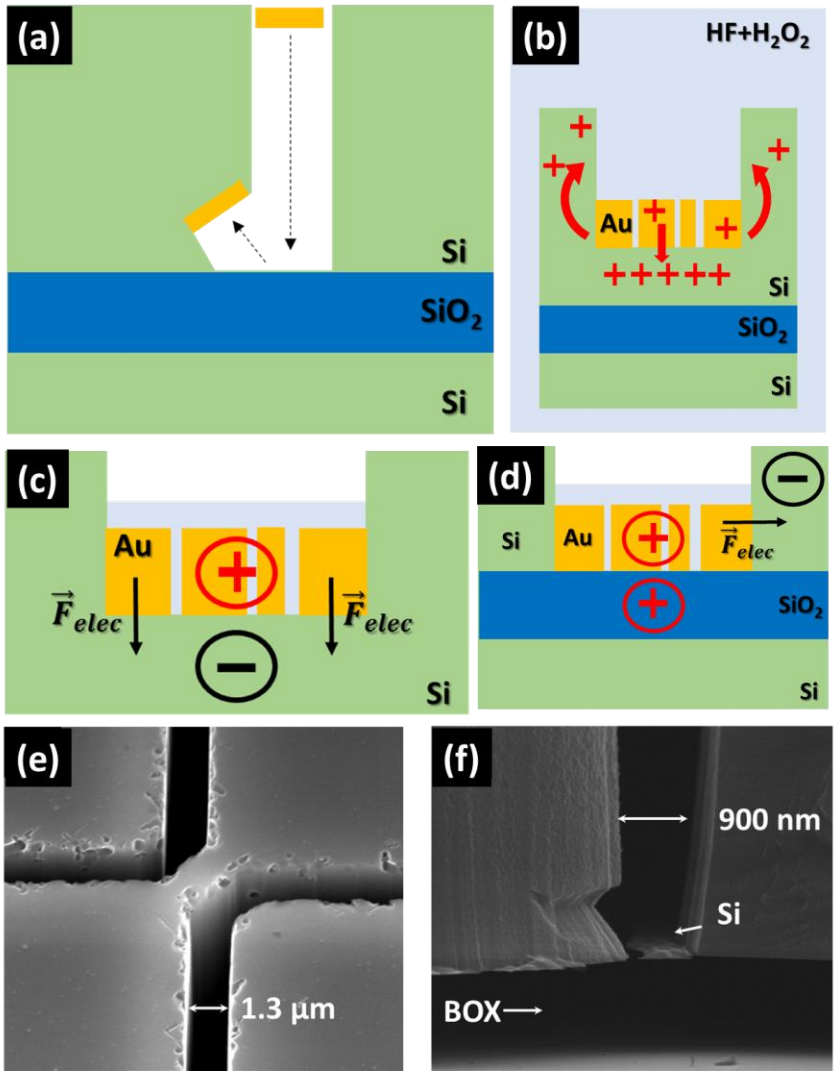

Figure 70 (a) Schematic of MaCE-induced notching (b) Charge transport in Si during MaCE (c) Electrostatic forces enable good adhesion of Au on Si (d) Charging of BOX layer induce notching (e) Formation of porous Si at the trench top (b) Bottom of trench with Si residue and an additional trench by bouncing back of Au.

The present main drawback of MaCE on SOI is due to the generation of excessive charges h^{+}_{exc} at the metal-semiconductor interface. It has been shown that h^{+}_{exc} mostly

diffuse inside Si and may reach the etchant solution from the side of the trenches [89]. If these charges interact with HF, then lateral dissolution of Si occurs leading to the formation of pSi at the vicinity of the trench. In particular, pSi is anisotropic: porosities are larger near the trench and decrease in size in the direction perpendicular to the surface of the material. Since the electrical conducitvity in pSi is lower than in bulk Si, the effective capacitive gap might be larger than 900-1300nm, as measured by SEM.

400μm×400μm×15μm^3 EBL- and 2mm×2mm×15μm^3 PL-patterned devices have been etched via MaCE and their resonance frequencies have been measured by LDV in vacuum (**Figure 71**). These results indicate complete release of various MaCE-defined resonators. Identical DRIE-defined devices with similar gap sizes have been capacitively measured and resonance frequency trimming results are shown for both MaCE and DRIE-defined resonators. [91] While MaCE suffers from CT of h^+_{exc} in Si and subsequent lateral etching, there exist several methods to alleviate formation of pSi. In particular, Electric Bias-Attenuated MaCE (EMaCE) has been recently investigated and shows promising control of h^+ charges in bulk Si (**Chapter 4**). EMaCE of SOI substrates will be researched in future work.

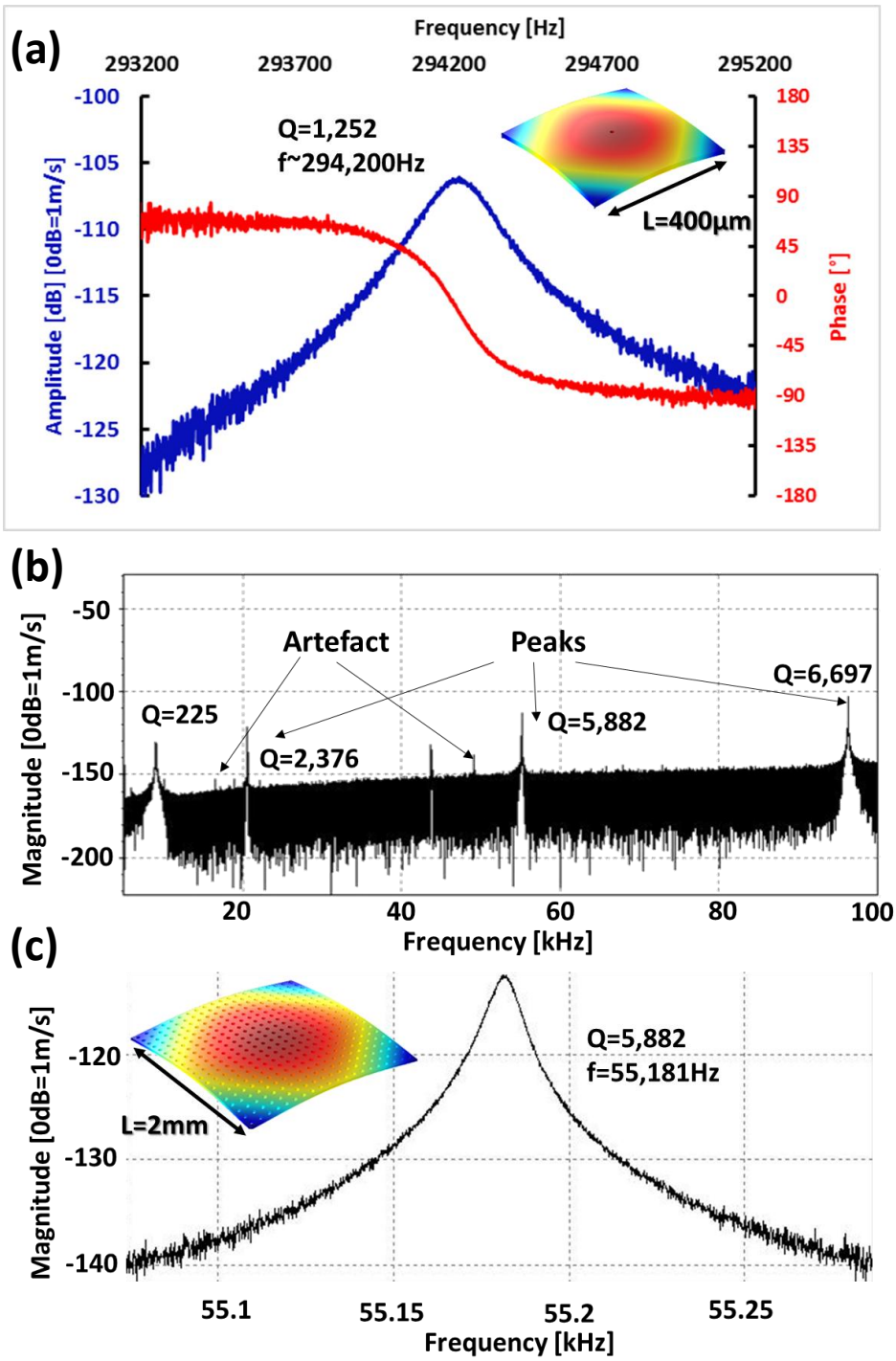

Figure 71 LDV measurements of a MaCE-defined resonator with HAR trenches (a) Magnitude (blue curve) and phase (red curve) of an EBL-patterned resonator (b) Sub-100 kHz frequency spectrum of a (c) PL-patterned resonator vibrating in its out-of-plane mode (inset).

6.4 Conclusion

16:1 aspect-ratio, scallop-free, smooth and vertical trenches have been etched on an SOI substrate using MaCE in 10 minutes. Fully released resonators have been measured by an LDV. MaCE-induced notching in SOI has been observed.

CHAPTER 7

COMBINING MACE AND FESA

7.1 Introduction

Fabrication of high-aspect-ratio (HAR) microstructures on Si (Si) is the fundamental process in manufacturing of advanced microelectromechanical systems (MEMS) [3, 8, 92], microfluidic channels [93-95], optoelectronic devices [96, 97] and components in microelectronic packaging [98-100]. The traditional strategy for producing these structures involves the use of photolithography to form patterns, followed by subsequent plasma etching to selectively remove a certain volume of Si. In photolithography, a layer of photosensitive materials, referred to as photoresist, is coated on Si. The photoresist is then exposed to UV-visible light with coverage of a photomask that carries patterns with designed geometry when the patterns are transferred on the photoresist. Subsequently, the patterns in photoresist are further transferred to a hard etching mask and finally to Si by two consecutive plasma-etching steps (**Figure 72** (a)-(d)). This traditional route is referred to as the photolithography-plasma etching route. Photolithography has been widely used in semiconductor industry with resolution down to tens of nanometers.[101] Plasma etching is also a primary deep Si etching method in industry which is capable for producing vertical deep trenches with a width on submicron scale and an aspect ratio over 100:1.[12, 102] However, the photolithography and plasma etching incur high instrumentation and materials costs. Moreover, as most of photoresist is heavily damaged in the plasma etching of Si, the hard etching mask is necessary to protect the Si from being etched. It is not surprising that the necessity of hard etching mask add additional cost to the overall process.

In order to lower the cost of HAR microstructures fabrication, several alternative methods have emerged to replace either the photolithography or plasma etching. For

example, to replace photolithography, nanoimprint lithography has been used to transfer patterns on a thermoplastic polymer materials via a stamping process.[103] Although this method is relatively cheaper than the photolithography by avoiding the use of UV-visible light, the instruments for thermal and mechanical treatment of the thermoplastic polymer is still expensive. As several alternatives to the plasma etching, the wet solution-based KOH etching [104, 105] or anodic etching[17, 106], have been developed. However, their ability to fabricate uniform HAR structures with defined geometries is still limited.

In this chapter, we report a viable and low-cost strategy for crafting HAR microstructures on Si by combining flow-enabled self-assembly (FESA) of polymer with metal-assisted chemical etching (MaCE). FESA is an effective pattern formation method which utilizes the self-assembly of polymer molecules with guidance of the flow of the polymer solution.[107-109] The width of the polymer lines (w_p) and the spacing distance between the lines (d_p) can be facilely and precisely controlled by the time of move and stop step of the translational stage (**Figure 72** (e)). Fabrication of uniform lines of polymer as well as other materials with w_p and d_p in few micrometer-scale by FESA has been successfully demonstrated within several minutes. There are several distinctive merits of FESA compared to currently available lithography technology: (1) patterns are directly formed in one-step on Si, no need for coating, curing, exposure and developing of polymer resist as those in photolithography and electron beam lithography; (2) block copolymer solution and a movable stage are used as the only materials and instrument, much cheaper than the photoresist and exposure tools and easier for implementation; (3) due to the unique fashion of pattern formation, patterns can be formed at high speed. Given these merits, FESA is potentially applicable in high-volume manufacturing of microscale patterns on Si with low cost and high throughput.

After the patterns are formed on Si by FESA, we propose to use MaCE to replace the plasma etching. MaCE is a novel wet etching method which uses the low-cost hydrofluoric acid (HF)-hydrogen peroxide (H_2O_2) solution as the etchant. In operation, the

Si with patterns is coated with a thin layer of metal catalyst, then immersed in HF-H_2O_2 for wet etching (**Figure 72** (f) and (g)) [24, 25, 34, 38, 69, 81, 110-113]:

$$Si+6HF+2H_2O_2 \xrightarrow{Metal} H_2SiF_6+4H_2O \quad (1)$$

As the etching proceeds, the metal catalyst moves into Si and keeps facilitating the etching. Recently, by using nanoscale engineered catalyst and etchant solution with rationalized composition, fabrication of uniform deep trenches and holes in micrometer-scale by MaCE have been demonstrated, where photolithography and electron beam lithography have been used for the pattern formation [53, 65, 76]. The lateral geometry of theses HAR structures, such as the top width (w_t), bottom width (w_b) and spacing distance (d) could be controlled by the lithography step as well as the etching condition(**Figure 72** (g)), which makes it standing out among other wet etching methods. It should be noted that only a thin layer of polymer, either photoresist (~1.5 μm-thick) or electron beam resist (~200 nm-thick), is able to serve as the etching mask in MaCE. This feature makes it possible that the polymer patterns fabricated by FESA can be directly used as the etching mask in MaCE, thus eliminating the need of hard mask and further lower the cost. In the following parts, the HAR microstructures fabricated by the proposed FESA-MaCE route will be demonstrated.

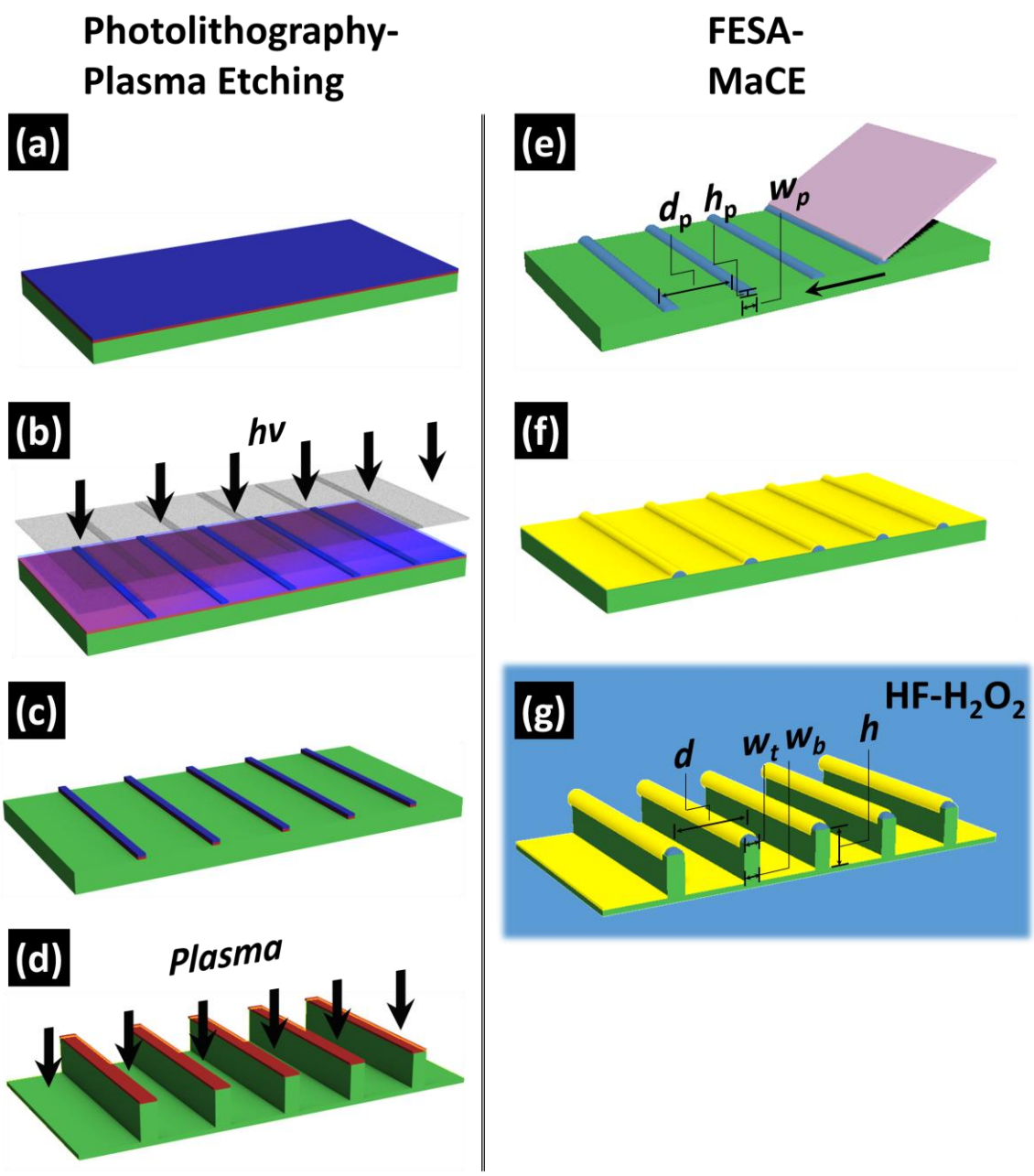

Figure 72 Schematic illustration of the photolithography-plasma etching route and the FESA-MaCE route for HAR microstructures fabrication on Si: (a) coating of hard etching mask and photoresist; (b) photolithography; (c) geometry transfer on hard etching mask; (d) plasma etching of Si; (e) FESA; (f) deposition of metal catalyst; (g) MaCE. The blocks shown in blue, red, green, purple and golden refer to photoresist/polymer, hard etching mask, Si substrate, plate and metal catalyst, respectively.

7.2 Methods

(100)-oriented single-crystalline Si wafers (phosphorous doped, resistivity=1-10 ohm cm^{-1}) were cut into 1×2 cm^2 pieces and wash by Piranha solution (mixture of 96 wt% H_2SO_4 and 30% H_2O_2 with volumetric ratio of 1:1) at 120 ^oC for 10 min before use. For FESA, parallel lines of polymer were formed on Si wafers by drying a drop of polymer solution in between two near-parallel plates. During FESA of polymer, the polymer solution is placed between a lower movable Si substrate and an upper slanting plate. The upper plate is fixed while the Si substrate is carried by a computer-controlled translational stage (Parker Hannifin Corp, mode: MX80LVixBL2b). As the Si substrate is moved by the stage, the polymer solution moves together with the edge of the plate; while the stage stops, due to the coffee-ring effect, the capillary flow induced by the higher evaporation rate at the drying front carries and makes polymer solutes deposited at the contact line, thus a polymer line is formed. The resolution of the translational stage is 100 nm. The moving speed of the Si substrate was set at 2mm/s with stop times ranging from 0.1s to 5s to control the width of the polymer lines

After the polymer patterns were formed on Si by FESA, a cleaning process was applied on the sample using argon (Ar)/ oxygen (O_2) plasma (referred to as "descum" process in the following discussion) in a RIE system (Vision RIE 320, Advanced Vacuum). During the descum process, the RF power was set at 22 W and the flow rate of Ar and O_2 were set at 45 sccm (standard cubic centimeter per minute) and 5 sccm, respectively. The chamber pressure was set at 100 mTorr. Then a layer of gold (Au) film was deposited on the sample by electron beam evaporation (Denton Explorer, Denton Vacuum) at a rate of 0.5 Å/s. The real thickness of the Au film was measured to be 14.3 ± 0.5 nm by atomic force microscope (AFM, Dimension Edge, Veeco). The MaCE was conducted by immersing the sample in a HF-H_2O_2 aqueous solution at room temperature. In the MaCE experiment with

electric bias, the backside of the Si sample was coated with 10 nm Ti/100 nm Cu by electron beam evaporation and mounted on a home-made Si carrier. The bias was provided by a potentiostat (VersaSTAT, Princeton Applied Research). The details of the experiment have been reported in **Chapter 4**. After etching, the sample was thoroughly rinsed with deionized (DI) water and dried under N_2 gas. The top surface and cross section of the samples after FESA-MaCE were viewed under SEM (Hitachi SU8010, Hitachi). For water contact angle measurement, the samples were rinsed by acetone and KI/I_2 aqueous solution consequently to remove the polymer and the Au. Then the sample was washed in Piranha solution at 120 ^oC. For silane surface treatment, the sample was immersed in a 3 mM solution of 1H,1H,2H,2H-perfluorooctyl-trichlorosilane in hexanes for one hour, followed by rinsing with isopropyl alcohol and heat treatment in atmospheric oven at 150 ^oC for one hour.

7.3 Results and Discussion

After FESA, highly uniform polymer lines were formed on Si surface (**Figure 73** (a)). AFM was used to measure the 3D geometry of these lines. The w_p and d_p were measured to be 8.31±0.08 μm and 22.0±1.0 μm, respectively. The polymer lines showed hill-shape cross sections under AFM with steep walls (**Figure 73** (b) and (f)). At the edge of the polymer lines, some polymer residue extended out into the bare Si area. Interestingly, the overall cross section of the polymer lines was slightly tilted, possibly due to the fact that the plate was slanted with respectively to the Si substrate during FESA. The maximum height of the polymer lines (h_p) was measured as 85.7±3.3 nm. All the above dimension values are the average of 5 separate measurements over the Si samples. In order to demonstrate the feasibility of using polymer as the etching mask for MaCE, the Si sample with polymer lines was immersed in the etchant solution of MaCE, i.e. HF-H_2O_2 solution for different time. Here we defined the term ρ=[HF]/([HF]+[H_2O_2]), where [HF] and [H_2O_2] stand for the concentration of HF and H_2O_2 in moles per liter (M). The composition

of HF-H_2O_2 solution is expressed in the format of $\rho(x)^y$, where $x = \rho$ and y=[HF]. Figure 73(c)-(e) show the AFM image of the polymer lines after immersion in $\rho(0.34)^{1.6}$ solution for 10 min, 20 min and 60 min, respectively. The corresponding cross sections are shown in **Figure 73** (f). Here since no metal catalyst was deposited, the etching of bare Si in the HF-H_2O_2 solution was negligible.[23] The w_p and h_p of the polymer lines are further plotted against the immersion time in **Figure 73** (g). In comparison, the overall profiles of the polymer lines do not have significant variation during the immersion, although the surface roughness slightly increased in the sample after immersion of 60 min.

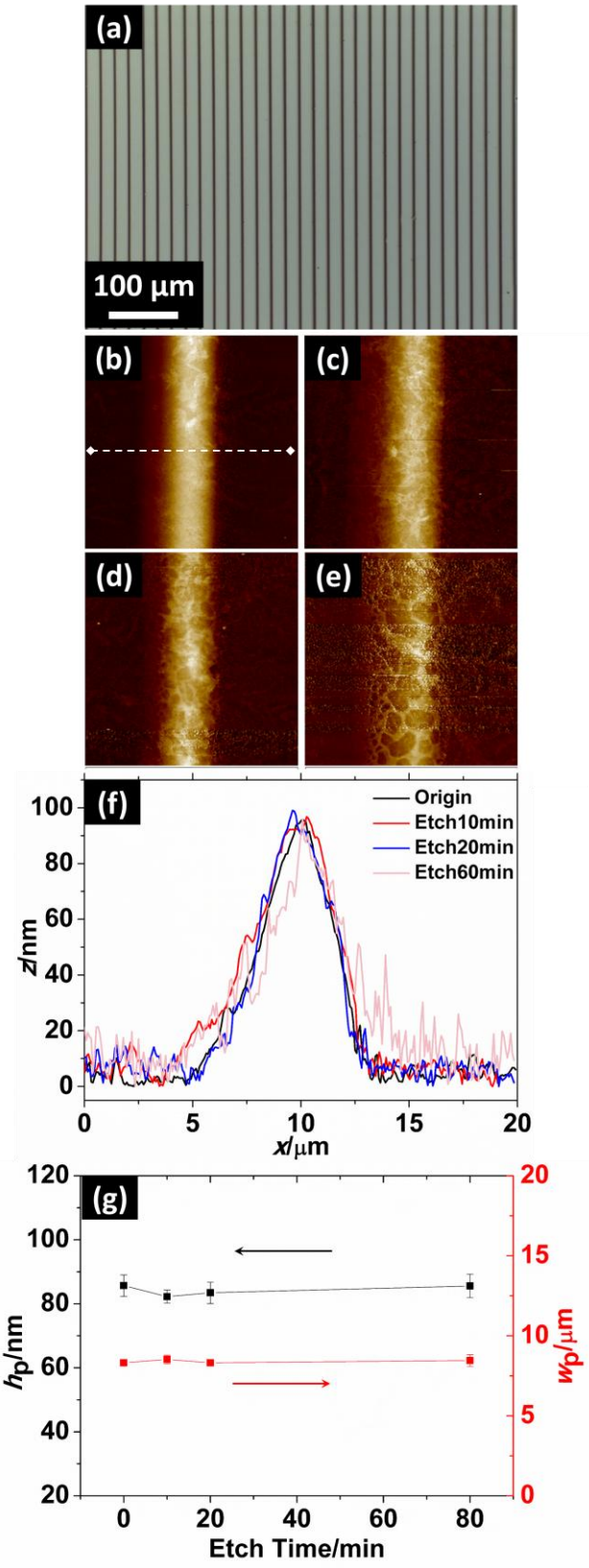
(a)
100 μm
(b)
(c)
(d)
(e)
(f)
Origin
Etch10min
Etch20min
Etch60min
z/nm
x/μm
(g)
h_p/nm
w_p/μm
Etch Time/min

Figure 73 (a) Optical microscope image of the Si surface after FESA. The polymer assemblies patterned by FESA appear as the vertical black lines, while the green area in between the lines represents bare Si surface. (b)-(e) AFM image of the polymer lines after immersion in for 0 min, 10 min, 20 min and 60 min, respectively. The actual window size is 20×20 μm^2.The corresponding AFM cross sections are shown in (f), while the h_p and w_p measured from the AFM cross sections are shown in (g).

The stability of the polymer lines under plasma cleaning was also investigated. Here we used Ar/O_2 plasma to clean the trace amount of residue on the bare Si surface (i.e. the descum process) so that the metal catalyst could directly contact the Si surface and facilitate subsequent MaCE. The size reduction of polystyrene microspheres upon Ar/O_2 plasma treatment has been reported [114]. Here for the polymer lines by FESA, we observed similar phenomenon. As shown in **Figure 74**, both w_p and h_p kept decreasing as the descum time increased. As the descum time was prolonged to 3.5 min, most of the polymer lines were cleared and bare Si surface within the polymer lines was exposed (**Figure 74** (g) and (h)). The results support our previous statement that polymer materials are damaged under plasma treatment, while being stable in the $HF-H_2O_2$ solution for MaCE.

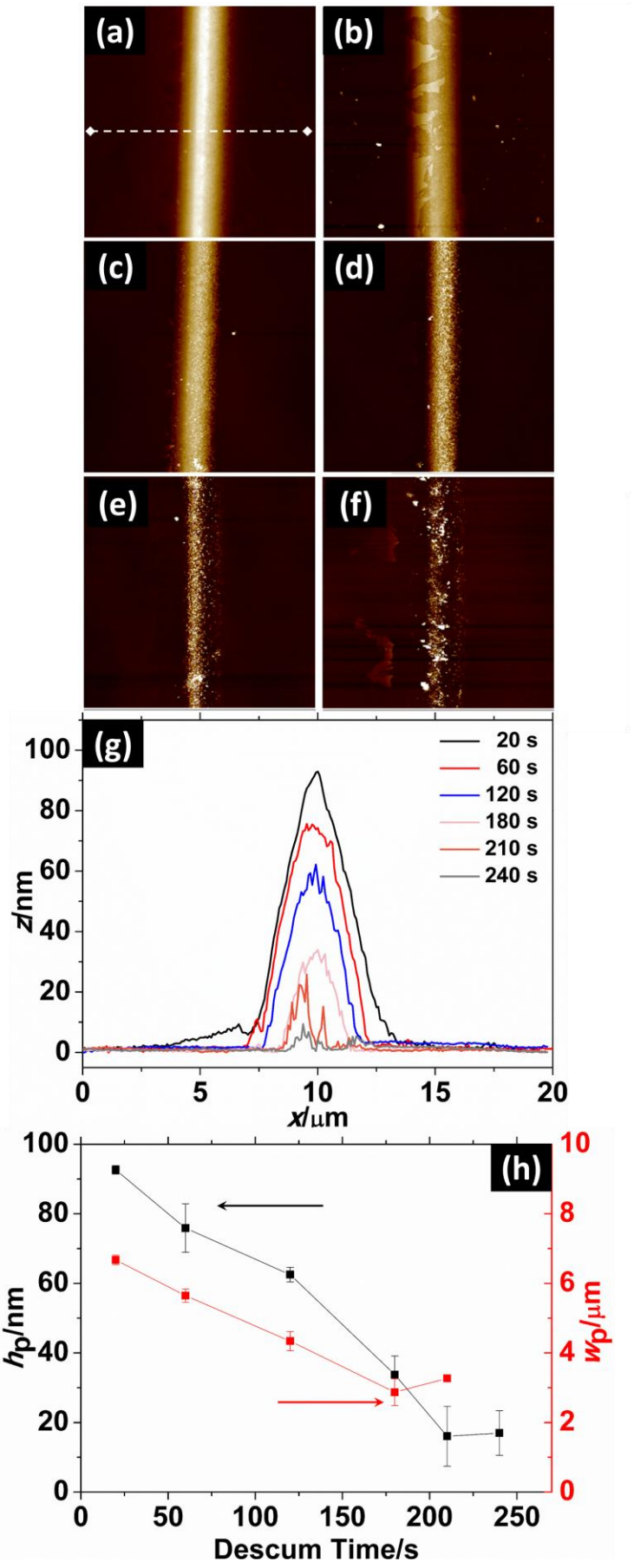
(a)
(b)
(c)
(d)
(e)
(f)
(g)
20 s
60 s
120 s
180 s
210 s
240 s
z/nm
x/μm
(h)
h_p/nm
w_p/μm
Descum Time/s

Figure 74 (a)-(f) AFM images of polymer lines patterned by FESA on Si after descum of 20 s, 60 s, 120 s, 180 s 210 s and 240 s, respectively. The corresponding cross sections are shown in (g), while the corresponding w_p and h_p descum time in (h).

After FESA and descum, Au thin film was deposited on the sample and MaCE was conducted in the $\rho(0.34)^{1.6}$ etchant solution. The thickness of Au film was controlled as 14.3 ± 0.5 nm, where nanopores existed within Au film to facilitate uniform etching (**Chapter 3**). Si under the polymer lines kept intact during MaCE. The metal catalyst does not penetrate into the Si under FESA patterns because: (1) the FESA patterns are not etched in the HF-H_2O_2 etching solution, as evidenced in **Figure 73**; (2) the FESA patterns are solid without pores for Au to penetrate. As shown in **Figure 75** (a)-(h), trenches/micrograting were formed after MaCE of 10 min on Si samples with different descum time. These structures possess smooth surface and geometric uniformity in both vertical and lateral direction (**Figure 75** (i) and (j)). The edge roughness, which is measured from maximum variation of the 3.2 μm–wide micrograting in Figure 75(j), was below 0.5 μm (**Figure 75** (j)). The high uniformity of the results is enabled by the excellent fabrication precision of both the FESA and MaCE steps and comparable to that of the conventional photolithography-plasma etching route.

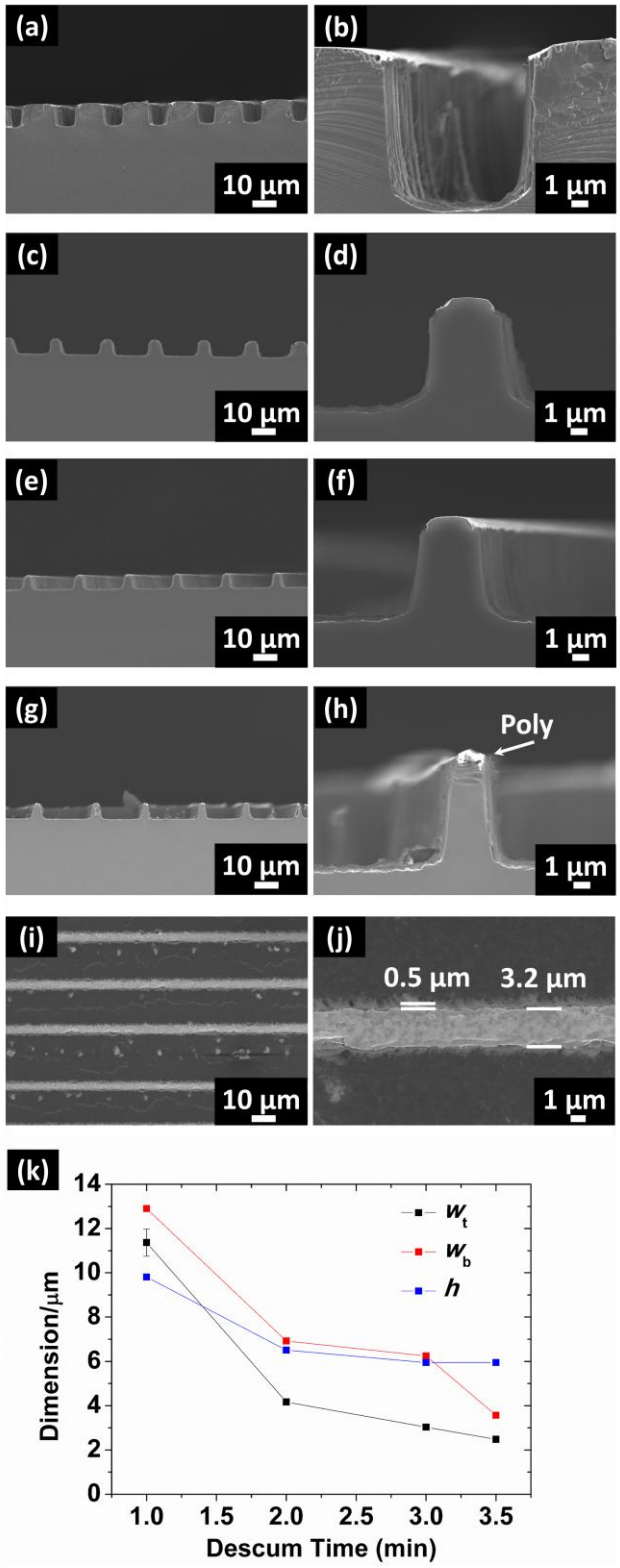

Figure 75 Cross-sectional SEM images of Si sample after FESA and MaCE for 10 min in $\rho(0.34)^{1.6}$ etchant with descum time of (a) 1 min, (c) 2 min, (e) 3 min and (g) 3.5 min. (b), (d), (f) and (h)

shows the sample in (a), (c), (e) and (g) with high magnification, respectively. Top-view SEM image of sample in (e) is shown in (i) and (j). The w_t, w_b and h of each sample are plotted against their corresponding descum time. Here the "Poly" refer to the polymer lines by FESA.

From the results in **Figure 75** (a)-(h), it is clear that the descum time significantly influences the lateral geometry, w_t and w_b, of the etching profile by adjusting the width of polymer lines. In principle, w_t and w_b should exactly follow the corresponding w_p. In experiments, when comparing **Figure 74** (h) and **Figure 75** (k), it can be found that w_t and w_b are larger than corresponding w_p for the sample with descum of 1 min. In this case, w_p was 5.6 μm, but the w_t and w_b were 11.3 μm and 12.9 μm, respectively. It should also be noted that for the sample with descum time of 20 s, although the w_p was measured as 6.7 μm, there was no observable etching phenomenon in the entire bare Si area. These results indicate that although most of the polymer were accumulated in the polymer lines after FESA, there were probably a thin layer of polymer residue on the bare Si area as well. These polymer residue made the actual coverage of polymer larger than the w_p that was measured by AFM, so w_t and w_b were generally larger w_p. During the descum process, the polymer residue were gradually removed together with the polymer in the line patterns. As the descum time reached 2 min and above, the w_t became very close to the corresponding w_p, indicating that most of the polymer residue were cleared in the bare Si area.

Another interesting phenomenon revealed by **Figure 75** (k) is that the w_b are larger than w_t in all samples. Actually in the SEM cross sections shown in **Figure 75** (a)-(j), the sidewall of the etched trenches/micrograting are slanted rather than vertically aligned. The Au film that was in contact with Si are found downward bending. This phenomenon can be explained by the half reactions shown in Eq. (2) and (3). In the $\rho(0.34)^{1.6}$ solution that was used as etchant, the H_2O_2 was abundant and the amount of h^+ generated in Eq. (2) might exceed the amount that could be consumed by Eq. (3). Therefore, the excessive h^+ might accumulate in the Au-Si interface and a spatial distribution of h^+ was formed. Based on previous modeling results, h^+ concentration near the edge of Au film was much lower

than that right under Au film, which led to a lower etching rate in this region [53, 76]. As the etching proceeds, the Au edge gradually tilted upward and some Si near the edge was not etched, resulting in slanted sidewalls. In this sense, the sidewall profile should be influenced by the composition of etchant. **Figure 76** (a)-(c) show the SEM cross sections of the samples after FESA-MaCE with descum time of 3 min in etchant solution of different compositions. In the three sets of etchant solution, [H_2O_2] were held constant while [HF] were 1.6 M, 2.3 M and 3.1 M, respectively. The physical-chemical meaning of the composition of HF-H_2O_2, which is represented by ρ in the manuscript, can be understanding using Eq. 2 and 3. As mentioned in the manuscript, Eq. 2 describes the process of h+ generation, while Eq. 3 describes the process of h+ consumption and Si dissolution. From the equations, it is conceivable that a higher concentration of H2O2 will render a higher amount of h^+, while a higher concentration of HF will make the consumption of h^+ faster. As h^+ are generated and consumed inside Si, the amount of h^+ at a certain moment is determined by the composition of HF-H_2O_2. Given the fact that h^+ may diffuse inside Si, the composition can be eventually correlated to the spatial distribution of h^+ inside Si, which determines the final etching profiles (**Chapter 4**). As the [HF] increased, the h^+ consumption rate in Eq. (3) was promoted and the difference of h^+ concentration between the edge of Au film and its center diminished, which induced an even etching rate across the Au film. In **Figure 76** (c), the sidewall angle approaches vertical and the w_t is nearly identical to w_b, indicating a complete removal of Si near the edge of Au. The results are in accordance with literature [113]. However, adding more HF may also increase the tendency of the breaking of Au catalyst (**Chapter 3**), as some Si whiskers that protruded out of the Au film could be observed in **Figure 76** (c).

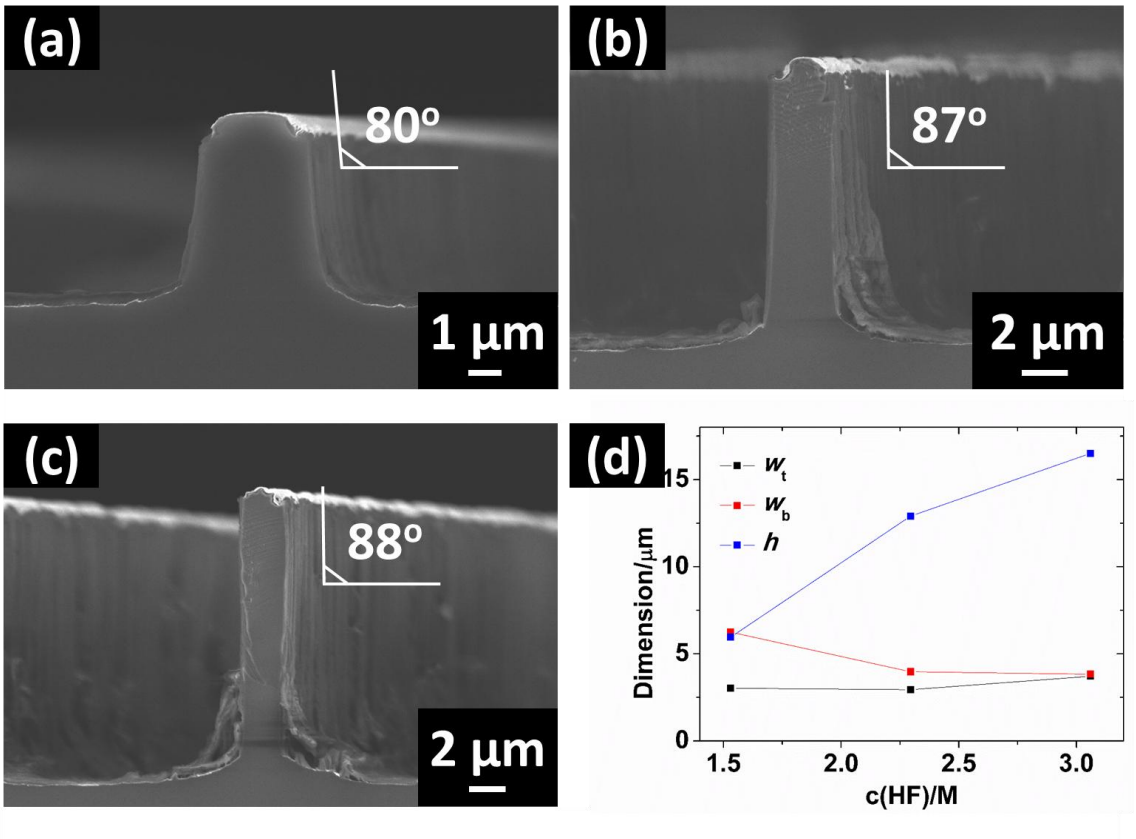

Figure 76 Cross-sectional SEM images of Si sample after FESA with descum time of 3 min and MaCE for 10 min in etchant of (a) $\rho(0.34)^{1.6}$, (b) $\rho(0.43)^{2.3}$ and (c) $\rho(0.50)^{3.1}$. The w_t, w_b and h of each sample are plotted against their corresponding [HF].

To investigate the possibility of fabricating higher aspect ratio by FESA-MaCE route, we conducted experiments with longer MaCE time. **Figure 77** (a) and (b) show the cross-sectional SEM images of the samples after MaCE time of 20 min in $\rho(0.34)^{1.6}$ etchant with descum of 2 min and 3 min, respectively. h in both samples increased to 14 µm. When the MaCE was prolonged to 60 min, h reached 56 µm and the aspect ratio of the microgratings were 16:1 (**Figure 77** (c)). However, a considerable amount of Si whiskers evolved at the bottom of the microgratings. We also observed that during MaCE, the polymer lines were gradually deformed (**Figure 77** (b)) and finally lift off from Si (inset of **Figure 77** (c)). As a control experiment, we used photolithography to form the patterns and then use MaCE to fabricate the microgratings. Here a 1.5 µm-thick polymer photoresist

served as the etching mask in MaCE. The micrograting made by the photolithography-MaCE strategy have similar w_t and h, but the bottom area was uniform and no Si whiskers were observed (**Figure 77** (d)). In this case, the PR were also observed lift-off but kept their original shape of stripes. In comparison, because the polymer lines in FESA were only ~30 nm-thick after descum, after lift-off they were easy break and the Au on the polymer lines might etch into Si to induce the formation of Si whiskers. The consequence of the low thickness of polymer lines can also illustrated by the etching results with descum time of 3.5 min (**Figure 75** (h)). It is clear that the polymer lines significantly deformed compared to those in **Figure 75** (d) and (f).Therefore, it is possible to form HAR micrograting FESA-MaCE without Si whiskers by optimization of the polymer lines in FESA. The optimization of polymer thickness requires systematic study on the type of the polymer, the geometry of the setup and many other parameters, which will be done in the future work. Further, we investigated the possibility of avoiding the lift-off of the polymers. As discussed above, in the $\rho(0.34)^{1.6}$ solution there may exist excessive h^+ in the Au-Si interfaces. These excessive h^+ had a chance to diffuse to the sidewall and even top of the micrograting so that an electrochemical etching process described in Eq. 5 could occur in these region (**Figure 77** (e), **Chapter 5**). Finally the Si in the top of the micrograting were removed and the polymer lines were lift off. One way to suppress the upward diffusion of excessive h^+ is to apply a negative bias from the bottom of the Si sample, so the excessive h^+ is driven away from the top surface Si (**Chapter 4).** In experiments, we observed that when the same sample in **Figure 77** (b) were etched with a -1.5 V negative bias, most of the damage in the top of micrograting were suppressed and the polymer lines kept their original flat profiles (**Figure 77** (f)). The result supports our proposed mechanism of h^+ transport and lift-off of polymer lines, and indicates that application of electric bias is an effective way to suppress the lift-off the etching mask.

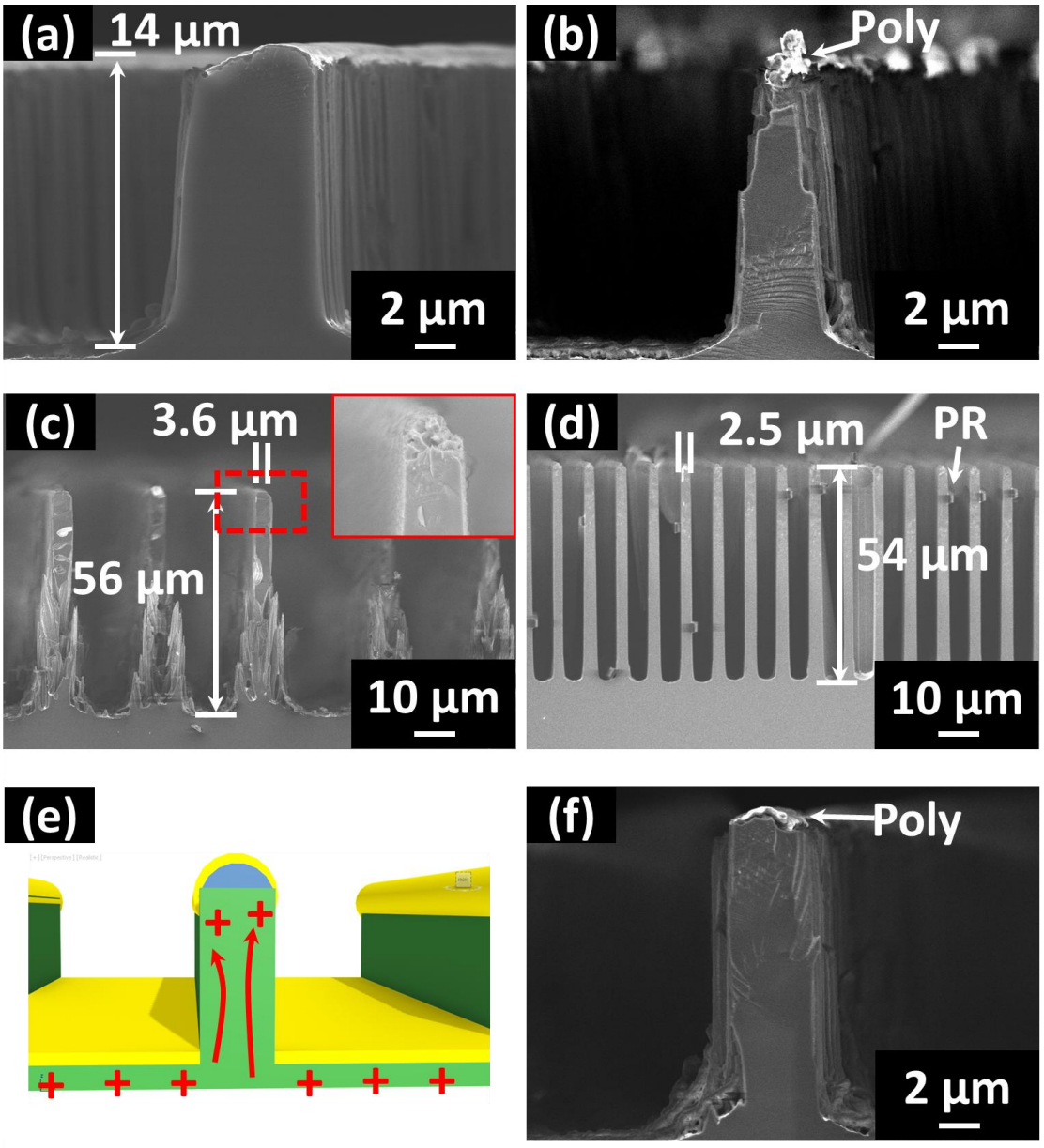

Figure 77 Cross-sectional SEM images of Si sample after FESA-MaCE in $\rho(0.34)^{1.6}$ with different descum time and MaCE time: (a) descum 2 min, MaCE 20 min; (b) descum 3 min, MaCE 20 min; (c) descum 3 min, MaCE 60 min. (d) shows the results of photolithography and MaCE for 60 min. (e) shows the schematic charge transport process during MaCE, where the blocks in green, blue and golden refer to Si, polymer lines and Au catalyst, respectively. (f) shows results of the same experiment in (b) with the addition of -1.5 V electric bias. Here "Poly" and "PR" refer to the polymer lines and photoresist used in FESA and photolithography, respectively.

As a demonstration of potential applications, we show that the FESA-MaCE process could realize controllable surface wettability on Si samples. Recently, controlled surface wettability has found important application in self-cleaning surface [115], microelectronic packaging [116] and energy harvesting [117]. It has been reported that the surface wettability can be adjusted by modification of either the surface chemistry or morphology in micro- or nanoscale. By treating the surface with low-surface energy, fluoro-containing species, the surface wettability is reduced and the water contact angle increases to above 90 °, suggesting a hydrophobic surface. Superhydrophobicity can be achieved with additional hierarchically structured surface, and adhesion strength can be tuned by the surface structure, such as the inclined angle, pitch, and depth.[26, 118] Here we quantified the surface wettability of the samples by measuring the water contact angle (θ) on their surface. The samples were treated by Piranha solution and then silane solution. Bare Si surface were used as the control sample. After Piranha solution treatment, θ on the bare Si surface was 0^o, while θ increased to 14^o on the sample after FESA-MaCE with descum time of 1 min, and 24^o on samples with descum time of both 2 min and 3 min. After silane treatment, θ on the bare Si surface increased to 114^o, while θ further increased to 141^o, 164^o and 167^o on the sample after FESA-MaCE with descum time of 1 min, 2 min and 3 min, respectively (**Figure 78**). We have tested the contact angle in open air, therefore the surface may be readily contaminated by the hydrocarbon and other contamination in the air. For the hydrophilic samples treated by piranha solution, their contact angle slowly increases from ~0^o to 60-70^o within 1 hr and stabilized overnight. For the hydrophobic samples treated by silane, their contact angle kept relatively constant at 150-160^o even overnight. The different θ on each sample can be attributed to the fact that after MaCE, the surface bears roughness in both microscale (trenches and micrograting) and nano-scale (the Si whiskers) with different geometry. The hierarchical structures can significantly increases the θ to different extents [26]. More importantly, the different θ between Si

samples with different descum time imply that the geometry of etching profiles effectively tunes the surface wettability in a continuous manner, which can be facilely controlled by the processing conditions in FESA-MaCE.

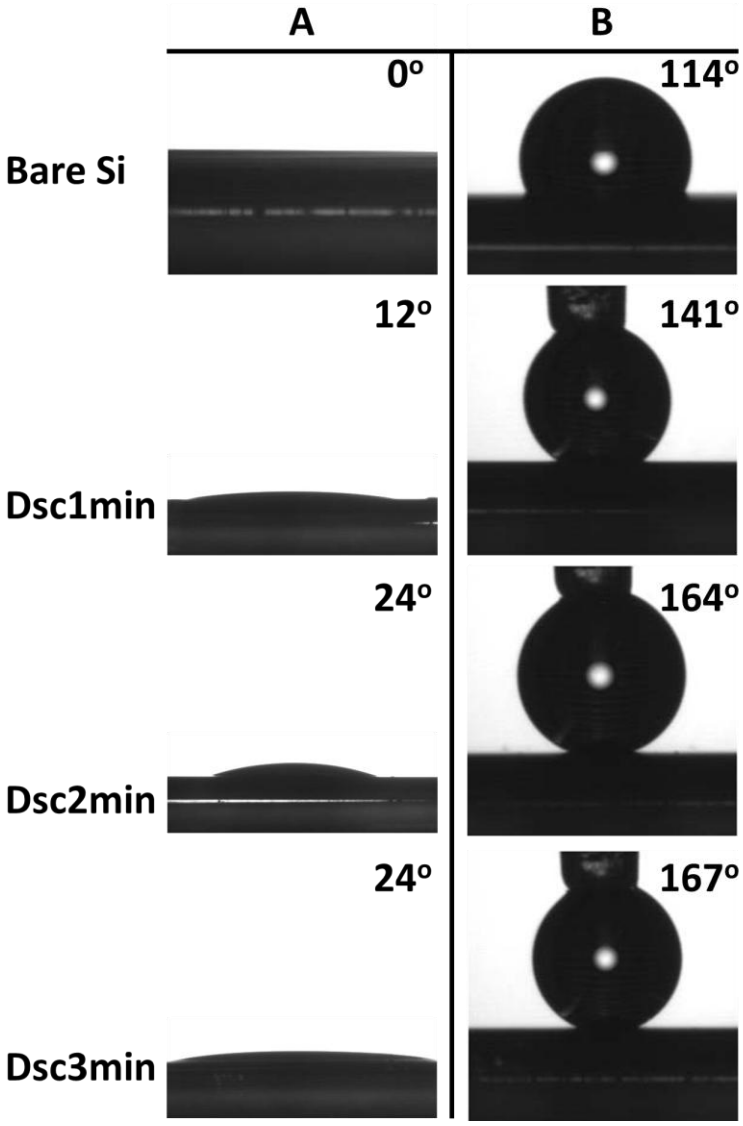

Figure 78 Optical image of water droplet on bare Si surface and Si surface after FESA-MaCE process with different descum time. Column A show the samples after washing in Piranha solution, while Column B show the samples after silane treatment.

7.4 Conclusion

In summary, we demonstrated a facile and low-cost route based on FESA and MaCE techniques to create uniform trenches and gratings with controllable width, heights and spacing distance at microscale. The aspect ratio of the structures was up to 16:1 and lateral edge roughness was below 0.5 μm. The polymer lines formed by FESA, even as thin as 30 nm, can be served as stable etching mask in MaCE during which Si was etched with a depth of 14 μm, yielding a remarkable selectivity of polymer lines over Si as 467:1. The geometry of polymer lines can be effectively adjusted by Ar/O_2 plasma, and in turn control the final etching profiles during MaCE. The 3D profiles were also found to depend on the MaCE conditions, such as the composition of etchant solution and application of electric bias. Interestingly, the geometry of the resulting etching was capable of tuning the surface wettability in a continuous manner. The low-cost nature of FESA and MaCE techniques, together with their compatibility with each other, make the FESA-MaCE route a promising manufacturing strategy for a broad range applications where HAR trenches/microgratings on Si play the key roles. We envision that the microstructures created by FESA-MaCE may open an avenue to judiciously combine MaCE with a variety of polymer self-assembly technologies for producing HAR structures with a broader range of dimensions. For example, when integrating MaCE with the nanoscale block-copolymer self-assembly,[119, 120] high-density vertical Si 2D nanosheets and nanowires may be created for advanced energy storage materials and devices.[121]

CHAPTER 8

WAFER-LEVEL MACE

8.1 Introduction

In previous chapters, the etching profile in MaCE is influenced by the etchant composition and properties of metal catalyst. The critical condition for fabricating HAR uniform microstructures on Si by MaCE has been discussed. Further, we demonstrated the effect of electric bias in controlling the sidewall tapering angle of the etching profile in MaCE. These findings pave the way for application of MaCE in TSV fabrication.

However, all the above results were obtained from MaCE on small pieces of Si. Because fabrication on large Si wafers is preferred to that on pieces of Si in industrial manufacturing, the capability of etching uniform structures across the whole wafer is essential for real application of MaCE. However, the feasibility of etching uniform deep holes in wafer-level has not been explored. It remains a critical and challenging question that how uniform the etching profiles over large wafer can be in wafer-level MaCE.

In this chapter, we demonstrate the feasibility of fabricating high-density TSV with high aspect ratio and excellent geometric uniformity over whole 4-inch Si wafer by MaCE. Because this work only focuses on the method of hole formation, the word “TSV” in the following text only refer to the vertical holes on Si for convenience of discussion. Previously, as an attempt, MaCE for TSV fabrication has been conducted on P-type Si (**Chapter 4**). After MaCE, the sidewall of TSVs were found severely roughened and tapered, unless a cathodic electric bias was applied on the Si during MaCE. It was then discovered that the tapering of sidewall was caused by an electrochemical etching process induced by excessive electron holes, which could be intrinsically passivated in the MaCE of N-type Si [23]. Therefore, TSV with vertical sidewall can be formed on N-type Si by simply immersing the Si in the etchant without cathodic bias. In this case, the complicated

experimental setup for applying bias is not necessary. Here, a facile MaCE method based on the concept of immersion-and-etching for wafer-level TSVs fabrication is presented. The contents in this chapter have been partially published in [122] and reprinted here with permission. Copyright 2015, IEEE.

8.2 Methods

All the chemicals were purchased from VWR International and used without further processing. N-type single crystalline Si wafers ((100)-oriented, phosphorus-doped, resistivity: 1-10 Ω cm, diameter: 10 cm (4 inch), thickness: 500 μm) were purchased from University Wafers, MA. Si wafers were cleaned by Piranha solution (H_2SO_4 (96 wt. %) and H_2O_2 (30 wt. %) with a volumetric ratio of 1:1) at 120 ^oC for 10 min. After dried in the N_2, a layer of photoresist (Futurrex NR9-1500PY) was spun cast on the Si and exposed under 365 nm light with a mask aligner (Karl Suss MA6). After exposure and developing, the thickness of photoresist was measured to be 1.50±0.10 μm. The patterned Si was cleaned by oxygen plasma in a RIE system (Advanced Vacuum Vision). Then Au was deposited as the catalyst for MaCE by an electron-beam evaporator (Denton Explorer) at a rate of 0.5Å/s in a vacuum of 3.0×10^{-6} Torr. Au was deposited on one wafer per batch. For Au deposition by sputtering, a Denton Desk II TSC DC sputtering system was used. MaCE experiments was conducted in a closed opaque plastic container with a Teflon-coated magnetic stirrer. A home-made plastic wafer carrier was used to hold the wafer in the etchant. The etchant solution was prepared by well mixing of 240.0 g deionized water, 200.0 mL H_2O_2 (30 wt.%), and 200.0 mL HF (10 wt.%). The etching was started by applying 1 mL etchant solution on the Si wafer for pre-etching of 3 min, and then immersing the wafer completely in the etchant solution (the 3 min pre-etching time is included in the overall etching time mentioned below). All the MaCE experiments were conducted at room temperature, where Si wafers were placed horizontally in the container with the Au side facing up. In the MaCE experiments with stirring of etchant solution, the

stirring started 30 min after the start of etching and proceeded at a constant rate of 350 rpm until the end of etching.

After MaCE, photoresist and Au were removed by acetone and potassium iodide (KI)/iodine (I_2) aqueous solution, respectively. The optical microscope (OM) and SEM images were obtained from an Olympus MX61 OM and a Hitachi SU8010 SEM or a SU8230 SEM equipped with an Oxford energy dispersive spectrum (EDS) detector, respectively. The cross-sectional SEM images were acquired by mechanical cleaving the Si wafers after etching and photoresist removal. The depth of TSV at different positions on the wafer is calculated by averaging 3 independent measured values at each position. The atomic force microscope (AFM) image was obtained from a Veeco Dimension Edge AFM with MP11100-10 tips. The polymer replica were fabricated by dropping the polymer mixture (17g EPON Resin 862, Hexion Special Chemicals Inc.; 20 g Lindride 52D, Lindau Chemicals; one drop of imidazole catalyst, Shikoku) on the surface of Si wafers after etching. The polymer on Si is cured at 150 ^{o}C in an oven with vacuum of 3.4 kPa for 2 hr. The replica was then isolated from Si by complete removal of Si in the mixture of HNO_3 (70 wt. %), HF (49 wt. %) and H_2O with a volumetric ratio of 1:1:1 for 10 min.

For copper filling of TSV, the Si sample after MaCE is immersed in acetone and the KI/I_2 aqueous solution to remove the photoresist and Au, respectively. Then a layer of SiO_2 was deposited on the surface of Si sample by a plasma-enhanced chemical vapor deposition tool (Oxford PECVD). Titanium (Ti) and copper (Cu) was sputtered sequentially on the SiO_2 layer as the seed layer for copper electroplating by a Denton Discovery sputtering tool. The TSV was finally filled by Cu through electroplating in a commercial plating bath provided by Dow Chemical with a potentiostat (Versastat, Princeton Applied Research) as the power source.

For Cu compatibility test, an array of 5×5 μm^2 Cu squares were fabricated on Si substrate by photolithography and electron beam evaporation as mentioned above. A Ti layer was used between copper and the Si substrate to enhance the adhesion. The nominal

thickness of Ti and Cu were 10 nm and 100 nm, respectively. The actual total thickness of Ti/Cu squares were measured as 139±2 nm by AFM. Then a layer of photoresist (Futurrex NR9-1500 PY) was spun cast on the Si sample to cover all the surface area. The edge part of the surface was further covered by polyimide tape (~60 μm thick, from VWR International). The sample was immersed in the same HF-H_2O_2 etching bath used for MaCE for 30 min. Finally the sample surface was characterized by SEM and AFM after removal of photoresist and polyimide tape.

8.3 Results and Discussion

The overall processing flow for TSV etching by MaCE is illustrated in **Figure 79**. In order to study the etching results at different positions across the whole wafer, a Cartesian CS is established. The geometric center of the wafer is set as the origin (0,0) of the CS, while its *y*-axis points from the primary cut of the wafer to its secondary cut (**Figure 79** (a)). Si wafers after photolithography are inspected under optical microscope (OM). Circular patterns with diameter of 28 μm and pitch size of 80 μm can be clearly observed (**Figure 80** (a) and (b)). The diameter of patterns is uniform across the whole wafer (**Table 10**). Based on the pitch size, the number of patterns over the whole Si wafer can be estimated to be ~1 million. Due to the resolution limitation of photolithography, the pattern edge has a submicrometer-scale deviation from perfect round shape (**Figure 80** (c)). After deposition of Au, Si inside the patterns is in direct contact with Au, while the other part is covered by photoresist. The thickness of Au catalyst is measured as 11.9 nm by AFM (**Figure 80** (d)). A nanoporous morphology of Au catalyst is revealed by both SEM (**Figure 80** (c) inset) and AFM (**Figure 80** (d)). The nanoporous morphology of Au catalyst ensures the stable movement of the catalyst during MaCE by transport of etchant solution through catalyst. It should be noted that the way of Au deposition has an influence on the MaCE results. As shown in **Figure 80** (e), if the Au is deposited by sputtering method, the sidewall of photoresist is coated with Au. These Au has a chance to move into Si substrate during

MaCE and causes sidewall roughening (data not shown). In contrast, if the Au is deposited by evaporation, the sidewall of photoresist is not coated with Au (**Figure 80** (f)). Thus, the Au in all the samples that are used in the following MaCE experiments is deposited by evaporation.

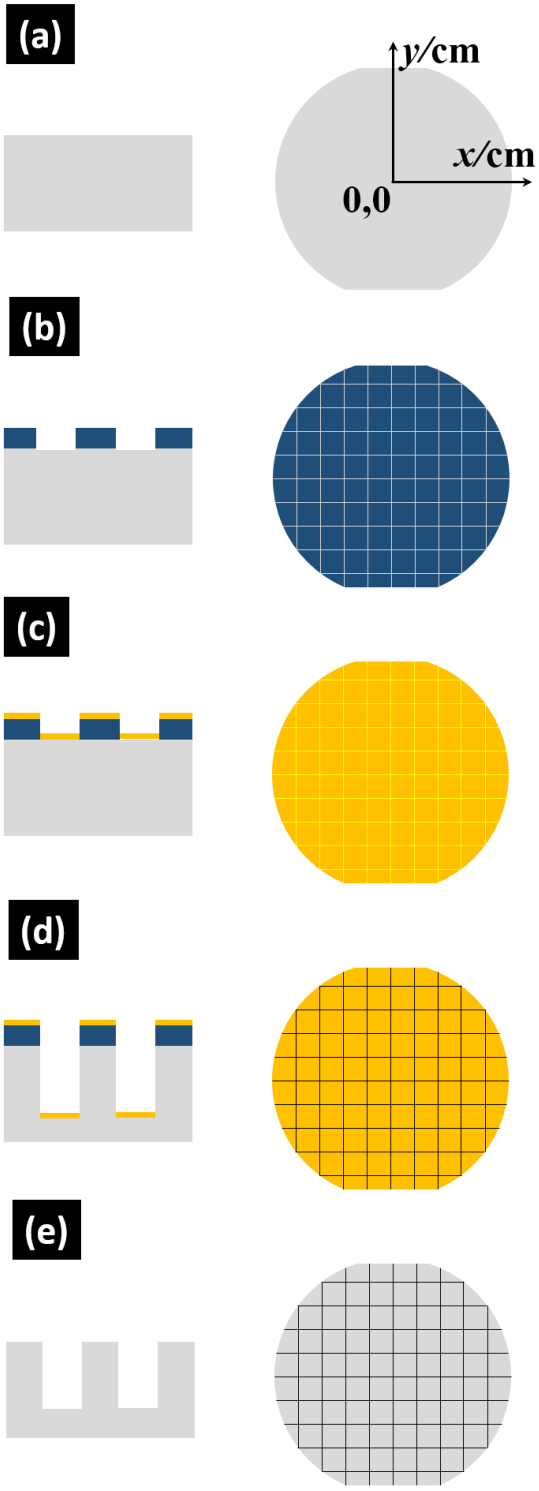

Figure 79 Schematic processing flow for TSV fabrication by MaCE: (a) cleaning of bare Si; (b) photolithography; (c) metal deposition; (d) MaCE; (e) removal of photoresist and metal.

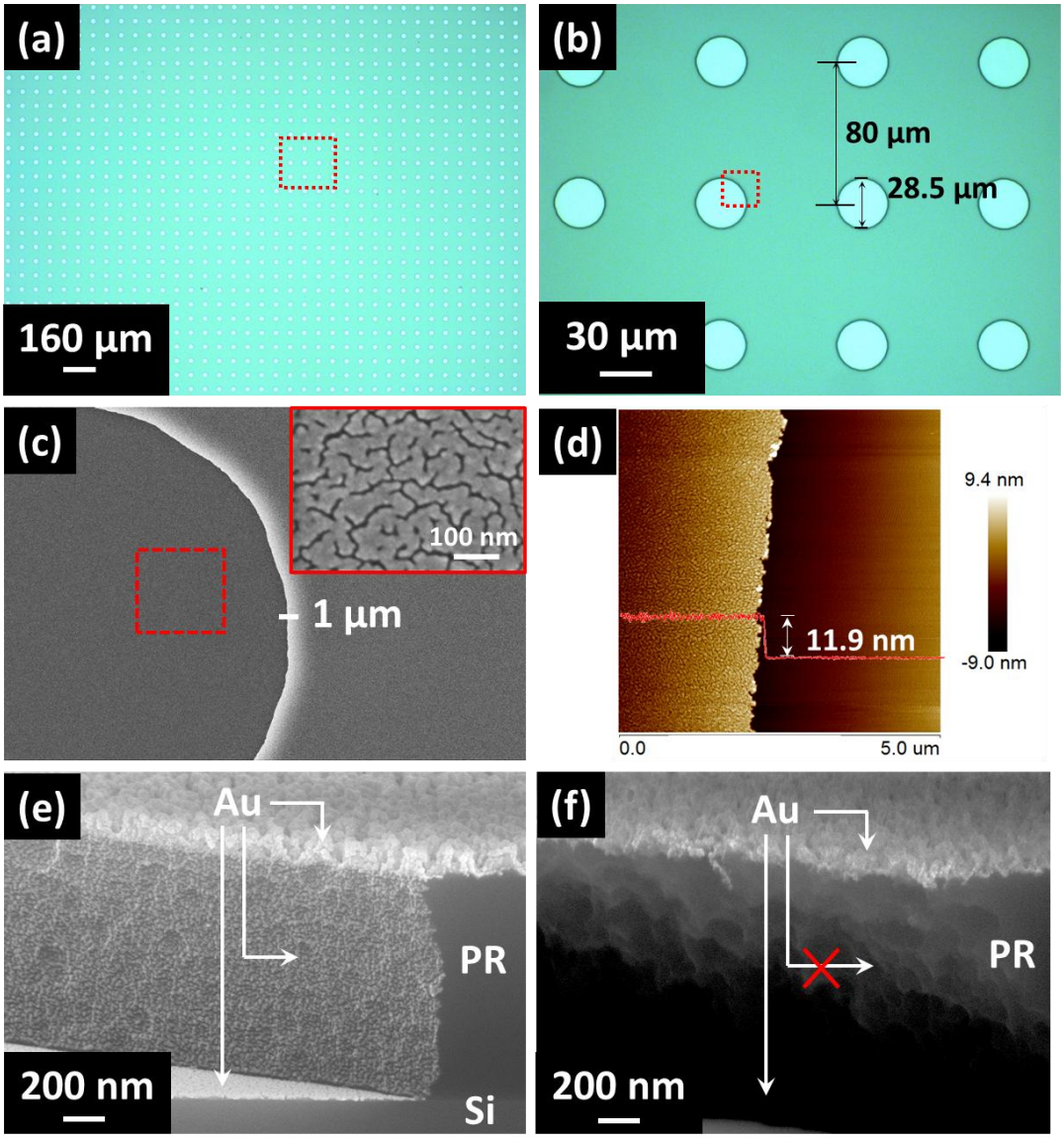

Figure 80 (a) Optical microscope (OM) image of Si wafers after photolithography; (b) enlarge OM image of the red circle in (a); (c) SEM image of the red circle in (b), inset shows the enlarged SEM of the red circle in (c); (d) AFM image and cross section of the red circle in (c); (e) cross-sectional SEM image of the Si sample after photolithography and Au deposition by sputtering. Au can be observed on top of the photoresist (PR) and Si, as well as the sidewall of the PR; (f) cross-sectional SEM image of the Si sample after photolithography and Au deposition by evaporation. Au can be observed on top of the photoresist (PR) and Si. No Au can be observed on the sidewall of PR, which is blurred under SEM due to the charging effect.

Table 10 Diameter of patterns after lithography and thickness of Au across 4-inch Si wafers.

Coordinate[1]	Diameter[2] (μm)		Thickness[3] (nm)	
	Ave.[4]	Std.[5]	Ave.	Std.
-4,0	28.68	0.22	12.1	0.15
-3,0	28.56	0.22	12.1	0.15
-2,0	28.48	0.06	12.0	0.25
-1,0	28.28	0.32	12.0	0.26
0,0	28.66	0.4	11.8	0.17
1,0	28.39	0.29	11.8	0.20
2,0	28.62	0.13	11.8	0.26
3,0	28.62	0.13	11.9	0.17
4,0	28.03	0.17	11.7	0.21
0,4	28.34	0.22	12.1	0.06
0,3	28.59	0.3	12.1	0.25
0,2	28.45	0.12	12.0	0.20
0,1	28.11	0.22	11.9	0.44
0,0	28.82	0.11	12.1	0.10
0,-1	28.37	0.17	11.7	0.10
0,-2	28.57	0.11	11.8	0.20
0,-3	28.88	0.17	11.3	0.15
0,-4	28.48	0.24	11.2	0.06

To demonstrate the idea that TSV with vertical sidewall can be formed by MaCE without electric bias on N-type Si, we first did a MaCE test on a 1×5 cm^2 Si slice. The slice was cut from a whole Si wafer with patterned Au catalyst mentioned above. After simply immersing the slice in the etchant for 2 h, Au in the patterns moved vertically into the Si (**Figure 81** (a)) and kept flat after etching. TSV with perfect vertical sidewall and depth of 85 μm could be observed (**Figure 81** (b)).The top opening width of the TSV is 28 μm, following the diameter of the patterns defined by photolithography. The sidewall and top surface of Si that is covered by the photoresist appear smooth and clean, indicating that no excessive etching occurred in this region. In contrast, if a P-type Si was used, the sidewall

and top surface of Si would become porous under the same etching. The result confirms that in MaCE of N-type Si, the etching on the sidewall of TSV is intrinsically suppressed, consistent to the results in **Chapter 5**.

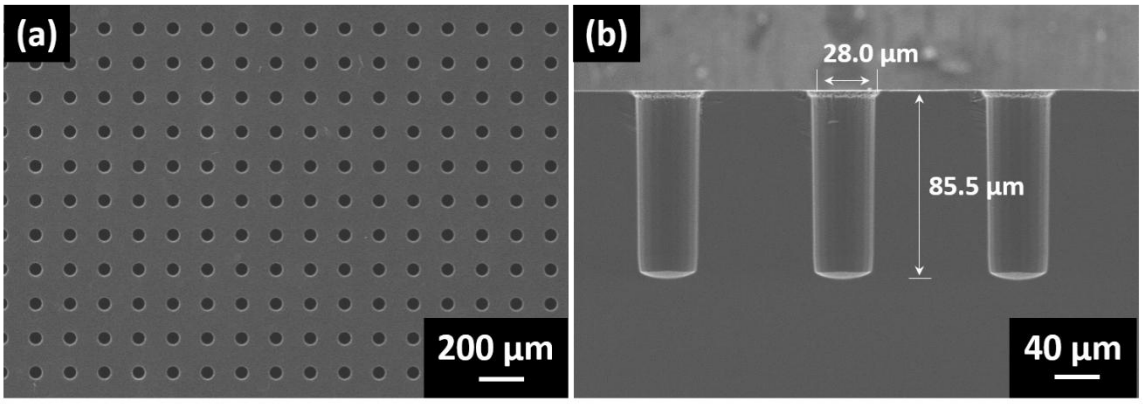

Figure 81 (a) Top-view and (b) cross-sectional SEM images of a 1 ×5 cm2 Si slice after MaCE of 2 h.

It should be noted that the uniformity of Au catalyst across the whole wafer critically influences the uniformity of etching in wafer level. As shown in **Figure 82**, in MaCE of Si slices, when the thickness of Au is reduced to 11.0 nm, Si inside TSV is not completely etched and some spikes of Si remain at the bottom of the TSV; when the thickness is increased to 13.5 nm, Au catalyst wrinkles and the sidewall adopts a randomly-curved profile. The result indicates that a deviation of 1 nanometer in Au thickness has a significant influence on the etching results.

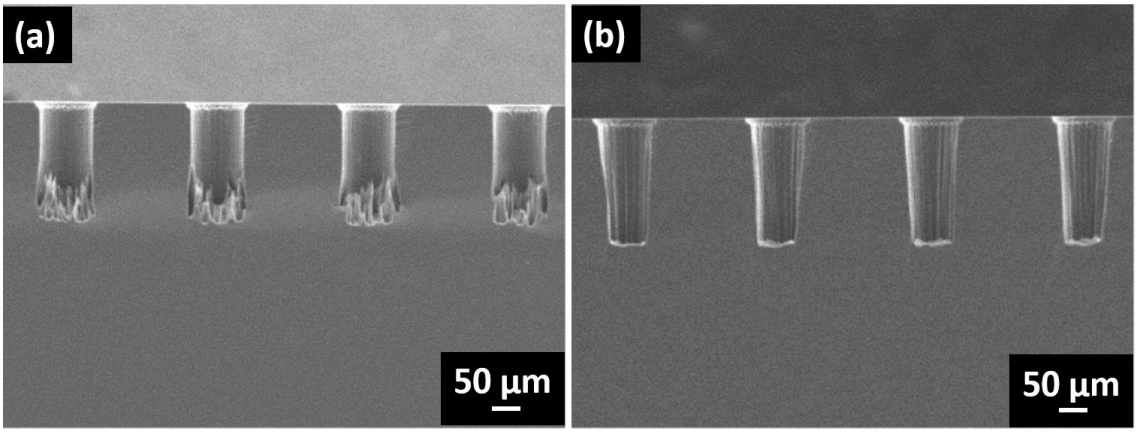

Figure 82 Cross-sectional SEM images of 1×5 cm2 Si slices after MaCE of 2 h with an average Au thickness of (a) 11.0 nm and (b) 13.5 nm.

By optimization of Au deposition condition, a narrow distribution of Au thickness around 11.9 nm is achieved. As shown in **Table 10**, the standard deviation of the Au thickness over the whole wafer is 0.25 nm. In this work, the standard deviation of Au thickness on different wafers is also controlled within 0.3 nm. Based on the result shown in **Table 10**, it is expected that the same TSV can be formed across the whole Si wafer when it is immersed into the same etchant. **Figure 83** (a) shows a whole Si wafer after MaCE of 2 h. Under visual inspection, the wafer surface remains the shining greenish purple color as that before MaCE, indicating no lift-off of the photoresist during MaCE. This result is consistent with our previous finding, confirming that a thin layer of photoresist is able to serve as a good mask layer for MaCE over long time. In contrast, in DRIE, photoresist tends to be consumed during the etching. A hard mask, such as Si oxide or nitride, is typically required in DRIE, which adds cost to the processing. When the photoresist is removed by acetone, the surface of the wafer shows the color of original bare Si as shinning greyish, indicating a minimized damage on the Si top surface (**Figure 83** (b)). Grid marker lines could also be observed on Si surface, which divided the wafer

surface into 1×1 cm^2 squares for further SEM characterization. The result of visual inspection in **Figure 83** is consistent with the results in **Figure 81**, further supporting that the etching on the sidewall and Si top surface is suppressed in MaCE of N-type Si.

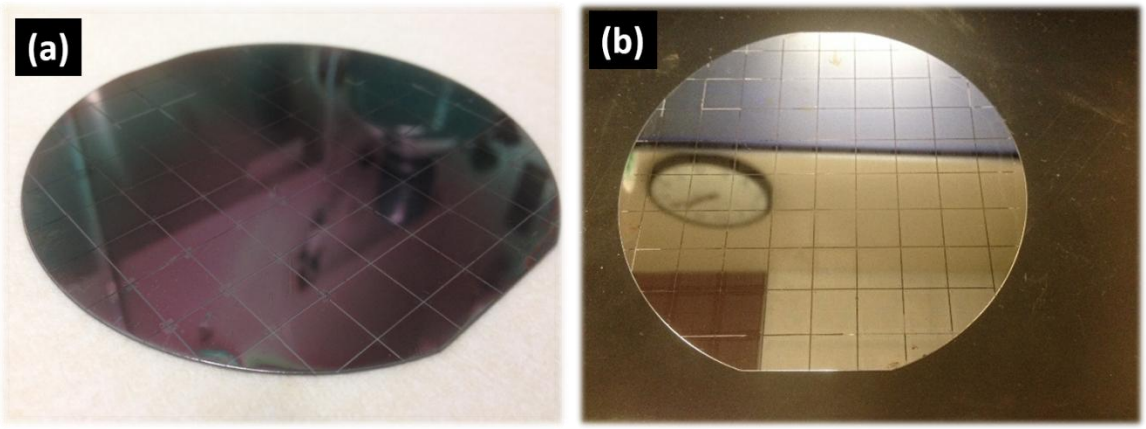

Figure 83 (a) A whole Si wafer after MaCE of 2 h. (b) shows the wafer in (a) after lift-off of photoresist.

However, when the cross sections at different positions of the wafer are viewed under SEM, TSV with non-uniform geometry can be observed (**Figure 84**). In the area near the wafer edge (referred to as "edge area", such as (1,5), (5,1) and etc.), TSV are deep and vertical with depth of 60-70 μm. In the area near the wafer center (referred to as "center area", such as (1,1), (1,2) and etc.), however, Au catalyst significant wrinkles and the sidewall of TSV randomly curved. The depth of TSV in this region is only 20 μm. Considering the fact that the Au thickness in the center area and edge area are nearly identical, the difference of etching results over the wafer should not be caused by the Au thickness variation. Here we propose that the difference in the etching behaviors at different positions is caused by the inefficient mass transport in the etchant solution. Ideally,

once the etchant is consumed on the Au surface, new etchant will be quickly replenished from the bulk solution, so that Au is able to keep moving into Si with a constant etchant concentration on its surface. Given the fact that the etchant is kept static in all above MaCE experiments, the etchant can be transported from the bulk solution to the Au surface only through diffusion. Compared to the MaCE of 1×5 cm^2 Si slice, more Si is etched in the wafer-level MaCE and a much higher amount of etchant is consumed. Because the size of Si wafer is large, it is more difficult for etchant to diffuse to the center than to the edge area (**Figure 85** (a)). Thus, the difference between the actual etchant concentration in the center area and that in the edge area can induce the different etching behaviors. To confirm this point, we conducted wafer-level MaCE experiments with stirring of the etchant solution. The transport of the etchant can be facilitated be the convection flow of the solution during the stirring. Two stirring schemes were adopted: the "edge-stir" scheme, where the stirrer was put on the edge of the wafer in the second quadrant of the CS and spun horizontally at the same height of wafer (**Figure 85** (b)); the "center-stir" scheme, where the stirrer was put at the center of the wafer and spun horizontally below the wafer.

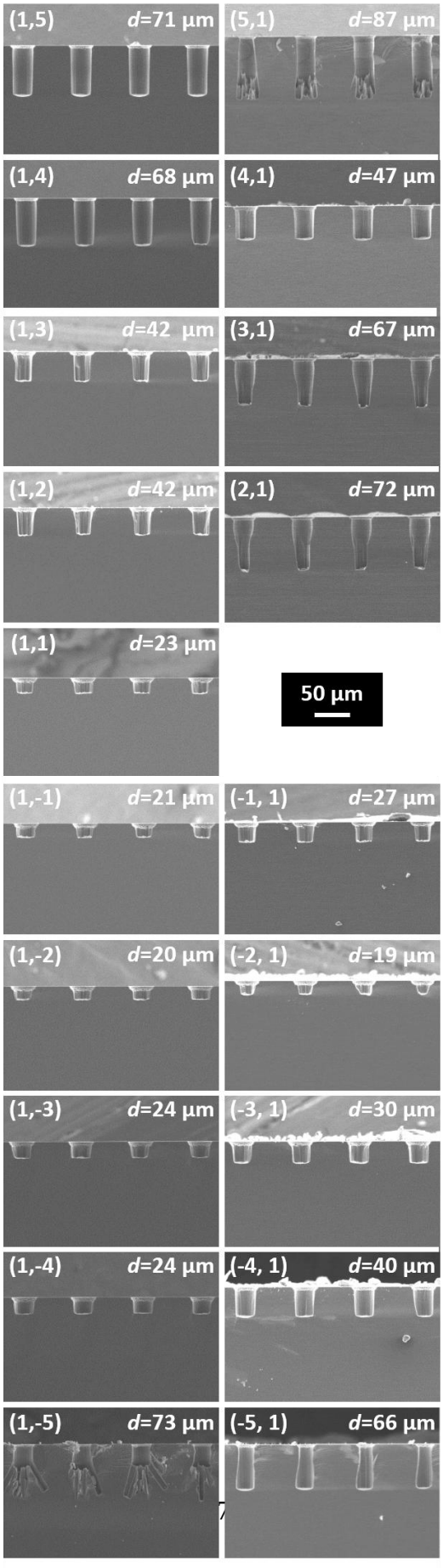
(1,5) d=71 µm
(5,1) d=87 µm
(1,4) d=68 µm
(4,1) d=47 µm
(1,3) d=42 µm
(3,1) d=67 µm
(1,2) d=42 µm
(2,1) d=72 µm
(1,1) d=23 µm
50 µm
(1,-1) d=21 µm
(-1, 1) d=27 µm
(1,-2) d=20 µm
(-2, 1) d=19 µm
(1,-3) d=24 µm
(-3, 1) d=30 µm
(1,-4) d=24 µm
(-4, 1) d=40 µm
(1,-5) d=73 µm
(-5, 1) d=66 µm

Figure 84 Cross-sectional SEM images of Si wafers after MaCE of 2 h without stirring. The coordinates of the position and the depth (*d*) of TSV are labeled in each image. The coordinates are defined in **Figure 79** (a). The same in the following figures.

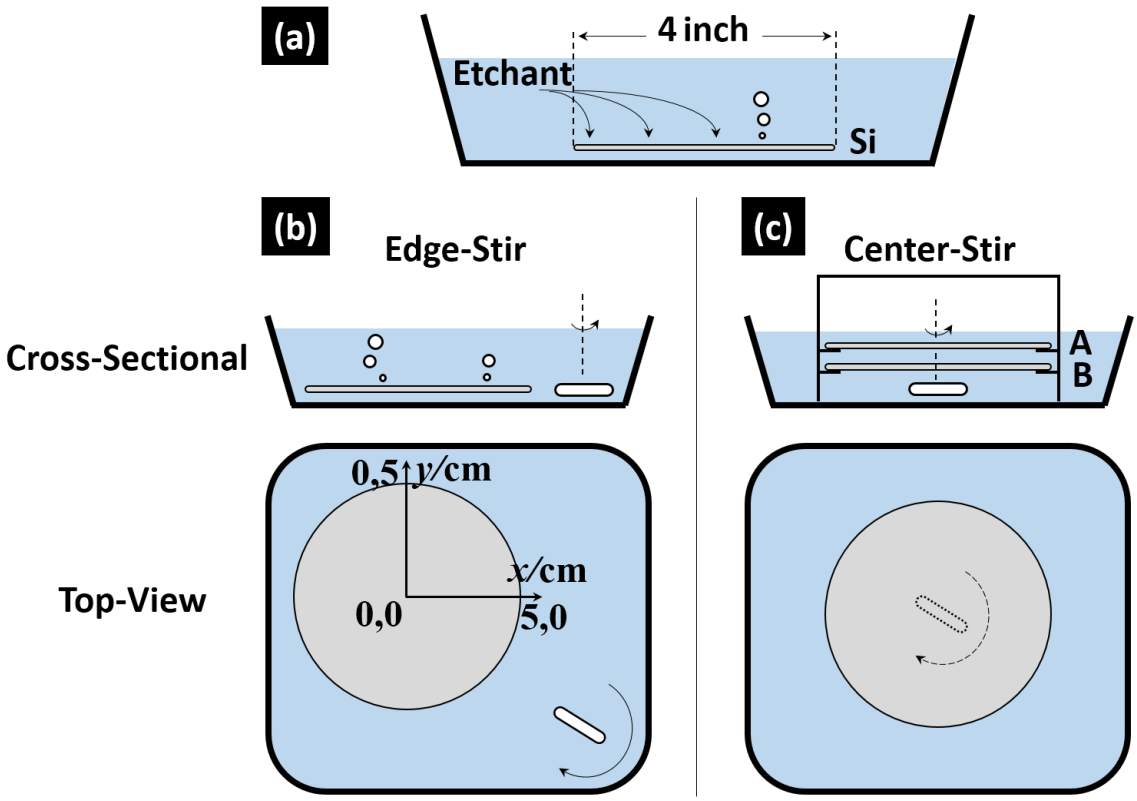

Figure 85 Schematics of stirring scheme during MaCE. (a) No stirring of etchant solution. (b) Corner-stir: the stir bar is put at the corner of the Si wafer and at the same height of Si. The stirrer spins horizontally; (c) Center-stir: the stir bar is put at the center of the Si wafer and below the Si. The stirrer spins horizontally.

Cross-sectional SEM images of the wafer after MaCE of 2 h under the edge-stir scheme are shown in **Figure 86**. In contrast to the results in **Figure 84**, here TSV with vertical sidewall were formed over the whole wafer, except in a small part of edge area (at position -5, 1). The range of TSV depth is narrowed down to 52-80 μm. However, in MaCE under the edge-stir scheme, the depth of TSV at the positions of (-1,1) to (-5,1) is lower than those in other parts. Because the stirrer spins at the edge of wafer, the flow of etchant may not be symmetric over the wafer and the actual etchant concentration at each position may be different. In this sense, the uniformity of TSV over the wafer can be further improved by using the center-stir scheme. As shown in **Figure 87**, the range of TSV depth is further narrowed down to 70-74 μm. Incomplete etching of Si inside TSV is observed at two position in the edge area: (5,1) and (1,-5). The etching depth in these two region is defined as the maximum penetrating depth of catalyst in the vertical direction. The effect of stirring on the etching uniformity supports the point that when the Au thickness over the whole wafer is uniform, the etching uniformity is influenced by the mass transport of etchant.

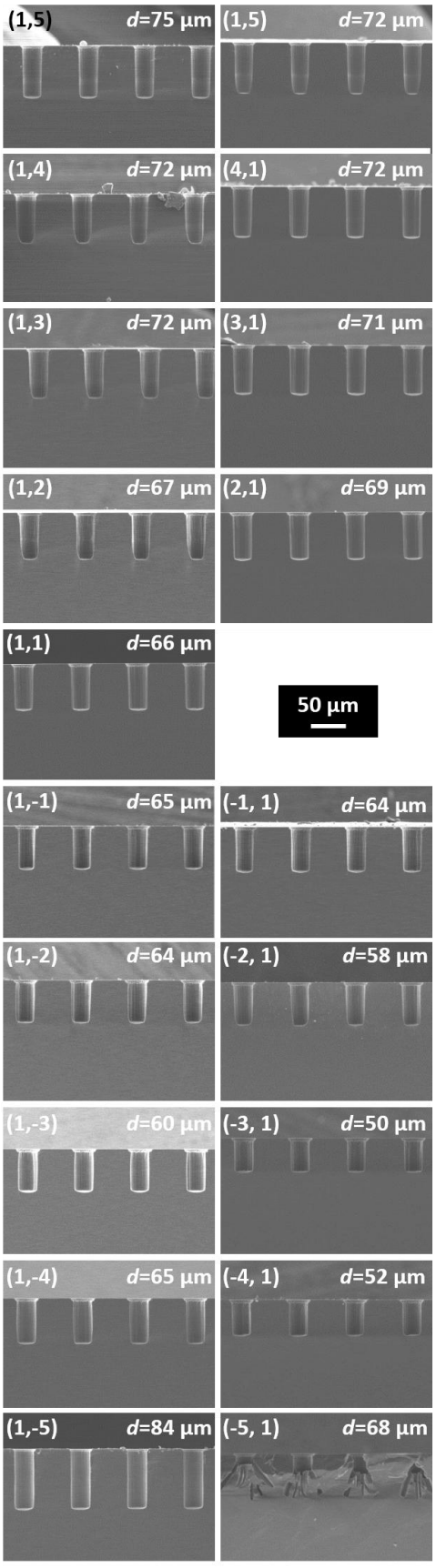
(1,5) d=75 µm
(1,5) d=72 µm
(1,4) d=72 µm
(4,1) d=72 µm
(1,3) d=72 µm
(3,1) d=71 µm
(1,2) d=67 µm
(2,1) d=69 µm
(1,1) d=66 µm
50 µm
(1,-1) d=65 µm
(-1, 1) d=64 µm
(1,-2) d=64 µm
(-2, 1) d=58 µm
(1,-3) d=60 µm
(-3, 1) d=50 µm
(1,-4) d=65 µm
(-4, 1) d=52 µm
(1,-5) d=84 µm
(-5, 1) d=68 µm

Figure 86 Cross-sectional SEM images of Si wafers after MaCE of 2 h under "edge-stir" scheme. The coordinates of the position and the depth (*d*) of TSV are labeled in each image.

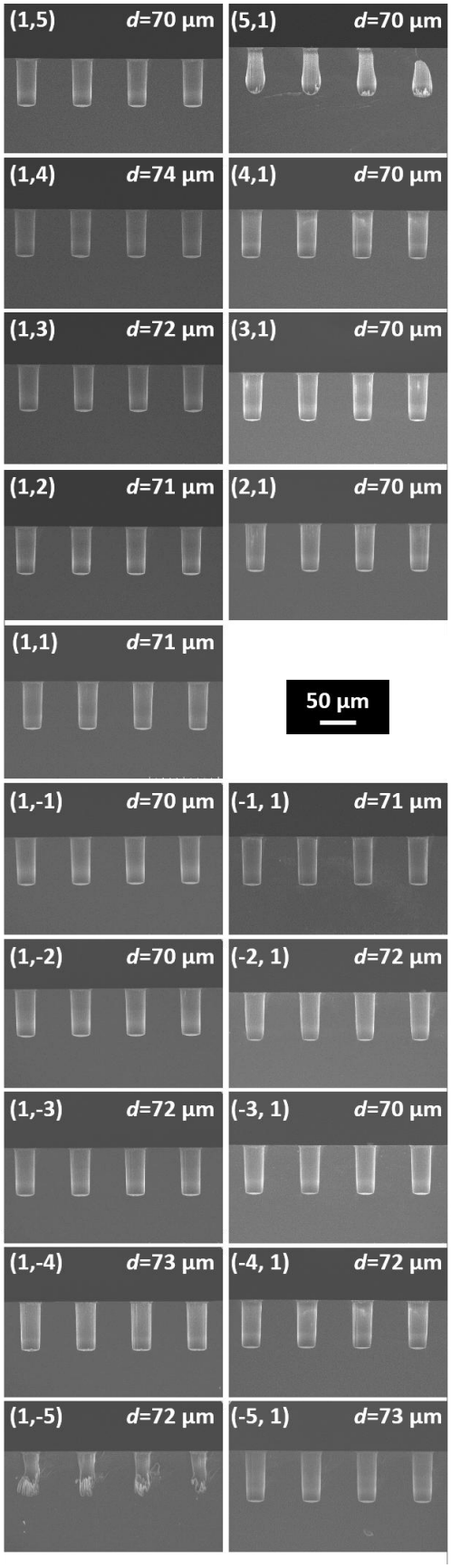
(1,5) d=70 µm
(5,1) d=70 µm
(1,4) d=74 µm
(4,1) d=70 µm
(1,3) d=72 µm
(3,1) d=70 µm
(1,2) d=71 µm
(2,1) d=70 µm
(1,1) d=71 µm
50 µm
(1,-1) d=70 µm
(-1, 1) d=71 µm
(1,-2) d=70 µm
(-2, 1) d=72 µm
(1,-3) d=72 µm
(-3, 1) d=70 µm
(1,-4) d=73 µm
(-4, 1) d=72 µm
(1,-5) d=72 µm
(-5, 1) d=73 µm

Figure 87 Cross-sectional SEM images of Si wafers after MaCE of 2 h under "center-stir" scheme. The coordinates of the position and the depth (d) of TSV are labeled in each image.

Under the same condition, when the etching time is elongated to 4 h, the depth of TSV increases to 159-164 μm (**Figure 88**), corresponding to a high aspect ratio over 5:1. Although the incomplete etching area slightly expands, impressive uniformity of the TSV in various dimension scale is achieved. **Figure 89** (a) shows the cross-sectional SEM images of the TSV over one 1×1 cm^2 area, which clearly demonstrates the uniform geometry of multiple adjacent TSV in parallel. Each TSV bears highly vertical and smooth sidewall (**Figure 89** (b)). Furthermore, when the sidewall is viewed under SEM with high magnification, a surface roughness below 50 nm can be observed (**Figure 89** (c)). Low sidewall surface roughness has been identified as the key factor for low leakage current and high reliability of TSV.[49] The ultra-low surface roughness in MaCE is originated from the nature of MaCE that the etching proceeds with the continuous movement of Au. In comparison, sidewall always bears roughness with scalloping features in conventional DRIE, due to its nature of pulsed etching manner.

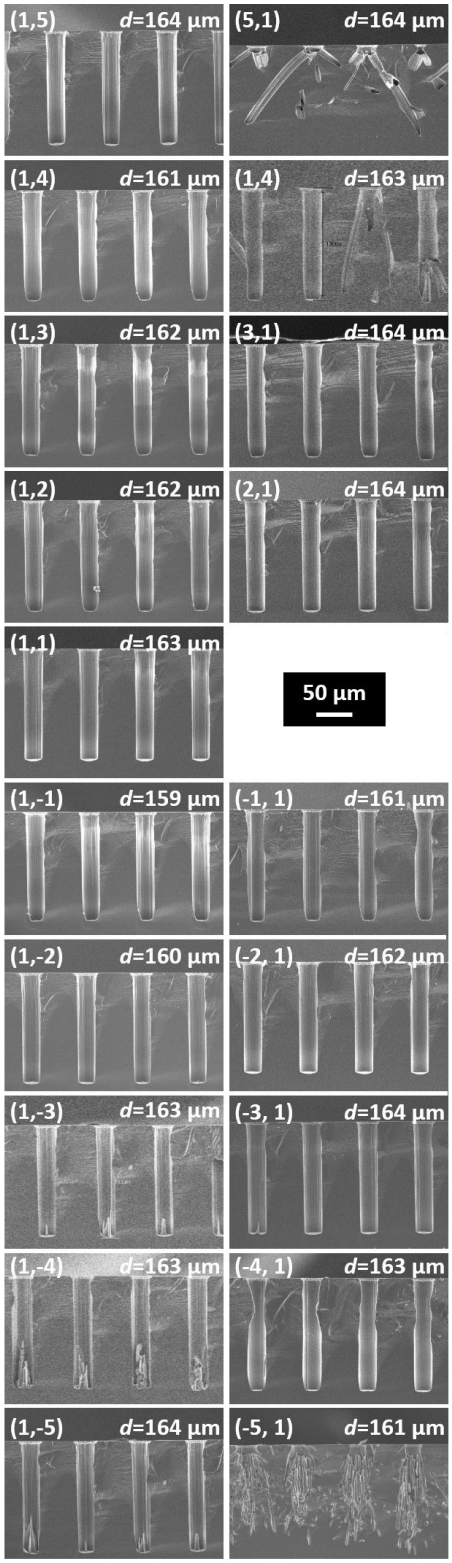

Figure 88 Cross-sectional SEM images of Si wafers after MaCE of 4 h under "center-stir" scheme. The coordinates of the position and the depth (d) of TSV are labeled in each image.

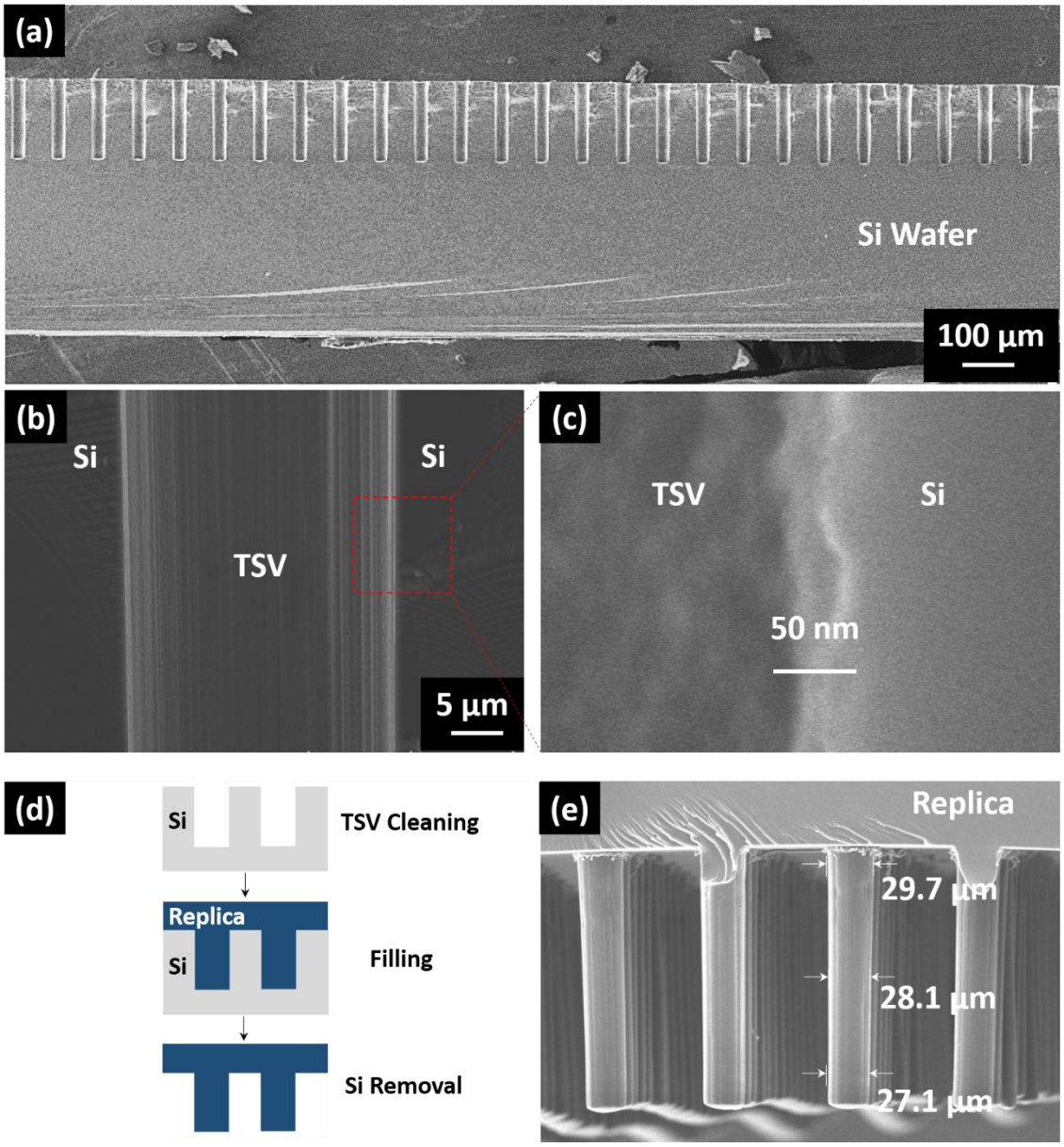

Figure 89 (a) SEM image of TSV by MaCE of 4 h at position (1,1). (b) Magnified cross-sectional SEM image of the middle of TSV shown in Fig. 10 at position (1,1). (c) SEM image of the red circle in (a). (d) Schematic processing flow for replica fabrication. (e) Cross section of the replica from TSV shown in (a).

Because the cross section of the TSV are prepared by mechanical cleaving, some TSV are only partially exposed under SEM observation. To reveal the real 3D geometry of the TSV, replica of the TSV was made by filling polymer into the TSV and removing the Si (**Figure 89** (d)). The cross section of the replica is shown in **Figure 89** (e). The geometry of replica reflects that the TSV possess uniform overall 3D geometry with highly vertical alignment towards the top surface of Si. The diameter of TSV at different height fall in the narrow range of 27.1-29.7 μm.

Another distinctive advantage of wet etching is the capability of processing multiple wafers in the same batch, which can hardly be achieved in DRIE. As a preliminary test, we did MaCE of two wafers simultaneously under the center-stir scheme. The wafers were stacked coaxially on top of each other by a wafer carrier. The top wafer and bottom wafer were named as wafer **A** and **B**, respectively (**Figure 85** (c)). The spacing between **A** and **B** was 5 mm. After MaCE of 4 h, uniform vertical TSV could be observed on both wafers (**Figure 90** and **Figure 91** respectively), similar to those in **Figure 88**. The depth of TSV on wafer **A** and **B** fall in the narrow range of 143-155 μm and 137-155 μm, respectively. However, compared to the results of single wafer etching in **Figure 88**, incomplete etching of Si expands to larger area on both wafer **A** and **B**. The increased amount of incompletely-etched TSVs may be caused by the fact since the amount of Si to be etched is increased in the double-wafer MaCE, the given amount of etchant may be insufficient or the mass transport may be less effective. By optimizing the amount of etchant as well as the wafer carrier setup in the future work, more TSV are expected to be completely etched in multiple-wafer MaCE.

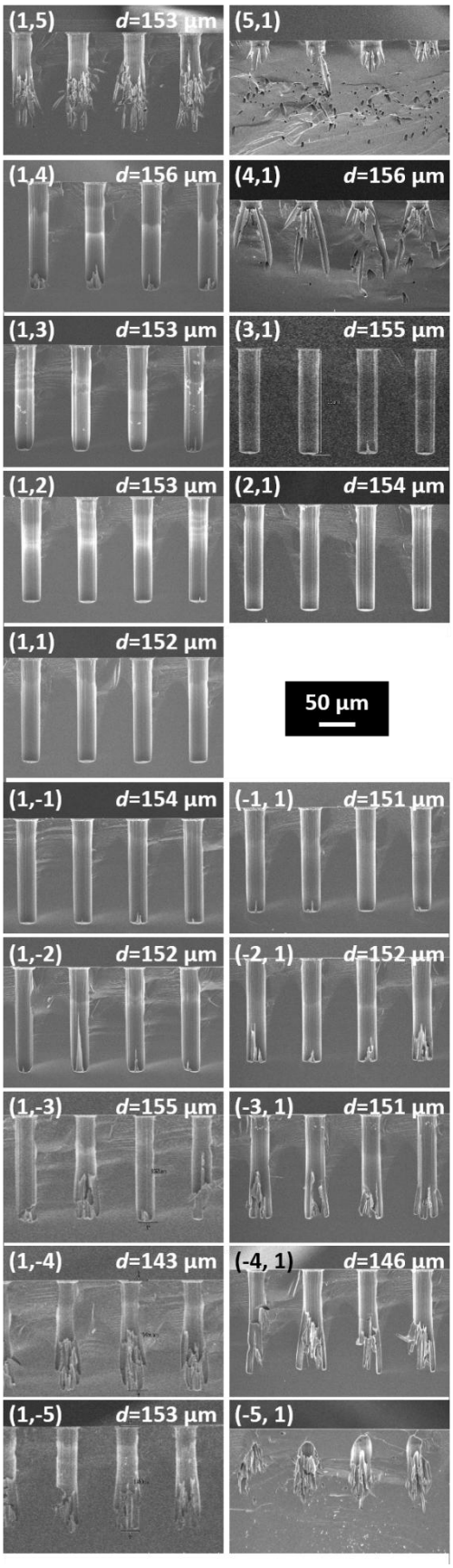
(1,5) d=153 µm
(5,1)
(1,4) d=156 µm
(4,1) d=156 µm
(1,3) d=153 µm
(3,1) d=155 µm
(1,2) d=153 µm
(2,1) d=154 µm
(1,1) d=152 µm
50 µm
(1,-1) d=154 µm
(-1, 1) d=151 µm
(1,-2) d=152 µm
(-2, 1) d=152 µm
(1,-3) d=155 µm
(-3, 1) d=151 µm
(1,-4) d=143 µm
(-4, 1) d=146 µm
(1,-5) d=153 µm
(-5, 1)

Figure 90 Cross-sectional SEM images of the top Si wafer (wafer A) after MaCE of 4 h on two Si wafers under the “center-stir” scheme. The coordinates of the position and the depth (d) of TSV are labeled in each image.

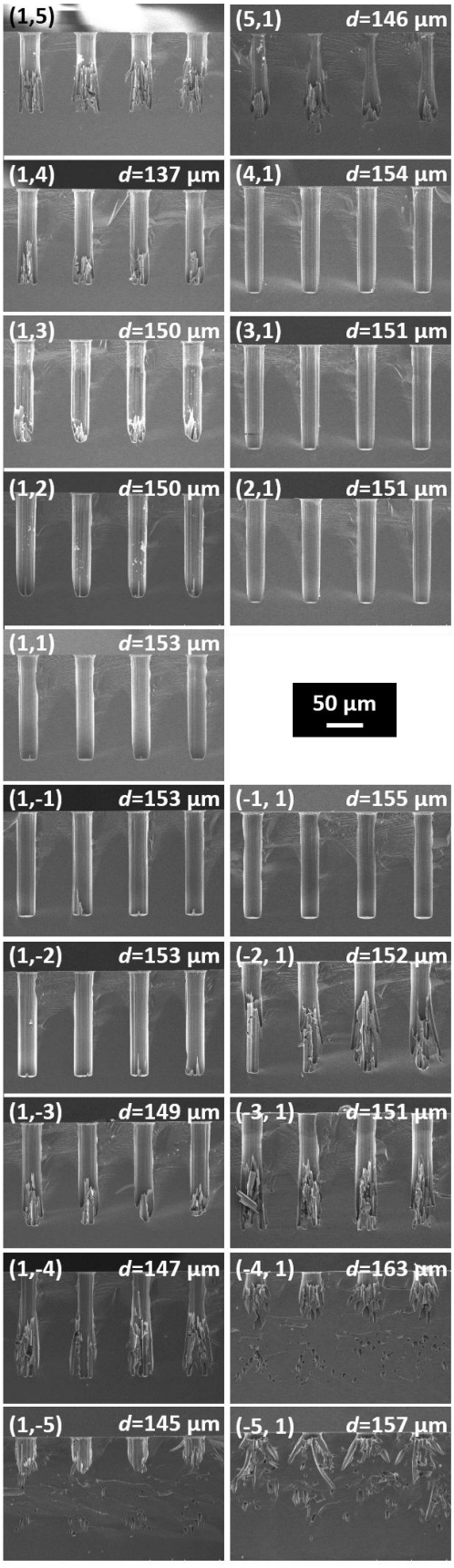
(1,5)
(5,1) d=146 µm
(1,4) d=137 µm
(4,1) d=154 µm
(1,3) d=150 µm
(3,1) d=151 µm
(1,2) d=150 µm
(2,1) d=151 µm
(1,1) d=153 µm
50 µm
(1,-1) d=153 µm
(-1, 1) d=155 µm
(1,-2) d=153 µm
(-2, 1) d=152 µm
(1,-3) d=149 µm
(-3, 1) d=151 µm
(1,-4) d=147 µm
(-4, 1) d=163 µm
(1,-5) d=145 µm
(-5, 1) d=157 µm

Figure 91 Cross-sectional SEM images of the bottom Si wafer (wafer B) after MaCE of 4 h on two Si wafers under the "center-stir" scheme. The coordinates of the position and the depth (d) of TSV are labeled in each image.

The above results show the successful etching of TSV with diameter of 29 μm. In **Figure 92**, we show uniform holes as large as 210 μm and as small as 6 μm can be formed by the same MaCE method on 1×1 cm^2 Si substrate. In wafer-level MaCE of TSV with different diameter, it is expected that etching uniform features with smaller diameter and higher aspect ratio is more challenging, because the diffusion of etchant into the etched holes is becoming more difficult.

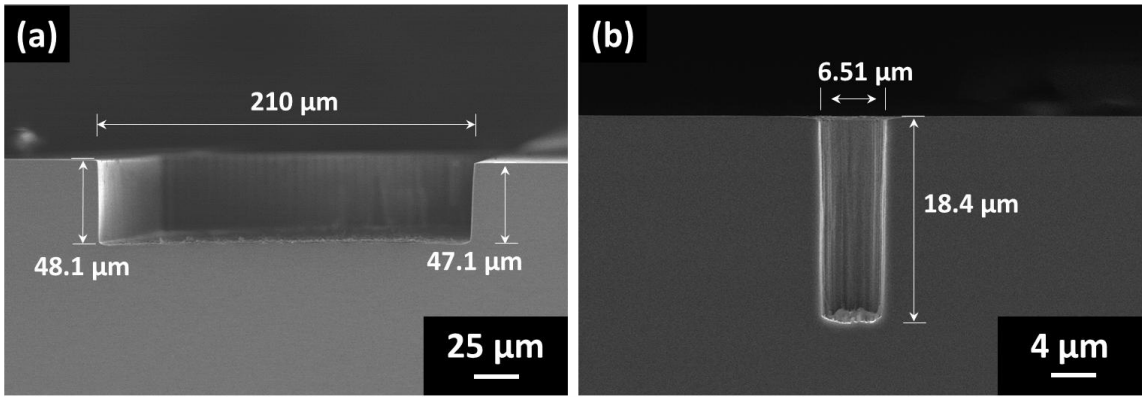

Figure 92 (a) Vertical holes with designed width of 200 μm after MaCE of 1 hr. (b) Vertical holes with designed width of 6 μm after MaCE of 1 hr. Results in both figures are obtained from MaCE on 1×1 cm^2 Si substrates.

The compatibility of MaCE with other processing and components in the overall fabrication flow of Si interposer is essential for the application of the reported method. It should be noted that for the overall fabrication flow can adopt different sequence, such as the "via first" approach and "via last" approach. In the "via first" approach, TSV is etched on the bare Si substrate, followed by passivation layer deposition and conductive filling. To demonstrate the compatibility of MaCE with these two processes, we used plasma-enhanced chemical vapor deposition (PECVD) to coat a layer of SiO_2 on the Si substrate after TSV etching by MaCE. All the surface of the Si substrate was found to be coated by SiO_2. The SiO_2 on the top surface of Si substrate was measured as 1.7 μm, while that on the sidewall and bottom of TSV has a smaller thickness of 250-400 nm. In principle, since the sidewall surface of TSV etched by MaCE is bare Si surface, these TSV are readily available for SiO_2 deposition with good bonding. In contrast, the TSV etched by traditional DRIE method generally have a layer of polymer on their sidewall. A cleaning step is required to remove the polymer layer before SiO_2 can be deposited. After SiO_2 deposition, the TSV were filled with Cu by electroplating. The cross section of TSV with SiO_2 and Cu is shown in **Figure 93** (a) and (b). The composition of each layer is further confirmed by energy dispersive spectrum mapping (**Figure 93** (c) to (e)). The results indicate that the TSV etched by MaCE is compatible with conformal coating SiO_2 and Cu filling.

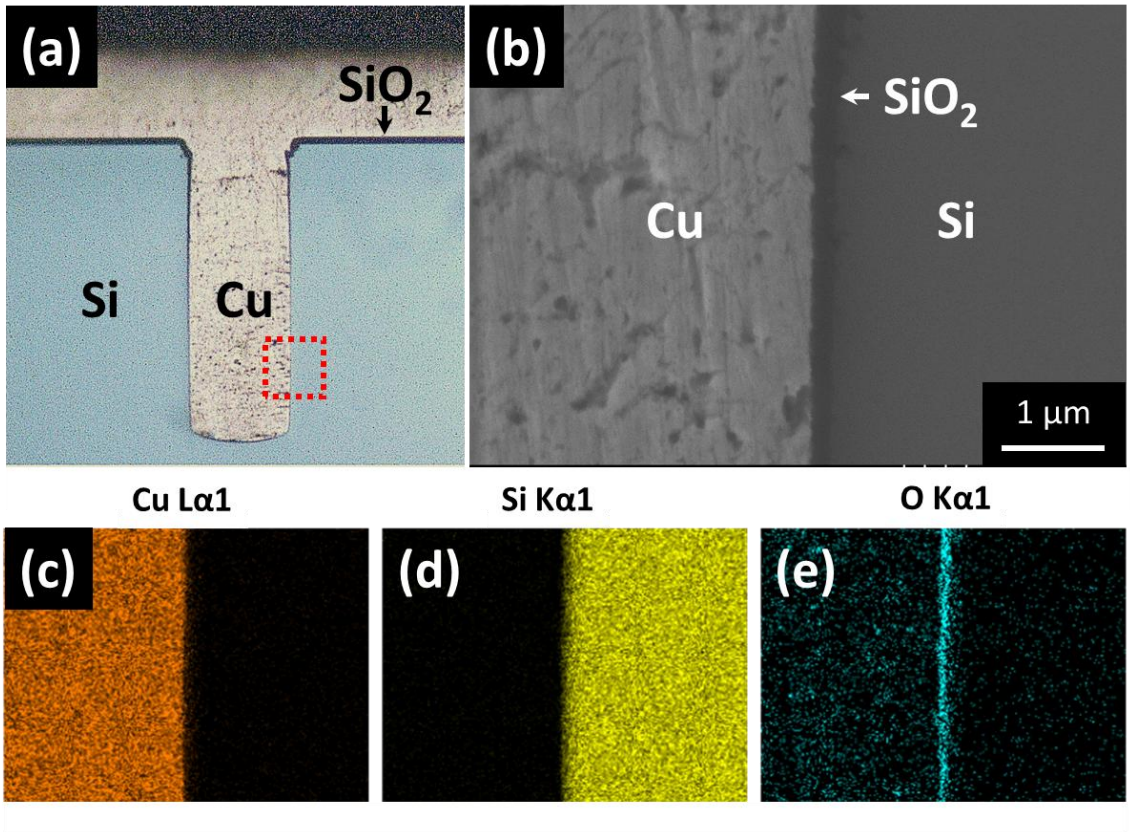

Figure 93 (a) Cross-sectional optical microscope image of a TSV in Fig. 9 which is filled by copper (Cu). A layer of SiO2 exists between Cu and Si substrate; (b) SEM of the red circle in (a) at high magnification; (c), (d) and (e) are the elemental signal maps of Cu, Si and oxygen (O), respectively, in the area of (b) by energy dispersive spectrometer.

In the "via-last" approach for interposer fabrication, the copper (Cu) redistribution line and other components are made on the Si substrate before the etching of TSV. To test the compatibility of MaCE with copper-containing components on the Si substrate, we fabricate a test vehicle consisting of Cu squares array. The Cu is covered by a layer of the same photoresist (NR9 1500PY) as that in MaCE. In the edge part of the sample an additional layer of polyimide tape. The region under the sole coverage of photoresist is named as PR region, while the region under photoresist and polyimide tape is named as

PM region (**Figure 94** (a) and (b)). The test vehicle was immersed in the same etching bath used in the MaCE experiments for 30 min. After immersion, the majority of Cu squares in the PR region is found to be removed and the Si underneath is roughened. However, the Cu squares in the PM region possess nearly identical geometry as the ones before immersion in etchant solution (**Figure 94** (c)-(e)). In a control experiment, bare Cu patterns without any coverage were found to be removed by immersion in the etchant solution within only 5 sec. The results indicate that the photoresist can separate metal catalyst from Si, thus preventing the excessive on the underneath Si in MaCE. However, molecules in the etchant have a chance to penetrate photoresist. These molecules may damage the Cu under photoresist and even the Si with assistance of Cu. These molecules, as may be present in the liquid or vapor form, may further impart reliability of other organic components on the interposer. However, the fact that Cu in the PM region is intact after immersion indicate that the penetration of etchant molecules may be effectively blocked by optimization of photoresist (i.e. the mask layer).

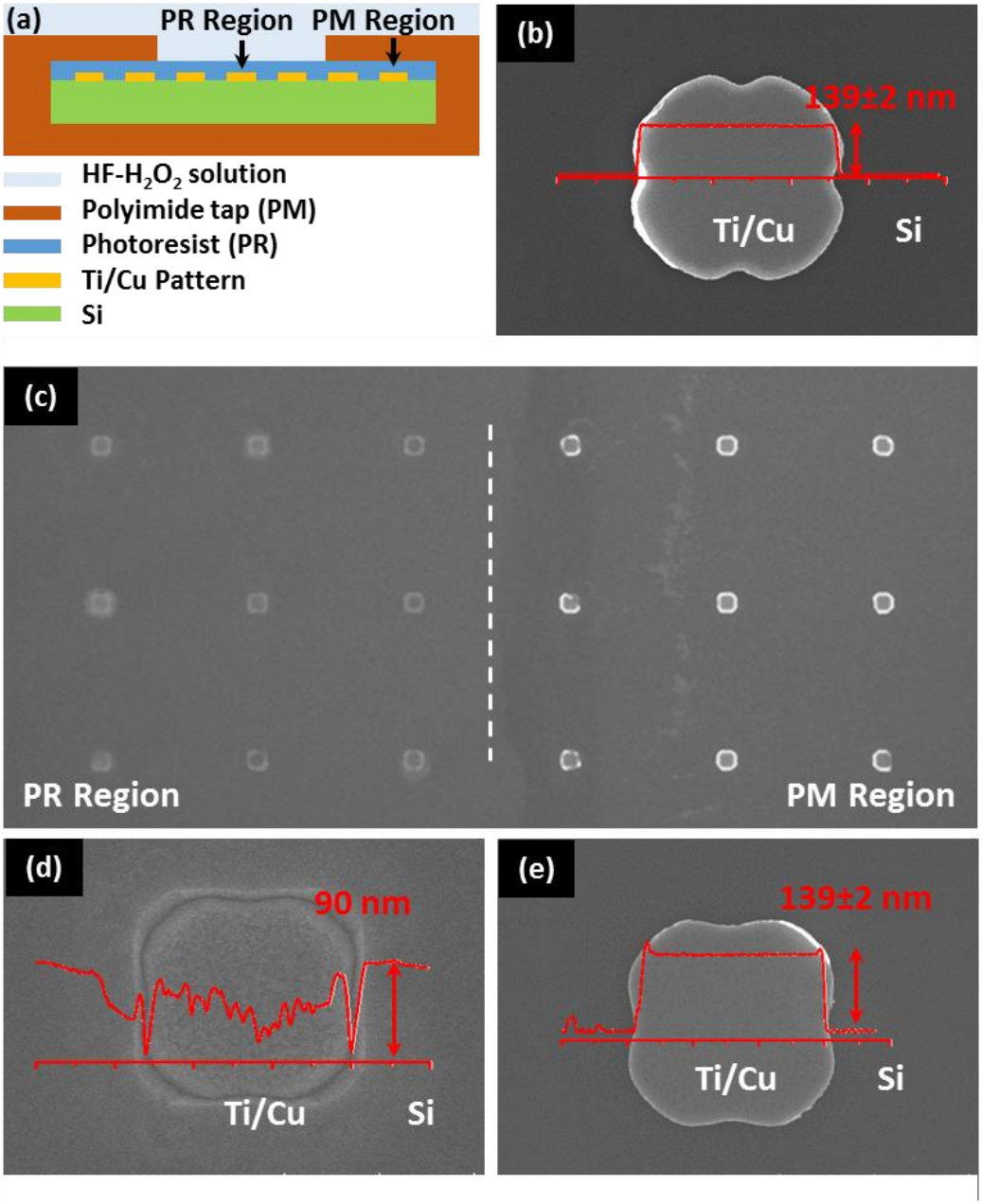

Figure 94 (a) Schematic layout of test vehicle for metal compatibility test in MaCE; (b) SEM image of a copper (Cu) pattern before covered by photoresist, a titanium (Ti) adhesion layer existed between Cu and Si substrate, the total thickness of the Ti/Cu pattern over the whole sample was measured to be 139±2 nm by AFM profile as shown in the embedded red curve; (c) SEM image of the test vehicle surface after immersion in HF-H_2O_2 solution for 30 min and removal of

photoresist and polyimide covering, the vertical dash line indicate the boundary between PR and PM region; (d) enlarged SEM image of the Cu pattern in the PR region with corresponding AFM profile as shown in the red curve; (d) enlarged SEM image of the Cu pattern in the PM region with corresponding AFM profile as shown in the red curve.

8.4 Conclusion

In conclusion, the uniformity of MaCE was found to be influenced by the uniformity of catalysts geometry and the mass transport of etchant solution. Under the optimized condition, the feasibility of etching uniform TSV by MaCE in wafer level is demonstrated. Several key attributes of MaCE can be highlighted:

-High etching uniformity: vertical TSV with depth range of 159-164 μm and diameter range of 27.1-29.7 μm were formed over the whole 4 inch wafer. A low sidewall surface roughness below 50 nm was observed;

-High throughput: ~1 million TSV are etched simultaneously on one Si wafer. Multiple wafers can be etched in one batch, which will result in orders-of-magnitude higher throughput with much lower cost;

-Compatibility with passivation layer deposition and copper conductive filling.

Considering its simplicity and superior performance, MaCE is promising to impact the manufacturing of TSV on Si interposers. Furthermore, due to the versatile capability of MACE in etching holes, trenches and other high-aspect-ratio structures with 3D geometric complexity, microfluidic devices, microelectromechanical systems and even novel Si-based devices can also be fabricated in wafer-level by the reported approach.

CHAPTER 9

CONCLUSION AND SUGGESTED FUTURE WORK

9.1 Conclusions

In this dissertation, we have established the fundamental theories about uniform HAR MaCE as a reliable method for fabrication of deep trenches and deep holes in micro- and nanoscale on Si. With the experimental results, several conclusion can be drawn:

1. Uniform MaCE can be realized in micro- and nanoscale on Si with a broad range of dopants types, doping levels and crystalline orientations;
2. The transport of HF and h^+ are the key microscopic processes that determine the uniformity of MaCE;
3. In order to facilitate transport of HF, a porous morphology of metal catalyst is desired;
4. In order to favor uniform etching, an electropolishing-type h^+ transport process is desired, which is enabled by a high concentration ratio of H_2O_2 to HF;
5. The transport of h^+ further influences the 3D etching profiles in MaCE, which can be experimentally controlled by an external electric field. 3D profiles of MaCE using Au lines with different line width (w_0), number (n) and spacing distance (s) on P-Si, N-Si, USi, P(+)-Si and N(+)-Si have been presented. Uniform trenches are formed on P-Si, N-Si, U-Si, P(+)-Si and N(+)-Si. The depth d and lateral width variation Δw_t of the 3D profiles on P-Si, N-Si and U-Si are measured and correlated to the CT1 and CT2, respectively. The depth follows the order of d(P-Si)<d(U-Si)< d(N-Si) ,while the Δw_t of N-Si is lower than that of U-Si and P-Si. The variation of d and Δw_t over the dopant type of Si can be explained by Schottky junction model, which indicates that CT1 is favored on N-Si and CT2 is favored on P-Si. The variation of Δw_t over w_0, n

and *s* can be further explained by the correlation between CT1 and CT2: in U-Si, h^+ in CT2 are mainly originated from excessive h^+ in CT1 through diffusion; in P-Si, the actual h^+ concentration in CT2 is much higher than that calculated from the diffusion model, which may be attributed to the drift of h^+;

6. Multiple deep trenches with vertical sidewalls can be formed on moderately-doped N-type Si without electric bias. Working MEMS resonators can be built on trenches etched by MaCE;
7. In contrast to the plasma etching, for MaCE only a polymer layer as thin as 100 nm can serve as an effective mask layer. MaCE shows compatibility with a novel lithography method, named FESA, which enables a novel low-cost approach for HAR structures fabrication based on MaCE and FESA.
8. Multiples wafers can be etched simultaneously using the MaCE method, where millions of deep holes are formed per wafer with depth variation of ~2% using simple lab apparatus. The deep holes etched by MaCE shows ultra-low sidewall roughness of below 50 nm and compatibility with dielectric coating and metal filling for TSVs formation.

9.2 Suggested Future Work

Overall, the above findings clearly demonstrate the capability of MaCE in fabricating HAR micro- and nanostructures on Si. To enhance the performance and expand the range of application of MaCE, the following future work is suggested:

1. Investigation of MaCE on semiconductors other than Si. Using MaCE methods for fabrication of nanowires on III-V compound semiconductors, such as GaAs [123] and InP [124], have been reported. The possible physical-chemical mechanism responsible for the etching reactions have been proposed. However, there is still lack of the detailed understanding. More importantly, uniform MaCE for deep trenches and deep holes on these substrates have been realized.

Considering the fundamental difference between MaCE of nanowires and that of deep trenches on Si, realizing uniform MaCE for deep trenches and deep holes on may incur novel design of the process and mechanisms. The work will make significant contributions to the devices fabrication where III-V semiconductors play roles, such high-frequency computers and light-emitting diodes;

2. Investigation of MaCE on Si with small gap and ultra-high aspect ratio. It has been proposed that deep trenches with width below 100 nm will render ultrahigh sensitivity when used in MEMS sensors. It is promising to use MaCE to fabricate such structures, but considering the scaling effect, the transport of HF and h^+ in such narrow trenches will be fundamentally different from those in MaCE in a few-microns or submicron scales;
3. Investigation of process-structures-performance relations. In Chapter 6, we demonstrate the performance of a MEMS resonator using deep trenches etched by MaCE. There are several distinctive features of the trenches: (1) the overall profiles of the trenches are slightly tilted/twisted, rather than perfectly vertical; (2) some porous regions appear on the sidewalls and edges of the openings of the trenches; (3) the metal catalyst bounces back after reaching the oxide layer and creates an extra notch. These structural features, which are unique to the trenches made by MaCE, may have influence on the performance of the devices where they are involved. The influence has not been investigated. Also the experimental conditions that control the generation of these features need fundamental researches.

APPENDIX A

MOLECULAR ENGINEERING OF AROMATIC AMINE SPACERS FOR HIGH-PERFORMANCE GRAPHENE-BASED SUPERCAPACITORS

A1. Introduction

Besides the work mentioned above, an independent project will be reported that has been finished during my PhD study. Parts of the contents have been published in [125] and reprinted here with permission. Copyright 2016, Elsevier.

Supercapacitors are electric energy storage devices which utilize the electric double-layer capacitance (EDLC) and/or pseudocapacitance.[126] The EDLC originates from the fast adsorption/desorption of electrolyte ions and the pseudocapacitance is created from the Faradaic reaction of the electrode materials. Supercapacitors possess outstanding charge/discharge rate over other types of energy storage devices. However, their capacitance is still far from satisfactory for applications in electric vehicles, large-scale energy storage, etc.[127] The capacitance of supercapacitors is primarily determined by the electrode materials. Ideal electrode materials should possess high surface area accessible to electrolyte, high electrical conductivity, high chemical stability and low density. Considering these parameters, graphene, one-atom-thick 2D sheet of carbon, has been considered as a promising supercapacitor electrode material.[128] In the isolated single-layer graphene, carbon atoms are connected by conjugated π bond which forms a sheet with high electrical conductivity. [129, 130] However, in the bulk materials of multi-layer graphene, the sheets have strong tendency to aggregate due to the strong π-π interaction between the sheets. The aggregation of graphene makes the space between the sheets too narrow to be accessed by the electrolyte.[131] The modification of graphene has been intensively investigated to prevent its heavy aggregation so that the specific

capacitance can be promoted. Based on the dimension of the materials used to modify graphene, these modifiers can be categorized into: (1) atomic modifiers (~1 Å), such as oxygen[132, 133] and nitrogen[134, 135] atoms doped in graphene sheets; (2) molecular modifiers (~1 nm), such as small organic molecules attached to or grafted on the graphene sheets[136-144]; (3) nanoscale modifiers (over 5 nm), such as nanoparticles, nanowires made of conductive polymers [145-147], metal oxides[148, 149], etc. Besides functioning as spacers between graphene sheets that increase the interlayer spacing, some of the modifiers could also add pseudocapacitance. Compared to the atomic modifiers and nanoscale modifiers mentioned above, here we demonstrated the following advantages of using molecular modifiers in promoting capacitance: (1) the size of the molecular modifiers is comparable to that of electrolyte ions, therefore they are capable of serving as spacers between graphene sheets to increase the accessible surface area in molecular level; (2) given the well-established science of organic chemistry, suitable molecules can be picked up from a huge inventory of commercially available chemicals with low cost. Their molecular structures can be finely tuned to render optimal capacitance with the rationalized organic reactions with graphene or its precursors. Covalent bonds between the molecules and graphene can be formed to ensure the high durability during charge/discharge cycles of the supercapacitors.[138]

Although using molecular modifiers in graphene-based supercapacitors has been reported, the mechanism of reaction between the molecules and graphene oxide was not clearly described, nor could the influence of the molecular structures be determined from these independent studies, which is fundamental for the discovery of electrode materials with even higher performance. In this report, we focus our study on the engineering of the chemical structures of molecular modifiers for high-performance graphene-based supercapacitors. Graphene oxide (GO), an oxidized form of graphene that can be dispersed in water (H_2O) in single-sheet form for large-scale production, is selected as the precursor for the formation of graphene nanostructures.[150, 151] Four types of aromatic amine,

1,2,5-triaminobenzene (**Tri**), 2,2'-diaminobenzendine (**Tetra**), 1,5-diaminonaphthalene (**Naph15**) and 1,8-diaminonaphthelene (**Naph18**) were employed as the molecular modifiers (**Figure A. 3**). The structures of the modifiers differ in the aromatic cores, number of the amino groups and position of the amino groups. The incorporation of amino groups in the spacers enable them to covalently bond to GO through nucleophilic substitution and amide formation reactions. The amino groups are conjugated with the aromatic cores, such as the benzene rings, which may further introduce pseudocapacitance by reversible benzoid-quinoid transition.[152]

In this study, these modifiers were mixed with GO separately in aqueous solution and underwent one-step hydrothermal reactions with identical conditions. The modifiers serve as molecular spacers that induce a larger interlayer spacing of up to 1.9 nm and an over three-fold higher specific capacitance as demonstrated below. From comparative study, covalent bonding between the modifiers and graphene are evidenced. Mechanism of reaction between these modifiers and GO during the hydrothermal process is elucidated and the effect of the variation in the molecular structures is revealed.

A2. Methods

Graphite flakes (Catalog#230U) were provided by Asbury Carbons, NJ. Deionized (DI) water was produced from a Barnstead Smart2Pure water purification system (Thermo Scientific). All other chemicals were purchased from Sigma Aldrich and used without further processing.

Modification of GO A GO aqueous slurry was prepared by a modified Hummers method as reported previously.[138] The GO slurry with known concentration was used in the wet form until the completion of modification. For modification, the spacer molecules were dissolved in 23 mL hydrochloric acid (HCl, 70 mmol/L) aqueous solution in an ultrasonication bath for 10 min. For **Tri**, its salt form, 1,2,5-triaminobenzene dihydrochloride, was used due to its commercial availability. The other three spacers were

used in their primary amine form. After complete dissolution, the solution was clear with color of purple for **Tri**, light yellow for **Tetra**, **and** red for **Naph15** and **Naph18**. No solid precipitate could be observed in these solution. GO slurry was added together with Na_2CO_3 aqueous solution into the solution of the spacers so that the concentration of GO and Na_2CO_3 were 1 mg/mL and 700 mmol/L, respectively. The total volume of the solution was 28 mL. The pH value of the mixture was measured as 11. The high pH value facilitated the dispersion of GO in H_2O as discussed below. After further sonication for 30 min, the GO-spacers mixture were transferred into a closed Teflon-lined autoclave and heated at 180 ^oC for 12 hr in oven. After ambient cooling, a black hydrogel was formed and the liquid phase was clear and colorless. The hydrogel were filtered out while rinsed by copious volume of DI water, and finally dried at 55 ^oC in oven for 24 hr to render black powder. The black powder was referred to as the as-prepared rGO-Spacers samples.

Characterization The as-prepared rGO-Spacers samples were viewed under SEM (Hitachi SU8230), transmission electron microscope (TEM, JEOL 100XC) and atomic force microscope (AFM, Veeco Dimension Edge, with Si tips MPP-11100-10 under tapping mode). GO samples for AFM characterization were prepared by spin coating of GO aqueous solution (1 mg/mL) on a Si substrate with 250 nm-thick thermal oxide on top at the spin speed of 500 rpm for 1 min. To characterize the as-prepared rGO-Spacers powder for AFM and TEM characterization, the powder was dispersed in N-methyl-2-pyrrolidone (NMP) and sonicated for 24 hr. Then the dispersion was drop cast on SiO_2/Si substrate and TEM copper grid, respectively. The samples were dried in oven at 55 ^oC for 24 hr before the characterization. UV-visible spectra were collected by a UV-2450 spectrometer (Shimadzu) using aqueous dispersion of the samples. Element composition of the samples was analyzed by X-ray photoelectron spectroscopy (Thermo K-Alpha XPS). Fourier-transform infrared (FT-IR) spectra were collected by Nicolet, Thermo Scientific using the KBr pellet method. Raman spectra were collected by Nicolet Almega, Thermo Scientific. Thermogravimetric analysis (TGA) was conducted in a TGA system (Q5000,

TA Instrument). The cyclic voltammetry (CV), galvanostatic charge/discharge (CD) and electrochemical impedance spectroscopy (EIS) were collected by an electrochemical work station (Versa STAT, Princeton Applied Research) using a two-electrode setup. For the two-electrode setup, the as-prepared rGO-Spacers powder were ground and mixed with polytetrafluoroethylene (PTFE) binder (weight ratio of 9:1 rGO-Spacers: PTFE). The mixture was then rolled into a free-standing film (40±10 μm thick). X-ray diffraction (XRD) patterns were collected from the free-standing film by PANalytical X'Pert PRO Alpha-1. Disks with a diameter of 6 mm were punched from the free-standing film. Two disks were used as the two electrodes and assembled in a stainless cell kit with glass microfiber paper as separator, carbon fiber paper as current collector and sulfuric acid (1 mol/L) as the electrolyte. The electrochemical activity of the materials was also characterized by CV in a three-electrode setup. In the three-electrode setup, the active materials were first dispersed in NMP of 24 hr. The dispersion was dropped cast on a glassy carbon electrode and dried at 55 ^{o}C in an oven to serve as the working electrode. An Ag/AgCl in a saturated KCl aqueous solution and a platinum wire were used as the reference electrode and the counter electrode, respectively. 1 M H_2SO_4 aqueous solution was also used the electrolyte.

Calculation of Electrochemical Properties The specific capacitance (C_s) of the active materials was calculated from CV by:

$$C_s = \frac{2 \times \int I_m dt}{V \times v} \quad (1)$$

Where I_m, V and v refer to the current density, voltage range and scan rate, respectively. The current density I_m was calculated by dividing the measured current by the mass of active materials (excluding that of PTFE binder) in the two electrodes. The term $\int I_m dt$ was calculated by integrating the area enclosed by the CV curves. The specific capacitance C_s was also calculated from CD by:

$$C_s = \frac{4 \times I_m \times (t - t_{iR})}{(V - V_{iR})} \quad (2)$$

where the same I_m, V were used as those in CV test. The term t refer to the total discharge time. V_{iR} and t_{iR} are the potential drop and time in the region of sharp potential drop caused by equivalent serial resistance (illustrated in **Figure A. 1**). The energy density E was calculated by

$$E = \frac{C_s \times (V - V_{iR})^2}{8} \quad (3)$$

where the specific capacitance term C_s was derived from CD measurement. The same V and V_{iR} were used as those in Cs calculation from CD.

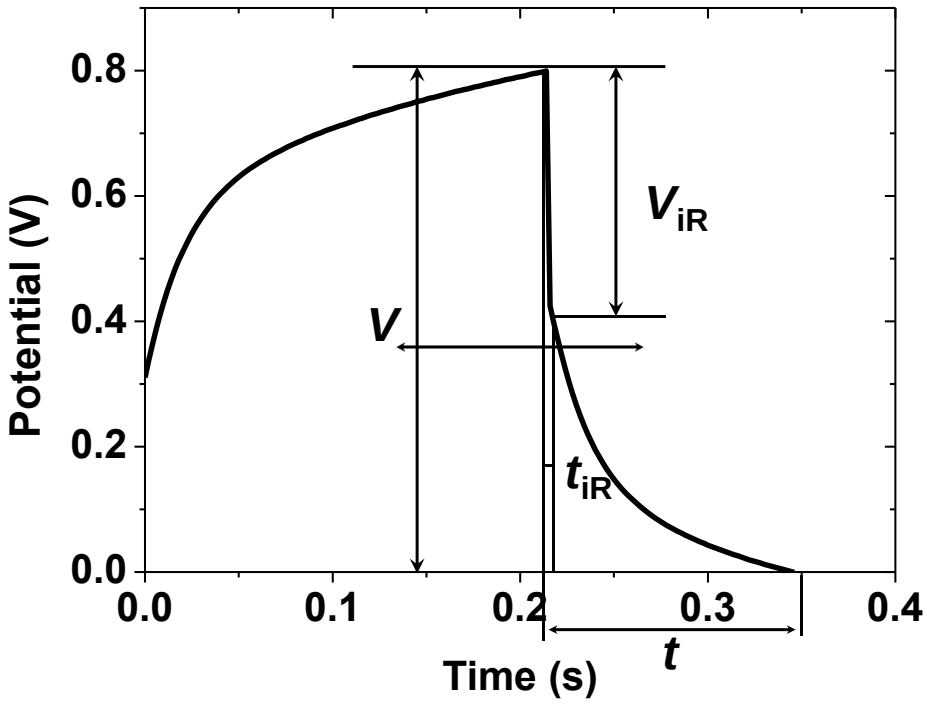

Figure A. 1 Illustration of parameters for calculation of specific capacitance from galvanostatic charge/discharge curve.

The power density P was calculated by

$$P = \frac{E}{(t - t_{iR})} \tag{4}$$

where E referred to the energy density, same t and t_{iR} were the same as those in calculation of E.

A.3 Results and Discussion

In this work, the amount of GO was fixed as 28 mg in each batch, and the amount of each type of spacers was set to 0.15 mmol and 0.30 mmol in separate experiments. Corresponding products of the reactions were named in the format of rGO XY, where X stood for the name of the spacers and Y was the amount of the spacers. For example, rGO Naph15030 refers to the product of the reaction between 28 mg GO and 0.30 mmol of **Naph15**. A general name rGO X was used in the discussion of results where the molar amount of spacers did not show significant influence. The product of the reaction without addition of spacers was named "rGO Bare" (the control sample).

The modification of graphene started with the dispersion of the spacer and GO in DI water. DI water was used as the solvent because GO was known to disperse well in water in single-layer form. AFM measurement of GO deposited on the SiO_2/Si substrate from 1 mg/mL aqueous solution (**Figure A. 2**) confirmed the existence of single-layer GO sheets with a step height of 1.2 nm. However, the step height of stacked GO sheets was measured as 0.8 nm. Here we consider the value of 0.8 nm as the thickness of GO because the residual H_2O on SiO_2 surface or the heterogeneous interaction between GO and SiO_2 account for the larger step height of the single layer GO (1.2 nm). Based on the result, we set the concentration of GO as 1 mg/mL during reaction. In order to effectively modify every graphene sheet, it is critical that the spacers are also dispersed well in the solution. Therefore, hydrochloric acid was added into pure DI water to promote the solubility of spacers by converting them into a salt form:

$$R\text{-}NH_2 + HCl \rightarrow R\text{-}NH_3^+Cl^- \quad (5)$$

Under naked-eye observation, the spacers solution with 70 mmol/L HCl was clear without any solid substance, indicating that the spacers were well dispersed (**Figure A. 3**, step a). It has been reported that the dispersion of GO was improved in a basic solution with a high pH value.[153] Therefore, when the GO slurry was added into the spacer solution, Na_2CO_3 solution was added simultaneously to adjust the pH of the final solution to 11 (**Figure A. 3**, step b). The hydrothermal reaction was undertaken at the pH of 11 in a closed container (**Figure A. 3**, step c). After a hydrothermal reaction, the samples without addition of spacers, i.e. rGO Bare, were stacked flat sheets under a SEM (**Figure A. 4**). In contrast, the rGO-Spacers samples appeared as crumpled sheets. Some of the sheets were semi-transparent, indicating their low thickness. The crumpled morphology of the sheets in rGO Spacers samples was retained after the samples were dried and redispersed in NMP with high-intensity ultrasonication, as illustrated in a representative AFM image (**Figure A. 5**) and TEM image (**Figure A. 6**). Furthermore, even the powder was grounded and rolled into thin film under high mechanic pressure, the crumpled feature could still be observed under SEM while the surface of rGO Bare remained flat (**Figure A. 7**). As discussed in papers where nitrogen atoms were bonded to graphene [134, 154], the crumpled morphology suggested that the amino groups in the spacers were chemically bonded to the graphene sheets and induced a structural change to the whole sheets in a micrometer scale. The existence of spacers can be further confirmed by mapping of energy dispersive spectroscope (EDS) signals. As shown in **Figure A. 6** (c), the distribution of carbon (C), oxygen (O) and nitrogen (N) replicated the profile of graphene sheets in the corresponding SEM image (**Figure A. 6** (b)). Given the fact that the spacers are the only source of the N signal, it can be inferred from the EDS mapping that the spacers are uniformly distributed over graphene sheets. It should be noted that throughout the SEM observation, only the smooth thin sheets appeared even at a magnification of 100,000X; no grains or fibrils could be observed. In contrast, in previously reported graphene materials

with nanoscale modifiers, grains or fibrils could be easily observed at this magnification and assigned to the modifiers themselves.[155] Therefore, here the molecular spacers were probably distributed in a molecular level on graphene sheets rather than self-aggregated. The morphology of crumpled thin sheets is favorable for fast electrolyte transport through the enlarged spacing between the sheets, and is expected to give rise to a high specific capacitance.

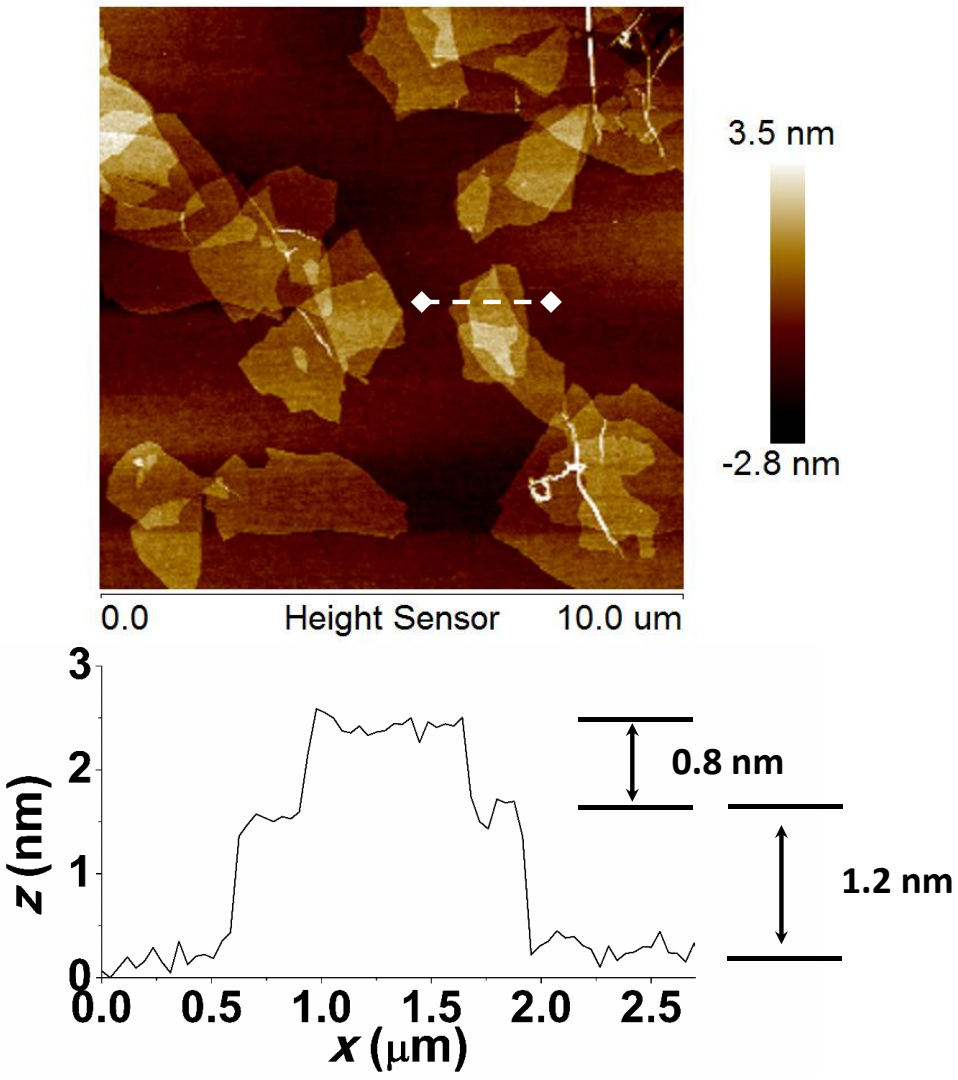

Figure A. 2 (Top) Atomic force microscope 2D image of graphene oxide deposited on SiO2/Si substrate; (bottom) cross section of the white line in (a).

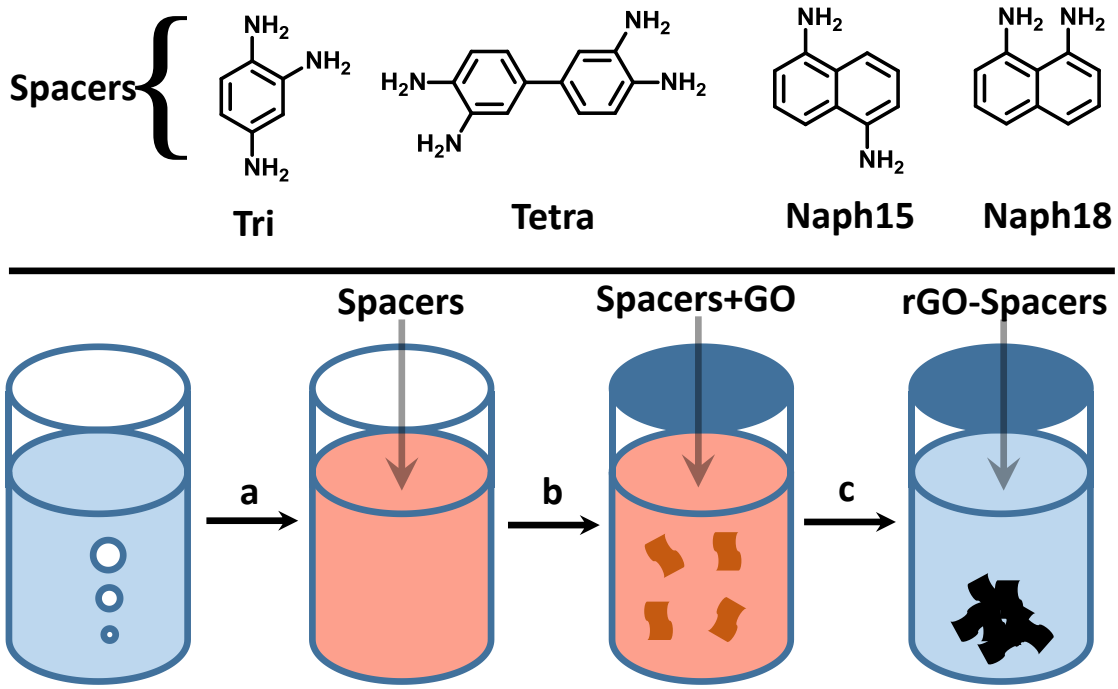

Figure A. 3 (Top) The chemical structure of the aromatic spacers: 1,2,5-triaminobenzene (**Tri**), 2,2'-diaminobenzendine (**Tetra**), 1,5-diaminonaphthalene (**Naph15**) and 1,8-diaminonaphthelen (**Naph18**). (Bottom) Schematic process flow for rGO-Spacers: a. dissolution of spacers in H_2O; b. dispersion of graphene oxide (GO) in spacer solution; c. hydrothermal processing of GO and spacers in closed container.

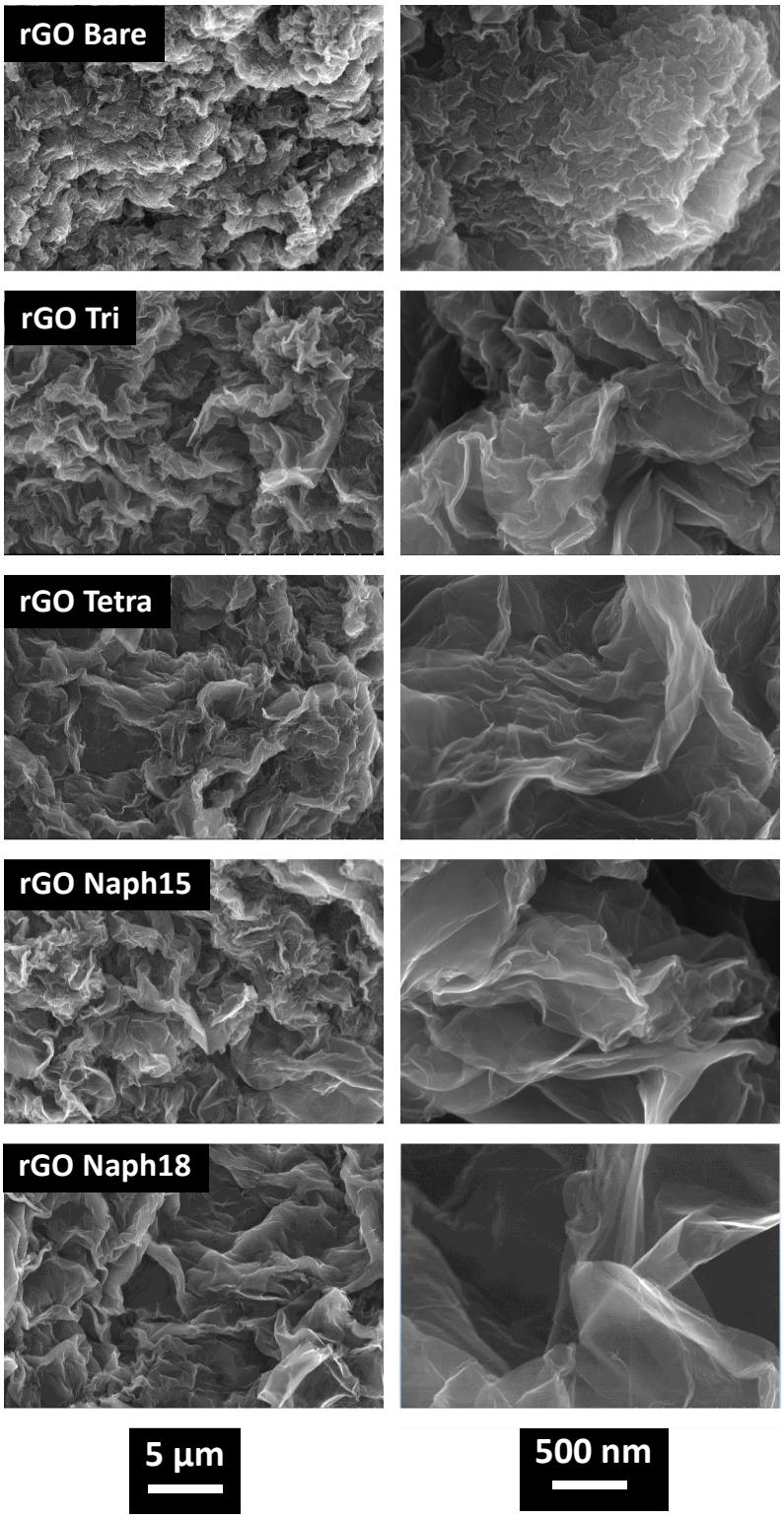

Figure A. 4 SEM image of the as-prepared samples under magnification of 5000X (left column) and 50000X (right column).

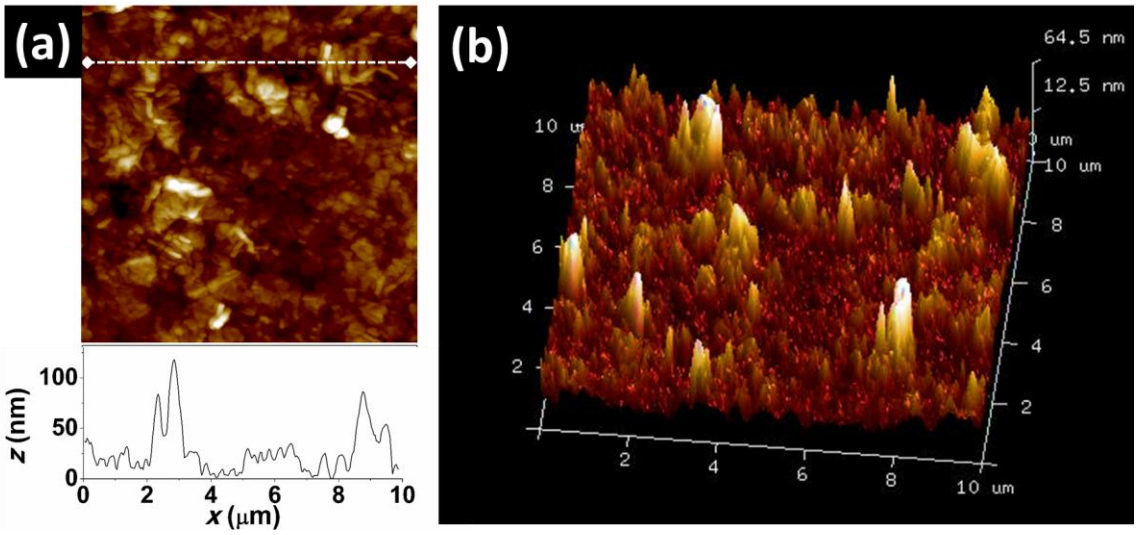

Figure A. 5 (a) Atomic force microscope (AFM) 2D image (top) and cross section (bottom) of the as-prepared rGO Naph15030 deposited on SiO_2/Si substrate; (b) 3D profile reconstructed from the 2D image in (a).

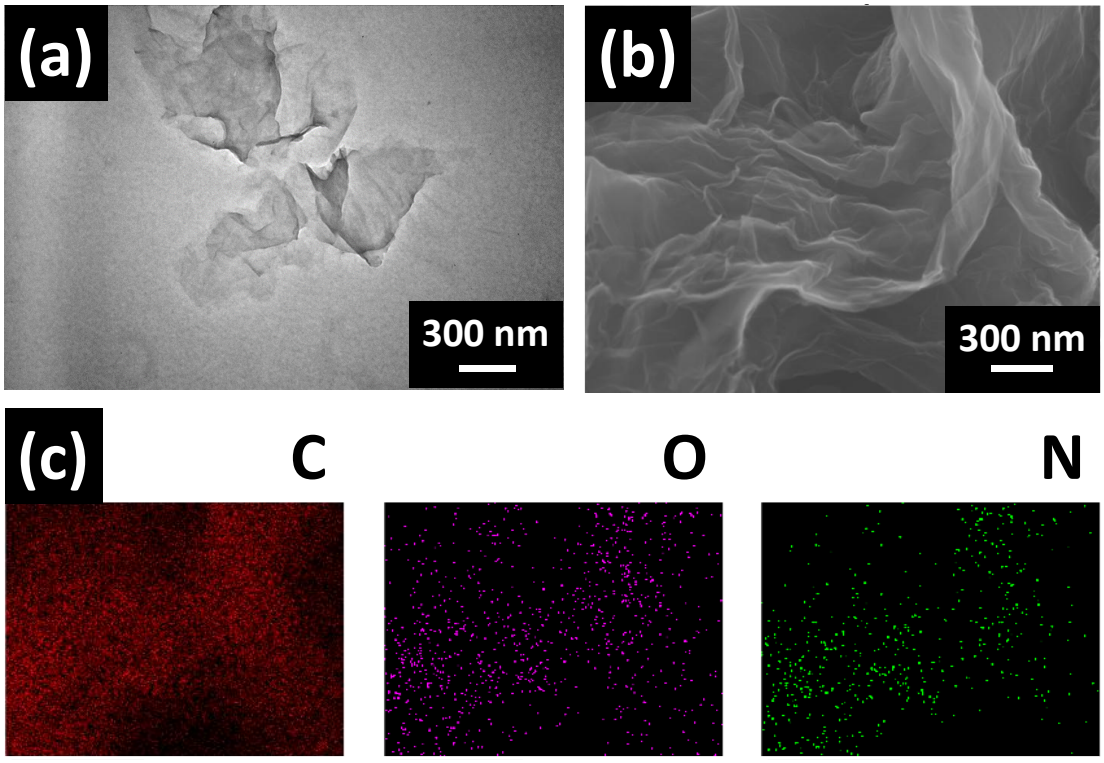

Figure A. 6 (a) Transmission electron microscope (TEM) image of rGO Naph15030; (b) SEM image of rGO Naph15030; (c) elements mapping of carbon (C), oxygen (O) and nitrogen (N) by energy dispersive spectrum in the area shown in (b).

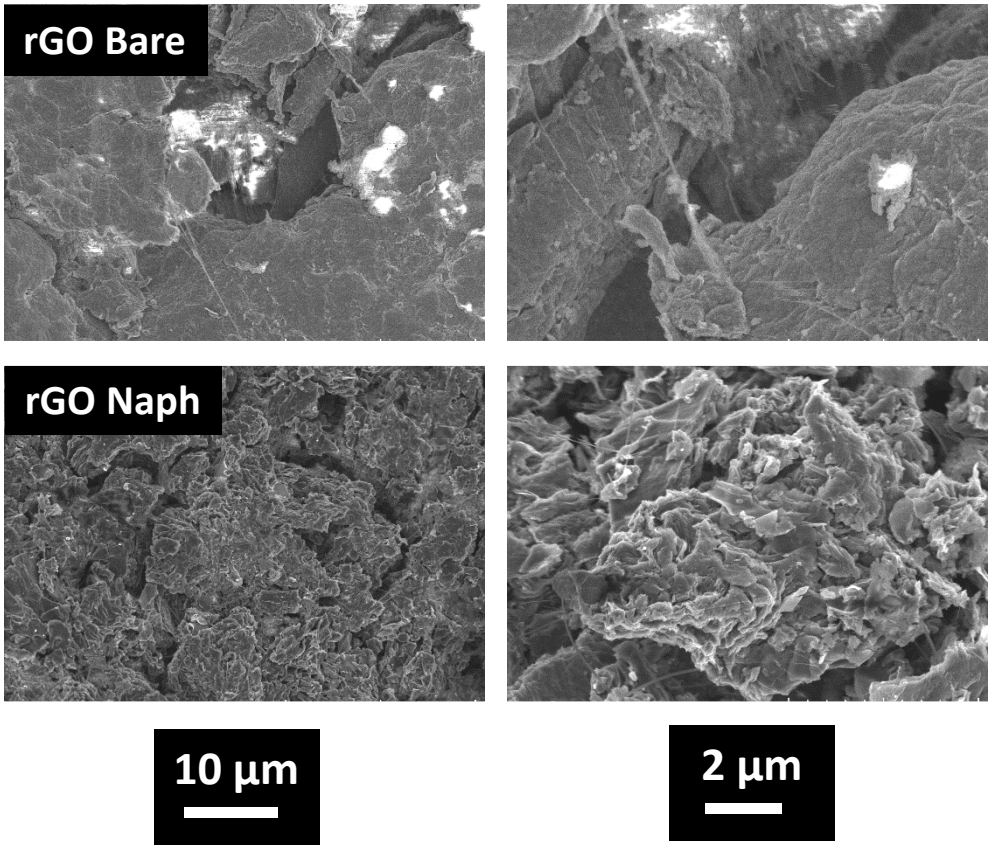

Figure A. 7 SEM image of the samples after prepared as thin-film electrode under magnification of 2500X (left column) and 10000X (right column). The fibrils and particles in the images can be assigned as the PTFE binder added during the preparation of thin film.

The specific capacitances (C_s), i.e. the capacitance per unit mass of the active materials in the electrodes, of the samples were calculated from both cyclic voltammetry (CV, **Figure A. 8** (a)) and galvanostatic charge-discharge (CD, **Figure A. 8** (b)) using a two-electrode setup at different scan rates and charge-discharge current densities, respectively. In the CV measurements, the rGO-Spacers showed remarkably higher C_s compared to that of rGO Bare at low scan rates of 2 mV/s, 10 mV/s and 20 mV/s. As the scan rate increases to 50 mV/s and higher, the C_s value of rGO Tri030, rGO Naph15030, rGO Tetra015 and rGO Tetra030 were still higher than that of rGO Bare. In the CD measurements, similar trends has been observed. In both measurements, C_s increases with a higher molar amount of spacers added in the reaction between GO and amine spacers. It

is noteworthy that among the rGO Spacers samples, rGO Tri030 shows the highest C_s of 617 F/g at 2 mV/s in the CV measurement, as well as 597 F/g at 0.5 A/g and 512 F/g at 10 A/g in the CD measurement. To our knowledge, those values rank among the highest in the literature where small molecules modifiers were employed.[137, 139] The CV curves of each sample are shown in **Figure A. 9**. The curves appear as quasi-rectangular at low scan rate, and started to tilt when the scan rate increased. The CD curves of each sample were shown in **Figure A. 10**. The CV and CD curves of rGO Bare are shown in **Figure A. 11**. Obvious bumps in CV and CD curves of rGO Tri030, rGO Tetra015 and rGO Tetra030 can be observed, indicating a considerable amount of pseudocapacitance contributing to the overall capacitance. The samples with high C_s shows the outstanding C_s retention after CD cycling test. As shown in **Figure A. 12** (a), rGO Tri015 shows a C_s of 497 F/g after 10,000 cycles at 10 A/g, accounting for 97% of its original value before cycling. For rGO Tetra030, rGO Naph15030 and rGO Naph18030, the C_s at 10 A/g shows slight increase after cycling (**Figure A. 12** (b)-(d)), which is possibly due to better wetting of the spacing between graphene sheets or introduction of more chemical species with pseudocapacitance.[133] The excellent cycling performance of the materials may be originated from the stable covalent bonding between graphene and the spacer molecules.

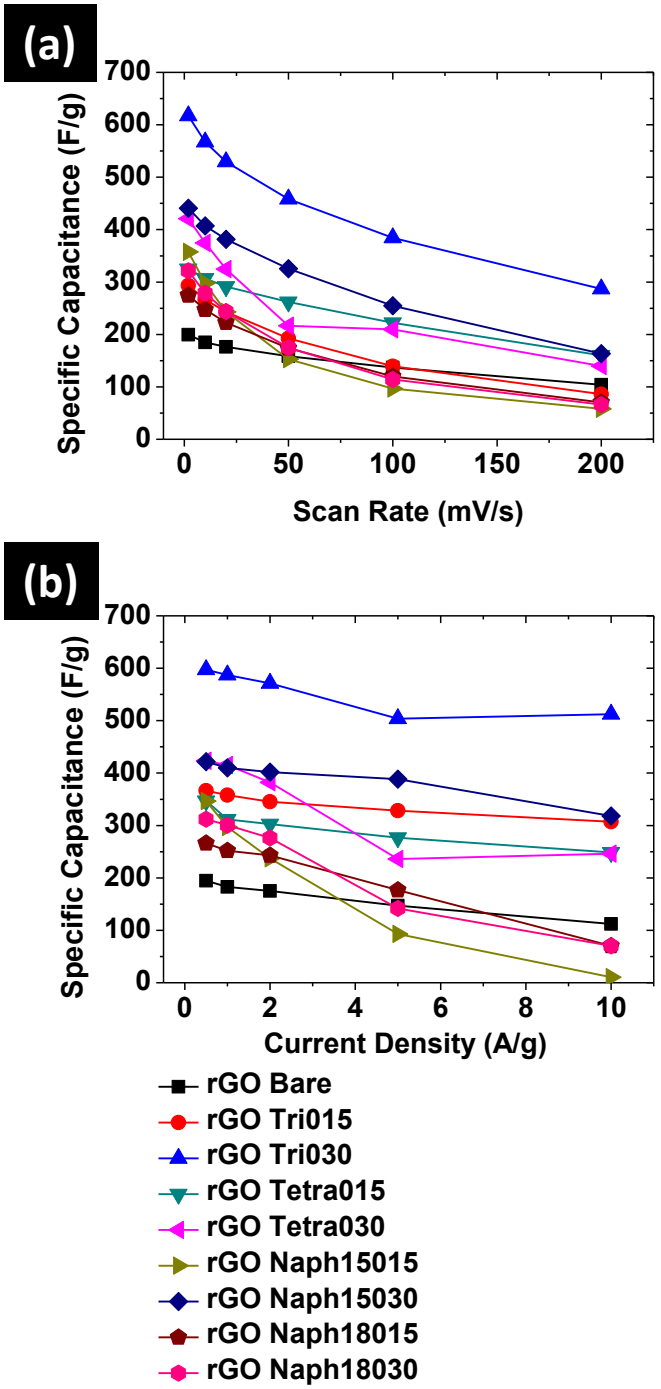

Figure A. 8 Specific capacitance of the samples measured from cyclic voltammetry (a) and galvanostatic charge-discharge (b) at different scan rates and current densities, respectively.

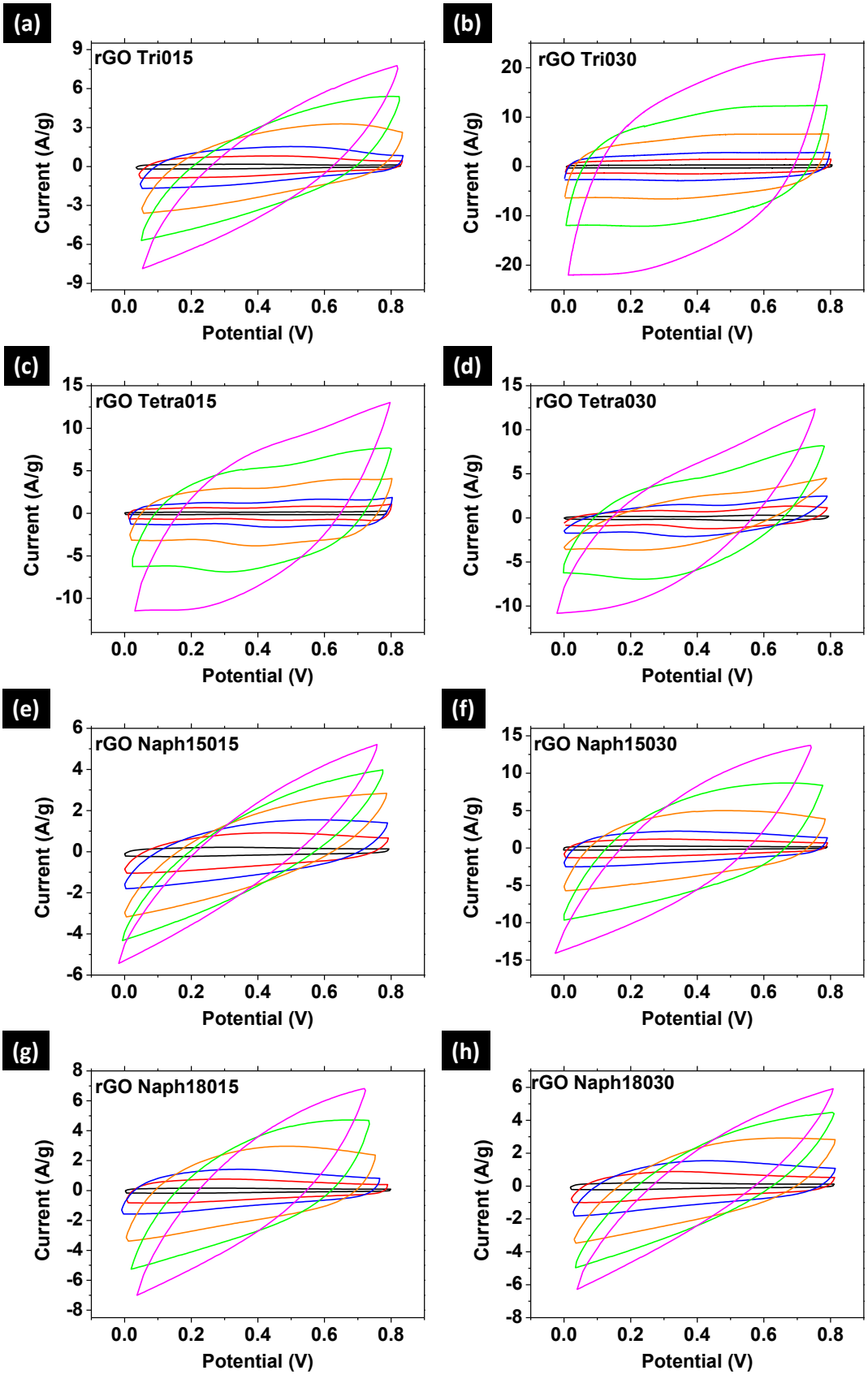
(a)
rGO Tri015
Current (A/g)
Potential (V)
(b)
rGO Tri030
Current (A/g)
Potential (V)
(c)
rGO Tetra015
Current (A/g)
Potential (V)
(d)
rGO Tetra030
Current (A/g)
Potential (V)
(e)
rGO Naph15015
Current (A/g)
Potential (V)
(f)
rGO Naph15030
Current (A/g)
Potential (V)
(g)
rGO Naph18015
Current (A/g)
Potential (V)
(h)
rGO Naph18030
Current (A/g)
Potential (V)

Figure A. 9 Cyclic voltammetry (CV) curves of the samples measured at scan rates of 2 mV/s (black lines—), 10 mV/s (red lines—), 20 mV/s (blue lines—), 50 mV/s (yellow lines—), 100 mV/s (green lines—) and 200 mV/s (magenta lines—)

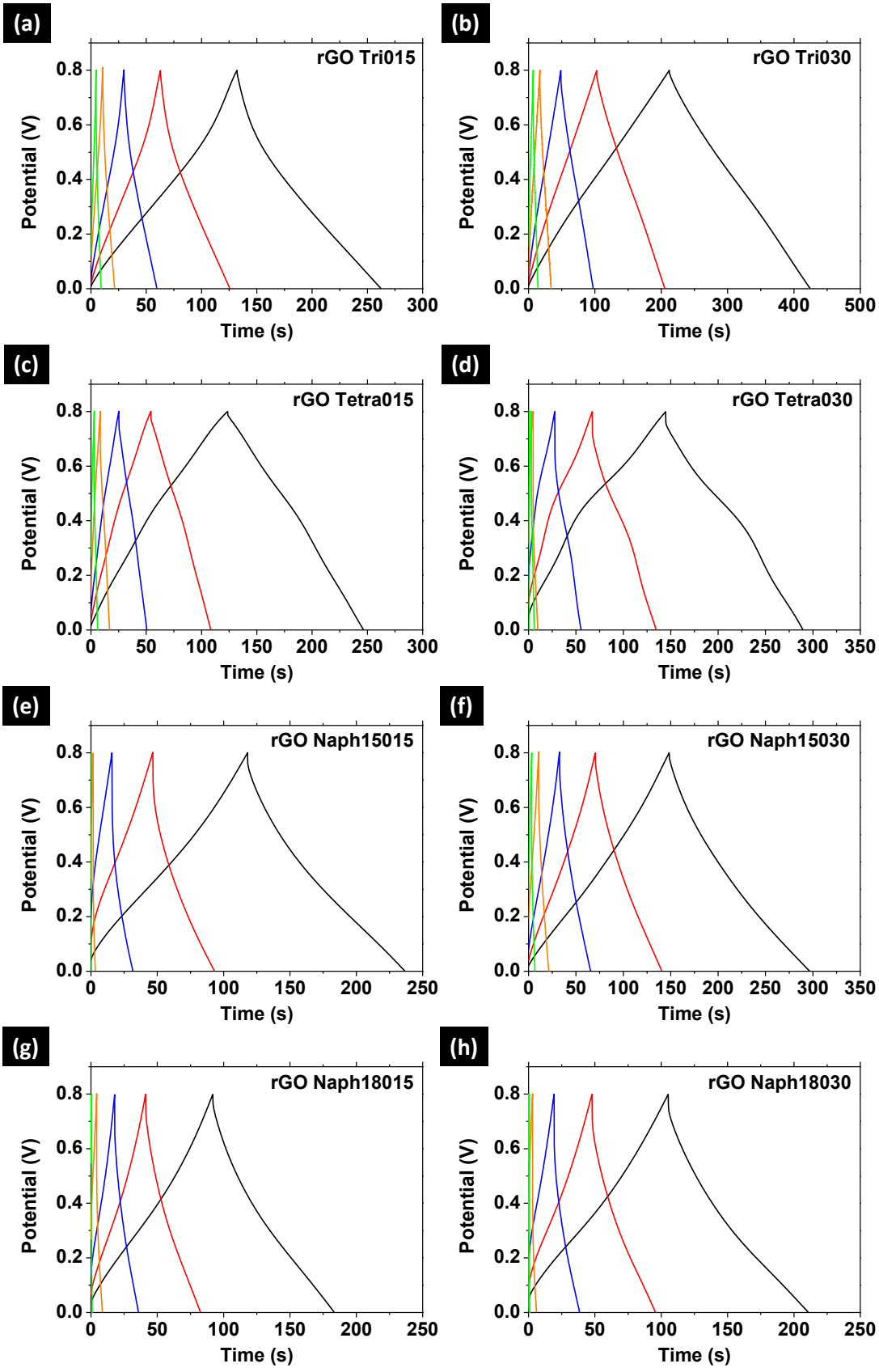
(a)
rGO Tri015
(b)
rGO Tri030
(c)
rGO Tetra015
(d)
rGO Tetra030
(e)
rGO Naph15015
(f)
rGO Naph15030
(g)
rGO Naph18015
(h)
rGO Naph18030
Potential (V)
Time (s)

Figure A. 10 Galvanostatic charge-discharge (CD) curves of the samples measured at current density of 0.5 A/g (black lines—), 1 A/g (red lines—), 2 A/g (blue lines—), 5 A/g (yellow lines—) and 10 A/g (green lines—).

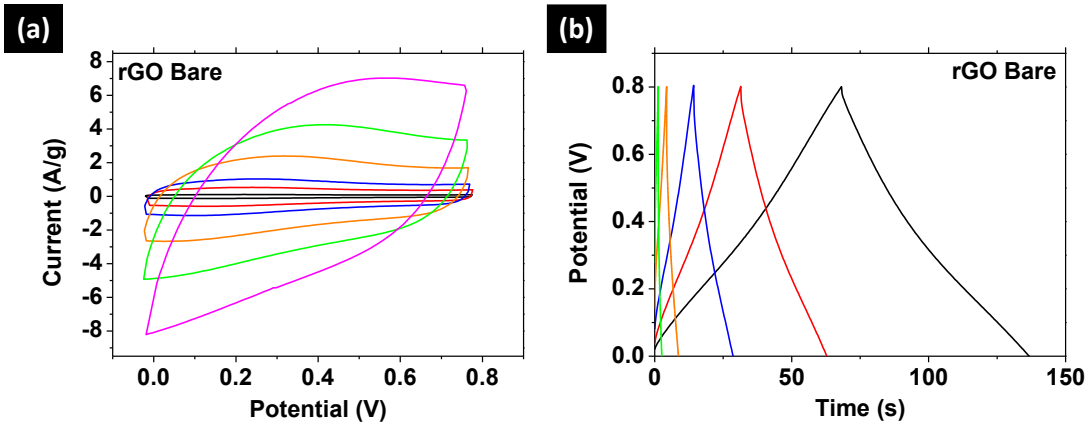

Figure A. 11 (a) Cyclic voltammetry curves of rGO Bare at different scan rates; (b) galvanostatic charge/discharge curves of rGO Bare at different current density.

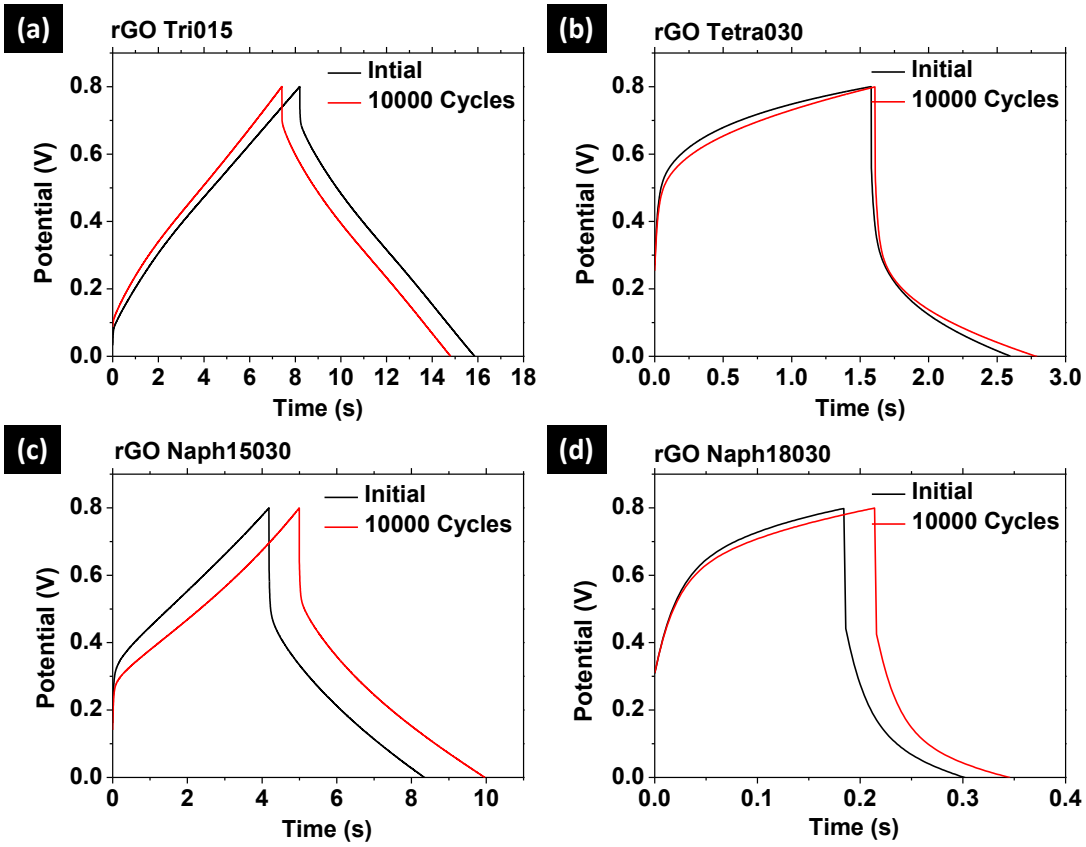

Figure A. 12 CD curves of the samples before and after CD cycling with current density of 10 A/g.

The electrochemical properties of the samples were further characterized by electrochemical impedance spectroscopy (EIS, **Figure A. 13** (a)). The low frequency regions of the EIS curves of rGO Tri030, rGO Tetra015, rGO Tetra030 and rGO Naph15030 appear more perpendicular towards the *Z*' axis, indicating a more ideal capacitance behavior. The high frequency regions of the EIS curves are magnified in **Figure A. 13** (b). The first and second intersects of the curves to the *Z*' axis represent equivalent series resistance (R_s) as well as the sum of R_s and charge transfer resistance (R_{ct}), respectively. The value of the samples are listed in **Table A. 1**. As the reference, rGO Bare shows R_s of 0.908 ohm and R_{ct} of 2.59 ohm. Among the rGO-Spacers samples, rGO

Tri030 shows the lowest R_s of 0.61 ohm and R_{ct} of 1.83 ohm. The low R_s and R_{ct} indicate an enhanced electrical conductivity and fast electrochemical reaction at the electrode-electrolyte interface of the material, explaining the high C_s of rGO Tri030 at a high charge-discharge current density rGO Tetra015, rGO Tetr030 and rGO Naph15030 also show low R_s or R_{ct}. All these samples with low R_s/R_{ct} show a much higher specific capacitance compared to those with a larger resistance, as illustrated in **Figure A. 8**. The power density and energy density of the samples are seen in a Ragone plot in **Figure A. 13** (c). Again, rGO Tri030 presents the prominent energy density of 46.5 W h kg^{-1} at the power density of 0.2 kW kg^{-1}, and 24.2 W h kg^{-1} at the power density of 3.4 kW kg^{-1}, respectively.

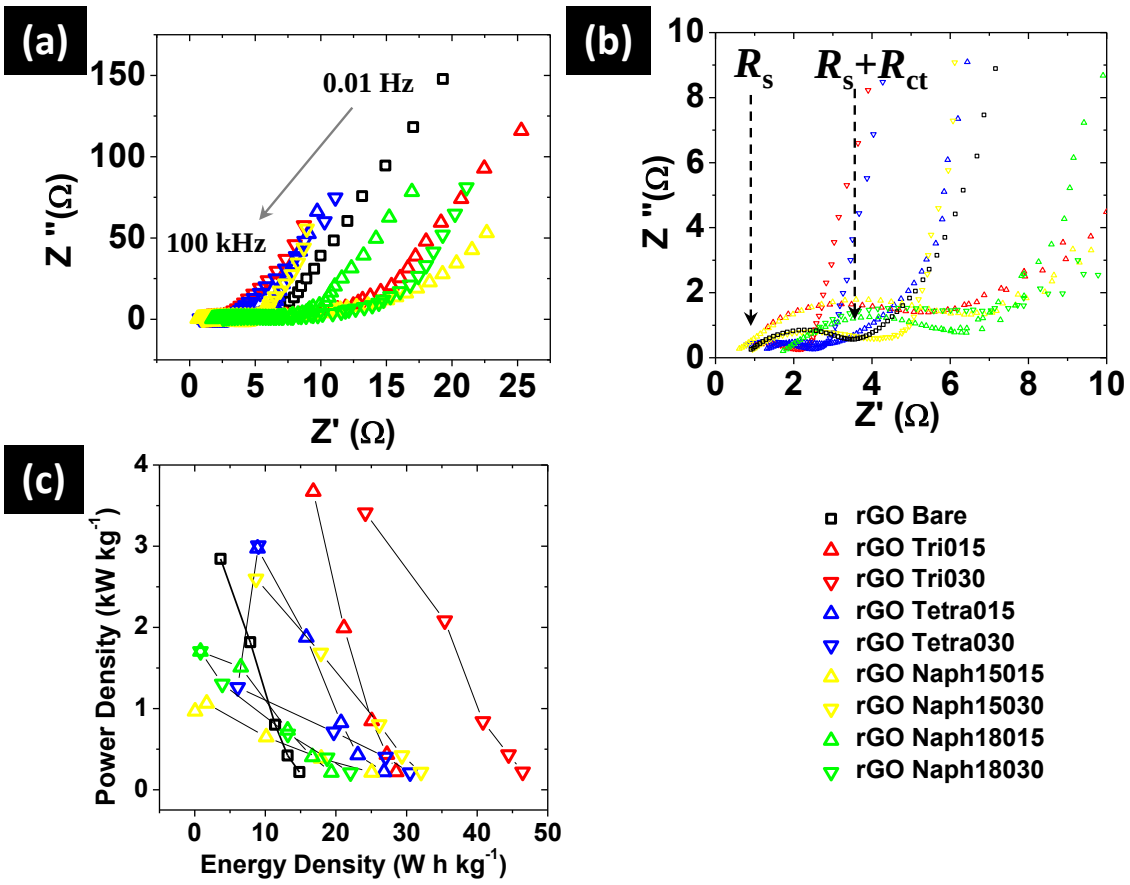

Figure A. 13 (a) Nyquist plot of the samples with frequency range of 0.01 Hz-100 kHz. Z' and Z'' stand for the real and the imaginary part of impedance, respectively; (b) the magnified plot showing the data in the high-frequency region in (a); (c) Ragone plot of samples.

Table A. 1 Equivalent series resistance (R_s) and charge-transfer resistance (R_{ct}) extracted from Nyquist plot shown in **Figure A. 13** (b).

Sample ID*	1	2	3	4	5	6	7	8	9
R_s(ohm)	0.91	1.34	0.61	1.32	0.79	0.61	0.95	1.73	2.57
R_{ct}(ohm)	2.59	3.91	1.83	1.45	1.58	5.93	3.1	4.56	3.02

To explore the electrochemical nature of the enhanced C_s of rGO-Spacers samples, we studied the CV curves of the samples using a three-electrode setup. Pseudocapacitance of chemical species may appear as reversible redox peaks in CV of three-electrode setup. CV curves of the original spacers, rGO Bare, rGO Spacers and original spacers are plotted in one graph for convenient comparison (**Figure A. 14**). For **Tri**, two reversible redox humps at 0.13 V and 0.37 V are shown. The redox hump can be assigned to the reversible benzoid-quinoid structure conversion.[156] In the potential range of 0.8-1.0 V, a non-reversible oxidation peak show up. The peak diminishes after several cycles. The behavior is characteristic of small aromatic amine molecules where the amino groups undergo anodic oxidation and subsequent polymerization through carbon-nitrogen bonds with other molecules.[157] Similar humps of amino group oxidation are observed in the CV curves of **Tetra**, **Naph15** and **Naph18**. In order to verify whether the spacers molecules could react with themselves during the hydrothermal reactions, control experiments were done where the spacers molecules were put in the reactor under the same condition without the presence of GO. After hydrothermal reaction without GO, the solution of the spacers remain their original color. Only trace amount of precipitation (less than 0.5 mg) could be filtered out from the solution. In contrast, as discussed in the experimental section, a large amount of hydrogel was produced in the GO-spacers reaction system and could be easily filtered out, while the filtrate solution was colorless, indicating most of amine spacers were in the hydrogel and few of them were left in the solvent. CV curves of the spacer solution after the reaction without GO (with 1 M H_2SO_4 as the electrolyte) show similar humps to the ones observed in their original CV curves. The retention of the major peaks of the spacers in the range of 0.8-1.0 V after hydrothermal reaction indicates that most of the primary amine groups in the amine molecules were unreacted during the hydrothermal reaction if GO were absent, and the spacers themselves are unlikely to form new chemical species, because the reaction between the amine spacer molecules themselves typically requires oxidative reagents, e.g. $K_2S_2O_8$, which is absent in this paper. [158] CV curve of

rGO Bare shows broad redox bump at 0.52 V. In comparison, new redox peaks also show up at 0.14 V and 0.50 V for rGO Tri030, 0.24 V, 0.58 V and 0.84 V for rGO Tetra030, 0.51 V for rGO Naph15030 and 0.52 V for Naph18030. The different positions of the bumps between the CV curves of rGO-Spacers samples and their precursors indicates that the capacitance of the samples is originated from the product of the reactions between the spacers and GO rather than themselves. The improved C_s value in the rGO-Spacers sample indicates the pivotal importance of engineering of the molecular structures of the spacers, which determines the pathway of the reactions and the structures of the final products. In this sense, the origin of the capacitance in rGO-Spacers is fundamentally different from graphene with other types of pseudocapacitant modifiers such as polyaniline and metal oxide which add their own pseudocapacitance to the whole electrode materials.

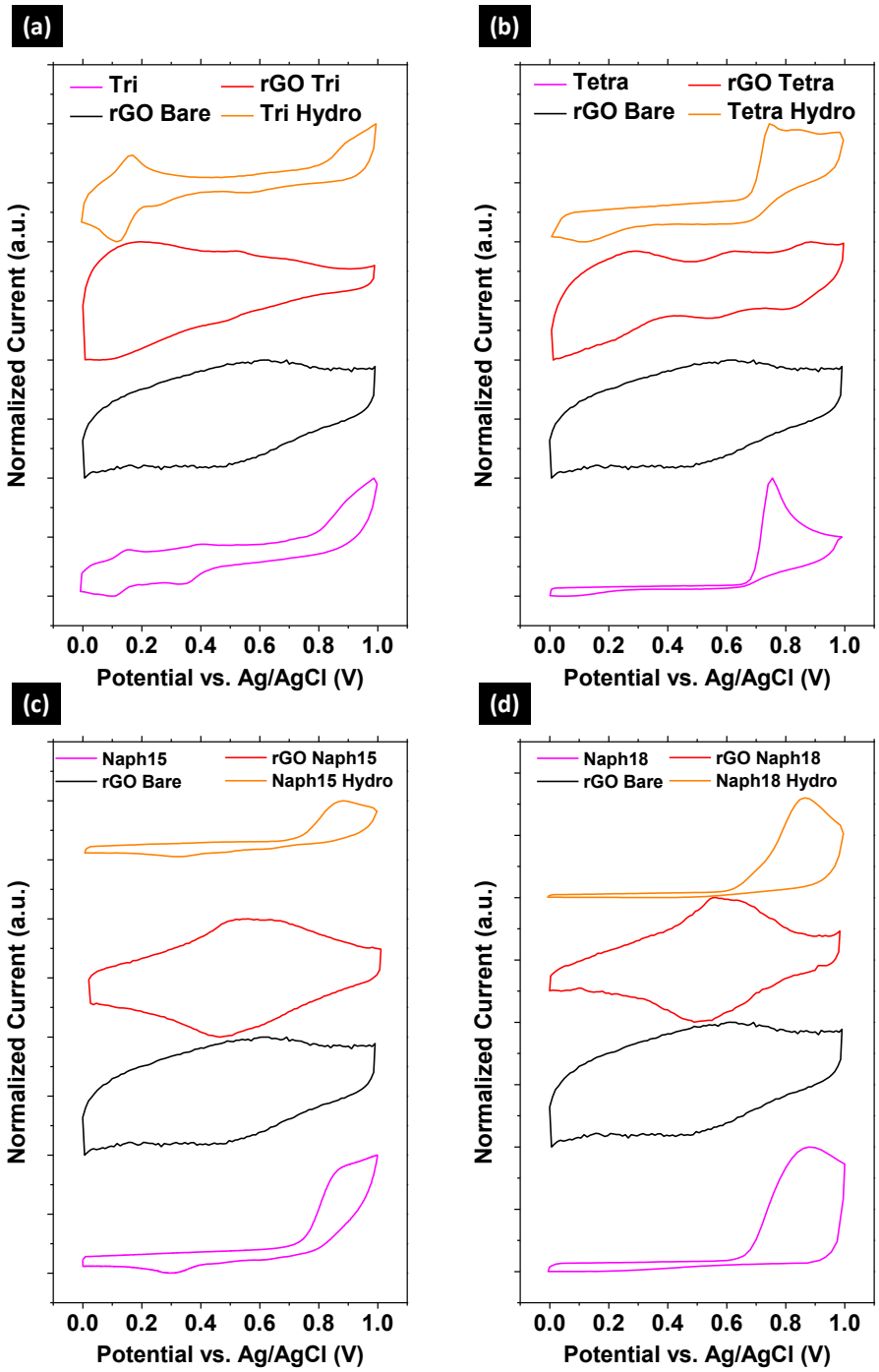

Figure A. 14 Cyclic voltammetry curve of amine spacers (magenta curves—), rGO Bare (black curves—), rGO Spacers (red curves—) and amines spacers after hydrothermal processing (yellow curves—) using three-electrode setup.

To elucidate the pathways of reactions between GO and the various spacers, we did further characterization of the samples. As a qualitative characterization, we conducted thermogravimetric analysis (TGA) on the samples. As shown in **Figure A. 15**, rGO Bare shows a gradual weight loss from 25 ^{o}C due to the loss of absorbed moisture. After 355 ^{o}C, the rGO Bare started to decompose. In comparison, the samples with the addition of spacers show a much higher onset temperature of decomposition at 420 ^{o}C-520 ^{o}C. The low decomposition temperature of rGO Bare may be caused by a larger content of labile oxygen groups remaining in the materials, as demonstrated in the following analysis of elemental compositions.

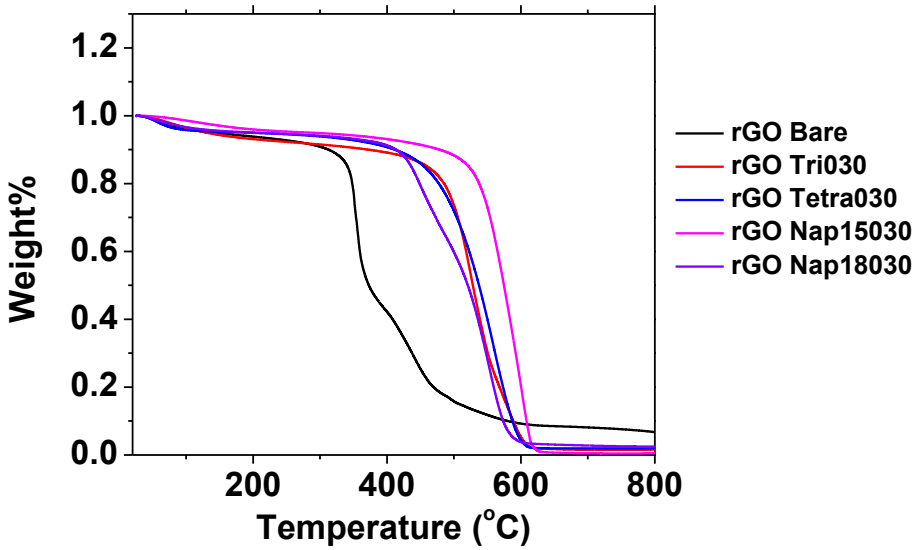

Figure A. 15 Thermal gravimetric analysis (TGA) curves of the samples under Air atmosphere.

In order to obtain the quantity of the spacers that reacted with GO, we first analyzed the weight of the products after hydrothermal reactions. In all the experiments, the amount

of GO, solvent, HCl and Na_2CO_3 were fixed, while only the amount of each type of spacer varied as 0.15 mmol and 0.30 mmol. After hydrothermal reaction, the weight of GO reduced from 28.0 mg to 14.5 mg when no spacers was added. The product of this reaction, i.e. rGO Bare, was considered as a form of reduced graphene oxide where defects of oxygen-containing groups in GO were partially removed and the conjugated carbon network was partially recovered.[133] Assuming that in all the rGO Spacers the weight of reduced graphene is constant, we defined the term "weight gain" of the spacers as the difference between the final weight of the rGO Spacers sample and the weight of rGO Bare, i.e. 14.5 mg. Given the known molecular weight of each type of spacer, the quantity of "mole gain" can be obtained from the weight gain to estimate how many moles of the spacers reside in the final products. As shown in **Table A. 2**, the mole gain is 0.15 mmol in both rGO Tri015 and rGO Tetra015, equaling to the amount of **Tri** and **Tetra** added as the reactants. In rGO Tri030, the mole gain is 0.24, which is the highest among all the samples. The information from the mole gain reveals that the reactivity of **Tri** and **Tetra** are higher than that of **Naph15** and **Naph18**. Also, when comparing the mole gain of rGO Tri015 and rGO Tri030, it can be found that the mole gain is not double when the amount of **Tri** as reactant is doubled. Samples with other spacers also show the same trend.

Table A. 2 Weight of reactants and products in modification of GO

Sample ID[1]	1	2	3	4	5	6	7	8	9
GO Weight (mg)	28	28	28	28	28	28	28	28	28
Spacer Weight (mg)	0	29.4	58.8	32.1	64.3	23.7	47.5	23.7	47.5
Spacer M.W.(g mol^{-1})	0	120.2	120.2	214.3	214.3	158.2	158.2	158.2	158.2
Final Weight (mg)2	14.5	32	43.2	46.9	57.8	33	38	26.3	30
rGO Weight (mg)[3]	14.5	14.5	14.5	14.5	14.5	14.5	14.5	14.5	14.5
Weight Gain (mg)[4]	0	17.5	28.7	32.4	43.3	18.5	23.5	11.8	15.5
Mole Gain (mmol)5	0	0.15	0.24	0.15	0.2	0.12	0.15	0.07	0.1

Note:

1. The sample ID refer to: 1. rGO Bare; 2. rGO Tri015; 3. rGO Tri030; 4. rGO Tetr015; 5. rGO Tetra003; 6. rGO Naph15015; 7. rGO Naph15030; 8. rGO Naph18015; 9. rGO Naph18030;
2. The final weight was averaged from products of three separate batches of reactions;
3. Assuming that all the samples contain the sample amount of "graphene" rGO with that in rGO Bare;
4. Weight Gain=Final Weight-rGO Weight;
5. Mole Gain=Weight Gain/Spacer M. W, where M.W. stands for molecular weight.

X-ray photoelectron spectroscope (XPS) was employed to provide more details in the chemical structures of the samples. As shown in the survey spectra (**Figure A. 16**), only C and O signals were observed from the curves of GO and rGO Bare, while C, N and O signals were found in other samples. The atomic ratio in each sample are derived from the survey spectra and listed in **Table A. 3**. For convenient comparison, the ratio of N and O are normalized to that of C. A similar quantity of mole gain of the spacers is also calculated based on the ratio of N to estimate the amount of spacer molecules in the rGO-Spacers samples. When looking at the ratio of O, it is clear that the ratio of O reduces to half after hydrothermal reaction without addition of spacers. The result supports our previous statement that the oxygen-containing groups are to be removed during the hydrothermal reaction. Given the fact that the pH of the reaction mixture was 11, the major reactions in the case of rGO Bare should be those between GO and hydroxide ion (OH^-), and/or the self-decomposition of GO.[159] For the rGO-Spacers samples, the atomic ratio of O is normalized to the ratio of C after deduction of those existed in the spacer molecules (referred to as $O_{at\%}$') to compare the quantity of O to that in rGO Bare. The $O_{at\%}$' of rGO Tri030 and rGO Tetra015 are lower than that of rGO Bare, while Oat% in other samples are higher than that of rGO Bare. The low ratio of O indicates a low density of defects in the graphene, which may explain the small R_s of rGO Tri030 and its outstanding specific

capacitance at discharge current density. By comparing the O_{at}%' of the samples with the same type of spacers, it is noteworthy that adding a higher amount of spacers, except **Tetra**, in the hydrothermal reaction results in a lower content of O in the final product, suggesting that the spacers may facilitate the removal of oxygen-containing groups in GO. By using the atomic ratio of N, mole gains of the spacers in each sample were also calculated. The mole gains values deviate from that obtained from the weight measurement in **Table A. 2**, because the latter is calculated from the net weight gain by assuming the "rGO Bare" content in each sample is identical. The atomic ratio information from XPS manifests that the actual "rGO Bare" content is different in each samples due to the involvement of spacers during the removal of oxygen-containing groups. However, the mole gain of rGO Tri030 still ranks the highest while rGO Naph15015 and rGO Naph18015 is the lowest among all the samples, supporting a higher reactivity of **Tri** to GO.

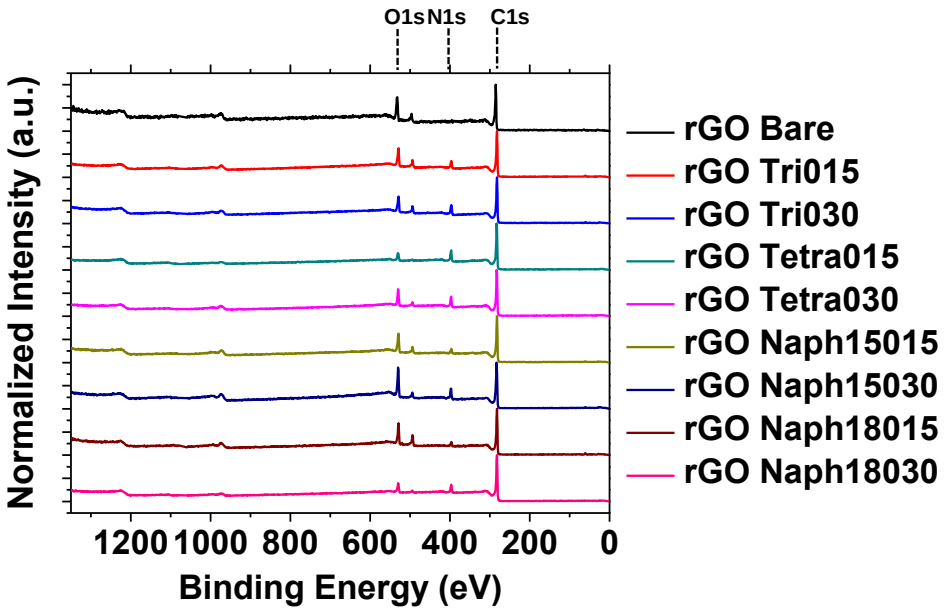

Figure A. 16 X-ray photoelectron spectroscopy (XPS) survey spectra of the samples.

Table A. 3 Atomic ratio of carbon (C), nitrogen (N) and oxygen (O) of the samples derived from X-ray photoelectron spectra (XPS) data.

Sample ID[1]	1	2	3	4	5	6	7	8	9	10
$C_{at\%}$[2]	1	1	1	1	1	1	1	1	1	1
$N_{at\%}$	0	0	0.109	0.137	0.154	0.129	0.077	0.097	0.091	0.108
$O_{at\%}$	0.422	0.223	0.188	0.094	0.098	0.164	0.197	0.116	0.13	0.097
$N_{at\%}$'[3]	0	0	0.139	0.189	0.285	0.211	0.124	0.19	0.169	0.234
$O_{at\%}$	0.422	0.22	0.24	0.13	0.181	0.268	0.32	0.225	0.239	0.21
Mole Gain[4]	0	0	0.077	0.128	0.117	0.114	0.078	0.122	0.078	0.107

1. The sample ID refer to: 1. GO; 2. rGO Bare; 3. rGO Tri015; 4. rGO Tri030; 5. rGO Tetr015; 6. rGO Tetra003; 7. rGO Naph15015; 8. rGO Naph15030; 9. rGO Naph18015; 10. rGO Naph18030.
2. Cat%, Nat% and Oat% refer to the atomic ratio of C, N and O, respectively, derived from the XPS survey spectrum. The ratio of C is normalized to 1.0. The ratio of N and O is normalized to that of C.
3. Nat%' and Oat%' refer to the atomic ratio of N and O, respectively, normalized to the ratio of C after deducting the content of C in the spacer molecules.
4. Mole Gain=Final Weight $\times N_{at\%}/[(m_C \times C_{at\%}+m_N \times N_{at\%}+m_O \times O_{at\%}) \times n_N]$, where Final Weight refers to the final weight of the product. $\underline{m}_C$, $\underline{m}_N$ and $\underline{m}_O$ are the molar mass of C, N, O. n_N is the number of N atoms per spacer molecule.

High-resolution scans on C 1s, N 1s and O 1s peaks from XPS are further analyzed to elucidate the chemical species in the samples. As the reference, the curves of GO, rGO Bare and **Naph15** were analyzed to obtain the binding energy of chemical species possibly involved in other samples (**Figure A. 17**). In GO, it has been widely accepted that the carbon atoms can be divided into those bonded to adjacent carbon atoms (C-C/C=C), to oxygen atoms through single bonds (C-O), to oxygen atoms in carbonyl groups of ketones and aldehydes (C=O) and to oxygen atoms in carboxylate groups (-O-C=O).[160] In the high resolution C1s XPS spectrum of GO (**Figure A. 17**), the overall curve was fitted by four peaks at binding energy of 284.5 eV (C-C/C=C), 286.5 eV (C-O), 287.9 eV (C=O)

and 289.0 eV (-O-C=O). The C 1s spectrum of rGO Bare is also fitted by the same peaks. Apparently, the prominent peaks of oxygen-contain species in GO were significantly reduced in rGO Bare, in consistent with the drop of oxygen atomic ratio from the survey spectrum. Further, we fitted the C1s spectrum of **Naph15** which contains only C atoms in the naphthalene ring without bonding to amino groups (C-C/C=C) and two equivalent C atoms bonding to amino groups (C-N). A peak at 285.5 eV is assigned to C-N. The existence of C-N peak at 285.5 eV is evident when comparing the C1s spectra of **Naph15** and that of rGO Bare which contains no C-N. A bump at ~290.0 eV can be observed in the C 1s spectrum of Naph15 as well, which can be assigned as a satellite peak caused by the π-π* transition of the aromatic cores.[161] The high-resolution XPS peaks of rGO-Spacers samples are shown in **Figure A. 18**-**Figure A. 21**.

By comparing the C 1s peak of rGO Bare with those of rGO-Spacers, it is clear that C-N peak can be found in peak of all the rGO-Spacers samples. For the N 1s peak, **Naph15** was used as the reference where all the N atoms exist in the chemically equivalent primary amine groups ($-NH_2$). The signal of the N in the primary amine group appears as one slim peak at 399.2 eV. N 1s of **Tetra** and **Naph18** also show similar features. For **Tri**, since some of the amino groups are protonated, another peak of $-NH_3^+$ appears at 400.8 eV.

In comparison to those of the spacers themselves, N 1s peaks of all the rGO-Spacers samples shows an evident shoulder peak at 400.2 eV, which can be assigned to the secondary amino group (-NH-).[162] The appearance of the secondary amino group is more evident when comparing the N 1s signal of rGO-Spacers with that of **Naph15**, which strongly shows that some of the primary amino groups in the spacers are covalently bonded to carbon atoms in graphene sheets, given the fact the reactions between the spacers are less possibly as shown in the three-electrode CV measurement (**Figure A. 14**). The O1s peaks of the rGO-Spacers sample also show distinctive features compared to that of rGO Bare. The O1s peak of rGO Bare shows two components at 531.1 eV and 533.2 eV with similar integrated area. The two components can be assigned to the C-O and C=O

species.[163] In all the rGO-Spacers, the integrated area of C-O components significantly drops relative to that of C=O components. The different contents of C-O and C=O in rGO Bare and rGO-Spacers further indicate that the removal of oxygen-containing groups in GO was caused from the spacers. The atomic ratio of $–NH_2$, -NH-, C-O and C=O species is calculated based on the integrated area of corresponding peaks and the normalized atomic ratio $N_{at\%}$' and $O_{at\%}$' obtained in **Table A. 4**. From the low content of C-O in rGO Tri030, its low R_s could be explained by a maximized removal of C-O defects in the graphene sheets accompanied by the recovery of the conjugated carbon network, since the C-O species, such as C-OH and C-O-C, are the major defects in the conjugated network of GO.[160]

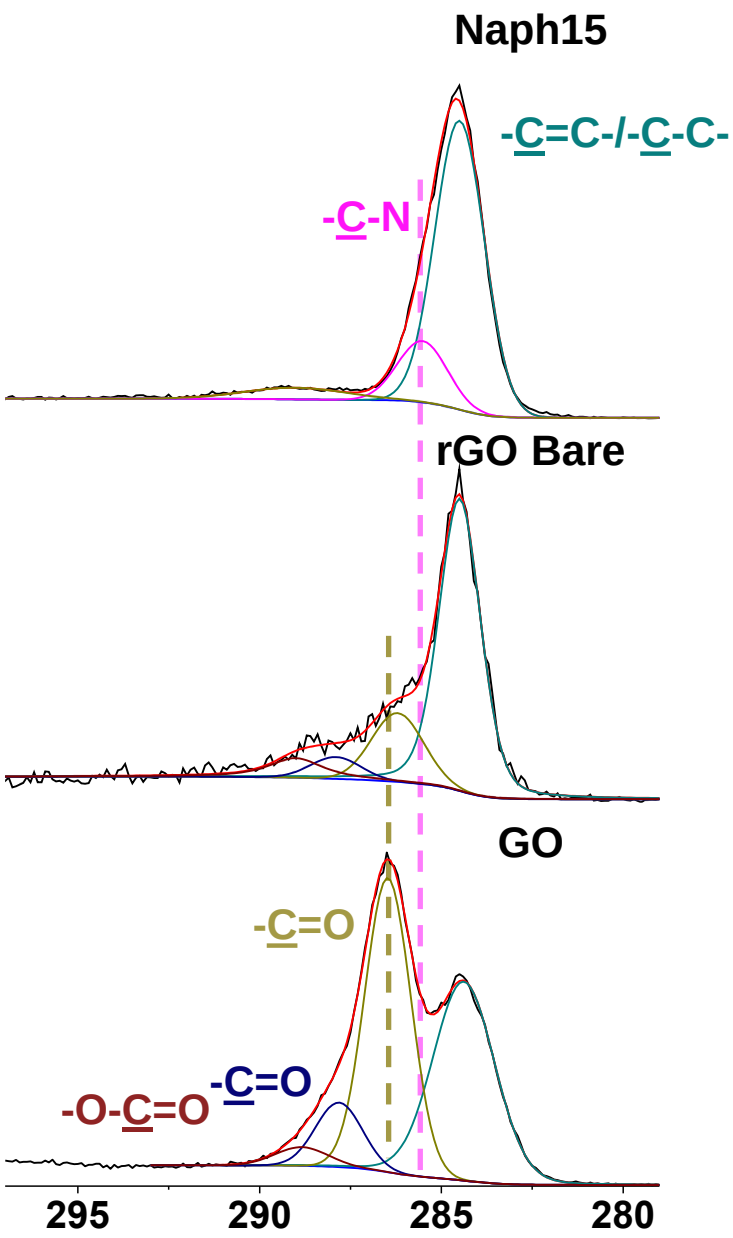

Figure A. 17 High-resolution XPS of C1s peak of GO, rGO Bare and **Naph15**.

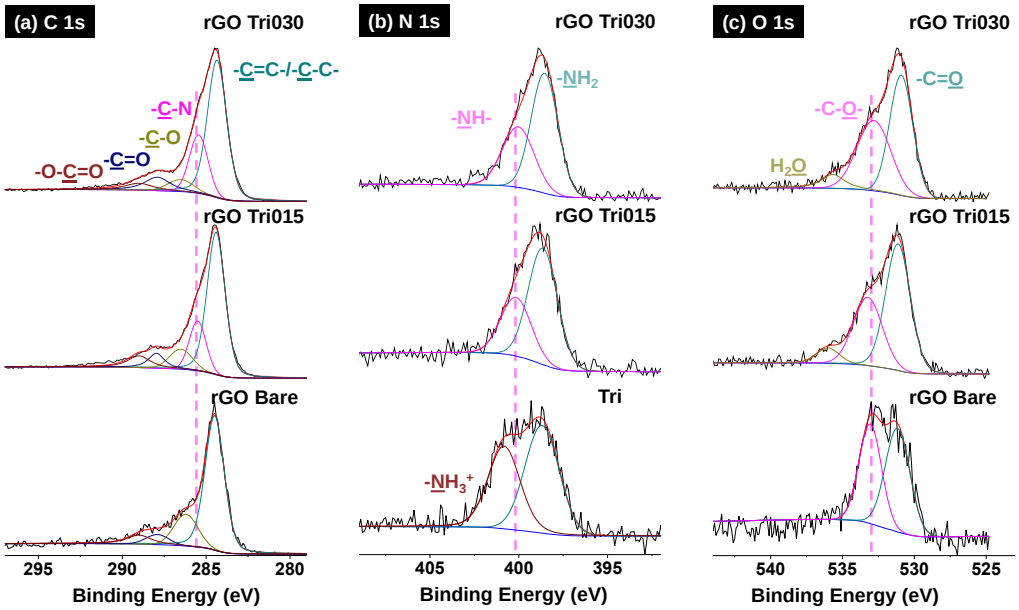

Figure A. 18 High-resolution C1s (a), N1s (b) and O1s (c) XPS spectra of GO, rGO Bare, rGO Tri015 and rGO Tri030.

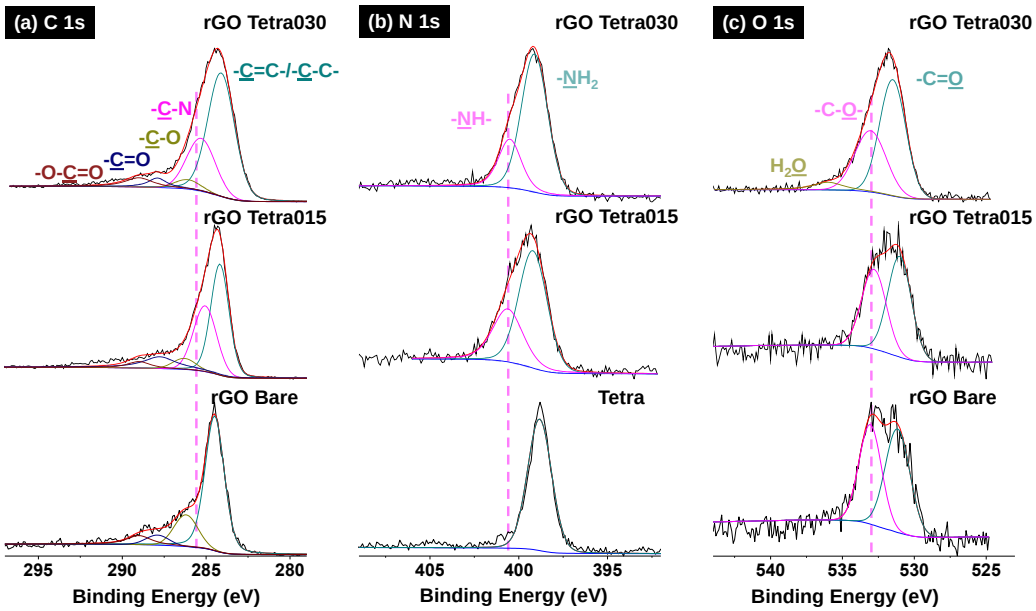

Figure A. 19 High-resolution C1s (a), N1s (b) and O1s (c) XPS spectra of GO, rGO Bare, rGO Tetra015 and rGO Tetra030.

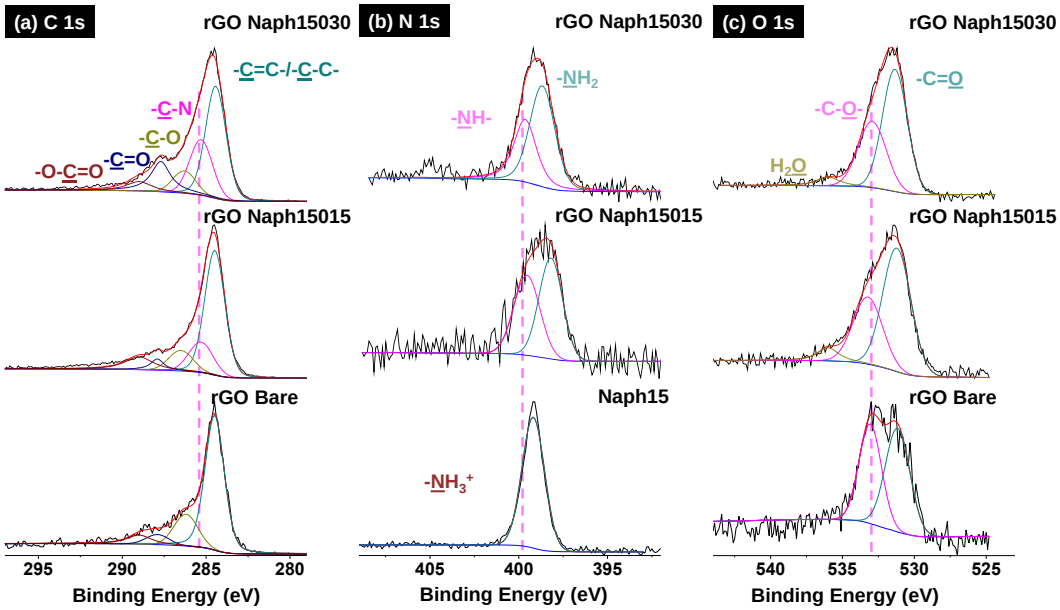

Figure A. 20 High-resolution C1s (a), N1s (b) and O1s (c) XPS spectra of GO, rGO Bare, rGO Naph15015 and rGO Naph15030.

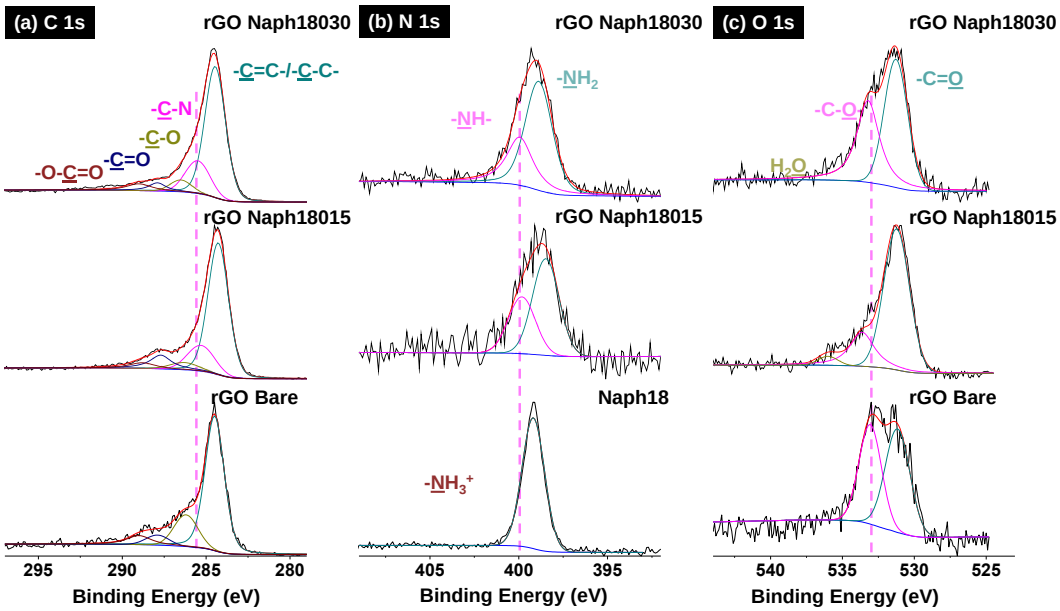

Figure A. 21 High-resolution C1s (a), N1s (b) and O1s (c) XPS spectra of GO, rGO Bare, rGO Naph18015 and rGO Naph18030.

Table A. 4 Ratio of chemical species from high-resolution N 1s and O 1s peak

Sample ID[1]	1	2	3	4	5	6	7	8	9
0	0	0.091	0.118	0.186	0.203	0.066	0.115	0.105	0.153
-**N**H-	0.000	0.048	0.071	0.1	0.069	0.058	0.075	0.063	0.082
C-**O**[3]	0.127	0.139	0.067	0.089	0.105	0.191	0.132	0.175	0.114
C=**O**	0.078	0.086	0.054	0.093	0.066	0.108	0.081	0.056	0.096

1. The sample ID refer to: 1. rGO Bare; 2. rGO Tri015; 3. rGO Tri030; 4. rGO Tetr015; 5. rGO Tetra003; 6. rGO Naph15015; 7. rGO Naph15030; 8. rGO Naph18015; 9. rGO Naph18030;

2. The ratio of $-\underline{N}H_2=N_{at\%}' \times A(\text{-}NH_2)/[A(\text{-}NH_2) + A(\text{-}NH\text{-})]$, where $N_{at\%}'$ is defined in **Table A.3**, $A(\text{-}NH_2)$ and $A(\text{-}NH\text{-})$ are the integrated area of peaks corresponding to $-NH_2$ and –NH-, respectively. The ratio of –NH- is calculated similarly.

3. The ratio of $-C\text{-}\underline{O}=O_{at\%}' \times A(\text{-}C\text{-}O)/[A(\text{-}C\text{-}O) + A(\text{-}C=O) + A(H_2O)]$, where $O_{at\%}'$ is defined in **Table A.4**, $A(\text{-}C\text{-}O)$, $A(\text{-}C=O)$ and $A(H_2O)$ are the integrated area of peaks corresponding to –C-O, –C=O and H_2O, respectively. The ratio of –NH- is calculated similarly.

The chemical bonds can be further revealed by FTIR shown in **Figure A. 22**-**Figure A. 25** . As the reference, the FTIR spectrum of GO shows typical O-H stretch as a very broad peak from 3500-2800 cm-1. The C-H stretching peaks show up at 2919 cm^{-1} and 2852 cm^{-1}. The stretching peaks of C=O and C=C appear at 1727 cm^{-1} and 1616 cm^{-1}. The stretching of C-O in epoxy groups can be located at 1230 cm^{-1}, and C-O in C-OH at 1060 cm^{-1}. The bending of C-O in epoxy groups can be found at 830 cm^{-1}.[164] After reduction, the O-H peak at 3500-3000 cm^{-1} is still observable, while the carbonyl peak at 1727 cm^{-1} is inconspicuous. The peaks around 1060 cm^{-1} can be assigned as the C-O peaks. The curve of **Tri** possesses a broad peak from 3500-2600 cm-1 from N-H stretch in the amino and protonated amino groups. The scissoring and wagging of N-H appear at 1620 cm^{-1} and 844 cm^{-1}, respectively. The stretching of C=C and C-N show up at 1550-1400 cm^{-1} and 1201 cm^{-1}. The spectra of **Tetra**, **Naph15** and **Naph18** also show corresponding peaks. After

reaction of GO with spacers, the broad peak at 3500-3000 cm^{-1} from O-H/N-H stretching and 2960-2850 cm^{-1} from C-H stretching can still be observed in the rGO-Spacers samples. Compared to the spectrum of rGO Bare, a new sharp peak around at 1730 cm^{-1} arises in that of rGO Tri, similar peaks also show up in the spectra of rGO Tetra, rGO Naph15 and rGO Naph18. Judging from the position, peaks at this range can be assigned as the stretching of C=O. Other new peaks at around 1620 cm^{-1} for scissoring of N-H and 840 cm^{-1} for wagging for N-H can also be observed in these samples, supporting the incorporation of spacers in this materials. On the other hand, the prominent peak at 1060 cm^{-1} for C-O in the curve of rGO Bare is obscure in the spectra of the rGO-Spacers samples. The higher intensity of C=O and lower intensity of C-O in FTIR spectra of rGO-Spacers samples are consistent with their XPS O1s spectra.

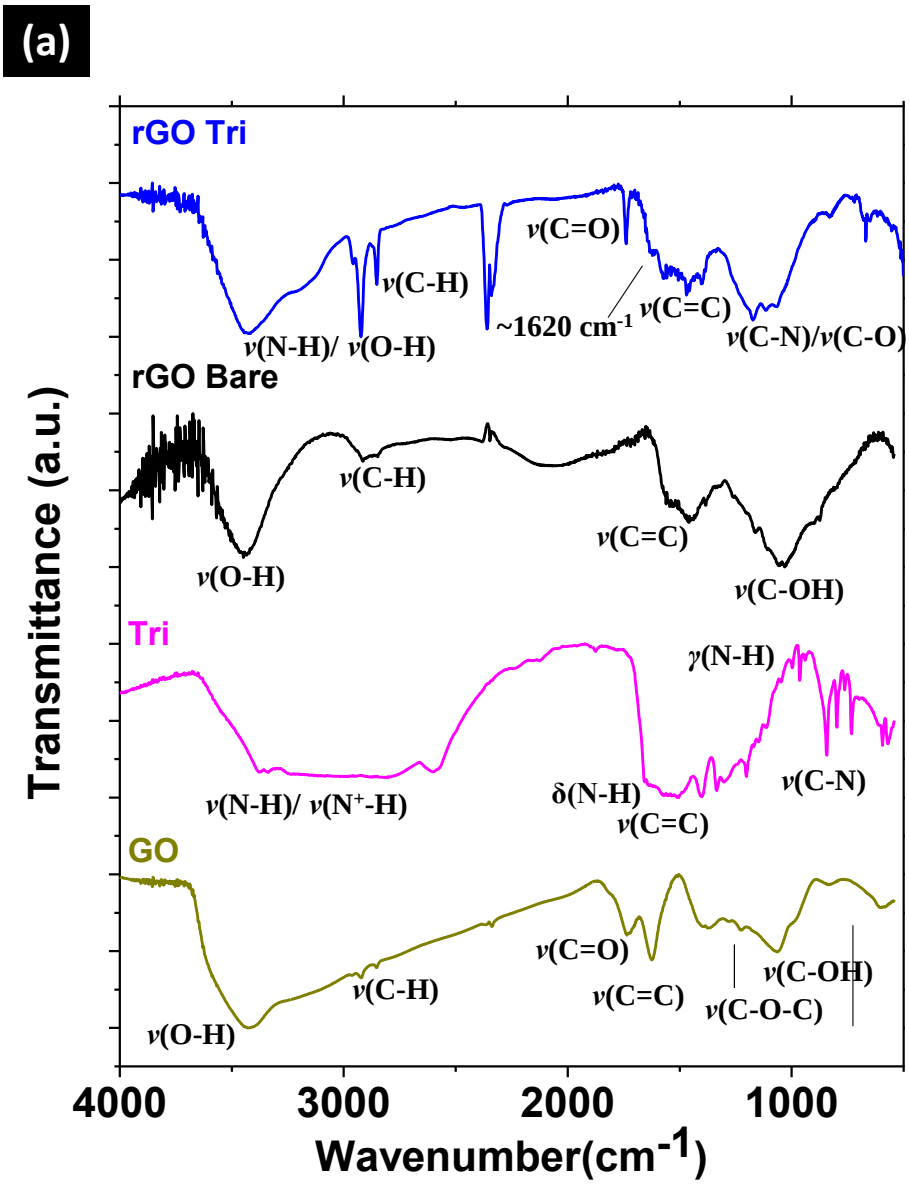

Figure A. 22 Fourier-transform infrared spectra (FTIR) of GO, Tri, rGO Bare, rGO Tri.

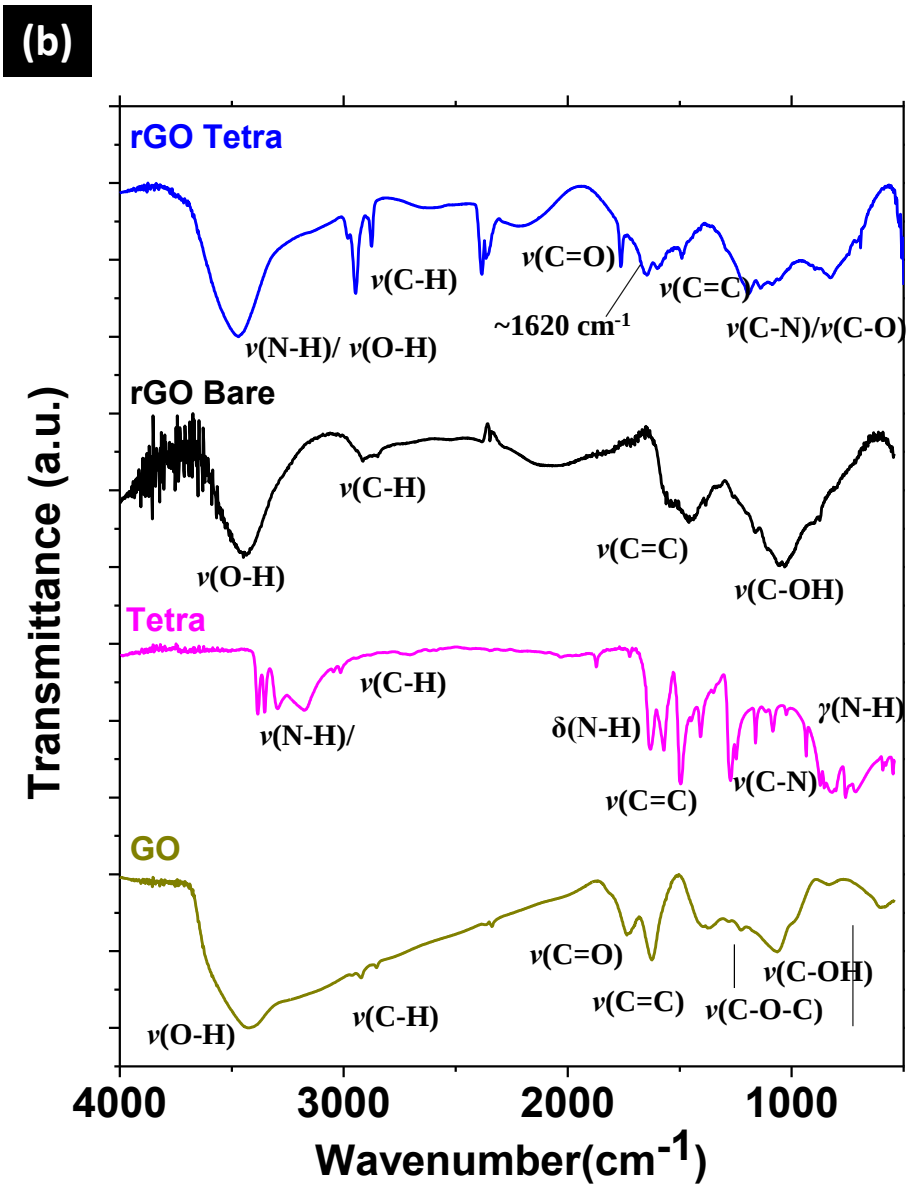

Figure A. 23 FTIR of GO, Tetra, rGO Bare, rGO Tetra015 and rGO Tetra030.

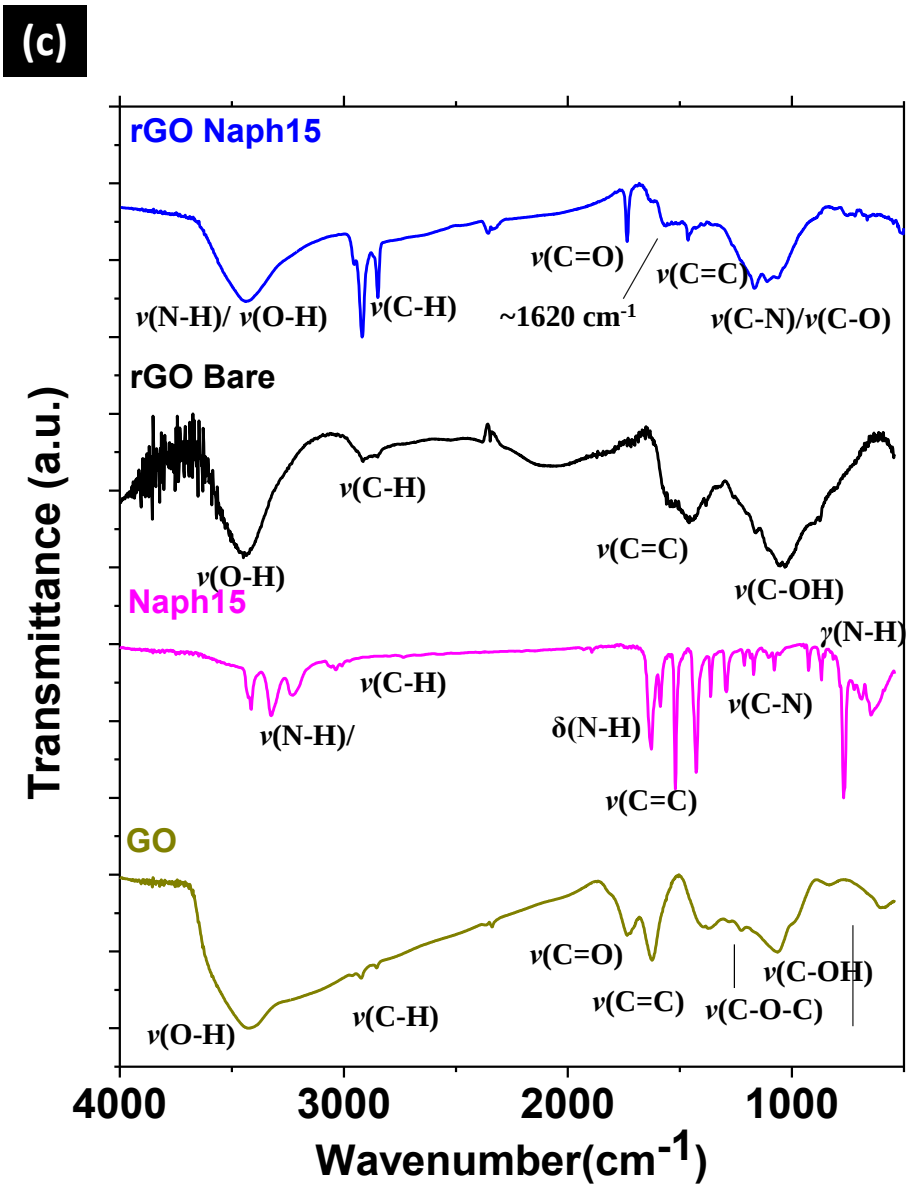

Figure A. 24 FTIR of GO, Naph15, rGO Bare, rGO Naph15015 and rGO Naph15030.

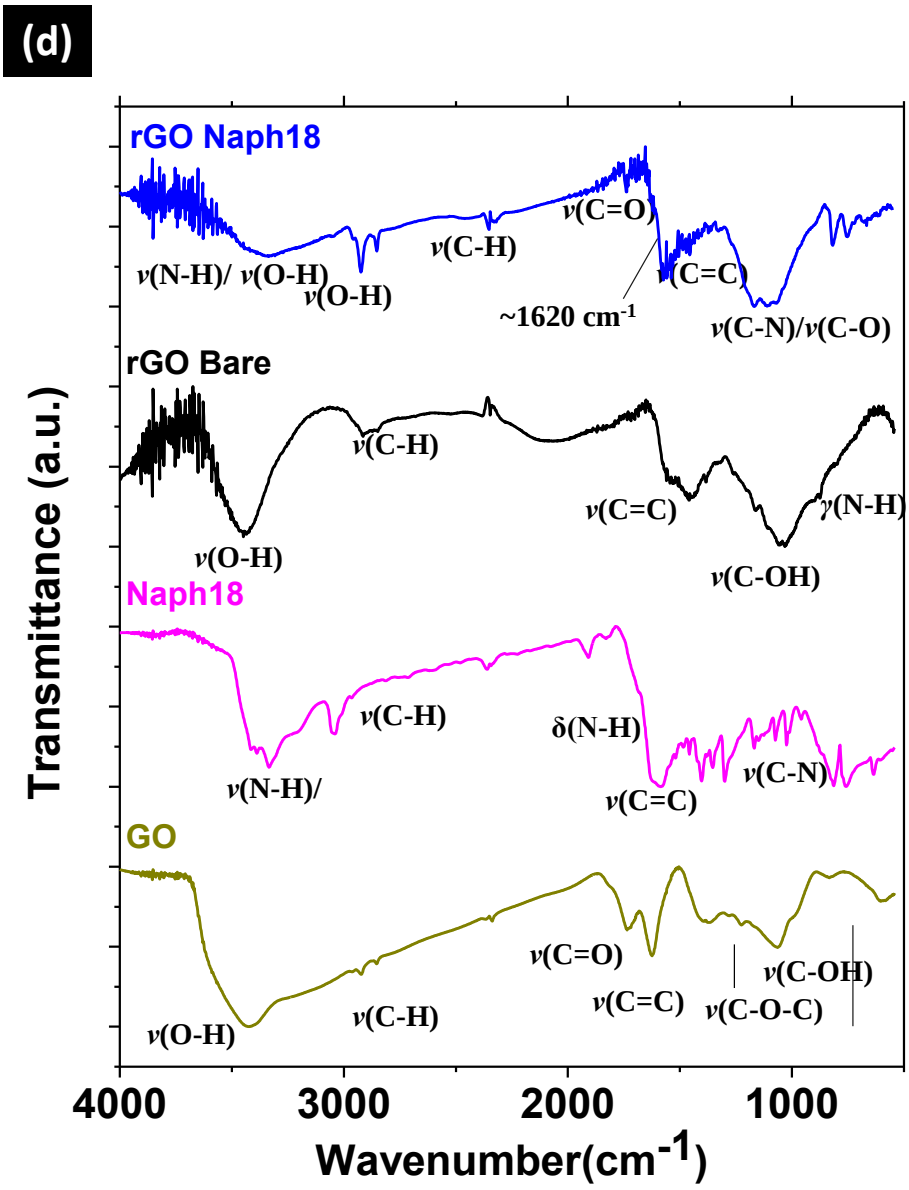

Figure A. 25 FTIR of GO, Naph15, rGO Bare, rGO Naph18015 and rGO Naph18030.

Raman spectroscopy was also employed to study the structural variations of the samples (**Figure A. 26**). The graphene oxide precursor shows *D* peak at 1359 cm^{-1} and *G* peak at 1602 cm^{-1} of graphitic structures. After hydrothermal reaction, rGO Bare shows the *D* and G peaks at 1360 cm^{-1} and 1599 cm^{-1}, respectively. The ratio of I_D/I_G increases from GO to rGO Bare, indicating more conjugated regions of sp^2 hybridized carbon with smaller area were generated during the hydrothermal reaction. The spacer molecule **Tri** shows peaks at 1235 cm^{-1} for C-N stretch, 1401 cm^{-1} and 1550 cm^{-1} for C=C stretch in benzene rings. A broad peak at 1510 cm^{-1} may be assigned to stretch of C-C and C-N^+ [165]. In Raman spectra of rGO Tri015 and rGO Tri030, two major peaks near the *D* peak and *G* peak of rGO Bare are observed. We name these two peak as *D* peak and *G* peak as well. However, the *D* peaks in rGO Tri015 and rGO Tri030 are increasingly broadened. The *G* peak in rGO Tri015 is broadened, while a new peak at 1507 cm^{-1} near the G peak of rGO Tri030 arises. The downshift of the *G* peak has been reported when the N atoms were incorporated into the conjugated system of graphene.[140, 166] Also a shoulder peak around 1200 cm^{-1} can be observed in rGO Tri015 and becomes more prominent in rGO Tri030. The peak position coincides with the C-N stretch at 1235 cm^{-1}, indicating the existence of C-N in the two samples. The downshifting of *G* peak were also observed in Raman spectra of rGO Tetra015 and rGO Tetra030, as well as the shoulder peak around 1200 cm^{-1}. In comparison, the spectrum of **Tetra** shows C-N stretch at 1194 cm-1, C-C stretch of the benzene ring at 1344 and 1600 cm^{-1}. No peak at 1530 cm^{-1} can be observed in the spectra of **Tetra**. Therefore, the shifted *G* peak at this position in rGO Tetra015 and rGO Tetra030 suggests that new chemical structures other than the rGO Bare or the original **Tetra** exist in these samples. Again, the shoulder bump around 1200 cm^{-1} also appeared in rGO Tetra015 and rGO Tetra030. Overall, **Tri** and **Tetra** render the valleys between *D* and *G* peaks getting higher, resulting in two bumps appearing less distinct. In comparison, the *D* and *G* peaks in rGO Naph15015, rGO Naph15030, rGO Naph18015 and rGO Naph18030 are only broadened without significant shift. The difference in Raman spectra

tell us that **Tri** and **Tetra** have a stronger capability than **Naph15** and **Naph18** in forming new conjugated systems with GO.

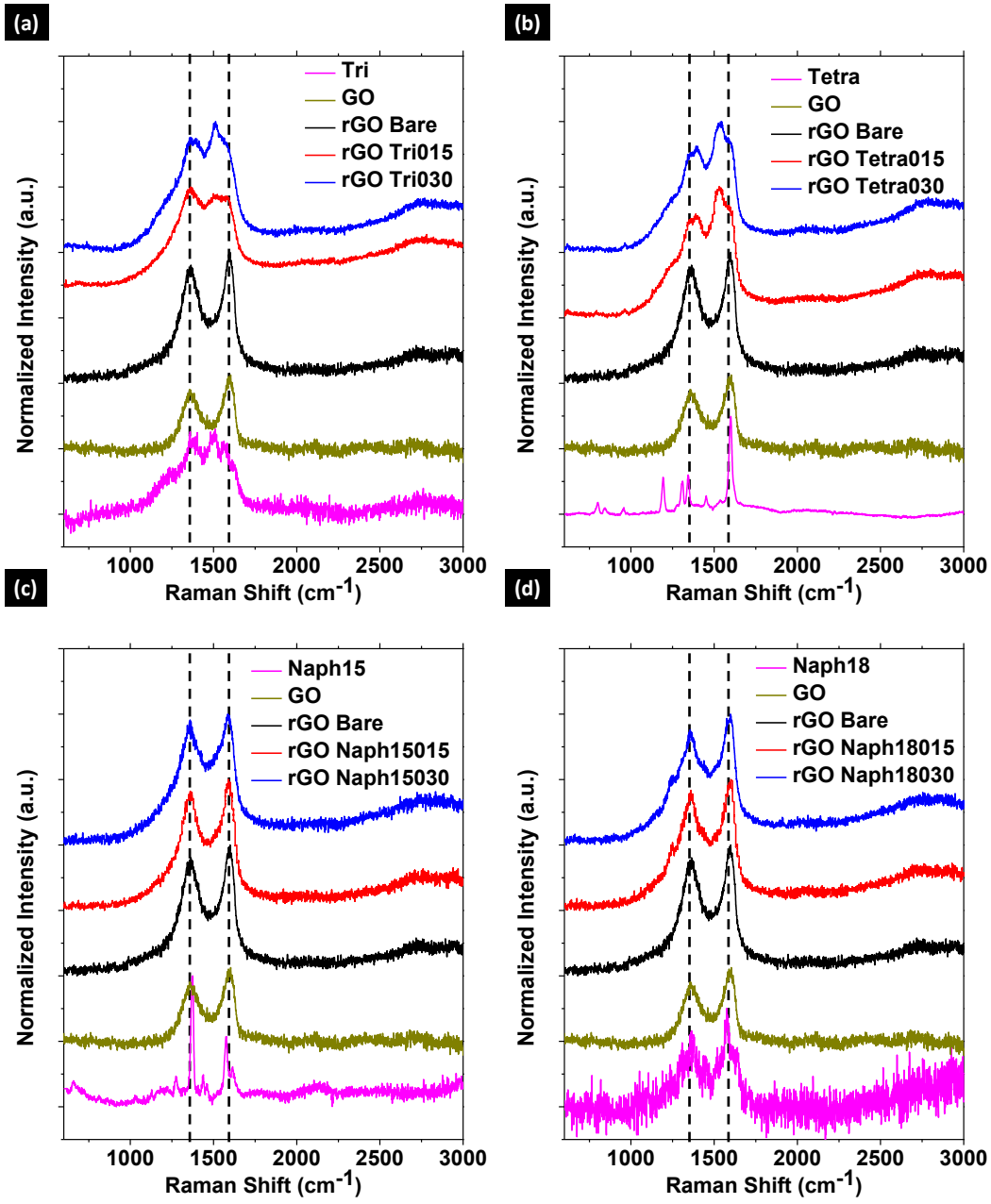

Figure A. 26 Raman spectra of the samples.

UV-visible spectra of the samples were used to analyze the chemical structures from the aspect of their conjugated systems (**Figure A. 27**). rGO Bare exhibits one major absorption peak at 260 nm and a broad tail in the higher wavelength region, which can be assigned to the π- π* transition of the conjugated carbon network (indicated by the black arrows).[167] The spacer molecules, **Tetra**, **Naph15** and **Naph18**, show absorption peaks at 247 nm, 264 nm and 266 nm from π- π* transition of biphenyl and naphthalene rings, with shoulder peaks at 20-40 nm higher wavelength corresponding to the n-π* transition from the lone-pair electrons of the conjugated $–NH_2$ groups. For **Tri**, since its HCl salt form is used and some of the $–NH_2$ groups are protonated, in addition to the peak at 264 nm of π- π* transition and the shoulder peak, two strong peaks at 457 nm and 489 nm appear, which can be assigned to the characteristically localized polaron of the protonated $–NH_2$ groups (i.e-NH_3^+) in aromatic amines.[168] For the rGO-Spacers, the π- π* peaks locate at 268 nm for rGO Tri015 and rGO Tri030, 279 nm for rGO Tetra015, 300 nm for rGO Tetra030, 264 nm for rGO Naph15015 and rGO Naph15030, 266 nm for rGO Naph18015 and Naph18030. These peaks were red shifted and broadened compared to that of rGO Bare. The red-shifting and broadening of the π- π* peaks indicate that the spacers may be either covalently bonded to or closely stacked to the carbon network of the graphene. With the existence of amino groups, the spacers have a high electron density, while the graphene oxide sheets a have lower electron density.[169] Introduction of the spacers may effectively increase the electron density of the conjugated system in graphene and induce the red shift of the absorption peak. Also, broad humps showed up around 489 nm for rGO Tri015 and rGO Tri030, 458 nm for rGO Tetra015 and rGO Ttetra030, 336 nm for rGO Naph15015 and Naph15030, 512 nm for rGO Naph18015 and rGO Naph18030. The broad peaks are characteristic charge transfer peaks between the electron-rich spacers (electron donor) and graphene oxide sheets (electron acceptor), which occurs when the electron donors and acceptors are closely attached (~4 Å or below).[170]

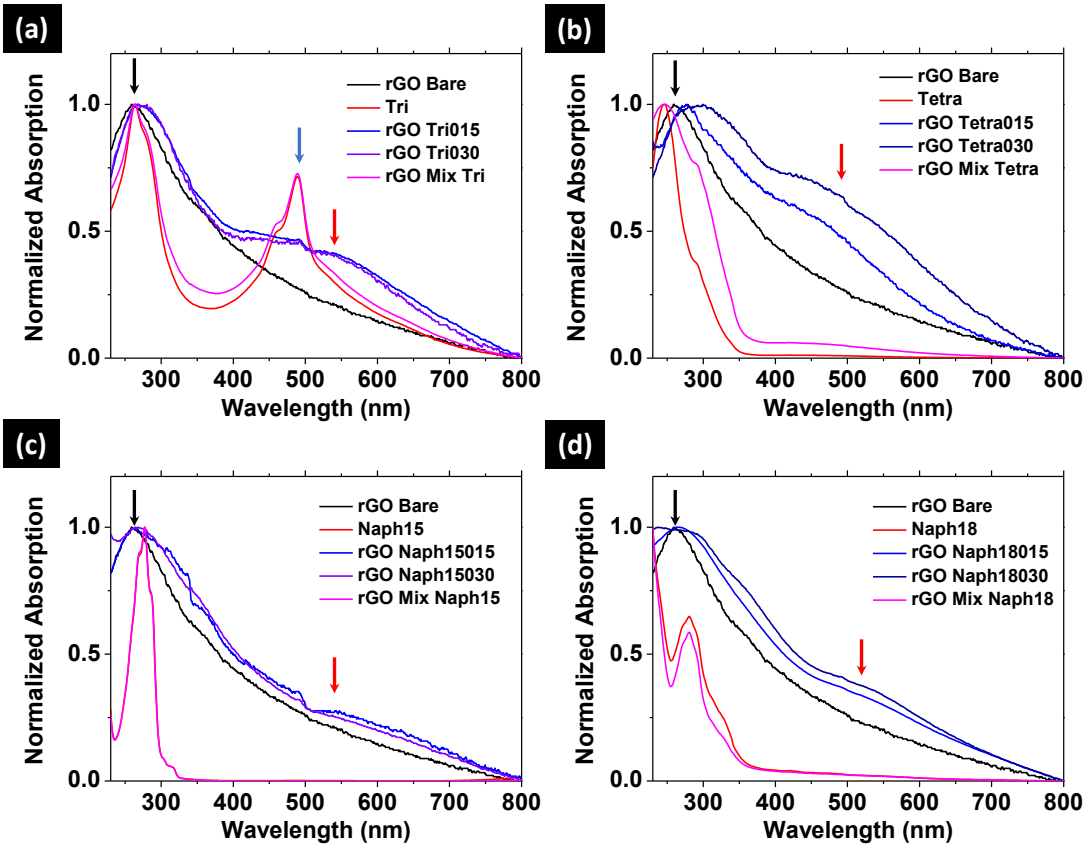

Figure A. 27 UV-vis spectra of the samples.

To confirm the effect of spacers on increasing the spacing between graphene sheets, the XRD patterns of the samples were collected (**Figure A. 28**). A sharp peak at 18° show up in all the rGO-Spacers sample, which is caused from the PTFE binder. As the reference, GO shows a sharp peak at 10.5°, corresponding to an interlayer distance (*d*) of 0.85 nm, which forms from the oxygen containing functional groups on GO such as hydroxyl, carboxyl and epoxide groups. After reduction, the major peak shifts to 24.8° (*d*=0.36 nm, referred to as **A** peak), which corresponds to the stacking of graphene sheets by removal of those oxygen containing groups. Since the oxygen-containing functional groups is partially removed, the graphene sheets stack much closer in rGO Bare compared to those in GO.

For rGO Tri015, the **A** peak shifts to 26.6° (*d*=0.33 nm), while a new broad peak at 10.5° (*d*=0.84 nm) arises (referred to as **B** peak). For rGO Tri030, the **A** and **B** peaks locate at 26.6° (*d*=0.33 nm) and 8.0° (*d*=1.1 nm). The position of peaks in other samples are listed in **Table A. 5**. Peak **B** can be found in rGO Naph15015, rGO Naph15030 and rGO Naph18030. The emergence of peak **B** indicates a new stacking form of graphene sheets exist in these samples with increased interlayer distance compared to that in rGO Bare, which can be assigned to the effect of spacers on the sheets, since the peak are not present in GO, rGO Bare as well as the spacers themselves. In rGO Tetra015 and rGO Tetra030, peak **B** are not obvious. However, peak **A** in these two samples are very broad and shallow, indicating that the graphene sheets are stacked in a much more random manner. The interlayer distance derived from peak **B** coincide with the trend of the axial dimension of the spacer molecules along the amino groups (**Figure A. 29**), suggesting that the emergence of **B** can be correlated to the spacing effect of spacers. Besides peak **B**, peak **A** also appears in all the XRD patterns of rGO-Spacers samples, but with higher angles (i.e. smaller interlayer distance). The existence of peak **A** in these samples indicates that there are some spacer-free regions on the graphene sheets, so they stack in a similar way as rGO Bare does. Since less oxygen-containing groups are present in this region, the interlayer distance is even smaller than that in rGO Bare.

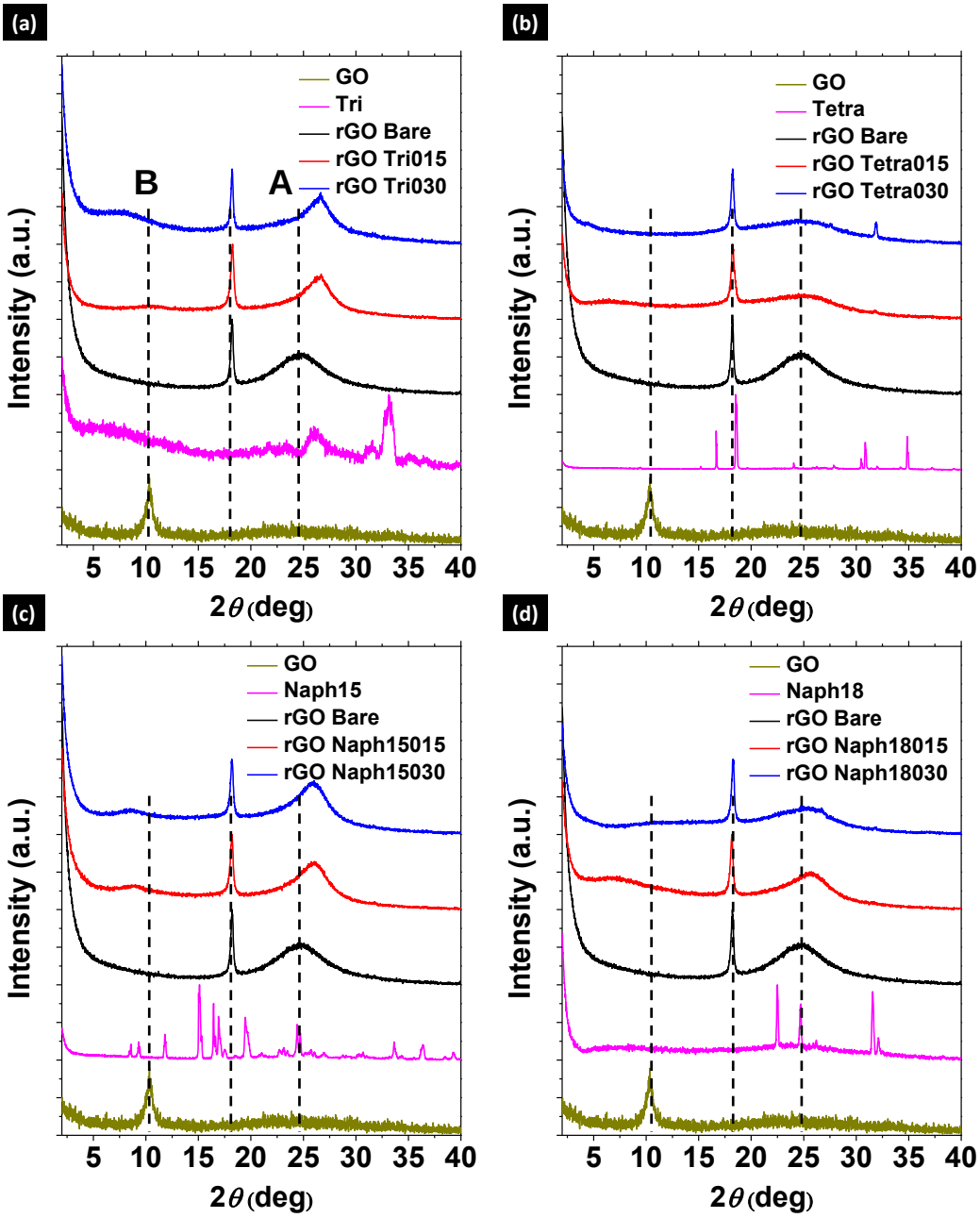

Figure A. 28 X-ray diffraction (XRD) patterns of the samples.

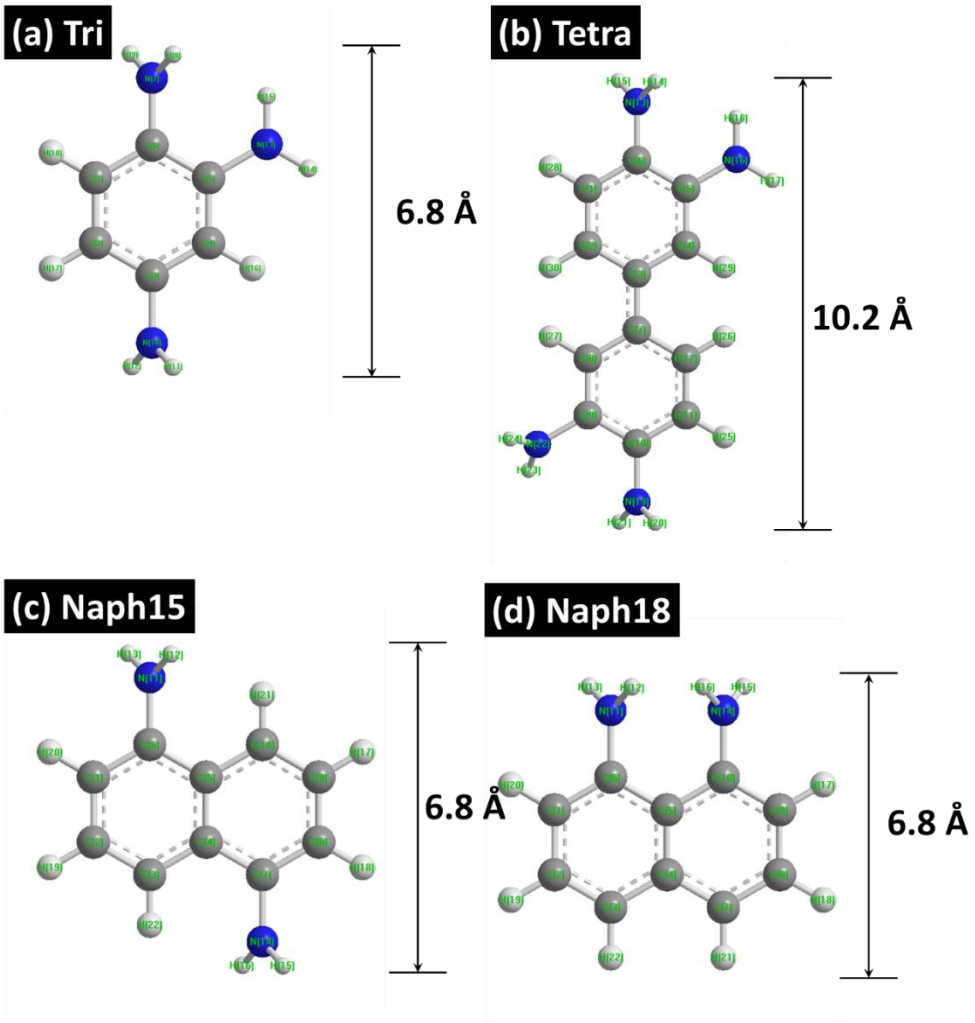

Figure A. 29 Schematic molecular structures and dimension of **Tri**, **Tetra**, **Naph15** and **Naph18** modeled by the software Chem3D Ultra 8.0.

Table A. 5 Position of peaks in XRD patterns and corresponding interlayer spacing[1]

Sample ID[2]	1	2	3	4	5	6	7	8	9	10
	10.3	24.8	10.5	8	6.1	4.5	9.1	8.2	7.2	
2θ/deg			26.6	26.6	25.4	25.4	26	26	25.7	26
					31.9	31.9				
	8.6	3.6	8.4	11	14.5	19.6	9.7	10.8	12.3	
d/Å			3.3	3.3	3.5	3.5	3.4	3.4	3.5	3.4
					2.8	2.8				

1. $d=\lambda/2\sin\theta$, where λ is the wavelength of the X-ray. Here λ=1.54 Å;

2. The sample ID refer to: 1. GO; 2. rGO Bare; 3. rGO Tri015; 4. rGO Tri030; 5. rGO Tetr015; 6. rGO Tetra003; 7. rGO Naph15015; 8. rGO Naph15030; 9. rGO Naph18015; 10. rGO Naph18030;

Based on the characterization results discussed above, we proposed the reaction pathway between GO and spacers (**Figure A. 30**). As mentioned earlier, during the reaction, GO can undergo self-decomposition, reactions with OH^- and reactions with amino groups in spacers (**Figure A. 30** (a)). It has long been known that OH^- can remove the carboxylic groups (**Figure A. 30** (b)) as well as open the epoxide rings at an elevated temperature ((**Figure A. 30** (c)).[171] The disappearance of the C=O peak at 1730 cm^{-1} in the FTIR spectrum of rGO Bare indicates that the carboxylic groups were effectively removed by OH^-. Also, the FTIR spectra of GO and rGO Bare showed similar peaks of -C-O-C- and C-O peaks in the 1000-1200 cm^{-1} region, implying that fewer –C-O-C and C-O were removed by OH^- compared to carboxylic groups. When the spacers were added during the reactions, sharp carbonyl peaks around 1730 cm^{-1} were together with peaks around 1620 cm^{-1}. These peaks can be assigned to the C=O stretching in unreacted carboxylate groups or the amide group formed by condensation between carboxylic group in GO and amino groups (**Figure A. 30** (d)). On the other hand, the C-O and C-O-C peaks in the 1000-1200 cm^{-1} region can be distinguished from those in GO and rGO Bare,

possibly caused by the ring opening of epoxide groups by amino groups (**Figure A. 30** (e)). The bonding between spacers and GO through ring open of epoxide can generate spacer moieties that protrude out of the graphene sheets and effectively increase the interlayer spacing. In addition to the possible reactions proposed here, the characterization results in this report do not exclude other reaction pathways such as the formation of heterocycles between spacers and the carboxylate group on GO (**Figure A. 30** (f)), as reported previously.[139] Although the occurrence of these reactions are evident in the reaction of GO with the four types of spacers, the reactivity of these spacers are different, which is shown in the weight measurement of the rGO-Spacers as well as the atomic ratio measurement from XPS. The different degrees of reactivity of the spacers may be explained by their molecular structures: in **Tri**, the size of the aromatic core, i.e. the benzene ring, is the smallest compared to the biphenyl ring in **Tetra** as well as naphthalene ring in **Naph15** and **Naph18**. The larger aromatic core may reduce the electron density in the amino groups due to the conjugation effect [171] and result in a weaker reactivity in the nucleophilic ring opening reaction in **Figure A. 30** (e). Furthermore, the existence of 8-H atom in **Naph15** and 8-NH_2 group in **Naph18** may place steric hindrance to the reaction to 1-NH_2 group, further reducing its reactivity. Therefore we observed the relation of mole gain as rGO Tri>rGO Tetra~rGO Naph15>rGO Naph18 in **Table A.3** and **Table A.4**, as well as the relation of C_s at a low scan rate of rGO Tri>rGO Tetra~rGO Naph15>rGO Naph18. In this sense, amine molecules with smaller aromatic cores, such as benzene rings or even five-member rings, could be regarded as preferred molecular spacers in future studies for ever higher C_s. Meanwhile, given the above findings, it is possible to further increase the C_s by promoting the reactivity of amine spacers through optimization other parameters in the reactions, such as the solvent, pH value, temperature and ionic strength.

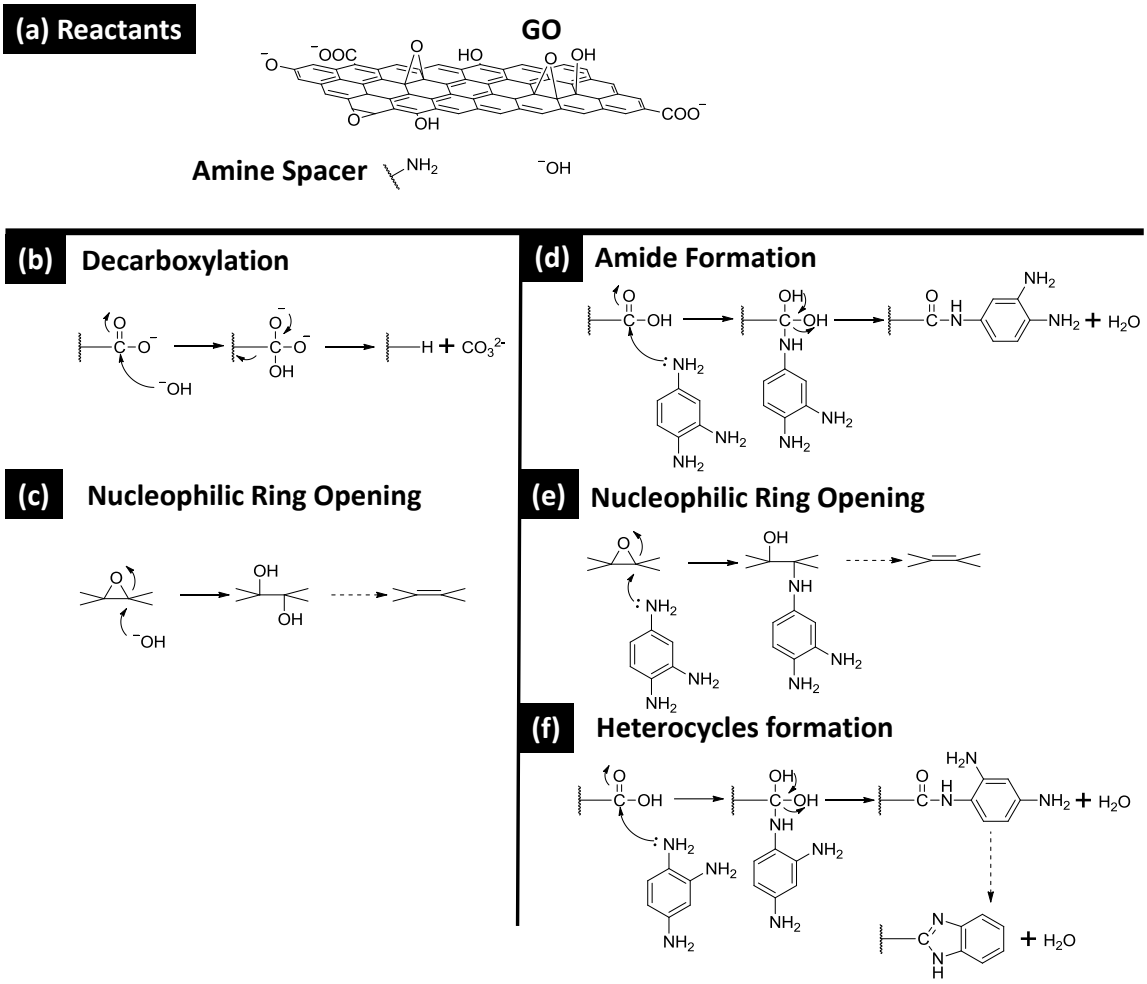

Figure A. 30 Possible chemical reactions involved during the hydrothermal process

A4.Conclusion

In conclusion, one-step hydrothermal reactions have been conducted between GO and four types of amine spacers. The rGO-Spacers samples show crumpled thin sheets morphology in micrometer scale under SEM and TEM, while the spacer molecules were found to disperse uniformly on the sheets by EDS mapping. Chemical reactions and covalent bonding formation between GO spacers and the spacers are supported by results of TGA, XPS, UV-vis, FTIR and Raman. An increased interlayer spacing in rGO-Spacers

was demonstrated by XRD. Among those spacer, **Tri** shows the highest reactivity as evidenced in the molar gain value from weight measurement and XPS element compositions analysis. The C_s of graphene-based supercapacitors can be effectively enhanced with addition of molecular spacers. Among the rGO-Spacers samples, rGO Tri030 shows the highest specific capacitance of 612 F/g at 2 mV/s in the CV measurement, 597 F/g at 0.5 A/g and 512 F/g at 10 A/g in the CD measurement. rGO Tri030 also shows the lowest R_s and R_{ct}. Excellent capacitance retention of 97% was achieved after 10,000 CD cycles. Unlike the previously reported graphene electrode with pseudocapacitive materials, e.g. polyaniline and metal oxide, here the enhanced specific capacitance was found originated from a synergistic effect of molecular spacing as well as pseudocapacitance of spacer-graphene compounds, rather than from the spacers themselves. From the results of these comparative study, it is clear that the engineering of the molecular structures plays the pivotal role in value of C_s. The findings provide guidance to achieve even higher C_s by optimization of the molecular structures of the spacers to promote their reaction with GO.

APPENDIX B

AUTHOR'S PUBLICATION

Referred Journal Publications (*:Co-1st authorship)

1. **Li, L.**; Song, B.; Maurer, L.; Lin,, Z.; Lian, G.; Tuan, C.-C.; Moon, K.-S.; Wong, C.-P. Molecular engineering of aromatic amine spacers for high-performance graphene-based supercapacitors. *Nano Energy* **2016,** *21*, 276-294.
2. **Li, L.**.; Zhang, G.; Wong, C. P. Formation of Through Silicon Vias in Wafer Level by Metal-assisted Chemical Etching for Silicon Interposer. *IEEE Transactions on Components, Packaging and Manufacturing Technology* **2015**, *5*, 1039.
3. **Li, L.**; Zhao, X.; Wong, C. P. Charge Transport in Uniform Metal-assisted Chemical Etching (UMaCE) for 3D High-Aspect Ratio Micro- and Nanofabrication on Silicon. *ECS. J. Solid State Sci. Technol.* **2015,** *4*, 337-346.
4. **Li, L.**; Zhao, X.; Wong, C.-P. Deep Etching of Single- and Polycrystalline Silicon with High Speed, High Aspect Ratio, High Uniformity and 3D Complexity by Electric Bias-Attenuated Metal-Assisted Chemical Etching (EMaCE). *ACS Appl. Mater. Interfaces* **2014**, *6*, 16782–16791.
5. **Li, L.**; Liu, Y.; Zhao, X.; Lin, Z.; Wong, C.-P. Uniform Vertical Trench Etching on Silicon with High Aspect Ratio by Metal-Assisted Chemical Etching Using Nanoporous Catalysts. *ACS Appl. Mater. Interfaces* **2014,** *6*, 575-584.
6. Wu, Z.; **Li, L.***; Lin, Z.; Song, B.; Li, Z.; Moon, K.-S.; Wong, C.-P.; Bai, S.-L. Alternating current line-filter based on electrochemical capacitor utilizing template-patterned graphene. *Sci. Rep.* **2015**, *5*.

7. Lu, X.; **Li, L.***; Song, B.; Moon, K.-S.; Hu, N.; Liao, G.; Shi, T.; Wong, C. Mechanistic Investigation of the Graphene Functionalization using p-Phenylenediamine and its Application for Supercapacitors. *Nano Energy* **2015**.
8. Song, B.; Tuan, C.-C.; Huang, X.; **Li, L.**; Moon, K.-S.; Wong, C.-P. Sulfonated polyaniline decorated graphene nanocomposites as supercapacitor electrodes. *Mater. Lett.* **2016,** *166*, 12-15.
9. Song, B.; **Li, L**.; Lin, Z.; Wu, Z.-K.; Moon, K.-S.; Wong, C.-P. Water-dispersible graphene/polyaniline composites for flexible micro-supercapacitors with high energy densities. *Nano Energy* **2015**, 16, 470-478.
10. Song, B.; Sizemore, C.; **Li, L.**; Huang, X.; Lin, Z.; Moon, K.-s.; Wong, C.-P. Triethanolamine functionalized graphene-based composites for high performance supercapacitors. *J. Mater. Chem. A* **2015,** *3*, 21789-21796.
11. Hao, P.; Zhao, Z.; **Li, L.**; Tuan, C.-C.; Li, H.; Sang, Y.; Jiang, H.; Wong, C.; Liu, H. Hybrid Nanostructure of MnCo2O4. 5 Nanoneedle/Carbon Aerogel for Symmetric Supercapacitors with High Energy Density. *Nanoscale* **2015**.
12. Li, Z.; Le, T.; Wu, Z.; Yao, Y.; **Li, L**.; Tentzeris, M.; Moon, K. S.; Wong, C. Rational Design of a Printable, Highly Conductive Silicone-based Electrically Conductive Adhesive for Stretchable Radio-Frequency Antennas *Adv. Funct. Mater.* **2015**, *25*, pp 464.
13. Gao, Y.; Zhao, S.; Zhang, G.; Deng, L.; Li, J.; Sun, R.; **Li, L**.; Wong, C.-P. In situ assembly of dispersed Ag nanoparticles on hierarchically porous organosilica microspheres for controllable reduction of 4-nitrophenol. *J. Mater. Sci.* **2015**, *50*, pp 3399.
14. Zhao, X.; **Li, L**.; Liu, Y.; Wong, C. P. UVA‐shielding silicone/zinc oxide nanocomposite coating for automobile windows. *Polymer Composites* **2015**, in press

15. Fang X.; Ding, Q.; **Li, L.-Y**.; Moon, K.-S.; Wong, C.-P.; Yu, Z.-T. Tunable thermal conduction character of graphite-nanosheets-enhanced composite phase change materials via cooling rate control. *Energy Convers. Manage.* **2015,** *103*, 251-258.
16. Wu, Z.-K.; Lin, Z.; Li, L.; Song, B.; Moon, K.-s.; Bai, S.-L.; Wong, C.-P. Flexible micro-supercapacitor based on in-situ assembled graphene on metal template at room temperature. *Nano Energy* **2014,** *10*, 222-228.
17. Chen, C.-Y.; **Li, L.**; Wong, C.-P. Evolution of Etching Kinetics and Directional Transition of Nanowires Formed on Pyramidal Microtextures. *Chem.-Asian J.* **2014,** *9*, 93-99.
18. Zhou, G.; Chen, C.-Y.; Lin, Z.; **Li, L.**; Tao, Z.; He, W.; Wong, C. Effects of Mn^{2+} on the electrical resistance of electrolessly plated Ni–P thin-film and its application as embedded resistor. *J. Mater. Sci.: Mater. Electron.* **2014,** *25*, 1341-1347.
19. Zhou, G.; Chen, C.-Y.; **Li, L.**; Tao, Z.; He, W.; Wong, C. P. Effect of MnSO4 on the Deposition of Electroless Nickel Phosphorus and its Mechanism. *Electrochimica Acta* **2014,** *127*, 276-282.
20. Zhou, G.; Chen, C.-Y.; **Li, L.**; Tao, Z.; He, W.; Wong, C. Effects of MnSO4 on microstructure and electrical resistance properties of electroless Ni− P thin-films and its application in embedded resistor inside PCB. *Circuit World* **2014**, *40,* pp 45.
21. Lin, Z.; Li, Z.; Moon, K.-s.; Fang, Y.; Yao, Y.; **Li, L.**; Wong, C.-P. Robust vertically aligned carbon nanotube–carbon fiber paper hybrid as versatile electrodes for supercapacitors and capacitive deionization. *Carbon* **2013**, *63,* pp 547.
22. Luo, J.; **Li, L.-Y.**; Song, Y.; Pei, J. A Piezochromic Luminescent Complex: Mechanical Force Induced Patterning with a High Contrast Ratio. *Chem. Eur. J* **2011,** *17*, 10515-10519.

23. Luo, J.; Chen, L.; Wang, J.-Y.; Lei, T.; **Li, L.-Y.**; Pei, J.; Song, Y. A co-assembly system of an aromatic donor and acceptor: charge transfer, electric bistability and photoconductivity. *New. J. Chem.* **2010,** *34*, 2530-2533.

Conference Proceedings (*:Co-1st authorship)

1. **Li, L.**; Wong, C.P. In *Formation of High-Aspect-Ratio Through Silicon Vias (TSV) with A Broad Range of Diameter from 1 to 100 μm by Uniform Metal-assisted Chemical Etching (MaCE)*, Electronic Components and Technology Conference (ECTC), 2016 IEEE 66th, accepted.
2. **Li, L.**; Zhang, G.; Tuan, C.C.; Moon, K.S.; Sun, R.; Wong, C.P. In *Formation of Polymer Insulation Layer (Liner) on Through Silicon Vias (TSV) with High Aspect Ratio over 5:1 by Direct Spin Coating*. Electronic Components and Technology Conference (ECTC), 2016 IEEE 66th, accepted.
3. **Li, L**.; Holmes, C.; Hah, J.; Hildreth, O.; Wong, C.P. Uniform Metal-assisted Chemical Etching and the Stability of Catalysts" MRS Proceeding, **2015**, *1801*, 15-2124427.
4. **Li, L**.; Wu, J.; Wong, C. P. In *Wafer-Level Wet Etching of High-Aspect-Ratio Through Silicon Vias (TSVs) with High Uniformity and Low Cost for Silicon Interposers with High-Density Interconnect of 3D Packaging*, Electronic Components and Technology Conference (ECTC), **2015** IEEE 65th, 2015, in press.
5. **Li, L.**; Li, B.; Lin, Z.; Wong, C. P. In *A Low-Cost Fabrication Route for Silicon Microchannels and Microgratings with Flow-Enabled Polymer Self-Assembly Patterning and Wet Etching*, Electronic Components and Technology Conference (ECTC), 2015 IEEE 65th, 2015, in press.
6. **Li, L.**; Wong, C. P. In *Wet etching of deep trenches on silicon with three-dimensional (3D) controllability*, Electronic Components and Technology Conference (ECTC), 2014 IEEE 64th, 2014.
7. **Li, L**.; Wong, C. P. In *High-speed wet etching of through silicon vias (TSVs) in micro- and nanoscale*, Electronic Components and Technology Conference (ECTC), 2014 IEEE 64th, 2014.

8. **Li, L.**; Wong, C. P. In *High aspect ratio sub-100 nm silicon vias (SVs) by metal-assisted chemical etching (MaCE) and copper filling*, Electronic Components and Technology Conference (ECTC), 2013 IEEE 63rd, 28-31 May 2013; 2013; pp 2326-2331.
9. **Li, L.**; Yao, Y.; Lin, Z.; Liu, Y.; Wong, C. P. In *Low-cost micrometer-scale silicon vias (SVs) fabrication by metal-assisted chemical etching (MaCE) and carbon nanotubes (CNTs) filling*, Electronic Components and Technology Conference (ECTC), 2013 IEEE 63rd, 28-31 May 2013; 2013; pp 581-585.
10. Hamelin, B.; **Li, L.***; Daruwalla, A.; Wong, C.-P.; Ayazi, F. In *High-aspect-ratio sub-micron trench etching on SOI using wet metal-assisted chemical etching (MaCE) process*, 2016 IEEE 29th International Conference on Micro Electro Mechanical Systems (MEMS), 24-28 Jan. 2016; 2016; pp 447-450.
11. Song, B.; **Li, L.**; Wu, Z.; Moon, K.-s.; Wu, J.; Wong, C. In *Solution-processed flexible solid-state micro-supercapacitors for on-chip energy storage devices*, Electronic Components and Technology Conference (ECTC), 2015 IEEE 65th, IEEE: 2015; pp 1483-1487.
12. Zhao, X.; **Li, L.**; Li, Z.; Wong, C.-P. In *Stretchable and transparent silicone/zinc oxide nanocomposite for advanced LED packaging*, Electronic Components and Technology Conference (ECTC), 2014 IEEE 64th, IEEE: 2014; pp 1745-1749.
13. Gandhi, S.; **Li, L.**; Hui, H.-Y.; Chakraborti, P.; Sharma, H.; Raj, P. M.; Wong, C.; Tummala, R. In *Nanowires-based high-density capacitors and thinfilm power sources in ultrathin 3D glass modules*, Electronic Components and Technology Conference (ECTC), 2014 IEEE 64th, IEEE: 2014; pp 1492-1497.

Patent

Li, L.; Wong, C.P., Zhao, X., Moon, K.S. "METAL-ASSISTED CHEMICAL ETCHING OF A SEMICONDUCTIVE SUBSTRATE WITH HIGH ASPECT RATIO, HIGH GEOMETIC UNIFORMITY, AND CONTROLLED 3D PROFILES", US Patent Application No. 14/930,161.

REFERENCES

1. URL: **http://www.intel.com/content/www/us/en/silicon-innovations/intel-14nm-technology.html**. Accessed on May 25, 2016.

2. M. Motoyoshi, "Through-Silicon Via (TSV)," *Proc. IEEE,* 2009, vol. 97, pp. 43-48.

3. F. Ayazi and K. Najafi, "High Aspect-Ratio Combined Poly and Single-Crystal Silicon (HARPSS) MEMS Technology," *J. Microelectromech. Syst.,* 2000, vol. 9, pp. 288-294.

4. C. R. King, D. Sekar, M. S. Bakir, B. Dang, J. Pikarsky, and J. D. Meindl, "3D stacking of chips with electrical and microfluidic I/O interconnects," in *Electronic Components and Technology Conference, 2008. ECTC 2008. 58th*, Orlando, Florida, 2008, pp. 1-7.

5. S. Takahashi, K. Suzuki, M. Okano, M. Imada, T. Nakamori, Y. Ota, K. Ishizaki, and S. Noda, "Direct creation of three-dimensional photonic crystals by a top-down approach," *Nat. Mater.,* 2009, vol. 8, pp. 721-725.

6. C. Pan, Z. Luo, C. Xu, J. Luo, R. Liang, G. Zhu, W. Wu, W. Guo, X. Yan, J. Xu, Z. L. Wang, and J. Zhu, "Wafer-Scale High-Throughput Ordered Arrays of Si and Coaxial Si/Si1–xGex Wires: Fabrication, Characterization, and Photovoltaic Application," *ACS Nano,* 2011, vol. 5, pp. 6629-6636.

7. L. Oakes, A. Westover, J. W. Mares, S. Chatterjee, W. R. Erwin, R. Bardhan, S. M. Weiss, and C. L. Pint, "Surface engineered porous silicon for stable, high performance electrochemical supercapacitors," *Sci. Rep.,* 2013, vol. 3.

8. F. Ayazi and K. Najafi, "A HARPSS Polysilicon Vibrating Ring Gyroscope," *J. Microelectromech. Syst.,* 2001, vol. 10, pp. 169-179.

9. J. Yeom, D. Ratchford, C. R. Field, T. H. Brintlinger, and P. E. Pehrsson, "Decoupling Diameter and Pitch in Silicon Nanowire Arrays Made by Metal-Assisted Chemical Etching," *Adv. Funct. Mater.,* 2014, vol. 24, pp. 106-116.

10. M. Ladanov, P. Algarin-Amaris, G. Matthews, M. Ram, S. Thomas, A. Kumar, and J. Wang, "Microfluidic hydrothermal growth of ZnO nanowires over high aspect ratio microstructures," *Nanotechnology*, 2013, vol. 24, p. 375301.

11. Y. Cui, L. J. Lauhon, M. S. Gudiksen, J. Wang, and C. M. Lieber, "Diameter-controlled synthesis of single-crystal silicon nanowires," *Appl. Phys. Lett.,* 2001, vol. 78, pp. 2214-2216.

12. J. Parasuraman, A. Summanwar, F. Marty, P. Basset, D. E. Angelescu, and T. Bourouina, "Deep Reactive Ion Etching of Sub-Micrometer Trenches with Ultra High Aspect Ratio," *Microelectron. Eng.,* 2014, vol. 113, pp. 35-39.

13. Y.-C. Hsin, C.-C. Chen, J. H. Lau, P.-J. Tzeng, S.-H. Shen, Y.-F. Hsu, S.-C. Chen, C.-Y. Wn, J.-C. Chen, T.-K. Ku, and M.-J. Kao, "Effects of etch rate on scallop of through-silicon vias (TSVs) in 200mm and 300mm wafers," in *Electronic Components and Technology Conference (ECTC), 2011 IEEE 61st*, Orlando, Florida, 2011, pp. 1130-1135.

14. X. D. Wang, W. X. Zeng, and E. Eisenbraun, "Sub-0.25 micron silicon via etching for 3D interconnects," *J. Micromech. Microeng.,* 2007, vol. 17, pp. 804-811.

15. M. Ahn, R. K. Heilmann, and M. L. Schattenburg, "Fabrication of ultrahigh aspect ratio freestanding gratings on silicon-on-insulator wafers," *J. Vac. Sci. Technol., B,* 2007, vol. 25, pp. 2593-2597.

16. T. Baum and D. J. Schiffrin, "AFM study of surface finish improvement by ultrasound in the anisotropic etching of Si < 100 > in KOH for micromachining applications," *J. Micromech. Microeng.*, 1997, vol. 7, pp. 338-342.

17. V. Lehmann and H. Föll, "Formation Mechanism and Properties of Electrochemically Etched Trenches in n-Type Silicon," *J. Electrochem. Soc.,* 1990, vol. 137, pp. 653-659.

18. V. Lehmann and U. Grüning, "The limits of macropore array fabrication," *Thin Solid Films,* 1997, vol. 297, pp. 13-17.

19. H. Föll, M. Christophersen, J. Carstensen, and G. Hasse, "Formation and application of porous silicon," *Mater. Sci. Eng., R,* 2002, vol. 39, pp. 93-141.

20. V. Lehmann, "The Physics of Macropore Formation in Low Doped n-Type Silicon," *J. Electrochem. Soc.,* 1993, vol. 140, pp. 2836-2843.

21. V. Lehmann, "Electrochemistry of Silicon," ed Weinheim: WILEY-VCH Verlag GmBH, 2002, p. 77.

22. S. Rönnebeck, J. Carstensen, S. Ottow, and H. Föll, "Crystal Orientation Dependence of Macropore Growth in n-Type Silicon," *Electrochem. Solid-State Lett.,* 1999, vol. 2, pp. 126-128.

23. C. Gondek, M. Lippold, I. Röver, K. Bohmhammel, and E. Kroke, "Etching Silicon with HF-H2O2-Based Mixtures: Reactivity Studies and Surface Investigations," *J. Phys. Chem. C,* 2014, vol. 118, pp. 2044-2051.

24. X. Li and P. W. Bohn, "Metal-assisted chemical etching in HF/H_2O_2 produces porous silicon," *Appl. Phys. Lett.,* 2000, vol. 77, pp. 2572-2574.

25. C. Chartier, S. Bastide, and C. Lévy-Clément, "Metal-Assisted Chemical Etching of Silicon in HF-H_2O_2," *Electrochim. Acta,* 2008, vol. 53, pp. 5509-5516.

26. Y. Xiu, L. Zhu, D. W. Hess, and C. P. Wong, "Hierarchical Silicon Etched Structures for Controlled Hydrophobicity/Superhydrophobicity," *Nano Lett.,* 2007, vol. 7, pp. 3388-3393.

27. Y. Xiu, S. Zhang, V. Yelundur, A. Rohatgi, D. W. Hess, and C. P. Wong, "Superhydrophobic and Low Light Reflectivity Silicon Surfaces Fabricated by Hierarchical Etching," *Langmuir,* 2008, vol. 24, pp. 10421-10426.

28. Y. Liu, Y. Xiu, D. W. Hess, and C. P. Wong, "Silicon Surface Structure-Controlled Oleophobicity," *Langmuir,* 2010, vol. 26, pp. 8908-8913.

29. K. Peng, M. Zhang, A. Lu, N.-B. Wong, R. Zhang, and S.-T. Lee, "Ordered silicon nanowire arrays via nanosphere lithography and metal-induced etching," *Appl. Phys. Lett.,* 2007, vol. 90, p. 163123.

30. Z. Huang, X. Zhang, M. Reiche, L. Liu, W. Lee, T. Shimizu, S. Senz, and U. Gösele, "Extended Arrays of Vertically Aligned Sub-10 nm Diameter [100] Si Nanowires by Metal-Assisted Chemical Etching," *Nano Lett.,* 2008, vol. 8, pp. 3046-3051.

31. Y. Qi, Z. Wang, M. Zhang, F. Yang, and X. Wang, "A Processing Window for Fabricating Heavily Doped Silicon Nanowires by Metal-Assisted Chemical Etching," *J. Phys. Chem. C,* 2013, vol. 117, pp. 25090-25096.

32. K. Balasundaram, J. S. Sadhu, J. C. Shin, B. Azeredo, D. Chanda, M. Malik, K. Hsu, J. A. Rogers, P. Ferreira, S. Sinha, and X. Li, "Porosity control in metal-assisted chemical etching of degenerately doped silicon nanowires," *Nanotechnology,* 2012, vol. 23, p. 305304.

33. Z. Huang, T. Shimizu, S. Senz, Z. Zhang, X. Zhang, W. Lee, N. Geyer, and U. Gösele, "Ordered Arrays of Vertically Aligned [110] Silicon Nanowires by Suppressing the Crystallographically Preferred <100> Etching Directions," *Nano Lett.,* 2009, vol. 9, pp. 2519-2525.

34. S. W. Chang, V. P. Chuang, S. T. Boles, and C. V. Thompson, "Metal-Catalyzed Etching of Vertically Aligned Polysilicon and Amorphous Silicon Nanowire Arrays by Etching Direction Confinement," *Adv. Funct. Mater.,* 2010, vol. 20, pp. 4364-4370.

35. H. A. Chen, H. Wang, X. H. Zhang, C. S. Lee, and S. T. Lee, "Wafer-Scale Synthesis of Single-Crystal Zigzag Silicon Nanowire Arrays with Controlled Turning Angles," *Nano Letters,* 2010, vol. 10, pp. 864-868.

36. J. Kim, Y. H. Kim, S.-H. Choi, and W. Lee, "Curved Silicon Nanowires with Ribbon-like Cross Sections by Metal-Assisted Chemical Etching," *ACS Nano,* 2011, vol. 5, pp. 5242-5248.

37. J. Kim, H. Han, Y. H. Kim, S.-H. Choi, J.-C. Kim, and W. Lee, "Au/Ag Bilayered Metal Mesh as a Si Etching Catalyst for Controlled Fabrication of Si Nanowires," *ACS Nano,* 2011, vol. 5, pp. 3222-3229.

38. O. J. Hildreth, W. Lin, and C. P. Wong, "Effect of Catalyst Shape and Etchant Composition on Etching Direction in Metal-Assisted Chemical Etching of Silicon to Fabricate 3D Nanostructures," *ACS Nano,* 2009, vol. 3, pp. 4033-4042.

39. O. J. Hildreth, A. G. Fedorov, and C. P. Wong, "3D Spirals with Controlled Chirality Fabricated Using Metal-Assisted Chemical Etching of Silicon," *ACS Nano,* 2012, vol. 6, pp. 10004-10012.

40. O. J. Hildreth, K. Rykaczewski, A. G. Fedorov, and C. P. Wong, "A DLVO model for catalyst motion in metal-assisted chemical etching based upon controlled out-of-plane rotational etching and force-displacement measurements," *Nanoscale,* 2013.

41. K. Rykaczewski, O. J. Hildreth, C. P. Wong, A. G. Fedorov, and J. H. J. Scott, "Guided Three-Dimensional Catalyst Folding during Metal-Assisted Chemical Etching of Silicon," *Nano Lett.,* 2011, vol. 11, pp. 2369-2374.

42. O. J. Hildreth, D. Brown, and C. P. Wong, "3D Out-of-Plane Rotational Etching with Pinned Catalysts in Metal-Assisted Chemical Etching of Silicon," *Adv. Funct. Mater.,* 2011, vol. 21, pp. 3119-3128.

43. K. Rykaczewski, O. J. Hildreth, C. P. Wong, A. G. Fedorov, and J. H. J. Scott, "Directed 2D-to-3D Pattern Transfer Method for Controlled Fabrication of Topologically Complex 3D Features in Silicon," *Adv. Mater.,* 2011, vol. 23, pp. 659-663.

44. O. J. Hildreth, K. Rykaczewski, A. G. Fedorov, and C. P. Wong, "A DLVO model for catalyst motion in metal-assisted chemical etching based upon controlled out-of-plane rotational etching and force-displacement measurements," *Nanoscale,* 2013, vol. 5, pp. 961-970.

45. L. Li and C. P. Wong, "High aspect ratio sub-100 nm silicon vias (SVs) by metal-assisted chemical etching (MaCE) and copper filling," in *Electronic Components and Technology Conference (ECTC), 2013 IEEE 63rd*, 2013, pp. 2326-2331.

46. J. Rouquerol, D. Avnir, C. W. Fairbridge, D. H. Everett, J. H. Haynes, N. Pernicone, J. D. F. Ramsay, K. S. W. Sing, and K. K. Unger, "Recommendations for the Characterization of Porous Solids," *Pure and Applied Chemistry,* 1994, vol. 66, pp. 1739-1758.

47. C.-L. Lee, K. Tsujino, Y. Kanda, S. Ikeda, and M. Matsumura, "Pore formation in silicon by wet etching using micrometre-sized metal particles as catalysts," *J. Mater. Chem.,* 2008, vol. 18, pp. 1015-1020.

48. C.-L. Lee, S. Tsuru, Y. Kanda, S. Ikeda, and M. Matsumura, "Formation of 100 μm Deep Vertical Pores in Si Wafers by Wet Etching and Cu Electrodeposition," *J. Electrochem. Soc.,* 2009, vol. 156, pp. D543-D547.

49. T. Nakamura, H. Kitada, Y. Mizushima, N. Maeda, K. Fujimoto, and T. Ohba, "Comparative study of side-wall roughness effects on leakage currents in through-silicon via interconnects," in *3D Systems Integration Conference (3DIC), 2011 IEEE International,* 2012, pp. 1-4.

50. Z.-Y. Li and Z.-Q. Zhang, "Fragility of photonic band gaps in inverse-opal photonic crystals," *Phys. Rev. B,* 2000, vol. 62, pp. 1516-1519.

51. P. Lianto, S. Yu, J. Wu, C. V. Thompson, and W. K. Choi, "Vertical etching with isolated catalysts in metal-assisted chemical etching of silicon," *Nanoscale,* 2012, vol. 4, pp. 7532-7539.

52. F. Güder, Y. Yang, U. M. Küçükbayrak, and M. Zacharias, "Tracing the Migration History of Metal Catalysts in Metal-Assisted Chemically Etched Silicon," *ACS Nano,* 2013, vol. 7, pp. 1583-1590.

53. L. Li, Y. Liu, X. Zhao, Z. Lin, and C.-P. Wong, "Uniform Vertical Trench Etching on Silicon with High Aspect Ratio by Metal-Assisted Chemical Etching Using Nanoporous Catalysts," *ACS Appl. Mater. Interfaces,* 2014, vol. 6, pp. 575-584.

54. N. Geyer, B. Fuhrmann, Z. Huang, J. de Boor, H. S. Leipner, and P. Werner, "Model for the Mass Transport during Metal-Assisted Chemical Etching with Contiguous Metal Films As Catalysts," *J. Phys. Chem. C.,* 2012, vol. 116, pp. 13446-13451.

55. K. Tsujino and M. Matsumura, "Morphology of nanoholes formed in silicon by wet etching in solutions containing HF and H2O2 at different concentrations using silver nanoparticles as catalysts," *Electrochim. Acta,* 2007, vol. 53, pp. 28-34.

56. R. Sangiorgi, M. L. Muolo, D. Chatain, and N. Eustathopoulos, "Wettability and Work of Adhesion of Nonreactive Liquid Metals on Silica," *J. Am. Ceram. Soc.,* 1988, vol. 71, pp. 742-748.

57. M. Boero, J. K. Vincent, J. C. Inkson, M. Mejias, C. Vieu, H. Launois, and P. A. Mulheran, "Simulation and growth of gold on silicon oxide in one-dimensional and quasi-one-dimensional arrays," *J. Appl. Phys.,* 2000, vol. 87, pp. 7261-7265.

58. C. Chang, Y.-F. Wang, Y. Kanamori, J.-J. Shih, Y. Kawai, C.-K. Lee, K.-C. Wu, and M. Esashi, "Etching submicrometer trenches by using the Bosch process and its application to the fabrication of antireflection structures," *J. Micromech. Microeng.,* 2005, vol. 15, pp. 580-585.

59. Z. Mohammad, F. Saeed Delaram, K. Mahdi, M. Hamed, E. Alireza, and Z. Firooz, "Deep and vertical silicon bulk micromachining using metal assisted chemical etching," *J. Micromech. Microeng.,* 2013, vol. 23, p. 055015.

60. S. C. Hung, S. C. Shiu, J. J. Chao, and C. F. Lin, "Fabrication of Deep Si Trenches by Self-Assembled Wet Chemical Etching Process," *J. Electrochem. Soc.,* 2010, vol. 157, pp. D496-D499.

61. Z. Huang, T. Shimizu, S. Senz, Z. Zhang, N. Geyer, and U. Gösele, "Oxidation Rate Effect on the Direction of Metal-Assisted Chemical and Electrochemical Etching of Silicon," *J. Phys. Chem. C,* 2010, vol. 114, pp. 10683-10690.

62. H. Robbins and B. Schwartz, "Chemical Etching of Silicon .1. The System Hf,Hno3, and H2o," *Journal of The Electrochemical Society,* 1959, vol. 106, pp. 505-508.

63. D. R. Turner, "Electropolishing Silicon in Hydrofluoric Acid Solutions," *Journal of The Electrochemical Society,* 1958, vol. 105, pp. 402-408.

64. K. R. Williams and R. S. Muller, "Etch rates for micromachining processing," *J. Microelectromech. Syst.,* 1996, vol. 5, pp. 256-269.

65. L. Li, X. Zhao, and C.-P. Wong, "Deep Etching of Single- and Polycrystalline Silicon with High Speed, High Aspect Ratio, High Uniformity, and 3D Complexity by Electric Bias-Attenuated Metal-Assisted Chemical Etching (EMaCE)," *ACS Appl. Mater. Interfaces,* 2014, vol. 6, pp. 16782-16791.

66. C. Gondek, M. Lippold, I. Rover, K. Bohmhammel, and E. Kroke, "Etching Silicon with HF-H2O2-Based Mixtures: Reactivity Studies and Surface Investigations," *J. Phys. Chem. C,* 2014, vol. 118, pp. 2044-2051.

67. S. L. Cheng, C. H. Chung, and H. C. Lee, "A study of the synthesis, characterization, and kinetics of vertical silicon nanowire arrays on (001)Si substrates," *J. Electrochem. Soc,* 2008, vol. 155, pp. D711-D714.

68. V. Lehmann and U. Gosele, "Porous silicon formation: A quantum wire effect," *Appl. Phys. Lett.,* 1991, vol. 58, pp. 856-858.

69. J. Kim, H. Rhu, and W. Lee, "A Continuous Process for Si Nanowires with Prescribed Lengths," *J. Mater. Chem.,* 2011, vol. 21, pp. 15889-15894.

70. Z. P. Huang, N. Geyer, L. F. Liu, M. Y. Li, and P. Zhong, "Metal-assisted electrochemical etching of silicon," *Nanotechnology,* 2010, vol. 21, p. 465301.

71. X. G. Zhang, *Electrochemistry of Silicon and Its Oxide*. New York: Kluwer Academic/Plenum Pulishers, 2001.

72. H. Jansen, M. Deboer, R. Legtenberg, and M. Elwenspoek, "The Black Silicon Method - a Universal Method for Determining the Parameter Setting of a Fluorine-Based Reactive Ion Etcher in Deep Silicon Trench Etching with Profile Control," *J. Micromech. Microeng.,* 1995, vol. 5, pp. 115-120.

73. M. Sato and Y. Arita, "Etched Shape Control of Single‐Crystal Silicon in Reactive Ion Etching Using Chlorine," *J. Electrochem. Soc.*, 1987, vol. 134, pp. 2856-2862.

74. S. Li, W. Ma, Y. Zhou, X. Chen, Y. Xiao, M. Ma, W. Zhu, and F. Wei, "Fabrication of porous silicon nanowires by MACE method in $HF/H_2O_2/AgNO_3$ system at room temperature," *Nanoscale Res. Lett.*, 2014, vol. 9, pp. 1-8.

75. M.-L. Zhang, K.-Q. Peng, X. Fan, J.-S. Jie, R.-Q. Zhang, S.-T. Lee, and N.-B. Wong, "Preparation of Large-Area Uniform Silicon Nanowires Arrays through Metal-Assisted Chemical Etching," *J. Phys. Chem. C*, 2008, vol. 112, pp. 4444-4450.

76. L. Li, X. Zhao, and C.-P. Wong, "Charge Transport in Uniform Metal-Assisted Chemical Etching for 3D High-Aspect-Ratio Micro- and Nanofabrication on Silicon," *ECS J. Solid State Sci. Technol.*, 2015, vol. 4, pp. 337-346.

77. *CRC Handbook of Chemistry and Physics*, 84th ed.: CRC Press, 2004.

78. H. Proksche, G. Nagorsen, and D. Ross, "The Influence of NH_4F on the Etch Rates of Undoped SiO2 in Buffered Oxide Etch," *J. Electrochem. Soc*, 1992, vol. 139, pp. 521-524.

79. J. S. Judge, "A Study of the Dissolution of SiO2 in Acidic Fluoride Solutions," *J. Electrochem. Soc*, 1971, vol. 118, pp. 1772-1775.

80. S. M. Sze, *Semiconductor Devices Physics and Technology*: John Wiley&Sons, Inc, 2002.

81. Z. Huang, N. Geyer, P. Werner, J. de Boor, and U. Gösele, "Metal-Assisted Chemical Etching of Silicon: A Review," *Adv. Mater.*, 2011, vol. 23, pp. 285-308.

82. X. Zhong, Y. Qu, Y.-C. Lin, L. Liao, and X. Duan, "Unveiling the Formation Pathway of Single Crystalline Porous Silicon Nanowires," *ACS Appl. Mater. Interfaces*, 2011, vol. 3, pp. 261-270.

83. V. Lehmann, R. Stengl, and A. Luigart, "On the morphology and the electrochemical formation mechanism of mesoporous silicon," *Mater. Sci. Eng. B*, 2000, vol. 69–70, pp. 11-22.

84. W.-K. To, C.-H. Tsang, H.-H. Li, and Z. Huang, "Fabrication of n-Type Mesoporous Silicon Nanowires by One-Step Etching," *Nano Lett.*, 2011, vol. 11, pp. 5252-5258.

85. J. Taler and P. Duda, *Solving Direct and Inverse Heat Conduction Problems*. Berlin: Springer-Verlag, 2006.

86. B. Hamelin, L. Li, A. Daruwalla, C.-P. Wong, and F. Ayazi, "High-aspect-ratio sub-micron trench etching on SOI using wet metal-assisted chemical etching (MaCE) process," in *2016 IEEE 29th International Conference on Micro Electro Mechanical Systems (MEMS)*, 2016, pp. 447-450.

87. L. Li, X. Zhao, Z. Lin, and C.-P. Wong, "Uniform Vertical trench Etching on Silicon with High Aspect Ratio by Metal-Assisted Chemical Etching Using Nanoporous Catalysts," *ACS Appl. Mater. Interfaces,* 2014, vol. 6, pp. 575-584.

88. L. Li, G. Zhang, and C.-P. Wong, "Formation of Through Silicon Vias for Silicon Interposer in Wafer Level by Metal-Assisted Chemical Etching," *IEEE Transactions on Components, Packaging, and Manufacturing Technology,* 2015, vol. 5, pp. 1039-1049.

89. L. Li, X. Zhao, and C.-P. Wong, "Charge Transport in Uniform Metal-Assisted Chemical Etching for 3D High-Aspect-Ratio Micro- and Nanofabrication on Silicon," *ECS Journal of Solid State Science and Technology,* 2015, pp. 337-346.

90. O. Hildreth, K. Rykaczewski, A. Fedorov, and C.-P. Wong, "A DLVO Model for Catalyst Motion in Metal-Assisted Chemical Etching based upon Controlled Out-of-plane Rotational Etching and Force-Displacement Measurements," *Nanoscale,* 2013, vol. 5, pp. 961-970.

91. B. Hamelin, A. Daruwalla, and F. Ayazi, "Stiffness trimming of high Q MEMS resonators by excimer laser annealing of germanium thin film on silicon," in *2016 IEEE 29th International Conference on Micro Electro Mechanical Systems (MEMS)*, 2016, pp. 1026-1029.

92. L. Jian, M. P. Brenner, J. H. Lang, A. H. Slocum, and R. Struempler, "DRIE-Fabricated Curved-Electrode Zipping Actuators with Low Pull-In Voltage," in *Transducers, Solid-State Sensors, Actuators and Microsystems, 12th International Conference on, 2003*, 2003, pp. 480-483 vol.1.

93. P. Pal and K. Sato, "Various Shapes of Silicon Freestanding Microfluidic Channels and Microstructures in One-Step Lithography," *J. Micromech. Microeng.,* 2009, vol. 19, p. 05003.

94. C. Wu, F. Bendriaa, F. Brunelle, and V. Senez, "Fabrication of AD/DA Microfluidic Converter Using Deep Reactive Ion Etching of Silicon and Low Temperature Wafer Bonding," *Microelectron. Eng.,* 2011, vol. 88, pp. 1878-1883.

95. G. M. Whitesides, "The Origins and the Future of Microfluidics," *Nature,* 2006, vol. 442, pp. 368-373.

96. G. Roelkens, D. Van Thourhout, and R. Baets, "High Efficiency Silicon-on-Insulator Grating Coupler Based on a poly-Silicon Overlay," *Opt. Express,* 2006, vol. 14, pp. 11622-11630.

97. D. Taillaert, P. Bienstman, and R. Baets, "Compact Efficient Broadband Grating Coupler for Silicon-on-Insulator Waveguides," *Opt. Lett.,* 2004, vol. 29, pp. 2749-2751.

98. M. Koyanagi, T. Fukushima, and T. Tanaka, "High-Density Through Silicon Vias for 3-D LSIs," *Proc. IEEE,* 2009, vol. 97, pp. 49-59.

99. P. A. Thadesar, A. Dembla, D. Brown, and M. S. Bakir, "Novel Through-Silicon Via Technologies for 3D System Integration," in *Interconnect Technology Conference (IITC), 2013 IEEE International*, 2013, pp. 1-3.

100. Y. Aibin, J. H. Lau, H. Soon Wee, A. Kumar, H. Wai Yin, L. Wen Sheng, J. Ming Ching, V. N. Sekhar, V. Kripesh, D. Pinjala, S. Chen, C. Chien-Feng, C. Chun-Chieh, C. Chi-Hsin, H. Chih-Ming, and C. Chen, "Fabrication of High Aspect Ratio TSV and Assembly With Fine-Pitch Low-Cost Solder Microbump for Si Interposer Technology With High-Density Interconnects," *IEEE Transactions on Components, Packaging and Manufacturing Technology,* 2011, vol. 1, pp. 1336-1344.

101. H. H. Solak, C. David, J. Gobrecht, V. Golovkina, F. Cerrina, S. O. Kim, and P. F. Nealey, "Sub-50 nm Period Patterns with EUV Interference Lithography," *Microelectron. Eng.,* 2003, vol. 67–68, pp. 56-62.

102. F. Marty, L. Rousseau, B. Saadany, B. Mercier, O. Francais, Y. Mita, and T. Bourouina, "Advanced etching of silicon based on deep reactive ion etching for silicon high aspect ratio microstructures and three-dimensional micro- and nanostructures," *Microelectron. J.,* 2005, vol. 36, pp. 673-677.

103. S. Y. Chou, P. R. Krauss, and P. J. Renstrom, "Imprint Lithography with 25-Nanometer Resolution," *Science,* 1996, vol. 272, pp. 85-87.

104. E. D. Palik, V. M. Bermudez, and O. J. Glembocki, "Ellipsometric Study of Orientation‐Dependent Etching of Silicon in Aqueous KOH" *J. Electrochem. Soc,* 1985, vol. 132, pp. 871-884.

105. E. D. Palik, O. J. Glembocki, I. Heard, P. S. Burno, and L. Tenerz, "Etching Roughness for (100) Silicon Surfaces in Aqueous Koh," *J. Appl. Phys.,* 1991, vol. 70, pp. 3291-3300.

106. M. J. J. Theunissen, "Etch Channel Formation during Anodic Dissolution of N‐Type Silicon in Aqueous Hydrofluoric Acid," *J. Electrochem. Soc.,* 1972, vol. 119, pp. 351-360.

107. B. Li, C. Zhang, B. Jiang, W. Han, and Z. Lin, "Flow-Enabled Self-Assembly of Large-Scale Aligned Nanowires," *Angew. Chem. Int. Ed.,* 2015, vol. 54, pp. 4250-4254.

108. B. Li, W. Han, B. Jiang, and Z. Lin, "Crafting Threads of Diblock Copolymer Micelles via Flow-Enabled Self-Assembly," *ACS Nano,* 2014, vol. 8, pp. 2936-2942.

109. W. Han, B. Li, and Z. Lin, "Drying-Mediated Assembly of Colloidal Nanoparticles into Large-Scale Microchannels," *ACS Nano*, 2013, vol. 7, pp. 6079-6085.

110. F. Bai, M. Li, D. Song, H. Yu, B. Jiang, and Y. Li, "Metal-Assisted Homogeneous Etching of Single Crystal Silicon: A Novel Approach to Obtain an Ultra-Thin Silicon Wafer," *Appl. Surf. Sci.*, 2013, vol. 273, pp. 107-110.

111. N. Megouda, T. Hadjersi, G. Piret, R. Boukherroub, and O. Elkechai, "Au-Assisted Electroless Etching of Silicon in Aqueous HF/H2O2 Solution," *Appl. Surf. Sci.*, 2009, vol. 255, pp. 6210-6216.

112. S.-C. Shiu, S.-B. Lin, S.-C. Hung, and C.-F. Lin, "Influence of pre-surface treatment on the morphology of silicon nanowires fabricated by metal-assisted etching," *Appl. Surf. Sci.*, 2011, vol. 257, pp. 1829-1834.

113. C.-Y. Chen, Y.-R. Liu, J.-C. Tseng, and P.-Y. Hsu, "Uniform Trench Arrays With Controllable Tilted Profiles Using Metal-Assisted Chemical Etching," *Appl. Surf. Sci.*, 2015, vol. 333, pp. 152-156.

114. B. Mikhael, B. Elise, M. Xavier, S. Sebastian, M. Johann, and P. Laetitia, "New Silicon Architectures by Gold-Assisted Chemical Etching," *ACS Appl. Mater. Interfaces*, 2011, vol. 3, pp. 3866-3873.

115. D. Qi, N. Lu, H. Xu, B. Yang, C. Huang, M. Xu, L. Gao, Z. Wang, and L. Chi, "Simple Approach to Wafer-Scale Self-Cleaning Antireflective Silicon Surfaces," *Langmuir*, 2009, vol. 25, pp. 7769-7772.

116. C.-C. Tuan, Z. Lin, Y. Liu, K.-S. Moon, and C.-P. Wong, "Self-Patterning, Pre-Applied Underfilling Technology for Stack-Die Packaging," in *Electronic Components and Technology Conference (ECTC), 2014 IEEE 64th*, 2014, pp. 2231-2235.

117. Y. Liu, A. Das, S. Xu, Z. Lin, C. Xu, Z. L. Wang, A. Rohatgi, and C. P. Wong, "Hybridizing ZnO Nanowires with Micropyramid Silicon Wafers as Superhydrophobic High‐Efficiency Solar Cells," *Adv. Energy Mater.*, 2012, vol. 2, pp. 47-51.

118. X. Gao, X. Yao, and L. Jiang, "Effects of Rugged Nanoprotrusions on the Surface Hydrophobicity and Water Adhesion of Anisotropic Micropatterns," *Langmuir*, 2007, vol. 23, pp. 4886-4891.

119. X. Gu, Z. Liu, I. Gunkel, S. T. Chourou, S. W. Hong, D. L. Olynick, and T. P. Russell, "High Aspect Ratio Sub-15 nm Silicon Trenches From Block Copolymer Templates," *Adv. Mater.*, 2012, vol. 24, pp. 5688-5694.

120. C. M. Bates, M. J. Maher, D. W. Janes, C. J. Ellison, and C. G. Willson, "Block Copolymer Lithography," *Macromolecules*, 2013, vol. 47, pp. 2-12.

121. W.-S. Kim, Y. Hwa, J.-H. Shin, M. Yang, H.-J. Sohn, and S.-H. Hong, "Scalable Synthesis of Silicon Nanosheets from Sand as an Anode for Li-ion Batteries," *Nanoscale,* 2014, vol. 6, pp. 4297-4302.

122. L. Li, G. Zhang, and C.-P. Wong, "Formation of Through Silicon Vias for Silicon Interposer in Wafer Level by Metal-Assisted Chemical Etching," *IEEE Transaction on Components, Packaging and Manufacturing Technology,* 2015, vol. 5, pp. 1039-1049.

123. P. K. Mohseni, S. H. Kim, X. Zhao, K. Balasundaram, J. D. Kim, L. Pan, J. A. Rogers, J. J. Coleman, and X. L. Li, "GaAs pillar array-based light emitting diodes fabricated by metal-assisted chemical etching," *J. Appl. Phys.,* 2013, vol. 114.

124. S. H. Kim, P. K. Mohseni, Y. Song, T. Ishihara, and X. Li, "Inverse Metal-Assisted Chemical Etching Produces Smooth High Aspect Ratio InP Nanostructures," *Nano Lett.,* 2015, vol. 15, pp. 641-648.

125. L. Li, B. Song, L. Maurer, Z. Lin, G. Lian, C.-C. Tuan, K.-S. Moon, and C.-P. Wong, "Molecular engineering of aromatic amine spacers for high-performance graphene-based supercapacitors," *Nano Energy,* 2016, vol. 21, pp. 276-294.

126. B. E. Conway, "Transition from "Supercapacitor" to "Battery" Behavior in Electrochemical Energy Storage," *J. Electrochem. Soc,* 1991, vol. 138, pp. 1539-1548.

127. P. Thounthong, S. Raël, and B. Davat, "Control strategy of fuel cell/supercapacitors hybrid power sources for electric vehicle," *J. Power Sources,* 2006, vol. 158, pp. 806-814.

128. P. Thangavelu and B. Jong-Beom, "Graphene based 2D-materials for supercapacitors," *2D Materials,* 2015, vol. 2, p. 032002.

129. A. K. Geim, "Graphene: Status and Prospects," *Science,* 2009, vol. 324, pp. 1530-1534.

130. A. H. Castro Neto, F. Guinea, N. M. R. Peres, K. S. Novoselov, and A. K. Geim, "The electronic properties of graphene," *Rev. Mod. Phys.,* 2009, vol. 81, pp. 109-162.

131. B. Zhao, P. Liu, Y. Jiang, D. Pan, H. Tao, J. Song, T. Fang, and W. Xu, "Supercapacitor performances of thermally reduced graphene oxide," *J. Power Sources,* 2012, vol. 198, pp. 423-427.

132. Y. W. Zhu, S. Murali, M. D. Stoller, K. J. Ganesh, W. W. Cai, P. J. Ferreira, A. Pirkle, R. M. Wallace, K. A. Cychosz, M. Thommes, D. Su, E. A. Stach, and R. S. Ruoff, "Carbon-Based Supercapacitors Produced by Activation of Graphene," *Science,* 2011, vol. 332, pp. 1537-1541.

133. Z. Lin, Y. Liu, Y. Yao, O. J. Hildreth, Z. Li, K. Moon, and C.-p. Wong, "Superior Capacitance of Functionalized Graphene," *J. Phys. Chem. C*, 2011, vol. 115, pp. 7120-7125.

134. Z. H. Wen, X. C. Wang, S. Mao, Z. Bo, H. Kim, S. M. Cui, G. H. Lu, X. L. Feng, and J. H. Chen, "Crumpled Nitrogen-Doped Graphene Nanosheets with Ultrahigh Pore Volume for High-Performance Supercapacitor," *Adv. Mater.*, 2012, vol. 24, pp. 5610-5616.

135. P. Hao, Z. Zhao, Y. Leng, J. Tian, Y. Sang, R. I. Boughton, C. P. Wong, H. Liu, and B. Yang, "Graphene-based nitrogen self-doped hierarchical porous carbon aerogels derived from chitosan for high performance supercapacitors," *Nano Energy*, 2015, vol. 15, pp. 9-23.

136. B. Song, C. Sizemore, L. Li, X. Huang, Z. Lin, K.-s. Moon, and C.-P. Wong, "Triethanolamine functionalized graphene-based composites for high performance supercapacitors," *J. Mater. Chem. A*, 2015, vol. 3, pp. 21789-21796.

137. P. Chen, J.-J. Yang, S.-S. Li, Z. Wang, T.-Y. Xiao, Y.-H. Qian, and S.-H. Yu, "Hydrothermal synthesis of macroscopic nitrogen-doped graphene hydrogels for ultrafast supercapacitor," *Nano Energy*, 2013, vol. 2, pp. 249-256.

138. X. Lu, L. Li, B. Song, K.-s. Moon, N. Hu, G. Liao, T. Shi, and C. Wong, "Mechanistic Investigation of the Graphene Functionalization using p-Phenylenediamine and its Application for Supercapacitors," *Nano Energy*, 2015, vol. 17, pp. 160-170.

139. Y. Cui, Q.-Y. Cheng, H. Wu, Z. Wei, and B.-H. Han, "Graphene oxide-based benzimidazole-crosslinked networks for high-performance supercapacitors," *Nanoscale*, 2013, vol. 5, pp. 8367-8374.

140. Y. Lu, F. Zhang, T. Zhang, K. Leng, L. Zhang, X. Yang, Y. Ma, Y. Huang, M. Zhang, and Y. Chen, "Synthesis and supercapacitor performance studies of N-doped graphene materials using o-phenylenediamine as the double-N precursor," *Carbon*, 2013, vol. 63, pp. 508-516.

141. E. Y. L. Teo, H. N. Lim, R. Jose, and K. F. Chong, "Aminopyrene functionalized reduced graphene oxide as a supercapacitor electrode," *RSC Adv.*, 2015, vol. 5, pp. 38111-38116.

142. Q. Wu, Y. Sun, H. Bai, and G. Shi, "High-performance supercapacitor electrodes based on graphene hydrogels modified with 2-aminoanthraquinone moieties," *Phys. Chem. Chem. Phys.*, 2011, vol. 13, pp. 11193-11198.

143. E. Jokar, S. Shahrokhian, and A. I. zad, "Electrochemical functionalization of graphene nanosheets with catechol derivatives as an effective method for preparation of highly performance supercapacitors," *Electrochimica Acta*, 2014, vol. 147, pp. 136-142.

144. M. M. Sk and C. Y. Yue, "Layer-by-layer (LBL) assembly of graphene with p-phenylenediamine (PPD) spacer for high performance supercapacitor applications," *RSC Adv.,* 2014, vol. 4, pp. 19908-19915.

145. B. Song, L. Li, Z. Lin, Z.-K. Wu, K.-s. Moon, and C.-P. Wong, "Water-dispersible graphene/polyaniline composites for flexible micro-supercapacitors with High energy Densities," *Nano Energy,* 2015.

146. K. Zhang, L. L. Zhang, X. S. Zhao, and J. Wu, "Graphene/Polyaniline Nanofiber Composites as Supercapacitor Electrodes," *Chem. Mater.,* 2010, vol. 22, pp. 1392-1401.

147. S. Biswas and L. T. Drzal, "Multilayered Nanoarchitecture of Graphene Nanosheets and Polypyrrole Nanowires for High Performance Supercapacitor Electrodes," *Chem. Mater.,* 2010, vol. 22, pp. 5667-5671.

148. P. Hao, Z. Zhao, L. Li, C.-C. Tuan, H. Li, Y. Sang, H. Jiang, C. Wong, and H. Liu, "Hybrid Nanostructure of MnCo2O4. 5 Nanoneedle/Carbon Aerogel for Symmetric Supercapacitors with High Energy Density," *Nanoscale,* 2015.

149. X. Wang, W. S. Liu, X. Lu, and P. S. Lee, "Dodecyl sulfate-induced fast faradic process in nickel cobalt oxide reduced graphite oxide composite material and its application for asymmetric supercapacitor device," *J. Mater. Chem.,* 2012, vol. 22, pp. 23114-23119.

150. M. D. Stoller, S. Park, Y. Zhu, J. An, and R. S. Ruoff, "Graphene-Based Ultracapacitors," *Nano Lett.,* 2008, vol. 8, pp. 3498-3502.

151. Y. Wang, Z. Shi, Y. Huang, Y. Ma, C. Wang, M. Chen, and Y. Chen, "Supercapacitor Devices Based on Graphene Materials," *J. Phys. Chem. C,* 2009, vol. 113, pp. 13103-13107.

152. E. Song and J.-W. Choi, "Conducting polyaniline nanowire and its applications in chemiresistive sensing," *Nanomaterials,* 2013, vol. 3, pp. 498-523.

153. C.-J. Shih, S. Lin, R. Sharma, M. S. Strano, and D. Blankschtein, "Understanding the pH-Dependent Behavior of Graphene Oxide Aqueous Solutions: A Comparative Experimental and Molecular Dynamics Simulation Study," *Langmuir,* 2011, vol. 28, pp. 235-241.

154. Y. Zou, I. A. Kinloch, and R. A. W. Dryfe, "Nitrogen-doped and crumpled graphene sheets with improved supercapacitance," *Journal of Materials Chemistry A,* 2014, vol. 2, pp. 19495-19499.

155. N. A. Kumar, H.-J. Choi, Y. R. Shin, D. W. Chang, L. Dai, and J.-B. Baek, "Polyaniline-Grafted Reduced Graphene Oxide for Efficient Electrochemical Supercapacitors," *ACS Nano,* 2012, vol. 6, pp. 1715-1723.

156. T. Nishiumi, Y. Chimoto, Y. Hagiwara, M. Higuchi, and K. Yamamoto, "First Redox Polymer Bearing One-Step Successive Two-Electron-Transfer Process Based on Redox Potential Inversion," *Macromolecules,* 2004, vol. 37, pp. 2661-2664.

157. M. R. Nateghi, M. H. Mosslemin, and H. Hadjimohammadi, "Electrochemical preparation and characterization of poly (3,3′-diaminobenzidine): A functionalized polymer," *React. Funct. Polym.,* 2005, vol. 64, pp. 103-109.

158. X.-G. Li, M.-R. Huang, W. Duan, and Y.-L. Yang, "Novel Multifunctional Polymers from Aromatic Diamines by Oxidative Polymerizations," *Chem. Rev.,* 2002, vol. 102, pp. 2925-3030.

159. C. Chen, W. Kong, H.-M. Duan, and J. Zhang, "Theoretical simulation of reduction mechanism of graphene oxide in sodium hydroxide solution," *Phys. Chem. Chem. Phys.,* 2014, vol. 16, pp. 12858-12864.

160. D. R. Dreyer, S. Park, C. W. Bielawski, and R. S. Ruoff, "The chemistry of graphene oxide," *Chem. Soc. Rev.,* 2010, vol. 39, pp. 228-240.

161. M. Jung, U. Baston, T. Porwol, H.-J. Freund, and E. Umbach, "The XPS peak structure of condensed aromatic anhydrides and imides," *arXiv preprint cond-mat/0408663,* 2004.

162. Y. Yu, H. Zhang, and S. Cui, "Fabrication of robust multilayer films by triggering the coupling reaction between phenol and primary amine groups with visible light irradiation," *Nanoscale,* 2011, vol. 3, pp. 3819-3824.

163. Y. C. G. Kwan, G. M. Ng, and C. H. A. Huan, "Identification of functional groups and determination of carboxyl formation temperature in graphene oxide using the XPS O 1s spectrum," *Thin Solid Films,* 2015, vol. 590, pp. 40-48.

164. M. Acik, G. Lee, C. Mattevi, M. Chhowalla, K. Cho, and Y. J. Chabal, "Unusual infrared-absorption mechanism in thermally reduced graphene oxide," *Nat. Mater.,* 2010, vol. 9, pp. 840-845.

165. S. Bilal, A.-u.-H. A. Shah, and R. Holze, "Raman spectroelectrochemical studies of copolymers of o-phenylenediamine and o-toluidine," *Vibrational Spectroscopy,* 2010, vol. 53, pp. 279-284.

166. Z. Lin, G. Waller, Y. Liu, M. Liu, and C. P. Wong, "Facile Synthesis of Nitrogen‐Doped Graphene via Pyrolysis of Graphene Oxide and Urea, and its Electrocatalytic Activity toward the Oxygen‐Reduction Reaction," *Adv. Energy Mater.,* 2012, vol. 2, pp. 884-888.

167. M. Mitra, C. Kulsi, K. Chatterjee, K. Kargupta, S. Ganguly, D. Banerjee, and S. Goswami, "Reduced graphene oxide-polyaniline composites-synthesis, characterization and optimization for thermoelectric applications," *RSC Adv.,* 2015, vol. 5, pp. 31039-31048.

168. A. A. Athawale, M. V. Kulkarni, and V. V. Chabukswar, "Studies on chemically synthesized soluble acrylic acid doped polyaniline," *Mater. Chem. Phys.*, 2002, vol. 73, pp. 106-110.

169. Z. Liu, Q. Liu, Y. Huang, Y. Ma, S. Yin, X. Zhang, W. Sun, and Y. Chen, "Organic Photovoltaic Devices Based on a Novel Acceptor Material: Graphene," *Adv. Mater.*, 2008, vol. 20, pp. 3924-3930.

170. R. Rathore, S. V. Lindeman, and J. K. Kochi, "Charge-Transfer Probes for Molecular Recognition via Steric Hindrance in Donor-Acceptor Pairs," *J. Am. Chem. Soc.*, 1997, vol. 119, pp. 9393-9404.

171. J. McMurry, *Organic Chemistry*, 5th ed. Pacific Grove, CA: Brooks/Cole, 1999.

VITA

LIYI LI

Liyi Li was born in Zhengzhou, Henan, P.R. China. He received his B.S. degree in Chemistry from Peking University, Beijing, P.R. China in 2011. In the same year, he came to Georgia Tech to pursue a Ph.D. degree in Materials Science and Engineering. When he is not working on his research, Liyi enjoys music, movies, sports and playing computer games.